Multinuclear NMR Investigations of Local Structure, Distortions and Redox Mechanisms in Layered Lithium Ion Battery Cathode Materials

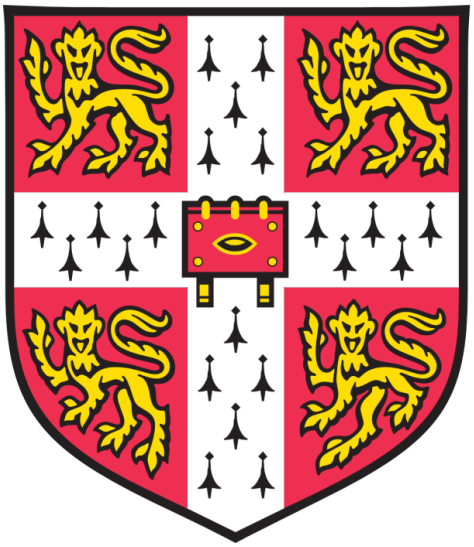

University of Cambridge
Department of Chemistry

Philip J. Reeves

Wolfson College

September 2019

This dissertation is submitted for the degree of

Doctor of Philosophy

This work is dedicated to my parents Julie and Mark Reeves

Declaration

I hereby declare that except where specific reference is made to the work of others, the contents of the dissertation are original and have not been submitted in whole or in part for consideration for any other degree or qualification in this, or any other University. This dissertation is the result of my own work and includes nothing that is the outcome of work done in collaboration except where specifically indicated in the text. This dissertation contains less than 60000 words excluding the table of contents, figure captions, bibliography and acknowledgements.

Philip James Reeves

September 2019

Acknowledgements

I would like to thank my wonderful supervisor Prof. Clare P. Grey for her guidance, encouragement and patience. I feel incredibly fortunate to work for not just an inspirational scientist but also someone who exemplifies what it means to lead from the front; her relentless hard work and willingness to throw the scientific kitchen (lab?) sink at projects definitely percolates down through the whole group. The greatest resource that I have been able to draw on in the last four years, is the willingness of so many brilliant people to offer their help, often without even having to be asked and I think a lot of that comes from the example that Clare sets for us all.

Dr Nicole Trease taught me so much about NMR and battery chemistry during the early days of my PhD. I am grateful for her taking me under her wing, helping shake down the scary post-docs for their 1.3mm rotors and for being a friend as well as a teacher. Dr Ieuan Seymour has been something of a scientific idol of mine, he always seems to know just what paper I need to read to understand my data better. I thank him for his brilliant insights into all aspects of solid-state chemistry and for encouraging me to conduct my work to his rigorous standards. His catchphrases still ring in my ears, notably “you’re not going to like this but...” generally followed by a suggestion that we check the magic angle. We have shared discussions and rotor crashes (although fortunately not in equal quantity).

I would like to thank every member of the Grey Group over the last four years. I have made many friends for life and I couldn't have wished for a better environment to work in. In particular I must thank my office mates: Dr Michael A. Hope, since day 1 in the cave I couldn't have asked for a better friend and scientific consigliere. Dr Matthew Dunstan for our fierce Race for Galaxy rivalry, which so often helped to decompress my brain after a tough day. Dr David Halat for his boundless enthusiasm for whacky NMR and Bananagrams and Dr Silvia Britto for having the best laugh in the group and using it generously regardless of the quality of my jokes.

I have been lucky enough to "supervise", day to day, two wonderful young scientists: Michael Jones and Euan Bassey, who as well as being a pleasure to work with, have been great sounding boards for ideas. Additionally, I thank Michael for quietly taking care of all my lab jobs whilst I was writing up and Euan for his discussions about the magnetism and EPR.

I must acknowledge the collaborators I have worked within the group and through NECCES. I am grateful to Dr Erlendur Jónsson for writing useful scripts for processing the VOCS spectra throughout this work. Dr Katharina Marker for sharing her scripts for modelling Li-motion in Chapter 2. I am grateful to Dr Brian May who provided the NCA precursors in Chapter 2. I thank Dr Antonin Grenier and Zachary Lebens-Higgins for our discussions about diffraction and XANES.

I thank the North East Center for Chemical Energy Storage (NECCES), an Energy Frontier Research Center funded by the U.S. Department of Energy, Office of Science, Office of Basic Energy Sciences, under award DE-SC0012583 for funding.

I must thank my parents and my siblings for their love and support which has given me strength during hard moments. Finally, I must thank Ruth for being a wonderful partner and teammate in all aspects of my life and for her love and kindness which fill me up with happiness every day.

Abstract

Lithium ion (Li-ion) battery technology has enabled a complete revolution in consumer electronics and is beginning to have a similar impact on transport. Increased adoption of electric vehicles is essential to reduce anthropogenic carbon emissions and combat climate change. For vehicular applications, improvements in specific and volumetric capacity are desirable, if they can be achieved without sacrificing safety, cost or cyclability. The redox mechanisms of many of the cathode materials with the highest capacities, particularly the "Li-excess" family, are poorly understood however, and such materials typically show accelerated degradation that makes commercial implementation impractical.

Solid state NMR is a powerful tool to study local structure and $^{6/7}$Li NMR has been used extensively to probe many aspects of local structure and dynamics in Li-ion batteries. Less commonly studied nuclei, such as ^{59}Co and ^{17}O can also offer complementary information, although their implementation and interpretation can be challenging. In this thesis the local structure, distortions and delithiation behaviours of two intriguing compounds are investigated: $LiNi_{0.8}Co_{0.15}Al_{0.05}O_2$ (NCA)—a commercial cathode material with complex redox behaviour—and Li_2RuO_3—a model compound for the highly promising Li-excess family of compounds.

Firstly, the structure of pristine NCA is characterised. The complex dynamics of the Ni^{3+} Jahn-Teller (JT) distortion are probed using ^{7}Li, ^{17}O, ^{27}Al and ^{59}Co NMR

spectroscopies and, by comparison with the expected statistical distribution of environments, a model emerges in which the JT distortions are dynamically disordered but the average structure is weighted towards thermodynamically favoured arrangements. This study is then extended to electrochemically delithiated NCA samples, which reveals enhanced Li mobility on delithiation from variable temperature (VT) ^{7}Li NMR measurements. Using an extension of the statistical model employed for the pristine material, the lineshapes are modelled and hopping rates for Li are estimated. At the onset of fast Li motion, two populations of Li are observed, indicating heterogeneous delithiation; this may suggest a kinetic origin for the reaction heterogeneity and poor first cycle coulombic efficiency observed in NCA. Finally, the redox mechanisms and electronic structure of NCA are investigated. ^{59}Co NMR reveals a population of Co^{3+} is present at the end of charge, demonstrating a deviation from the conventional cation redox model. The unintuitive evolution of the ^{59}Co peak position further reveals an evolution of the Co^{3+} electronic structure which is consistent with the observed long-range structural changes.

Li_2RuO_3 and its doped analogues are commonly employed as model compounds to understand redox mechanisms in Li-excess cathode materials. Despite its single redox centre and well-ordered Ru-layer, ^{7}Li and ^{17}O NMR, along with magnetic susceptibility measurements confirm that that the Ru^{4+} ions form dimers and the effect of dimerisation on the observed ^{17}O NMR shifts is elucidated. The dimers, which are ordered at room temperature, lose their long-range ordering above 260 °C when Li_2RuO_3 undergoes a phase transition. This phase transition is characterised using laser-heated VT NMR and the changes observed, via ^{7}Li and ^{17}O NMR, reflect the changes in susceptibility and confirm the room temperature assignments. The changes in the structure, dimerisation of Ru and electronic structure in Li_2RuO_3 on delithiation are then investigated, which have implications for the understanding of the redox mechanisms in this highly studied compound and other Li-excess compounds. Notably,

it is found that the Ru-dimerisation, which is highly influential in the pristine material, appears to remain throughout the discharging process.

List of Publications

Chapter 3:contains material from the publication:

Reeves, P. J.; Seymour, I. D.; Griffith, K. J.; Grey, C. P. Characterizing the Structure and Phase Transition of Li_2RuO_3 Using Variable-Temperature ^{17}O and ^{7}Li NMR Spectroscopy. *Chem. Mater.* 2019, *31*, 2814–2821.

Publications not included in this thesis:

Marker, K.; Reeves, P. J.; Xu, C.; Griffith, K. J.; Grey, C. P. Evolution of Structure and Lithium Dynamics in LiNi 0.8 Mn 0.1 Co 0.1 O 2 (NMC811) Cathodes during Electrochemical Cycling. *Chem. Mater.* 2019, *2*.

Jones, M. A.; Reeves, P. J.; Seymour, I. D.; Cliffe, M.; Dutton, S. E. E.; Grey, C. P. Short-Range Ordering in Battery Electrode, the 'Cation-Disordered' Rocksalt Li $_{1.25}$ Nb $_{0.25}$ Mn $_{0.5}$ O $_{2}$. *Chem. Commun.* 2019, 2–5.

Lebens-Higgins, Z. W.; Faenza, N. V.; Radin, M. D.; Liu, H.; Sallis, S.; Rana, J.; Vinckeviciute, J.; Reeves, P. J.; Zuba, M. J.; Badway, F.; et al. Revisiting the Charge Compensation Mechanisms in LiNi $_{0.8}$ Co $_{0.2-y}$ Al $_{y}$ O $_{2}$ Systems. *Mater. Horizons* 2019.

Shi, Y.; Zhou, H.; Seymour, I.; Britto, S.; Rana, J.; Wangoh, L.; Huang, Y.; Yin, Q.; Reeves, P.; Zuba, M.; et al. Electrochemical Performance of Nanosized Disordered $LiVOPO_4$. *ACS Omega 3*, 7310–7323.

Contents

List of Figures

List of Tables

List of Abbreviations

ccp	Cubic close packed
CEI	Cathode electrolyte interface
CSA	Chemical shift anisotropy
DFT	Density functional theory
EEI	Electrode electrolyte interface
EFG	Electric field gradient
EXAFS	Extended x-ray absorption fine structure
HAXPES	Hard x-ray photoemission spectroscopy
hcp	Hexagonal close packed
MAS	Magic angle spinning
mRIXS	Mapping resonant inelastic x-ray spectroscopy
NCA	$LiNi_{0.8}Co_{0.15}Al_{0.05}O_2$
NMC	$LiNi_xMn_yCo_zO_2$
NMR	Nuclear magnetic resonance
RF	Radio frequency
RIXs	Resonant inelastic x-ray spectroscopy
SEI	Surface electrolyte interface
VOCS	Variable offset cumulative spectroscopy/spectrum
VT	Variable temperature

XANES	X-ray absorption near edge spectroscopy
XAS	X-ray absorption spectroscopy
XPS	X-ray photoelectron spectroscopy
XRD	X-ray diffraction
B_0	External magnetic field
C_Q	Quadrupolar coupling constant
η_Q	Quadrupolar asymmetry
T_1	Longitudinal (spin-lattice) relaxation time constant
T_2	Transverse (spin-spin) relaxation time constant
τ	Hahn-echo delay period
ω_0	Larmor frequency

Chapter 1: Introduction

1.1 Li-Ion Batteries

The impact of Li-ion batteries since the first commercialization of the cathode/anode chemistry $LiCoO_2/C$ by Sony in 1991 has been extraordinary;[1] the mass adoption of electronic devices such as smart phones and portable computers has been driven by the high gravimetric and volumetric energy densities achieved with Li-ion battery chemistries. The development of batteries that are optimized for use in electric vehicles (EVs) is of great commercial, scientific and environmental interest, as battery powered EVs offer the lowest energy demand per kilometre of any current vehicle power system; they offer a lower environmental impact than a gasoline based vehicle, even if the electricity used to charge them is generated by the burning of fossil fuels.[2] The current market share for EVs is relatively low, with plug-in hybrid (PHEV) and battery electric vehicles (BEV) together accounting for 1.7 % of all car and van sales in the UK in 2017, but this proportion is projected to rise, with a recent recommendation by 2035 that 60% of new car and van sales in the UK should be BEVs or PHEVs if the UK is to reach its 2050 climate change targets.[3] If this increase is to occur in line with or ahead of these projections, then it is essential that EV battery cost drop substantially, to \$120 per kWh from the figure of \$350 per kWh in 2014[4]. In order to realize this possibility, new battery chemistries that deliver high gravimetric energy densities at low cost, need to be developed.

1.1.1 Fundamentals of Batteries

A battery, which is made of an array of electrochemical cells, is a transducer converting stored chemical energy into electrical energy. In the case of a rechargeable or secondary battery this process is reversible. A cell may be thought of as the reaction of two chemical species, in which the motion of ions and electrons have been separated. The

chemical species must be conductive or hosted in a conductive medium and are called electrodes; the difference in the chemical potentials of the electrodes determines the electrical potential that may be drawn from the cell (Figure 1.1).

$$\Delta G_r^\circ = -zFV_{oc} \tag{1.1}$$

Equation (1.1) demonstrates the balance in energies present when the battery is under open circuit conditions (the external circuit is broken and no current is flowing). The standard Gibbs free energy (ΔG_r°) is the energy that would be liberated if the two electrodes where to react together under standard conditions. This is balanced by an electrostatic energy, where z is the charge number of the ions transported in the reaction, F is the Faraday constant and V_{oc} is the open circuit voltage of the cell.[5]

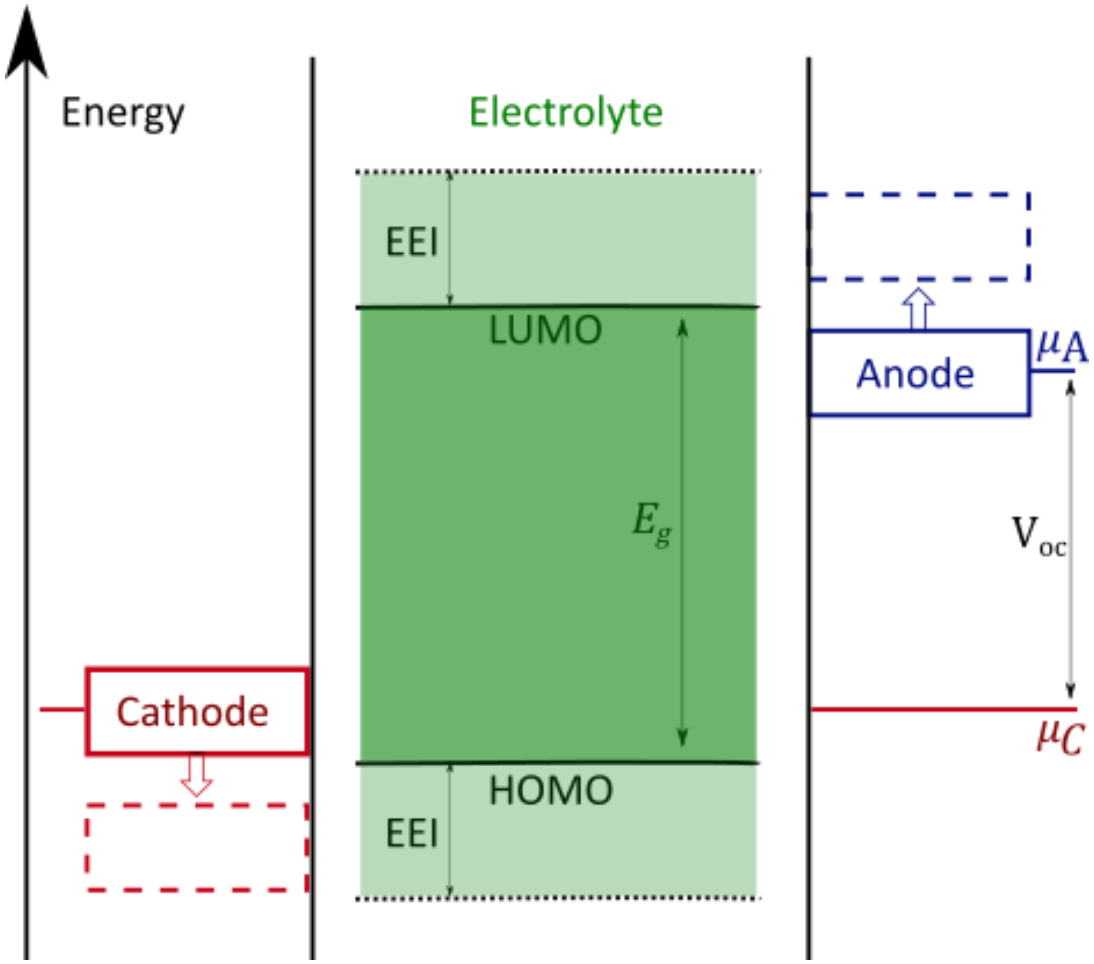

Figure 1.1 Energy scale of an electrochemical cell showing the energy gaps that give rise to the open circuit voltage (V_{OC}) and electrolyte voltage window (E_g) as well as the extension of this window by passivating EEI formation. The arrows show how the cathode and anode energies vary on charging, that is lithium is intercalated from cathode and into the anode, evidently at these higher potentials, electrolyte degradation is more likely. Figure adapted from Goodenough and Kim[6]

An electrolyte mediates the flow of ions between the two electrodes, but to act as a separator it must be electrically insulating; forcing the electrons to flow through an external circuit. In addition, the electrolyte must not react with either electrode. The anode, which has a high chemical potential (μ_a), will donate electrons into the lowest unoccupied molecular orbital (LUMO) of the electrolyte and reduce it, if it is higher in energy. Conversely the cathode, which has a low chemical potential (μ_C) will remove electrons from the electrolyte if it lies lower in energy than the highest occupied molecular orbital (HOMO) of the electrolyte causing oxidation.[6] Figure 1.1 demonstrates the voltage window that all electrolytes are limited by E_g, the energy separation of the HOMO and LUMO. The window may be extended if the degradation

of the electrolyte leads to the formation of a stable and electronically insulating electrode electrolyte interface (EEI) which is responsible for the large voltage windows useable in many common Li-ion batteries. The anode EEI is very well studied due to its importance in stabilising the voltage window of the cell and is commonly referred to as solid electrolyte interface (SEI), conversely cathode EEI is less well studied and is commonly referred to as cathode electrolyte interface (CEI).

Each component of a cell has materials challenges that offer opportunities to improve current battery performance; however, with a view to reducing cost, improving safety characteristics and increasing capacity, the cathode is where there is most room for improvement. Anodes in current commercial cells are typically graphitic carbon which is relatively inexpensive and has a larger practical capacity than the classic cathode material $LiCoO_2$ (~372 $mAhg^{-1}$ compared to ~140$mAhg^{-1}$)[7,8]. Cathodes are the limiting component in the system and a great deal of effort is directed towards developing new cathode materials, understanding the mechanisms involved in charge and discharge and overcoming issues which plague the commercial implementation of many promising materials.

1.1.2 Intercalation Batteries

Most rechargeable battery materials have an open framework structure that is a stable host into which mobile guest species (such as Li^+ ions) can be inserted and extracted. These hosts often, particularly in the case of commercial batteries, have a layered structure with space between the layers that can be occupied by the guest species, for example the ubiquitous $LiCoO_2$ (Figure 1.3).[9] The insertion and extraction of the guest species, often referred to as intercalation and deintercalation respectively, can take place in two main ways. For the case the of insertion atoms, guests may be entered by forming a second phase, which can be ordered or disordered, this phase nucleates and spreads across the whole structure as more guests are added (Figure 1.2a). On the other hand, they may be inserted so that the first phase is preserved but the guest

concentration gradually rises across the whole structure, in which case the composition of the structure changes smoothly and there is no interface or division of phases: a solid solution (Figure 1.2b). The electrochemical response of these two situations is quite distinct. The potential of the cell is still determined by the chemical potential of products of the reaction between the electrodes: in a solid solution the composition and hence the electrochemical potential of one is constantly changing, this leads to a sloped response (Figure 1.2b). A two phase reactions gives rise to a plateau with constant potential as the composition of the structure into which the guests are entering is effectively constant, only its fraction of the total changes, until the entire structure has become the second phase (Figure 1.2a) .

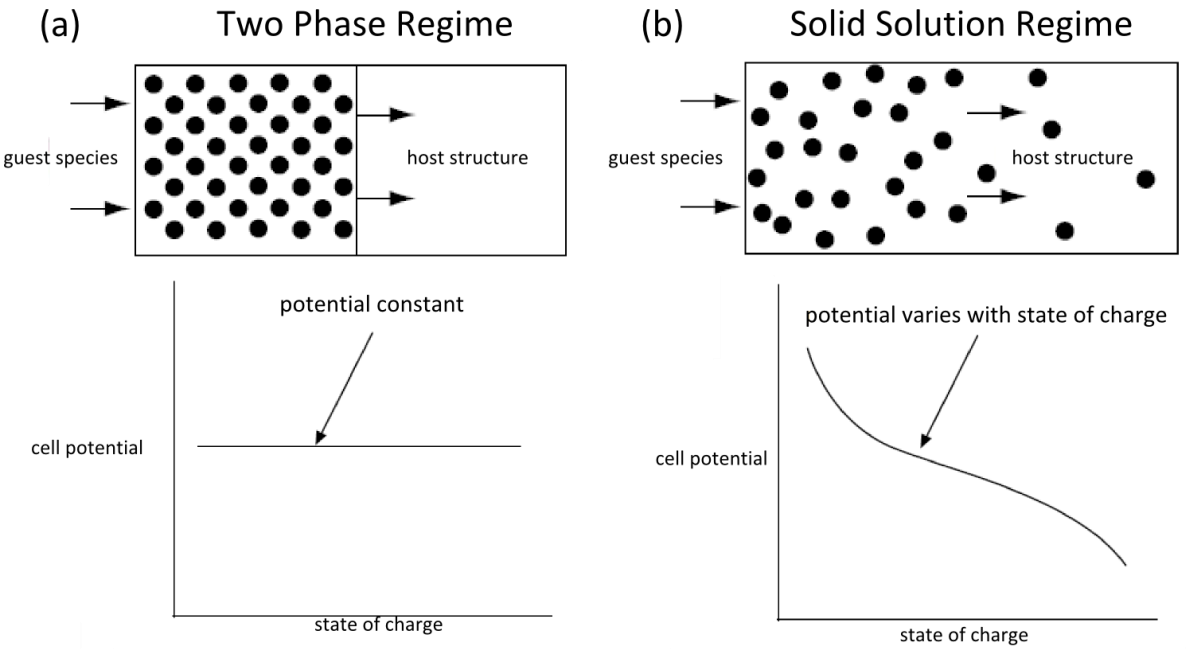

Figure 1.2 Schematic representation of intercalation of guest species into a host via either a two phase (a) or solid solution (b) mechanism and the expected response of the potential on discharging. The two-phase regime has been shown as an ordered two-phase reaction but the newly formed phase can also be disordered.

1.2 Stoichiometric Layered Rocksalts

The $LiTMO_2$ structure type, to which a large swathe of Li-ion cathode materials belong, is part a larger family of rocksalt-type materials. This encompasses all the phases which,

in analogy to the cubic NaCl structure, have a face centred cubic (FCC) lattice of O with metal cations (Li and other metals) occupying the octahedral interstices, forming a second FCC lattice. If all the metal sublattice sites are equivalent, then the structure is a cation-disordered rocksalt (α-$LiFeO_2$ structure type). Some battery materials of this type do exist—$Li_{1.211}Mo_{0.467}Cr_{0.3}O_2$[10], $Li_{1.25}Mn_{0.5}Nb_{0.25}O_3$[11], $Li_x Ni_{2-4x/3} Sb_{x/3} O_2$[12] and others[13–15]—and are the subject of much research activity.[16] The archetypical Li-ion battery material is $LiCoO_2$, which has a layered arrangement of Li^+ and Co^{3+}, in the same structural framework as α-$NaFeO_2$ (Figure 1.3) and it is this class of materials, both 'stoichiometric' (with a Li:TM ratio equal to 1) and 'Li-excess' (with a Li:TM ratio greater than 1), which are the subject of this work. Initially $LiCoO_2$ will be discussed as understanding this benchmark material is essential in order to understand newer and less explored materials. Despite the ubiquity of $LiCoO_2$, Co is less desirable as a TM for use in Li-ion cathodes due to its high cost and toxicity. Replacing it with one or more cheaper and less toxic TMs has been an extremely active area of investigation and we will briefly review the challenges and successes associated with these efforts.

1.2.1 $LiCoO_2$

$LiCoO_2$ is currently the established material for Li-ion battery cathodes. It rose to dominance after it's commercialisation during the 1980's, thanks to its easy synthesis and higher redox potential (by comparison to the original Li-ion cathode material: $LiTiS_2$).[17] The high voltage of $LiCoO_2$ enabled the use of the much safer graphitic carbon as the anode over Li metal; the loss of cell potential, that results from using graphite over Li metal, reduced the cell potential to unfeasibly low levels for $LiTiS_2$[17]. The discharge potential of $LiCoO_2$ is around 4 V with respect to Li metal with a theoretical capacity of 272 $mAhg^{-1}$. [18] This assumes that all of Li can be removed, although in practice the capacity of $LiCoO_2$ is usually limited to ~140 $mAhg^{-1}$, due to phase transitions that occur beyond $Li_{0.5}CoO_2$ which reduce its cyclability.

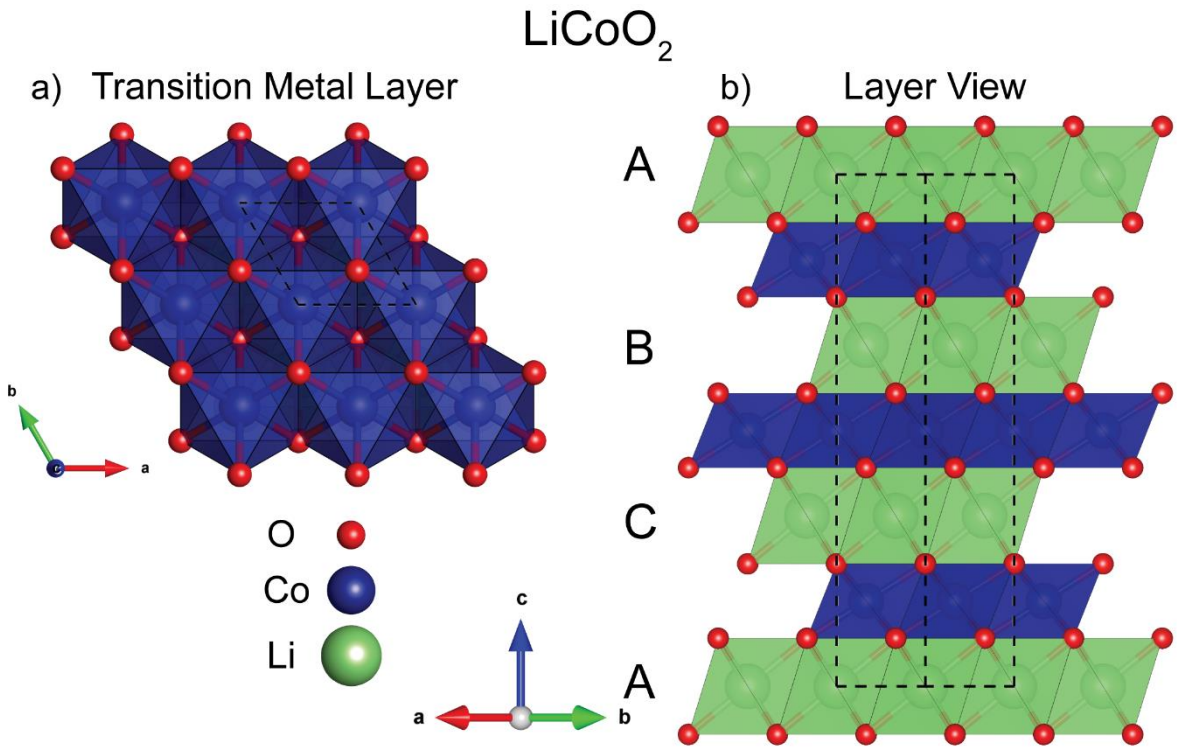

Figure 1.3 Crystal structure representations of $LiCoO_2$. a) The view along the c axis showing the network of edge sharing Co^{3+} octahedra. b) View across the ab plane showing the layered structure. The stacking of the layers is ABC–repeating after 3 layers. The $R\bar{3}m$ unit cell is shown by dashed lines.

$LiCoO_2$ has a rhombohedral unit cell $R\bar{3}m$ (Figure 1.3) with layers of edge sharing octahedra of Li^+ and Co^{3+} stacked such that there are three layers in each repeat unit. This ABC type stacking is often referred to, using the notation devised by Delmas et al.[19], as O3 (octahedral and with the layers repeating about three units). In Li-ion battery cathodes, both tetrahedral and octahedral coordination of Li occurs, although in the layered $LiTMO_2$ materials in this report, the Li coordination is primarily octahedral. In contrast tetrahedral sites are generally not observed in Na-ion batteries, in which the Na coordination is generally octahedral or prismatic (P in Delmas' scheme).

The practical limit of 0.5 Li removed per formula unit is caused by several factors. At $x = 0.5$ (where x corresponds to the fraction of Li remaining, per formula unit) the Li undergoes an order/disorder transition caused by the ordering of the Li ions into chains[20,21] and as a consequence a reduction in symmetry from rhombohedral to

monoclinic. On continued delithiation the stacking sequence changes from the original O3 stacking, via an intermediate 'hybrid' O3-O1 phase (often termed H1-3), to another monoclinic phase with O1 stacking.[22] These first order phase transitions can cause the mechanical degradation of the $LiCoO_2$ particles.[23,24] Mechanical degradation can also be caused simply by changes in unit cell volume causing fracturing of secondary particle and loss of electronic contact. The general trend for layered materials on delithiation is an initial expansion of the c-lattice parameter followed by a collapse of the c-lattice at high states of charge. The expansion is caused by increased electrostatic repulsion between the TMO slabs as Li is removed.[25] The TM–O bond distances also become shorter, as the ionic radii of the redox active TM ions, which are oxidised as the Li is removed, become smaller.[26,27] This leads to an increase in the Li–O slab size initially. The collapse of the c lattice parameter is thought to be caused by an increase in Van der Waals interactions between the TM–O slabs and causes the Li–O slabs to shrink.[28] The slab size changes have serious effects on the Li-mobility in many layered oxides as will be discussed in more detail in Chapter 2.[26]

$LiCoO_2$ undergoes a metal–insulator transition upon delithiation: the onset of the metallic state occurs between $Li_{0.75}CoO_2$ and $Li_{0.95}CoO_2$, depending on the degree of "stoichiometry" of the sample. More "stoichiometric" samples (i.e. those with minimal Li excess) have an earlier onset of the transition.[29,30] Co^{3+} is d6 low spin in $LiCoO_2$ and this means that it has a smaller ionic radius than Ni^{3+} despite the latter's greater nuclear charge. In addition, the location of the valence electrons in $LiCoO_2$ in the t_{2g} orbitals (Figure 1.5) causes the average redox potential of $LiCoO_2$ to be higher than for example $LiNiO_2$ or $LiMnO_2$ whose valence electrons are contained in the e_g* orbitals (more detail section 1.2.5).

1.2.2 $LiNiO_2$

The substitution of Co^{3+} with Ni^{3+} in $LTMO_2$ is attractive due to the lower cost of Ni and the structural similarity between $LiCoO_2$ and $LiNiO_2$.[31] $LiNiO_2$ and other Ni

substituted $LiCoO_2$ analogues have lower average redox potentials than $LiCoO_2$, due to the fact that Ni^{3+} is a d7 low spin ion ($t_{2g}^6 e_g^{*1}$) and hence the higher energy e_g^* states are partially occupied.[32] Due to its partially filled e_g^* states Ni^{3+} is also a Jahn-Teller ion and undergoes an elongation of 1 axis of its oxygen octahedron, along with the compression of the other Ni–O bonds (Figure 1.4b). In $LiNiO_2$ the Jahn-Teller distortions are not cooperative and do not induce a coordinated distortion of the lattice (at least above 30K).[33–35]

Stoichiometric $LiNiO_2$ is difficult to synthesise. Some degree of Ni-excess, which is easily accommodated as Ni^{2+} in the Li layer, is almost inevitable and it is more accurate to write the formula for lithium nickel oxide as $Li_{1-x}Ni_{1+x}O_2$.[36] Disorder of this kind is endemic in all Ni containing $LiTMO_2$ materials due to the similar charges and ionic radii of Li^+ (0.76Å) and Ni^{2+} (0.69Å).[37] Substitution of the Ni^{2+} into the Li-layer must be charge compensated. In $LiNiO_2$ the dominant mechanism for this is the reduction of Ni^{3+} in the TM-layer, to Ni^{2+} (i.e. Li^+ and Ni^{3+} are replaced by $2Ni^{2+}$). Another possible mechanism of charge compensation is the formation of true antisite defects (where Li^+ and Ni^{2+} occupy one another's sites). Neutron diffraction studies suggest that antisite defect formation is not really observed in $LiNiO_2$.[38] This is likely because accommodating Ni^{2+} in the TM-layer (as required by the Ni reduction mechanism) is easier that accommodating Li^+, which is larger and more different in charge (as required by the antisite mechanism).

Li is volatile at the high synthesis temperatures required to form layered $LiTMO_2$ (>700°C)[39] and therefore it is common to include additional Li (5-10 % is typical) during the synthesis to account for this volatility.[40,41] The presence of TMs in the Li layer is easily detected by XRD due to the high contrast between electron rich TM ions and the Li whose sites they occupy. The ratio between the (003) and (104) peaks can be used to estimate the fraction of TM ions in the Li-layer, even without performing a full Rietveld refinement, although obviously for proper quantification refinement of

the site occupancies is necessary.[42,43] Li/Ni disorder is also evident from magnetic measurements. Due to the well separated TM and Li layers interlayer exchange interactions are very weak in well layered $LiTMO_2$ materials. If there is Ni in the Li layer then the interlayer 180° superexchange pathway is very strongly antiferromagnetic, particularly if there is Ni^{2+} in the TM layer (as will be the case for Mn containing $LiTMO_2$). [44–47]

1.2.3 $LiMnO_2$

A Mn analogue to $LiCoO_2$ was sought after for a long time, as a cheaper less toxic possibility for Li-ion cathodes, however synthesis via conventional methods produce an orthorhombic phase (*o*-$LiMnO_2$) with the space group *Pmmn*. Mn^{3+} is a high spin d4 ion with degenerate partially occupied e_g^* orbitals ($t_{2g}^3 e_g^{*1}$) and undergoes a positive Jahn-Teller distortion (Figure 1.4b). In *o*-$LiMnO_2$ this gives rise to cooperative JT distortion along the b direction (Figure 1.4d). It was shown that it is possible to form a layered phase of $LiMnO_2$ via ion exchange from α-$NaMnO_2$[48,49] (the larger ionic size of the Na^+ stabilises the layered form) and that this layered $LiMnO_2$ is metastable with respect to the orthorhombic "corrugated" phase. Layered $LiMnO_2$ also has a cooperative Jahn-Teller distortion that lowers the symmetry from $R\bar{3}m$ to $C2/m$ (Figure 1.4c).

Layered $LiMnO_2$ suffers from poor cyclability as it is rapidly transformed into a spinel like phase.[50] This transformation involves $\frac{1}{4}$ of the Mn ions migrating into the Li layer, along with Li ions moving to occupy tetrahedral sites. One reason this transformation occurs so readily is that no rearrangement of the oxygen lattice is required. On delithiation, many layered compounds transform to the corresponding spinel phase on heating,[51–53] indeed first principles calculations have shown that at a composition of x=0.5, the spinel phase is more thermodynamically stable than the layered phase for $Li_{0.5}CoO_2$, $Li_{0.5}NiO_2$ and $Li_{0.5}MnO_2$.[54,55] Whether or not a material undergoes a layered to spinel transformation is largely determined by the energetic penalty associated with migration of TM to the octahedral Li layer sites; this migration occurs via an

intermediate tetrahedral site.[56,57] As the intermediate site is tetrahedral, the propensity of a layered material to undergo a spinel transformation is greater if the migrating ion is relatively stable in tetrahedral versus octahedral coordination.[58,59] For $LiMnO_2$ migration of Mn into tetrahedral sites is particularly easy: There is only a small energy barrier for Mn^{3+} to disproportionate, producing Mn^{2+} and Mn^{4+}. The Mn^{2+} has no site preference for octahedral sites as the crystal field stabilisation energy is identical between tetrahedral and octahedral sites, therefore it readily migrates.[59] $LiCoO_2$ by contrast is much more energetically costly. It is notable that the oxidation state of the migrating Mn ion is predicted by first principles calculations to be 2+; As Mn^{3+} or Mn^{4+} have lower ionic size, they might be expected to be more easily accommodated in the tetrahedral size, however the greater crystal field stabilisation for Mn^{2+} dominates the size considerations.[59]

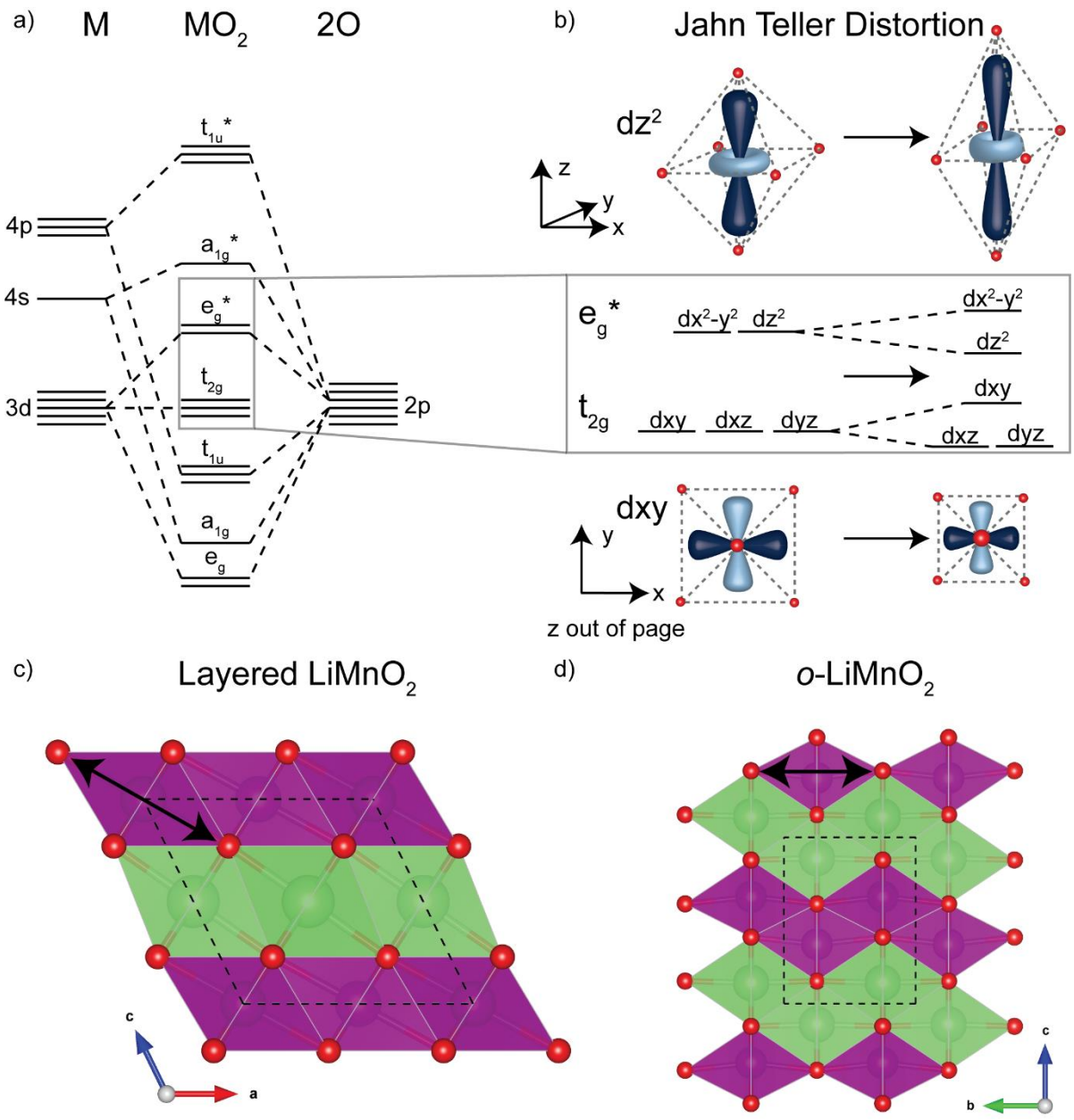

Figure 1.4 a) Schematic representation of the band structure expected for $LiTMO_2$ compounds adapted from Aydinol et al,[27] b) schematic representation of 3d orbitals in $LiTMO_2$ highlighting the effect of a Jahn-Teller distortion on the energy levels and the corresponding coordination geometry changes. c,d) Crystal structures of (c) layered and (d) orthorhombic $LiMnO_2$ showing a view along the "layers" demonstrating the α-$NaFeO_2$ like structure for "layered $LiMnO_2$" and the corrugation of the layers in the *o*-$LiMnO_2$. Unit cells are shown with dashed lines and the direction of the cooperative Jahn-Teller distortion is shown by the black arrows.

1.2.4 NMC and NCA

The current state of the art materials for commercial Li-ion battery materials are so called "alloy" materials in which multiple TMs are employed. One immediate and obvious benefit of using multiple TMs is reducing the amount of toxic and expensive cobalt required. In addition to this, the characteristics of the TMs used often combine in cooperative fashion such that mixed TM $LiTMO_2$ compounds, particularly $LiNi_xMn_yCo_zO_2$ (NMC) and $LiNi_{0.8}Co_{0.15}Al_{0.05}O_2$ (NCA), have become the commercial favourites.

The electrochemical profile of both NMC and NCA are much smoother and lack the kinks and plateaus associated with the phase transitions and Li-vacancy ordering that occur in the single TM materials (Figure 1.5). The mixed TM layer, which shows no long range order, suppresses the cooperative charge ordering that gives rise to the Li-vacancy orderings in $LiCoO_2$ and $LiNiO_2$.[36] The reason that O3→O1 transitions are not generally observed in NCA and NMCs is less clear but it is a fairly universal observation; even in Ni-rich NMCs ($LiNi_{0.8}Mn_{0.1}Co_{0.1}O_2$)—which is so nickel rich that it might be expected to show similar characteristics to $LiNiO_2$—no O3→O1 transition is observed[26].

Another key effect of alloying is a reduction of Ni^{2+} substitution on the Li sites in both NMC and NCA. This has been attributed to both the Co^{3+} and the Al^{3+} reducing the TM-slab size and inhibiting the Ni reduction mechanism of charge compensation discussed previously (section 1.2.2) by destabilising Ni^{2+} in the metal layer. Al and Co cannot be oxidised easily to 2+ and are strictly trivalent in $LiTMO_2$.[60,61] This makes the synthesis of high quality, Ni-rich materials (which due to their relatively low cost and good performance) relatively straightforward, this is part of the reason these are some of the most popular commercial materials.

1.2.5 Redox Mechanisms in Stoichiometric Layered Rocksalts

In order to improve cathode materials, an understanding of the electronic structure, how it changes on cycling and the redox mechanisms, is vital. The model generally invoked for TMs in octahedral coordination involves the splitting of the d orbitals into e_g ($d_{x^2-y^2}$ and d_{z^2}) and t_{2g} (d_{xy}, d_{yz} and d_{xz}). The e_g orbitals have the correct symmetry to overlap with the O2p orbitals and form bonding and antibonding orbitals. The bonding orbitals lie very low in energy, are mostly localised on the O atoms and are not really involved in the redox chemistry. The antibonding orbitals which have mostly TM character are occupied in the case of $Ni^{2/3+}$ and Mn^{3+} and usually lie at the fermi level and are therefore the most easily oxidised states. The t_{2g} orbitals, which point between the O ligands do not have the correct symmetry to form σ overlaps with the O2p orbitals and are generally considered to be non-bonding and localised on the TM. Due to its valence electrons being held in the lower energy t_{2g} orbitals Co^{3+} requires the highest potentials out of Co^{3+}, $Ni^{2/3+}$ and Mn^{3+}, in order to oxidise it. $Ni^{2/3+}$ and $Ni^{3/4+}$ both require higher potentials than Mn^{3+}/Mn^{4+}. This hierarchy of potentials can be observed in the different voltages observed for $LiCoO_2$, $LiMnO_2$ and $LiNiO_2$ (Figure 1.5).

In practice the redox energy mechanisms in alloyed materials like NMC and NCA rarely proceed in a linear sequential manner. Firstly, in NMC, as the $Mn^{3+} \rightarrow Mn^{4+}$ redox couple is higher in energy than $Ni^{2+} \rightarrow Ni^{3+}$, Mn^{3+} donates electrons to Ni^{3+} forming Mn^{4+} and Ni^{2+}. This mechanism is present across all the Ni/Mn alloy compounds. If the ratio Mn/Ni=1 then all the TMs will "disproportionate" in this manner; an excess of Ni or Mn will result in some 3+ ions of that species being present. Secondly ionic size plays a role, as in a mixed metal slab, not all the M–O distances can be optimised for each metal and the energy level of the TM–O bands will be different from the single TM complex. An example would be NCA, for which there is some evidence that the

sequential $Ni^{3+} \rightarrow Ni^{4+}$ then $Co^{3+} \rightarrow Co^{4+}$ redox processes expected occur with some overlap or simply simultaneously.[62,63]

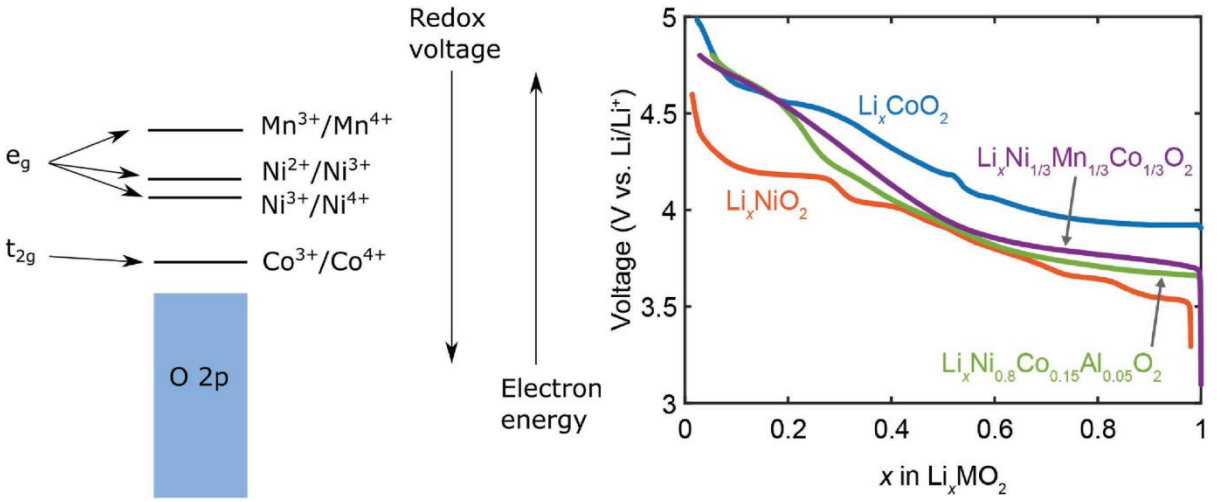

Figure 1.5 a) schematic representation of the energy levels of Ni, Mn and Co. b) representative electrochemical voltage curves for $LiCoO_2$, $LiNiO_2$, NMC333 and NCA. Reproduced from reference [64] with permission from Advanced Energy Materials.

The edge shifts observed in x-ray absorption near edge structure (XANES) are often used to track the oxidation states of the redox centres. This element specific technique probes the energy required to excite and electron from a core level (1s for K-edge or 2p for L-edge) to a higher state. The absorption edge is expected to shift to higher energy as the effective nuclear charge of the probed ion increases and exciting an electron (in the case of K-edge from 1s to mostly 4p states) requires more energy. The K-edge spectra for Ni and Mn are generally well behaved and evolve as expected to higher energy on charge.[34,65,66] Notably the Co K-edge XANES spectra of $LiCoO_2$ do not show a continuous evolution with change upon delithiation.[67] The $L_{II,III}$-edge XANES, which are sensitive to transitions from 2p→3d, show for both L_{II} and L_{III} a shift to higher energy, however due to the absence of any clear edge shift in the K-edge spectra this cannot simply be attributed to an increase in effective nuclear charge on Co. As the transitions occur from the 2p states to the vacant Co–O e_g* antibonding states, the shift in the L-edge spectra indicate that these states are pushed up in energy on delithiation (and the Co–O e_g bonding states are consequently pushed down in energy),

indicating an increase in Co–O covalency.[67] For $LiCoO_2$, which in addition to changes in bond covalency (which are expected for all $LiMO_2$ materials on delithiation) undergoes a metal-insulator transition, it is naïve to consider the Co–O framework in completely ionic terms. It has been noted that Co displays a poorly defined oxidation state which may be related to the delocalisation of electrons that it seems to promote.[68] The charge compensation most likely involves some change in the formal charge on the Co but it is also clear that electrons are withdrawn from Co–O hybrid orbitals as well.[69,70] As will be discussed in section 1.5.1 the view of each TM ion with a defined oxidation state and a hierarchy of potentials is often not suitable at high states of charge but it is a very useful framework to start from.

1.2.6 Surface Reconstructions in Stoichiometric Layered Rocksalts

A key driver of performance loss in almost all layered cathode materials are the transformations that occur at the surface of the particles, particularly at high states of charge. As previously mentioned (section 1.2.3) there is a thermodynamic preference for formation of the spinel phases of $LiTMO_2$ once more than 0.5 Li are extracted.[54,55] In addition, there is a thermodynamic driver for further transformation via loss of Li and O to form a densified disordered rocksalt phase;[55] the required Li loss can of course by assisted by electrochemical delithiation. Surface phases are typically observed in samples which have undergone extensive delithiation, regardless of their current state of charge i.e. it is an irreversible process. Generally disorder rocksalt phases containing TM^{2+} make up most of the surface whilst a bridging layer of spinel-like regions lies between this densified surface layer and the core of the particle.[71] Interestingly it has been shown that such reconstructed surfaces can form by simple exposure to electrolyte, although the layers are less thick (Figure 1.6).[72]

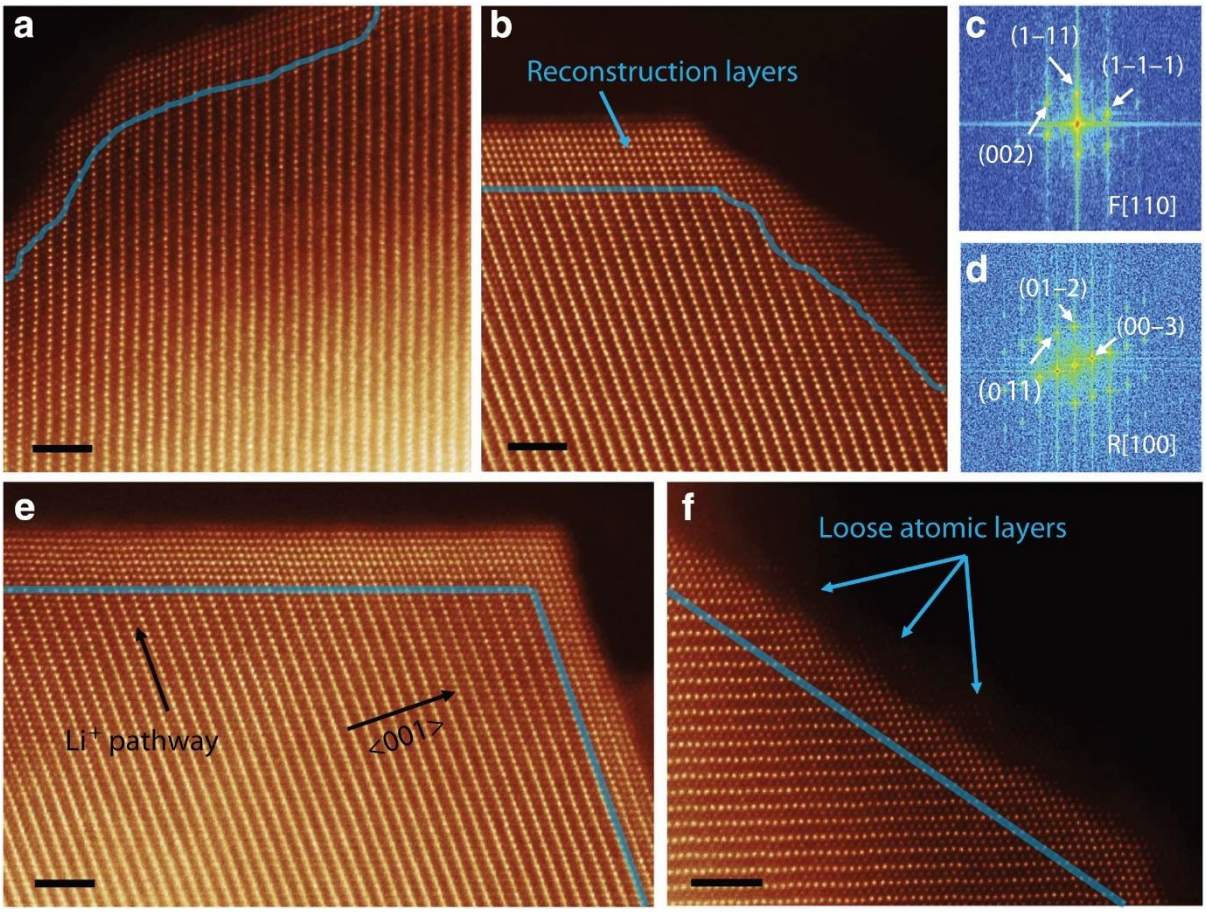

Figure 1.6 Annular dark field scanning transmission electron microscopy (ABF-STEM) images of $LiNi_{0.4}Mn_{0.4}Co_{0.18}Ti_{0.02}O_2$. surface reconstruction layers are shown by the blue lines in each image a) electrolyte exposure for 30 h (i.e. the duration of one electrochemical cycle for cycled samples shown in the other images). b) after one charge-discharge cycle from 2.0-4.7 V. c,d) FFT results showing the densified rocksalt surface layer ($Fm\bar{3}m$ [110] zone axis) and the layered bulk structure ($R\bar{3}m$ [100] zone axis). e) showing differences in layer thickness after one cycle for different surfaces. f) Loose atomic layers on the surface of NMC after one cycle 2.0-4.7 V. Reproduced from reference [72] with permission from Nature publishing group.

1.3 Li and Mn Rich Compounds: $Li[Ni_xLi_{1/3-2x/3}Mn_{2/3-x/3}]O_2$

Since 2001 and the synthesis of the family of Li-excess materials (i.e. those with a Li:TM ratio >1) by the group of Dahn, a broad area in the search for the next generation of Li-ion cathodes has opened up.[73] It has been shown that incorporating Li

into the TM-layer can give yield materials with extremely high specific capacity,[74,75] for example the Li–Mn–Ni family of compounds with the general formula $Li[Ni_xLi_{(1/3-2x/3)}Mn_{(2/3-x/3)}]O_2$ have demonstrated reversible capacities of up to 230 $mAhg^{-1}$, exceeding the theoretical capacity if only the transition metals are considered redox active.[76] There are however several draw backs that inhibit their implementation. Very high first charge capacity loss, poor rate capability and a fade in the average voltage, leading to a loss of power output, with each cycle.[77]

1.3.1 Li_2MnO_3

As with the "stoichiometric" compounds (those whose ratio Li:TM=1) single TM complexes can offer important insights into the whole family of materials, as such Li_2MnO_3 the x=0 end member of the $Li[Ni_xLi_{(1/3-2x/3)}Mn_{(2/3-x/3)}]O_2$ family is a well-studied and important model compound. It has an O3 structure like $LiCoO_2$ but due to its Li-excess, 1/3rd of the TM^{3+} are substituted for Li^+. This leads to a mixed TM/Li layer with the composition $[Li_{1/3}Mn_{2/3}]$; it can be useful to write the formula for Li-excess materials using a notation that emphasises the composition of their layers and their analogy to stoichiometric Li-ion cathode materials e.g. $Li[Li_{1/3}Mn_{2/3}]O_2$ for Li_2MnO_3. In order to form a Li-excess compound it is necessary to charge compensate for the substitution of TM^{3+} ions with Li^+ by oxidising all, or part of, the remaining TMs into oxidation states greater or equal to 4+. Mn is stable in the 4+ oxidation state which means it is very commonly found in Li-excess compounds although other TM species that are stable in high oxidation states such as Nb, Ru, Ir etc. can also be used.[74,75,78–80] In Li_2MnO_3, the TM-layer is well ordered, with each Li^+ surrounded by 6 Mn^{4+} in a honeycomb arrangement (Figure 1.7). This splits the TM-layer sites into two distinct crystallographic sites—2b or α sites for Li^+ and 4g or β sites for Mn^{4+}—and lowers the symmetry from the rhombohedral $R\bar{3}m$ space group of the α-$NaFeO_2$ structure to a monoclinic $C2/m$ unit cell (Figure 1.7) [81,82]. This ordering of the TM-later gives rise to superlattice reflections observed in diffraction patterns (Figure 1.8).

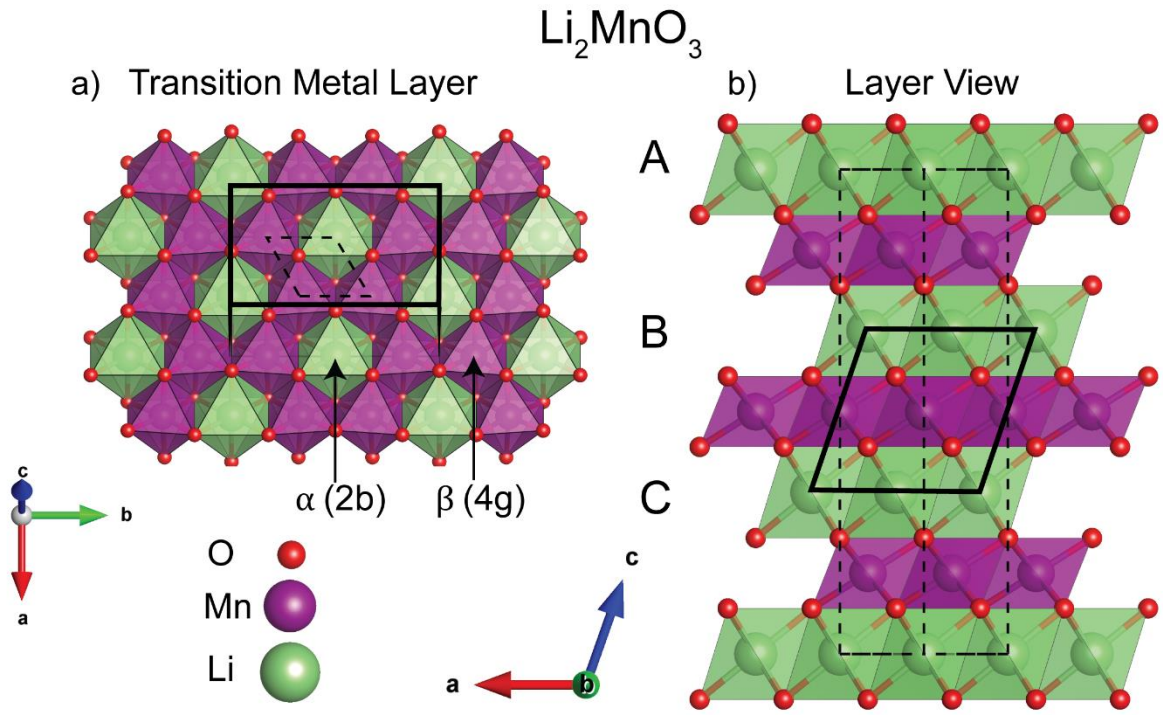

Figure 1.7 Crystal structure representations of Li_2MnO_3. a) the view perpendicular to the ab-plane showing the honeycomb ordering which requires the reduction in symmetry from $R\bar{3}m$ (dashed lines) to $C2/m$ (thick solid lines) The two crystallographic sites are labelled with α and β which are conventional descriptors and with their Wyckoff positions. b) The view down the b axis showing the showing the same O3 ABC layered structure as $LiCoO_2$, the parent $R\bar{3}m$ (dashed lines) and the Li_2MnO_3 $C2/m$ (thick solid lines) unit cells are shown. Axes displayed relate to the monoclinic $C2/m$ space group.

1.3.2 $Li[Ni_x Li_{(1/3-2x/3)}Mn_{(2/3-x/3)}]O_2$

The introduction of Ni, which is incorporated as Ni^{2+}, yields a series of compounds which are attractive candidates for Li-ion cathodes. Alongside their high capacities these materials can overcome some of the drawbacks associated with $LiMnO_2$ and $LiNiO_2$ without incorporating any Co. As in Li_2MnO_3, the manganese is in the 4+ oxidation state and is not reduced to 3+ at any point. This avoids both the issues of structural distortion associated with Mn^{3+}, due to its propensity to undergo Jahn-Teller distortions. It also prevents the disproportionation of Mn^{3+} to Mn^{4+} and Mn^{2+}; Mn^{2+} facilitates the transformation to the spinel structure observed in layered $LiMnO_2$ (see section 1.2.3),[83] and may also be dissolved from the surface by the electrolyte.[84] Unfortunately, $Li[Ni_x Li_{(1/3-2x/3)}Mn_{(2/3-x/3)}]O_2$ samples, similar to $LiNiO_2$ and Ni-rich

NMCs, suffer from Ni^{2+} occupying sites in the Li layer. As mentioned previously (section 1.2.4) mixed TM compounds like NCA avoid large scale Ni^{2+} occupation of Li-layer sites by discouraging the formation of Ni^{2+} in the TM-layer, which is necessary to charge compensate the Ni^{2+} in the Li layer. In $Li[Ni_x Li_{(1/3-2x/3)}Mn_{(2/3-x/3)}]O_2$ all the Ni is already Ni^{2+}, so oxidation of $Ni^{3+} \rightarrow Ni^{2+}$ cannot charge compensate the Ni^{2+} in the Li-layer. However, as Li^+ is already present in the TM-layer it is quite likely that some amount of antisite defects (where Li^+ and Ni^{2+} simply occupy one another's sites) occurs and this explains how Ni^{2+} in the Li-layer is charge compensated in Li-excess compounds. The exact amount of this anti-site disorder reported varies based on composition and method of quantification, however it does increase with x (i.e. increasing nickel content).[85–88]

1.3.3 Transition Metal Layer Ordering in $Li[Ni_x Li_{(1/3-2x/3)}Mn_{(2/3-x/3)}]O_2$

Diffraction patterns of $Li[Ni_x Li_{(1/3-2x/3)}Mn_{(2/3-x/3)}]O_2$ display the super lattice reflections—analogous to but weaker than Li_2MnO_3—indicating that some long range order in the TM-layer exists (Figure 1.8). Some ordering might be expected on electrostatic grounds, given the wide range of oxidations states (Li^+,Ni^{2+} and Mn^{4+}), in contrast to NCA, whose TM-layers contain only 3+ ions and are disordered. Indeed, ab-intio calculations, conducted on the x=0.5 end member $Li[Ni_{0.5}Mn_{0.5}]O_2$, suggest that energetic differences between different TM-layer orderings are large enough to overcome the configurational entropy term, although at synthesis temperatures (>700°C) a random distribution is likely;[89] cooling rate will play a role in the TM-layer ordering. The presence of Ni means a perfect honeycomb ordering is not possible and various ordering schemes have been proposed for example: chains, zig-zag and flower orderings (Figure 1.8).[90] $Li[Ni_{0.5}Mn_{0.5}]O_2$, which when conventionally synthesised displays large amounts of Ni/Li antisite disorder (~10%),[65,87,91] can be synthesised in a near perfect layered configuration by ion exchange from the Na analogue;[92] samples of this kind, probed by neutron pair distribution function (PDF) analysis, showed local

structure indicating a preference for zig-zag ordering which had predicted to be the lowest energy arrangement.[90,93]

For the Li-Mn-Ni compositions between the two end members i.e. $0<x<0.5$, ^{6}Li NMR shows that Li is preferentially coordinated by Mn^{4+}, with fewer Ni^{2+} neigbours than would be expected for a random distribution of cations in the TM layer.[94,95] One possible ordering for $Li[Ni_{x}Li_{(1/3-2x/3)}Mn_{(2/3-x/3)}]O_2$ ($0<x<0.5$) is modification of the honeycomb ordering present in Li_2MnO_3, in which the Li^{+} and Mn^{4+} still occupy exclusively α and β sites respectively and the Ni^{2+} is subtituted onto both sites randomly; this is a logical initial guess based on the Li_2MnO_3-like features in the NMR and diffraction. PDF data shows that Ni tends to be surrounded by more Mn in its first coordination shell and by more Ni and Li in it's second, with Mn showing a complimentary trend, reverse monte carlo (RMC) modelling starting from a Ni substituted honeycomb structure accommodates this trend by forming a disordered version of the flower structure (Figure 1.8).[96]

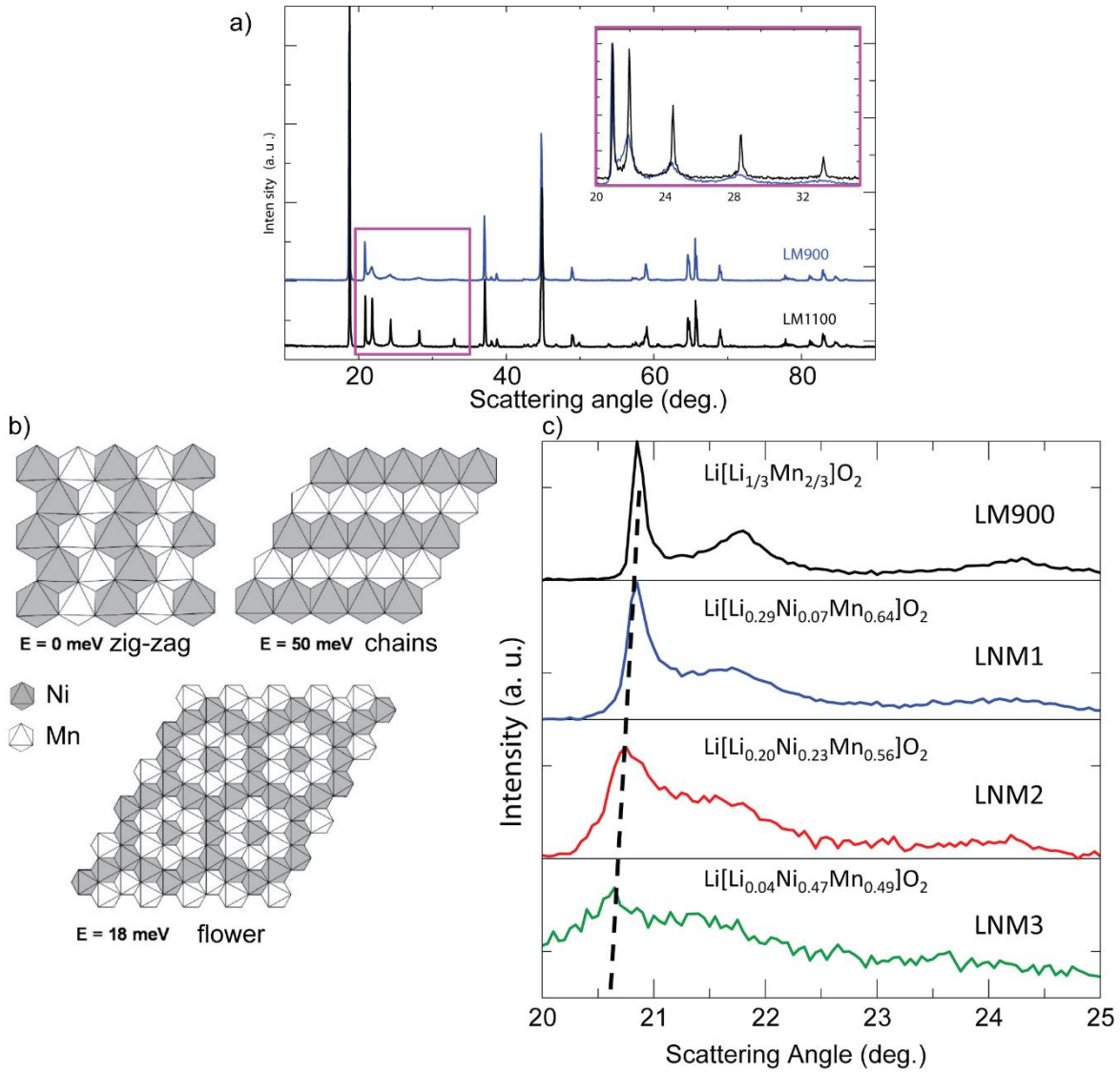

Figure 1.8 a) X-ray diffraction patterns for Li_2MnO_3 synthesised at 900°C (LM900) and 1100°C (LM1100). Pink box and the inset highlight the superlattice reflections. b) idealised orderings of $Li[Ni_x Li_{(1/3-2x/3)}Mn_{(2/3-x/3)}]O_2$ showing zig-zag, chain and flower type orderings along with their relative energies calculated by DFT for the end member $Li(Ni_{0.5}Mn_{0.5})O_2$. c) Zoomed in super lattice portion of the diffraction patterns for different compositions of $Li[Ni_x Li_{(1/3-2x/3)}Mn_{(2/3-x/3)}]O_2$ with increasing Ni contents. The black dotted line highlights the evolution of the (020) peak showing the lattice parameter of the superstructure evolves with Ni content which is incompatible with a two phase composite model for $Li[Ni_x Li_{(1/3-2x/3)}Mn_{(2/3-x/3)}]O_2$. a,c) reproduced from reference [97] with permission from Nature publishing group. b) reproduced from reference [90] with permission from Nature publishing group.

1.3.4 Stacking Faults in $Li[Ni_x Li_{(1/3-2x/3)}Mn_{(2/3-x/3)}]O_2$

So far the discussion of ordering has focused on the ab-planes and TM-layer however stacking sequence changes have a profound impact on the shape of the superlattice

reflections observed in the diffraction[98] and as stacking sequences changes on delithiation are a cause of degradation in cathode materials they must be considered.[99].

Li_2MnO_3 is very prone to stacking faults as there are several stacking sequences which are similar in energy.[97] The superlattice reflections which arise from the ordering in the TM-layer are very sensitive to the concentration of stacking faults and are broaden significantly in samples with greater degrees of stacking disorder; longer and higher temperature annealing times yield samples with fewer stacking faults and sharper superstructure (Figure 1.8a).[97,100] Stacking sequence differences are also visible in ^{6,7}Li and ^{17}O NMR, where more peaks than expected are observed in samples with stacking disorder.[100–103] Analysis of the broadening of superlattice reflections in $Li[Ni_x Li_{(1/3-2x/3)}Mn_{(2/3-x/3)}]O_2$ ($0 \leq x \leq 0.5$) using the FAULTS program, have show that the stacking fault probability increases with greater Ni content with the expected translation vector (1/3, 1/3, 1/3) occuring between layers ~80% of the time in Li_2MnO_3 but only 53% of the time for the Ni-rich composition $Li(Li_{0.04}Ni_{0.47}Mn_{0.49})O_2$.[97]

Many of the local structure probes can be rationalised if $Li[Ni_XLi_{1/3-2X/3}Mn_{2/3-X/3}]O_2$ is considered to be a composite between Li_2MnO_3-like regions and a Ni-rich $LiMO_2$ regions. This has led to a debate about whether the $Li[Ni_XLi_{1/3-2X/3}Mn_{2/3-X/3}]O_2$ family is a true solid solution or not, with some authors favouring a two phase notation $(1-2x)Li_2MnO_3 \cdot (3x)LiNi_{0.5}Mn_{0.5}O_2$.[77,104–106] In the composite hypothesis, the super lattice reflections observed in the diffraction are a consequence of Li_2MnO_3 domains and the broadening observed as the Ni concentration increases is a reflection of decreasing Li_2MnO_3 domain size.[107,108] Studies using high-angle annular dark field (HAADF) scanning transmission electron microscopy (STEM) show that structure is a uniformly monoclinic ($C2/m$), with disrupted stacking and that no disordered rhombohedral ($R\bar{3}m$) regions exist.[109] This model of stacking fault rich solid-solution fits well with the diffraction data, in which the superlattice reflections move to higher

d-spacing as x increases (Figure 1.8), such an evolution would not be expected if the superlattice reflections were caused by Li_2MnO_3 regions as they contain no Ni.[97]

As discussed, both the TM-ordering and the stacking of the planes, are not rigid and well defined in these phases. It is therefore feasible to imagine either individual layers or three-dimensional regions, where the stoichiometry and ordering is close to Li_2MnO_3 and others where the composition is more Ni-rich. The proponents of a two phase hypothesis state that, "[$Li[Ni_xLi_{1/3-2x/3}Mn_{2/3-x/3}]O_2$ materials] are characterized by Mn and M cation disorder between the Li_2MnO_3 and $LiMO_2$ components".[104] Small domains, whose compositions are different, but between which there is cation disorder, do not constitute different phases and that the difference between these two hypotheses are largely semantic, therefore when discussing these materials the "solid-solution" notation will be adopted.

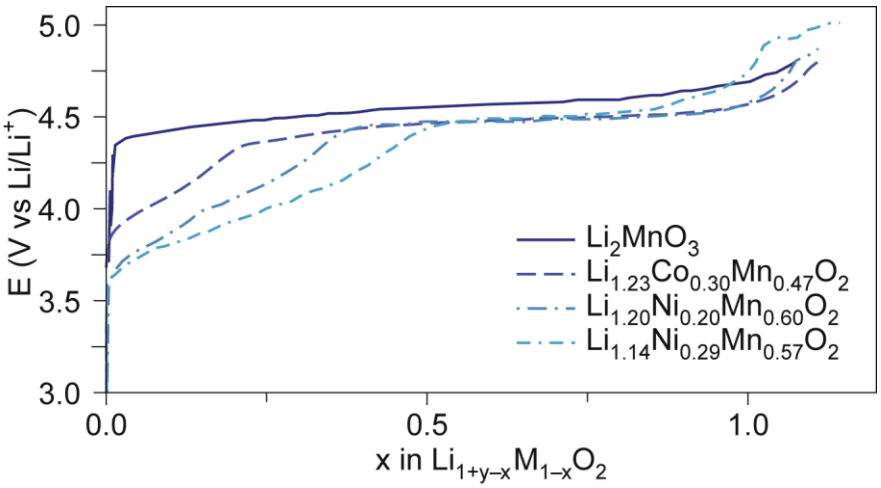

Figure 1.9 Electrochemical voltage curves for Li_2MnO_3 and some Ni and Co doped analogues. During the initial period of charge, a region of sloping voltage for the Ni and Co doped samples is observed. The high voltage plateau typical of Li-excess materials is observed in all cases and is close to the voltage observed throughout the charge for undoped Li_2MnO_3. Reproduced from reference [110] with permission from Nature publishing group

1.3.5 High Voltage Processes in $Li[Ni_xLi_{1/3-2x/3}Mn_{2/3-x/3}]O_2$

The traditional view for cathode materials is that as Li^+ is extracted (on charge) a transition metal ion undergoes oxidation to balance the charge lost, giving up electrons in the process. For $Li[Ni_xLi_{1/3-2x/3}Mn_{2/3-x/3}]O_2$, $Ni^{2+} \rightarrow Ni^{4+}$ is the active metal redox

process, the Mn being inactive as Mn^{4+}.[65,111] However, it is a characteristic of many Li-rich materials that they display capacities that are larger than anticipated if only this "conventional" redox activity is considered. The typical first charge voltage profile of a Li-excess compound has two parts (Figure 1.9): the first is a sloping region, indicative of a solid-solution type reaction (section 1.1.2) and typical of most layered compounds, up to ~4.4V, the second is a high voltage plateau more typical of a two-phase reaction around 4.5V (section 1.1.2). The first part of the charge is accounted for by the conventional redox processes, in this case $Ni^{2+} \rightarrow Ni^{4+}$, however the electrochemical origin of the second part is more complex. Understanding the processes is the key to understanding the origins of both the massive capacities of Li-excess compounds but also the first cycle capacity loss and voltage fading as both do not occur if the material is charged only within the "conventional" redox region;[91] charging within a more conservative voltage window on first charge, prevents the "activation" of the material.

Early explanations for the anomalous capacity observed during the high voltage plateau suggested simultaneous extraction of Li and O during charge.[91] The plateau occurs at high enough voltage that some amount of electrolyte decomposition is expected, considering this others suggested that exchange of Li^+ and H^+ (produced by electrolyte decomposition) could account for some of the capacity alongside O loss,[112,113] however the amount of H^+ incorporated, is correlated with the duration that the cell is operated at high voltage, rather than the amount of capacity extracted on the plateau, indicating that H^+ incorporation is really a function of the amount of electrolyte breakdown rather than a direct consequence of the high voltage plateau.[114]

As stated in section 1.2.6, surface transformations are known to occur most severely at high voltages.[71,115,116] With the caveat that some degree of surface reconstruction is expected, it is worth considering the transformations that are reported to occur on the surface of the $Li[Ni_xLi_{1/3-2x/3}Mn_{2/3-x/3}]O_2$ family during the plateau region. Some

amount of oxygen loss is necessary to form the disordered rocksalt layers commonly observed on all layered Li-ion battery cathodes.[64] Under such conditions high valent transition metals such as Mn^{4+} are unstable and must either: migrate into octahedral sites (newly vacated by Li) away from the surface, be coordinated by oxygen migrating to the surface from the bulk,[114] or else dissolve into the electrolyte.[117,118] Transformed surface layers, which form after the first cycle (or perhaps simply on contact with electrolyte[72]) have been shown to develop TM concentration gradients on multiple cycles with the surface gradual becoming more Ni-rich/Mn-poor.[119] This suggests either Mn dissolution or Mn migration. Surface densification with the loss of O (and possibly Mn) may be responsible for some of the first charge capacity loss. Additionally, migration of TM ions (Mn^{2+}) into sites within the Li-layer (either tetrahedral or octahedral) will block Li diffusion and prevent occupation of the neighbouring Li sites, leading to further capacity loss and poorer rate capability. The final consequence of TM migration is to alter the redox potential of the TM—particularly in the case of tetrahedral site occupation where the crystal field is dramatically different—which may be responsible for the change in voltage profile. Reversible migration will give rise to a hysteresis, whilst irreversible migration, particularly if new ions migrate on each subsequent cycle, will lead to a voltage fade.[120]

Despite the densification and oxygen loss occurring at the surface Li-excess compounds can continue to reversibly cycle more Li than would be expected from TM redox alone. This has led to hypothesis of irreversible oxygen loss and densification on the surface, paired with reversible oxidation of the O lattice within the bulk.[121,122] The assertion that oxygen is reversible oxidised is supported by mass spectrometry conducted *in-operando* (called online or differential electrochemical mass spectrometry: OEMS or DEMS) which identified that too little O, CO and CO_2 are evolved to account for the observed capacity.[123] Further discussion of the evidence for and the mechanisms of reversible O redox will be given in section 1.5.

1.4 Li_2RuO_3

In order to understand oxygen redox mechanisms many model compounds have been studied in order to elucidate as much as possible about the role of different TMs, TM-O hybridisation and to better understand how universal the mechanisms for O redox are across all Li-excess compounds. One such family of compounds are Li_2RuO_3 and its substituted analogues.

Li_2RuO_3 has been proposed as a useful and nominally simple model compound because of its single, well characterized, TM redox couple (Ru^{4+} → Ru^{5+}) as well as it's well ordered TM layer; Ru^{4+} is arranged in a honeycomb pattern with Li^+ analogous to Li_2MnO_3.[79,124] The structure of Li_2RuO_3 is often described as adopting the $C2/c$ unit cell, as was reported in much of the early literature.[79,124,125] This reported structure is O3 although the $Li_{1/3}Ru_{2/3}$ layers are displaced from on another by (0 ½ ½) rather than (⅓ ⅓ ⅓) as in Li_2MnO_3.[79,97] Owing to the significant influence of the Ru dimerization upon the magnetism, heat capacity and resistivity, it's effect on the structure been more thoroughly explored by the physics community. Miura et al. used powder neutron diffraction to show that the structure adopts space group $P2_1/m$, in which the dimers form an "armchair" configuration at low temperatures; at high temperature the space group is $C2/m$.[126] .The pristine structure and phase transitions of Li_2RuO_3 will be discussed in detail in Chapter 3:.

1.4.1 Electrochemical Behaviour of Li_2RuO_3

The electrochemical charge profile of Li_2RuO_3 is like many Li-excess materials in that it can be divided into two sections. The first of these is accounted for by oxidation of Ru^{4+}→Ru^{5+}during a plateau at ca. 3.7 V, then a high voltage plateau (ca. 4.3 V) associated with anionic redox processes (Figure 1.10).[127] Notably the first charge profile of Li_2RuO_3 is step-like, indicating that the material undergoes several phase changes on charging. There are three phases involved in the first charge process. The first is

naturally the pristine material described above and in some detail in Chapter 3. The second is a related phase which is reported with the formula $Li_{1.27}RuO_3$ and which maintains the $P2_1/m$ space group, although with slightly different lattice parameters.[128] On further delithiation a 3rd phase $Li_{0.9}RuO_3$ is formed, which is reported to be rhombohedral with space group $R\bar{3}m$.[129] Both of these transitions occur during the first part of charge and on the high voltage plateau the $R\bar{3}m$ phase is further delithiated via a solid solution type reaction. The structural evolution of Li_2RuO_3 on delithiation is not well characterised despite its relevance as a model compound. Many of the studies which focus on the electrochemical processed focus on $Li_2Ru_{1-x}M_xO_3$ where M is typically Sn or Mn.[130–132]

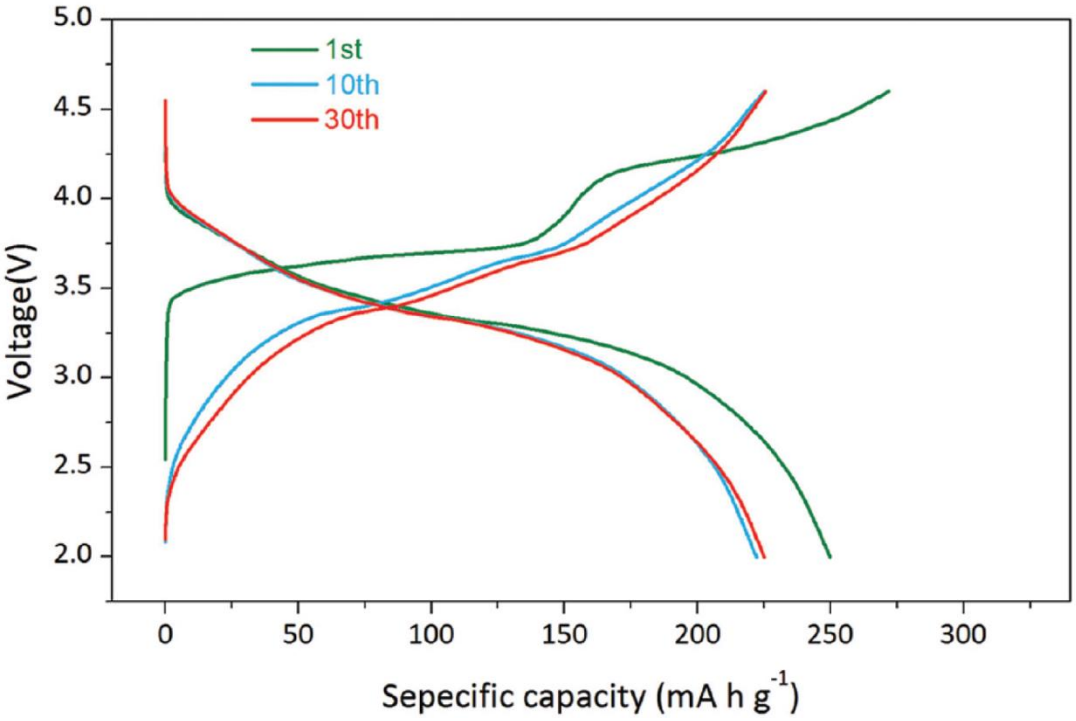

Figure 1.10 Typical electrochemical voltage curves for Li_2RuO_3. The first charge (green) shows an initial plateau ca. 3.7 V corresponding to the $Ru^{4+} \rightarrow Ru^{5+}$ redox process. The second plateau at ca. 4.3 V has been attributed to oxidation of oxygen. First discharge and subsequent cycles do not show the same plateaus and are more S-shaped, additionally capacity and voltage fading, typical for Li-excess compounds, is observed from cycle 1 (green) to cycles 10 and 30 (blue and red respectively). Reproduced from reference [127] with permission from John Wiley and Sons.

1.5 Oxygen Redox

To understand the redox processes in Li-ion cathodes better it is necessary to examine the factors that affect positioning of the bands and hence which states are available for oxidation on charge.

1.5.1 Electronic Structure Considerations

The separation between the TM–O and the TM–O* bands depends on the difference in electronegativity between the TM and O. This charge transfer term (referred to as Δ by some authors[133]) is a measure of the ionic/covalent character of the bond; a larger Δ indicates a more ionic bond with TM–O bonding orbital being essentially localised on the O. The TM–O* band in most Li-ion cathodes is essentialy of metal only character and therefore the redox process is considered purely cationic. Notably, for $LiCoO_2$ the TM–O* states are essentially empty and therefore the Co, t_{2g}, non-bonding states are depopulated first. These low-lying TM orbitals overlap with the primarily O-character states (t_{1u} states in Figure 1.4a), which may also be depopulated on continuing discharge, which leads to oxidation which appears more "anionic", [27,67,134] although, as no capacity beyond that expected for TM oxidation can be extracted, this is distinct from the anion redox phenomena that are characteristic of the Li-excess materials.

The partially filled TM–O* band is split by the Mott-Hubbard splitting (U) into upper and lower Hubbard bands (UHB and LHB).[133] This splitting is a result of the energy penalty experienced by an electron if it is delocalised from its original site to another already half-filled site in the crystal. It is a measure of the onsite repulsion experienced determined by $U = I - A$, where I is the ionisation energy (the energy required to remove the electron from its site) and A is the electron affinity (the energy gained by the electron occupying it's new site). The bands are split by this energy and there is a band gap if the bandwidth $W < U$. The bandwidths are broadened as the intersite

overlap increases and hence the size of the U splitting decreases with increasing orbital volume or as the TM–TM distances become shorter.

So far, all O orbitals have been considered to be in TM–O hybrid orbitals. In a layered compound O has three neighbours in the TM-layer and three in the Li-layer, therefore in a stoichiometric material the O has exactly three TM neighbours on one face of it's octahedron and three Li on the opposite face (Figure 1.11a). Each of these 180° TM–O–Li connections involves the hybridisation of one of the 2p orbitals on O forming hybrid orbitals as described above. In the case of Li-excess materials, some number of TMs are replaced by Li hence some O ions will have Li–O–Li connections (Figure 1.11b), which gives rise to 2p orbitals on O which are not hybridised with any TM centre. These "orphaned" 2p states form their own non-bonding band above the TM–O band. The presence of these high energy O states been predicted by DFT calculations, with spin density maps demonstrating that their location and shape match that expected for isolated 2p states.[135] The interplay between the charge transfer term and the Hubbard splitting determines the ordering of the bands. Highly ionic metal centres for which the TM–O separation is very large and therefore $\Delta \gg U$ will proceed first via cationic and then via anionic redox. If $\Delta \approx U/2$ then the O 2p and the LHB will overlap hence the anionic and cationic redox processes may occur simultaneously (Figure 1.11e-f). Another factor in the relative positions of the LHB and O 2p orphan bands is the effect that changes in oxidation state, lattice parameter changes and migration of cations has on the energy of the bands (further discussion section 1.5.2.3).

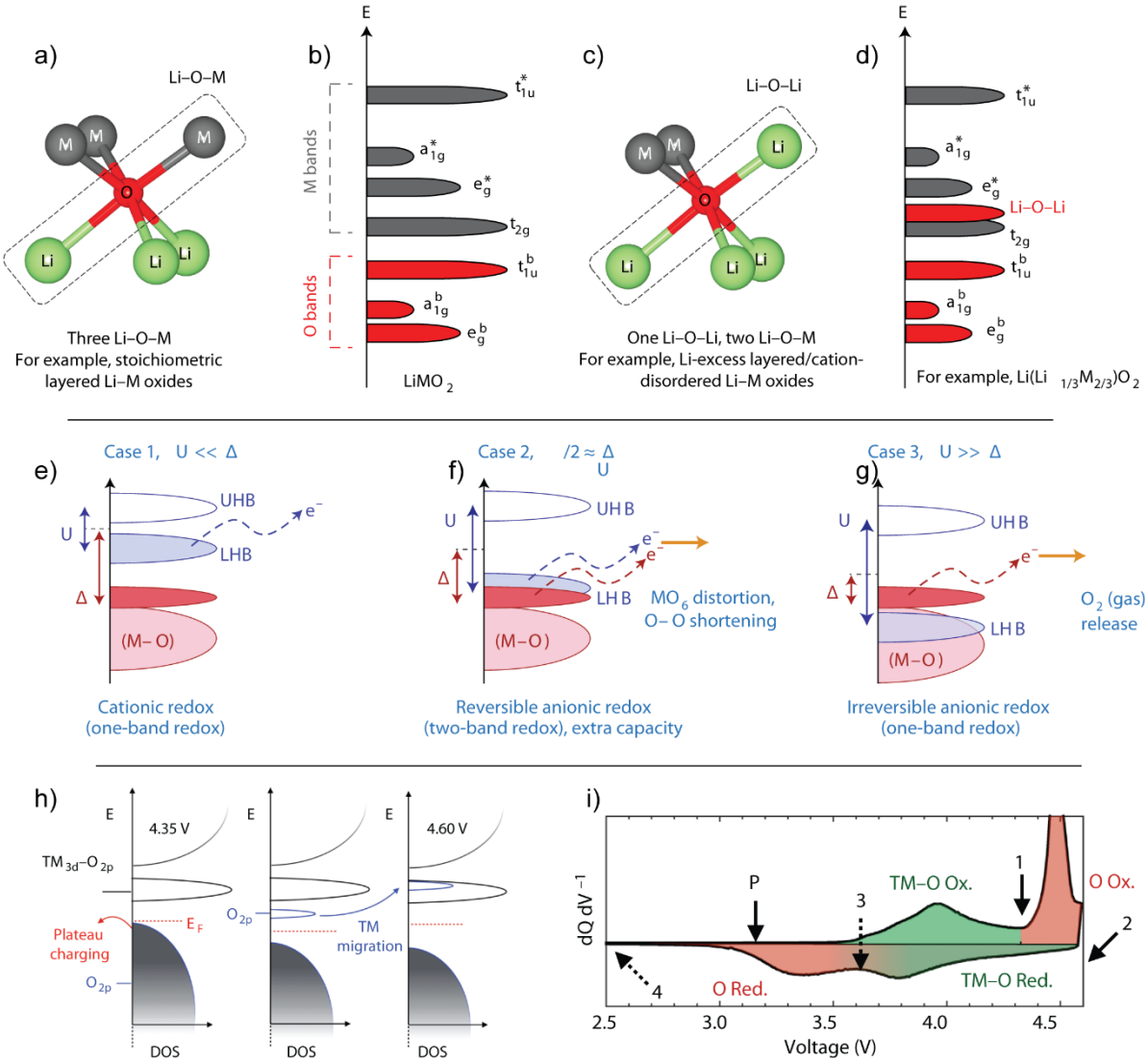

Figure 1.11 a) Coordination environment for a stoichiometric layered metal oxide $LiTMO_2$ i.e. 3 Li–O–TM connections. b) schematic of the band structure for a stoichiometric layered metal oxide. c) Coordination environment for a Li-excess layered metal oxide, in this case $Li(Li_{1/3}TM_{2/3})O_2$ i.e. 2 Li–O–TM connections and 2 Li–O–Li connection. d) schematic of the band structure for a Li-excess layered metal oxide showing the high energy Li–O–Li $O_{2p\text{-orphaned}}$ state. e-g) Effect of variation in Δ (the charge transfer band gap) and U (the Mott-Hubbard splitting) on the expected ordering of the band structure for Li-excess metal oxides. h) schematic representation of the reorganisation of the band structure in a Li-excess metal oxide following O-redox and structural rearrangement. i) dQ/dV plot for $Li_{1.17}Ni_{0.21}Co_{0.08}Mn_{0.54}O_2$ highlighting the TM-O redox process (green), which shows very little hysteresis and the O-redox process (red) which, as a result of TM rearrangement, shows a large hysteresis. a-d) Reproduced from reference [135] with permission from Nature publishing group. e-g) Reproduced from reference [133] with permission from Nature publishing group. h,i) Reproduced from reference [136] with permission from Nature publishing group.

1.5.2 Stabilisation of Oxidised Oxygen Species

What happens to O once it is oxidised is the source of much debate and is an essential question as the answer holds the key to not just detecting O-redox (by means other than by electrochemical implication) but also stabilising the oxidised O species. Several, not necessarily mutually exclusive, mechanisms have been proposed.

1.5.2.1 Formation of Peroxo-like O–O Species

The formation of O–O peroxo-like species through the distortion of the MO_6 octahedra has been proposed as a mechanism for stabilising the holes generated on O.[137,138] It has been suggested that, the origin of this structural rearrangement is the overlapping of the O 2p orphaned states and the M–O* LHB.[133] The hypothesis is that the degenerate levels at the Fermi energy are unstable and will undergo a structural distortion in order to stabilise. For peroxo-like environment formation to be stabilising, two oxidised Li–O–Li states must be able rotate to hybridise with one another without giving up much TM–O hybridisation. Therefore, the directionality and strength of the other bonds experienced by the O are essential in determining whether a peroxo-like species may form.[135] TM–O bonds are highly directional therefore Li–O–Li states whose other O 2p states only form hybrids with metals with closed d orbital shells (d^0 or d^{10}) may be more able to rotate. For example, DFT calculations on delithiated $Li_2Ru_{0.5}Sn_{0.5}O_3$ show that O with one Li–O–Li and two Li–O–Sn rotate and form peroxo-like species whereas those with Li–O–Ru orbitals do not.[135] There is also a geometric consideration as two adjacent oxidised O 2p states which are both able to rotate must be available to form a peroxo-like configuration.

1.5.2.2 Localised O Holes

Another possible outcome of O redox is that holes are localised on O and that these are stabilised due to their specific local environments.[123] In Li-excess NMC, in the absence of peroxo-like $(O_2)^{n-}$ species, O^- species seem to be most stable near Mn^{4+}.[123] This may be due to the more ionic Mn^{4+}–O interactions, or, due to fact that Li^+ and

Mn^{4+} tend to be near each other in Li and Mn rich materials, the Li–O–Li states may simply occur near Mn^{4+} more often. Oxidised O^{2-} is expected to be highly unstable but apart from the densification at the surface there is surprisingly little O evolution.[123,139] It may be that even where stabilisation by formation of peroxo-like species is not permitted by strong directional TM–O hybridisation, it may be that same hybridisation that prevents migration of oxidised O^{2-} to the surface and its loss as O_2 gas or by reaction with the electrolyte.

1.5.2.3 Migration of TM ions

A key feature of materials exhibiting anionic redox is a large voltage hysteresis. Structural changes on cycling which are kinetically slow (thus creating overpotentials) and which can affect the electronic structure (shifting redox potentials on charge vs discharge) may explain this characteristic behaviour. The increase in disordering within the ab-planes and the increase in the number of TM ions in the Li layer on charge, observed in diffraction by the loss of superstructure reflections and shift in (003)/(104) ratio respectively, suggest that O redox may be linked to these structural rearrangements. Multi-technique studies of Li-excess NMC suggest that, on delithiation migration of Mn or (most likely) Ni into vacated Li sites, leads to uncoordinated oxygen environments which raises the level of the depopulated $O_{2p\text{-orphaned}}$ states.[136] This explains the observed charging behaviour as on charge: first the "cationic" redox processes occur (removing electrons from TM–O LHB states), then at high voltage the anionic process takes over (removing electrons from the $O_{2p\text{-orphaned}}$ states). Then at high states of charge the TM migration occurs and the depopulated $O_{2p\text{-orphaned}}$ states are pushed up so they are higher in energy than the TM-O* LHB states and hence on discharge the "cationic redox" happens first (at a similar voltage as on delithiation) and then newly formed high energy (low voltage) $O_{2p\text{-orphaned}}$ states are filled. This leads to the observed voltage hysteresis as, triggered by the structural rearrangements, the O-redox process has its redox potential shifted more than 1V. (Figure 1.11h-i).[136]

Once TM migration has occurred the precise mechanism of O rehybridization that follows is not clear and will depend strongly on the identity of the coordinating TM ions. Recent work has suggested that $Li_2Ir_{1-x}Sn_xO_3$ delithiation results in Sn migration, whereas in Li_2IrO_3 there is no Ir migration and no oxygen redox. The structural rearrangements proposed in this case involve either formation of O–Ir bonds with a bond order greater than one, or O–O dimer formation dependent of Sn concentration. Although this appears to suggest that the metal migration hypothesis is compatible with O–O peroxo species formation, the bond length predicted by DFT are 1.76 -1.79Å, much shorter than the slightly contracted 2.5Å distances observed by TEM.[138,140] Additionally the authors claim that Li_2IrO_3, which doesn't show the characteristic Li-excess voltage hysteresis, cannot be considered a true O redox material as electrons are never withdrawn from the $O_{2p\text{-orphaned}}$ band and no rearrangement occurs.[140]

1.5.3 Evidence for O redox

Oxygen redox is a challenging phenomenon to observe. Depending on the structural and electronic results of O redox the signatures that are expected will be different. The role of oxygen is implied from the electrochemistry along with results from DEMS studies which suggest insufficient O is evolved from the lattice to explain the capacity.[123] As mentioned previously, HAADF-STEM has been used to try to visualise peroxo-like dimer formation in Li_2IrO_3.[138] However the resolution required for such measurements and the highly degree of difficulty of sample preparation mean that other reports using this methodology have not emerged at the time of writing.

Electron paramagnetic resonance spectroscopy (EPR also called ESR) has also been employed in order to characterise the unpaired S=1/2 electron that should be formed by the oxidation of O^{2-}. Most of the EPR work has focused on the 4d/5d metals due to the multitude of signals that results from the various TMs in 3d compounds. Charged paramagnetic (S=1/2) species are observed arising from the conductive carbon used in the electrode fabrication, which can complicate the assignment of the spectrum.

Nevertheless, for $LiRu_{0.5}Sn_{0.5}O_3$ at 4.6V, 4K EPR signals resembling the O–O containing CaO_2 have been observed (Figure 1.12b), which seem to support the peroxo-like or genuine O–O bond formation hypotheses.[137]

The use of x-ray photoelectron spectroscopy (XPS) and hard x-ray photoelectron spectroscopy (HAXPES) have also be used to study O redox phenomena.[130,131,141,142] Owing to the surface sensitivity of XPS, HAXPES which can offer greater bulk sensitivity is often used as complementary technique, particularly as the signatures of irreversible oxygen loss at the surface and cathode electrolyte interface (CEI) growth affect the XPS signal greatly.[63]

Soft x-ray absorption spectroscopy (sXAS) has also been employed to study O-redox, however lineshape changes, which have been attributed to O-redox processes,[78,123,143] are also observed in systems where the main redox centre is the TM (e.g. $LiFePO_4$).[141] Photon in photon out (PIPO) techniques such as mapping resonant inelastic x-ray scattering (mRIXS), which is analogous to a 2-dimensional sXAS experiment can be used. Incident x-ray energies are scanned and at each a full spectrum of emission energies is measured. In a RIXS experiment three kinds of emission can occur once a core electron is excited: i) elastic emission, where excited state relaxes by emitting and electron at the same energy as the excitation, ii) normal fluorescence, where a valence electron fills the core-hole and releases a photon at an energy that is defined by the energy difference between the core-hole and the valence band or iii) "energy loss fluorescence", where after the initial excitation the core-hole stabilises itself by some second excitation, the core-hole is then filled from the valence band a photon is emitted (Figure 1.12c).

A sharp feature, at 530.7 eV excitation energy and 522.8 eV emission energy, is often observed in systems thought to undergo O redox, on the high voltage plateau (Figure 1.12d). This energy loss fluorescence feature, which is a result of the process described in (iii), is considered a key signature of O-redox. Although the origin of the energetic

relaxation that give rise to the loss observed is not certain, its presence as a sharp feature suggests its origin is not decay from the occupied O^- states which would lead to a broader normal fluorescence type feature.[141] The precise excitation that gives rise to the RIXS loss feature is not clear however similar features are observed in species with O–O bonds such as O_2 gas[144] and Li_2O_2.[145] Whatever the origins of this feature it has been an influential "fingerprint" for many O-redox studies.[123,136,140,146–148] Interestingly recent studies on various stoichiometric cathode materials (NCA, $LiCoO_2$, $LiNi_{0.8}Al_{0.20}O_2$) have shown the presence of the RIXS loss feature at high potentials, suggesting a revaluation of the redox mechanisms in these materials and/or the origin of the RIXs loss feature.[63]

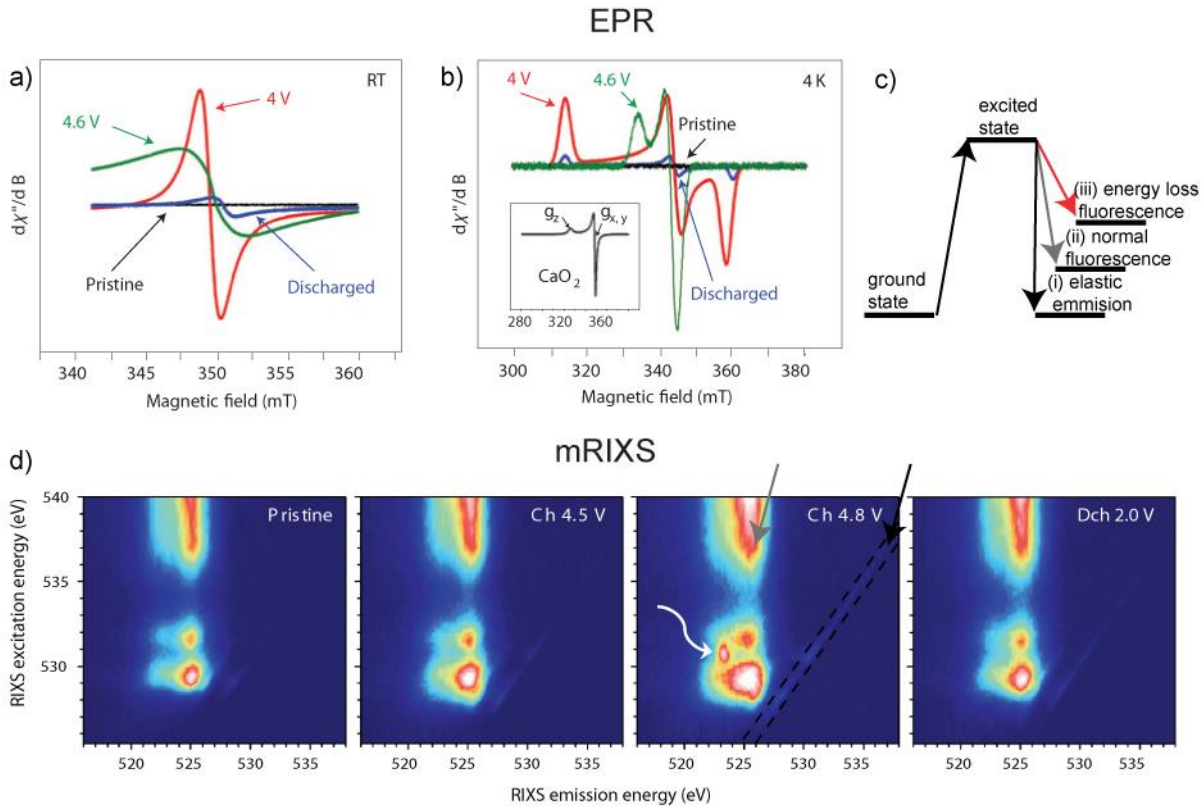

Figure 1.12 a) and b) X-band EPR spectra for $Li_2Ru_{0.5}Sn_{0.5}O_3$ at various states of charge recorded at room temperature and 4 K respectively. c) schematic representation of the RIXS process with the different types of emission described in the text. d) mRIXS maps for $Li_{1/2}Ni_{0.2}Mn_{0.6}O_2$ at various states of charge and discharge. The white arrow shows the sharp mRIXS loss feature described in the text. The grey arrow highlights the normal fluorescence emission from the TM–O* orbitals. The black arrow and black dashed lines show the elastic peak. a) & b) Reproduced with permission from reference [132] from Nature publishing group. d) Reproduced with permission from reference [148] from Nature publishing group.

1.6 NMR in the Solid State

NMR probes transitions between nuclear spin energy levels. A nucleus with a spin quantum number I has $2I + 1$ spin states with the magnetic quantum numbers $m_l = (-I, -I + 1, ... + I)$, which on the application of an external field B_0 are split by the nuclear Zeeman interaction giving an energy separation:

$$\Delta E = -\hbar\gamma_l B_0 \tag{1.2}$$

Where $\hbar$ is the reduced Planck's constant and γ_l is the gyromagnetic ratio of the nucleus. B_0 and γ_l are combined to give the Lamor frequency ω_0 which defines the energy of the transitions between the Zeeman states with the condition $\Delta m_l = \pm 1$.

$$-\gamma_l B_0 = \omega_0 \tag{1.3}$$

The populations of the energy levels are given by a Boltzmann distribution, which leads to a population difference between the states and a net magnetization M parallel to the applied field B_0, normally labelled the z direction by convention (Figure 1.13a). During an NMR experiment the equilibrium is perturbed by the application of a second field (B_1) perpendicular to the B_0 field by the use a pulse of radio frequency (RF) generated by a coil surrounding the sample. This pulse induces a "nutation" about the B_1 field with the flip angle determined by the duration and field strength of the applied pulse. The RF pulse induces and oscillating field, which can be decomposed into two oppositely rotating fields $B_1^+$and B_1^-, both with frequency ω_{RF}. Only the field which induces rotation in the same direction as the Larmor frequency, has a significant effect on the magnetisation.[149] If the axis system is considered to rotate in the same direction as the Larmor frequency at the frequency ω_{RF}, the so called "rotating frame", then the field induced by the pulse appears as a static field (by convention along x). Within the

rotating frame, the apparent Larmor frequency or offset (Ω) is given by $\Omega = \omega_0 - \omega_{RF}$ and it follows that the apparent magnetic field, called the reduced field (ΔB), is given by $\Delta B = -\Omega/\gamma_l$. In the laboratory frame, the magnitude of the B_0 field is much greater than the B_1 field so in the general case, the effective field experienced by the spins is dominated by the B_0 field. However, if the value of Ω is small then the reduced field is also small which means the B_1 field can induce an effective rotation of the magnetisation. For this reason, an applied RF pulse must have a frequency (ω_{RF}) close to the Larmor frequency (ω_0) in order to perturb the magnetisation significantly.[149]

The simplest NMR experiment, the so-called one-pulse experiment, a "$\pi/2$ pulse" rotates the magnetisation M, through 90° ($\pi/2$ radians), into the xy-plane (Figure 1.13b). The magnetisation then precesses in the xy-plane and gradually relaxes to equilibrium, which is measured by the coil over time (Figure 1.13c). This decay, called the free induction decay (FID), is Fourier transformed into the frequency domain which gives the NMR spectrum. The return of the system to equilibrium is characterised by two time constants: T_1 describes the return of the magnetisation to the z-direction called longitudinal or spin-lattice relaxation, whilst T_2 describes the decay of the xy-component, called transverse or spin-spin relaxation.

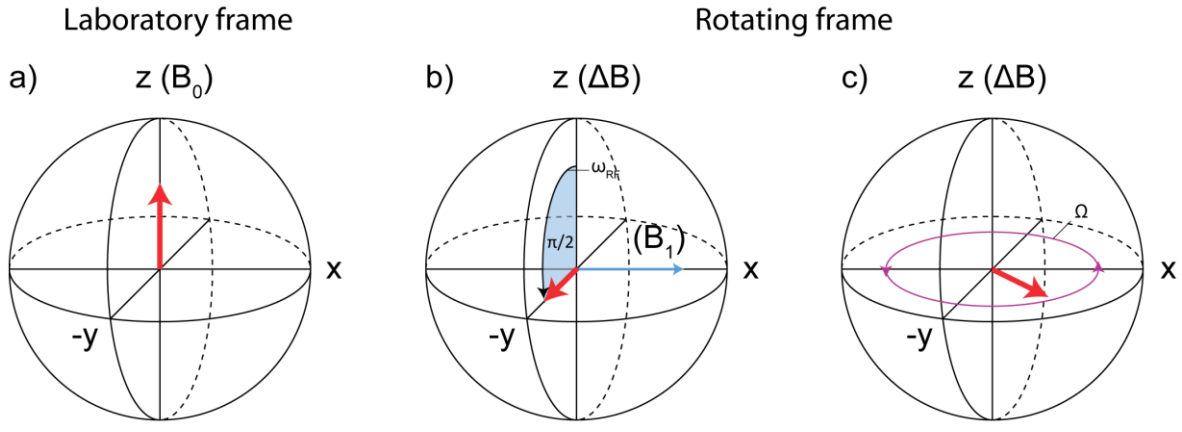

Figure 1.13 "Grapefruit" diagram showing the evolution of the bulk magnetisation M during a one-pulse NMR experiment. a) the equilibrium magnetisation M (red arrow) is aligned along the direction of the B_0 field (z). b) a $\pi/2$ pulse is applied along B_1 (x) and the magnetisation is rotated into the xy-plane. c) the Magnetisation precesses in xy-plane (purple arrows) and is this procession is measured in the coil. Adapted from reference [149]

1.6.1 The Hahn-Echo

The one-pulse experiment is the simplest NMR experiment possible, however there are drawbacks to its simplicity. The coil which applies the RF pulse is also used to acquire the signal and between the application of the pulse and acquisition a dead time must be left in order to allow the coil to switch between modes, during which period, signal is effectively lost. In addition, the effects of the pulse on the coil and other RF circuitry, are often observed as distortions of the baseline of the Fourier transformed spectrum, despite the dead time. This "ring down" effect and the signal loss can be mitigated by using a Hahn-echo (also called a spin-echo) sequence. In this sequence the initial $\pi/2$ (90°) pulse is followed, after a delay τ, by a π pulse (180°) which flips the spins about the B_1 axis and back into the xy-plane, after another delay τ, the signal is detected. During the initial period τ, the individual spins, which precess at slightly different Larmor frequencies (as they experience different local fields) begin to dephase in the xy-plane. The π "refocussing" pulse rotates the spins so that the phase they have acquired is inverted. During the second delay the spins again precess at their individual frequencies, gradually cancelling out the inverted phase they had acquired after the π pulse. As the acquisition begins after the second delay period, the relative phases of all spins are zero. The dead time for the coil can then be as long as τ and the FID recorded without ring down or loss of the initial signal. Furthermore, as the π pulse will only effectively refocus signals from within the coil, the Hahn-echo helps to suppress background signals from the probe etc. These attributes make the Hahn-echo extremely important for fast relaxing samples, for which the loss of the initial points of the FID is highly significant and for signals with poor signal/noise ratios for which the suppression of baseline distortion and background signals is vital. Most spectra in this work were recorded as Hahn-echoes for these reasons.

1.6.2 Magic Angle Spinning

In solution phase NMR, many of the spatially anisotropic interactions between an NMR active nucleus and its surroundings are averaged out to an isotropic value by rapid motion (tumbling). In a solid, due to the fixed orientation of crystallites with respect to the applied field, these interactions are not averaged out and the total shift for an individual nucleus will depend on the relative orientation of its crystallite. In a powder, where all orientations are assumed to be present, this leads to very broad line shapes, even if there is single chemical environment in the crystal, reducing the resolution compared to a liquid spectrum. The orientation dependence of many anisotropic interactions is given by $3cos^2\theta - 1$, where ϑ is the angle between the spin interaction tensor and the applied B_0 field. In a powder ϑ is assumed to take all values, however spinning the sample at an angle of ϑ_R with respect to the external field, the time averaged orientation dependence is given by:

$$\langle 3\cos^2\theta - 1\rangle = \frac{1}{2}(3\cos^2\theta_R - 1)(3\cos^2\beta - 1) \qquad (1.4)$$

Where β describes the orientation of the spin interaction tensor with respect to ϑ_R, which will like ϑ, take all values in the powder. If ϑ_R is set at 54.74° (the "magic" angle) then the $\langle 3\cos^2\theta - 1\rangle$ is equal to zero. Therefore, spinning the sample at the magic angle, provided spinning is fast enough compared to the anisotropic spin interaction, will reduce the anisotropy to zero. The effects of chemical shift anisotropy (CSA), dipolar coupling and the 1st order quadrupolar coupling can be mitigated by magic angle spinning (MAS), provided the spinning is fast enough—3-4 times larger than the frequency of the anisotropic interaction.[150] If the spinning is not fast enough then a pattern of spinning sidebands, which are peaks radiating out from the isotropic peak at intervals of the spinning speed, will be present (Figure 1.14).

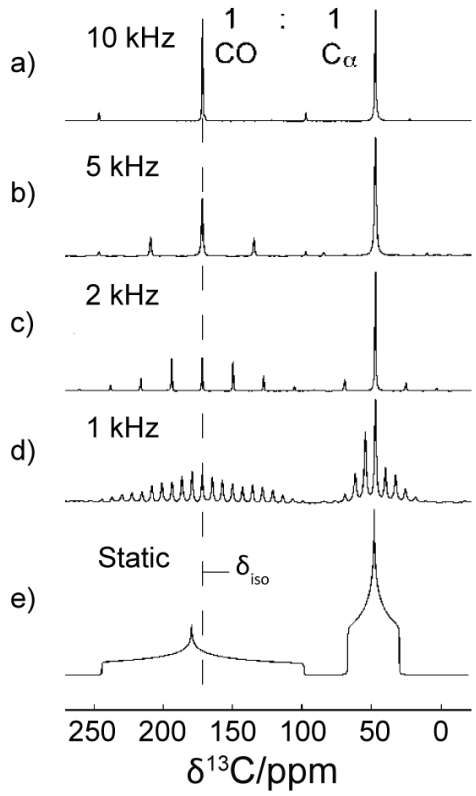

Figure 1.14 Solid state ^{13}C NMR spectrum of a 10% ^{13}C labelled glycine sample acquired with ^{1}H decoupling. Demonstrating the effects of slower or faster MAS frequency on the CSA. e) shows a simulated static spectrum. Adapted with permission from ref [151] with permission from John Wiley and Sons.

1.7 Paramagnetic NMR

Transition metal redox activity is at the foundation of all current battery cathodes, meaning that at some point during cycling (and often at all points) there are paramagnetic ions in the sample. The so-called "hyperfine" coupling of localised unpaired electrons and nuclear spins gives rise to paramagnetic effects in NMR spectra; leading to both shifts and broadening. The "spin only" case is considered here, however the spin angular momentum (S) may couple to the orbital angular momentum (L) if it is not quenched and give rise to an additional "pseudo-contact" NMR shift.[152] This shift is typically much smaller than the shifts arising from the Fermi-contact shift (described below) and will be ignored in this work.[153] The hyperfine coupling can be described by the Hamiltonian $\widehat{H}_{IS}$.

$$\widehat{H}_{IS} = \widehat{\boldsymbol{I}} \cdot \boldsymbol{A} \cdot \widehat{\boldsymbol{S}} \tag{1.5}$$

Where $\widehat{\boldsymbol{I}}$ and $\widehat{\boldsymbol{S}}$ are the nuclear spin and electron spin operators and $\boldsymbol{A}$ is the hyperfine coupling tensor. The hyperfine coupling tensor $\boldsymbol{A}$ can be separated into two components: The Fermi-contact interaction and the electron-nuclear (e-n) dipolar interaction. Electrons have much shorter relaxation times (10^{-8} to 10^{-12} s) compared to the NMR (T_1) relaxation times (ca. 10-10^{-3}s).[154] This means that the coupling of the nuclear spins occurs with the z-component of the time average of the electron spins $\langle S_z \rangle$. Additionally, electrons possess a much higher gyromagnetic ratio than any nuclear spin rather than with each electron spin state which means that the effects of the hyperfine coupling are typically large.

1.7.1 Fermi Contact Interaction

The Fermi-Contact interaction is the through bond interaction from the orbitals containing unpaired electrons to the nucleus of interest. Unpaired electron spin density is transferred via the intervening orbitals to the s-orbitals of the probed nucleus, as only the s-orbitals have a finite probability at the nucleus.[155] The presence of unpaired spin density at the nucleus induces a magnetic field and a shift in the nuclear energy levels. The isotropic hyperfine coupling constant A_{iso} determines the shift.

$$A_{iso} = \frac{\mu_0 \mu_B g_e \hbar \gamma_l}{3S} \rho^{\alpha-\beta}(\boldsymbol{R_N}) \tag{1.6}$$

Where μ_0 is the permeability of free space, $\mu_B$is the Bohr magneton, g_e is the electron g-factor, γ_l is the gyromagnetic ratio of the nucleus, S is the formal electron spin and $\rho^{\alpha-\beta}(\boldsymbol{R_N})$ describes the unpaired spin density at the nuclear position $\boldsymbol{R_N}$. This gives the Fermi contact shift contribution δ_{iso} (ppm).

$$\delta_{iso} = \frac{10^6 A_{iso}\langle S_Z \rangle}{\hbar \omega_0} \tag{1.7}$$

The Fermi-contact shift is generally large and dominates the NMR spectra of $LiTMO_2$ materials which contain paramagnetic centers. It's size and sign can be rationalized, thanks to the through bond mediation of the unpaired spin density, by considering the local coordination and geometry of the target nucleus (section 1.9.1).

1.7.2 Electron-Nuclear Dipolar Interaction

There is a through space contribution to the hyperfine interaction between the nuclear spins and $\langle S_Z \rangle$ and is described by the e-n dipolar coupling tensor $\boldsymbol{A_{ij}^{dip}}$. If the electrons are assumed to be point dipoles, then the tensor elements are given by:

$$\boldsymbol{A_{ij}^{dip}} = \frac{\mu_0 \mu_B g_e \hbar \gamma_l}{4\pi r^3}[3e_i e_j - \delta_{ij}] \tag{1.8}$$

Here, r is the distance between the electron and nuclear spins, δ_{ij} is the Kronecker delta and e_i and e_j are the x, y and z components of a unit vector pointing to the electron spin from the nuclear spin.[152] For paramagnetic ions with no orbital angular momentum contribution, $\boldsymbol{A_{ij}^{dip}}$ is traceless and doesn't effect the isotropic shift δ_{iso}, however it is often the major source of broadening in the paramagnetic NMR spectra. The principal components δ_{kk} (ppm) may be written:

$$\delta_{kk} = \frac{10^6 \boldsymbol{A_{ij}^{dip}}}{2\omega_0 \hbar} \frac{\langle S_Z \rangle}{S} \tag{1.9}$$

There are various conventions for expressing the shape of the $\boldsymbol{A_{ij}^{dip}}$, using the Haeberlen convention and arranging the principal components as $|\delta_{zz}| \geq |\delta_{xx}| \geq |\delta_{yy}|$, two parameters: the anisotropy ($\Delta\delta_D$) and the asymmetry (η_D) are defined as:

$$\Delta\delta_D = \delta_{zz} - \left(\frac{\delta_{xx} + \delta_{yy}}{2}\right) \tag{1.10}$$

and

$$\eta_D = \frac{\delta_{yy} - \delta_{xx}}{\delta_{zz}} \tag{1.11}$$

The e-n dipolar interaction can be averaged under MAS if the spinning frequency is sufficiently high, however typically, even with the most advanced hardware available, the strength of the e-n dipolar interaction is too large to be spun out entirely. For this reason, broad manifolds of spinning sideband are typically present in paramagnetic spectra which can complicate assignments.

Both the e-n dipolar and the Fermi-contact interactions depend on $\langle S_Z \rangle$ (the time averaged z component of the electron spin), which is inversely proportional to temperature and proportional to the B_0 field,[154] hence lower fields are typically chosen for strongly paramagnetic samples to help alleviate the effects of the e-n dipolar interaction and increasing the temperature will reduce the Fermi-contact shift and e-n dipolar broadening.

1.8 Quadrupolar Nuclei

Nuclei with spin I $>$ 1/2 have a nuclear electric quadrupole moment (Q), which interacts with the electric field gradient (EFG) at the nucleus. The quadrupolar Hamiltonian is given by:

$$\hat{H}_Q = \frac{eQ}{2I(2I-1)\hbar}\hat{\boldsymbol{I}} \cdot \boldsymbol{V} \cdot \hat{\boldsymbol{I}} \tag{1.12}$$

Where $\boldsymbol{V}$ is the EFG tensor and e is the electron charge.[150] The anisotropy (eq) and asymmetry (η_Q) of the EFG tensor can be defined as:

$$eq = V_{zz} \tag{1.13}$$

and

$$\eta_Q = \frac{V_{xx} - V_{yy}}{V_{zz}} \tag{1.14}$$

Where $|V_{zz}| \geq |V_{xx}| \geq |V_{yy}|$ are the principal components of $\boldsymbol{V}$. The quadrupolar coupling constant (C_Q), which combines the EFG tensor anisotropy and the nuclear quadrupole moment, is generally the parameter, which is reported, along with the asymmetry, in order to characterise the quadrupolar interaction for a given nucleus/site. It is given by:

$$C_Q = \frac{e^2qQ}{h} \tag{1.15}$$

Although the quadrupole coupling can be large, it is generally sufficient to consider it a perturbation to the Zeeman splitting. To first order, the energy separation of the central transition (½ ↔ −½) is not affected but the other transitions, termed satellite transitions (ST), are split evenly by $2\omega_Q$ were $\omega_Q = \frac{3C_Q}{4I(2I-1)}$.[156] If the $C_Q$is large, then it is necessary to treat the quadrupolar coupling to a second order, in which case the frequency of both the central transition (CT) and the STs are affected. The effect of the second order quadrupolar coupling are a second order shift of the CT to lower frequency and to induce a more complex pattern of STs. Crucially, whilst the first order quadrupolar interaction has an angular dependence of $(3\cos^2\theta - 1)$ and is therefore averaged under sufficiently fast MAS, the second order interaction has a different orientational dependence and therefore cannot be averaged under normal MAS conditions. The second order quadrupolar interaction is inversely proportional to the Larmor frequency and therefore at higher fields it's effects can be ameliorated. In the

case of paramagnetic nuclei with a large C_Q, often as a comprise, an intermediate field must be chosen in order to prevent severe broadening from either contribution.

1.8.1 Quadrupolar Effects on Nutation

Another important practical aspect of quadrupolar NMR experiments is the effect that the quadrupolar coupling has on the RF pulses. The energy separation between the CT and the STs, caused by the first order quadrupolar shift can be large and lead to changes in the nutation frequency (Figure 1.15). If $\omega_1 \gg \omega_Q$ (where ω_1 is RF field strength), then the RF pulse is said to be "non-selective", i.e. it excites both the CT and the STs, effectively behaving as if the system were non-quadrupolar. In the case $\omega_1 \ll \omega_Q$ then the RF pulse is said to "selective" i.e. it will only excite the CT. Due to the fact that only a subset of spins are excited the effective power of the pulse is greater by a factor of $(I + \frac{1}{2})$. Therefore, the flip angle of the pulse has changed and for example: a π/2-pulse, optimised on a non-quadrupolar reference compound, for ^{17}O (I = 5/2) will, for a strongly quadrupolar sample, effectively cause a flip angle of 3π/2. In the intermediate case the optimum flip angle lies between the two limits and the nutation has a non-sinusoidal form. In a real sample, there may be multiple sites with different C_Qs and therefore different nutation behaviour. This means that in order to ensure equal excitation between all sites and thus enable quantitative comparison of the intensities a shorter pulse should be used, so that for all the nuclei the excitation is effectively in the linear region (Figure 1.15). This nutation difference behaviour can be exploited to gain chemical information, in the most basic case by observing which signals are more effectively excited by the non-quadrupolar pulse as these signals must have smaller $C_Q$values and hence lower EFG anisotropy. In work, as a compromise for signal/noise reasons, and with the knowledge that many of the signals will be in the intermediate regime, the "quadrupolar pulse lengths" $\frac{\pi}{2I+1}$ will be used in general.

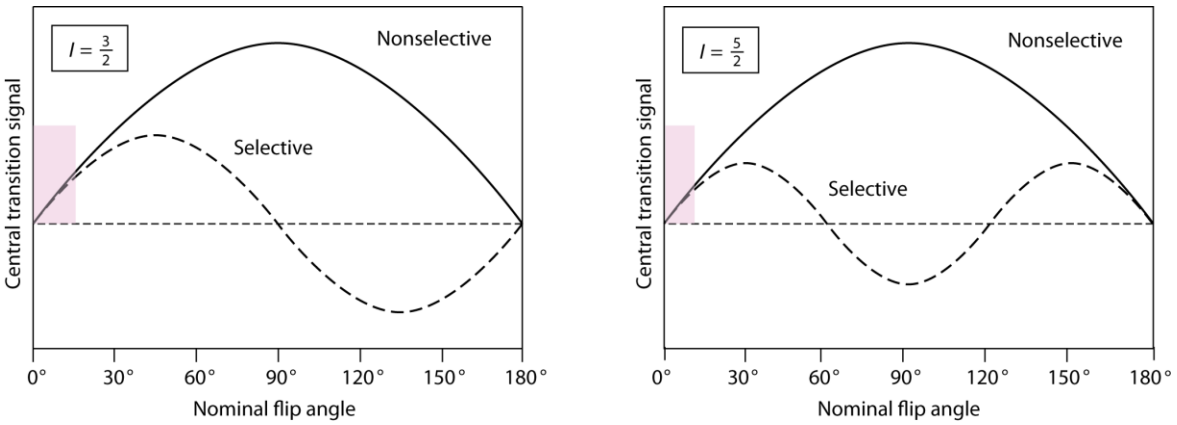

Figure 1.15 Signal intensity of the central transition (CT) resulting from a pulse with a nominal flip angles between 0 and 180°. Filled black lines show the signal intensity vs flip angle for the "non-selective" limit $\omega_1 \gg \omega_Q$, in which the applied RF pulse excites the CT and STs causing the nutation to behave like a $S = \frac{1}{2}$ nucleus. Dashed lines show the "selective" limit $\omega_1 \ll \omega_Q$ in which the RF pulse excites only the CT and the signal is maximised at a nominal flip angle of $\frac{\pi}{2I+1}$. The pink box indicates the linear region where the signal intensity will be the same for both the selective and non-selective limits. Reproduced from reference[157] with permission from John Wiley and Sons.

1.9 NMR of Li-ion Battery Cathodes

In this section, NMR interactions discuss in the previous sections will be placed into the context of the materials in this thesis and some methods for the interpretation of spectra will be discussed. The methodology for studying the NMR of Li-ion battery materials and has been reviewed extensively,[152,158,159] so this section will be specific to the layered $LiTMO_2$ materials.

1.9.1 Bond Pathway Approach

The Fermi-contact shift tends to dominate the spectra of samples containing paramagnetic ions and therefore its interpretation is essential to understanding the spectra. The Fermi-contact shift can be considered, to a very good approximation, additive—i.e. the overall of the Fermi-contact shift for an ion is given by the sum of the contributions from each paramagnetic ion in the vicinity.[160] The magnitude and sign of the spin density transferred to the nucleus ($\rho^{\alpha-\beta}(\boldsymbol{R_N})$) depends on the bond angle, bond lengths and the symmetry of the orbital containing the unpaired spin

density.[155] The compounds considered in this work are all layered rocksalt type structures and all the atoms are in octahedral coordination. This leads to two main spin transfer pathways for Li and other cations (Al, Co): a nearest neighbour pathway (via a .ca 90° TM–O–Li bond) and a next-nearest neighbour pathway (via a .ca 180° TM–O–Li bond). The coordination environment for Li in the Li-layer of Li_2RuO_3 is shown in Figure 1.16 highlighting the bond pathways it experiences. The 90° pathways go via two oxygens, however as it usually more convenient to consider the Fermi-contact from the perspective of the number of nearest and next-nearest neighbours this "bidentate" interaction is usually treated as a single pathway. Only a single Li is shown in the Li-layer for clarity and although it has neighbours within the Li-layer with 90° bond pathways, as it is assumed all these sites contain Li and Li has no unpaired spins, they can be ignored most of the time. A Li-layer Li in $LiTMO_2$ can therefore be said to have 6 90° neighbours and 6 180° neighbours. In Li_2RuO_3, due to its ordered TM-layer, these can be defined as exactly 4Ru and 2Li for both 90° and 180° neighbours. Similarly, a Li (or other cation) in the TM layer, has only Li neighbours in the layers above and below and therefore its only possible paramagnetic neighbours are the 6 90° neighbours that surround it in the TM-layer (Figure 1.16b).

The size and sign of the spin transfer from the TM centres can be rationalised by considering the effect the unpaired spins will have on the TM–O–Li hybrid orbitals as these contain contribution from the Li s-orbitals (mainly 2s) and therefore have a finite probability at the nucleus. There are two main mechanisms: polarisation and delocalisation. For delocalisation, the orbital which contains the unpaired spin is part of the TM–O–Li hybrid orbital and therefore it's alignment with the B_0 field is delocalised over the whole orbital and net positive (aligned with the field) spin transfer is experienced at the nuclear position. In the polarisation mechanism the unpaired spin does not form part of the TM–O–Li hybrid orbital itself but polarises this orbital, which is orthogonal to it, via the exchange interaction; the electron in the TM–O–Li hybrid orbital with same spin spends more time close to the TM nucleus and the rest of the

orbital (including the Li s-orbital) experiences a net negative spin (aligned against the field).[155] Polarisation generally leads to small negative shifts, whilst delocalisation gives positive shifts which tend to be larger. Which mechanism is active depends on the TM species, it's electron configuration and the bonding geometry, this is summarised schematically in Figure 1.16c. The calculation of the bond pathway contributions for each neighbour in a structure can be determined experimentally,[152,161,162] or else by first principals calculations utilising the 'spin flip' bond pathway decomposition approach.[163]

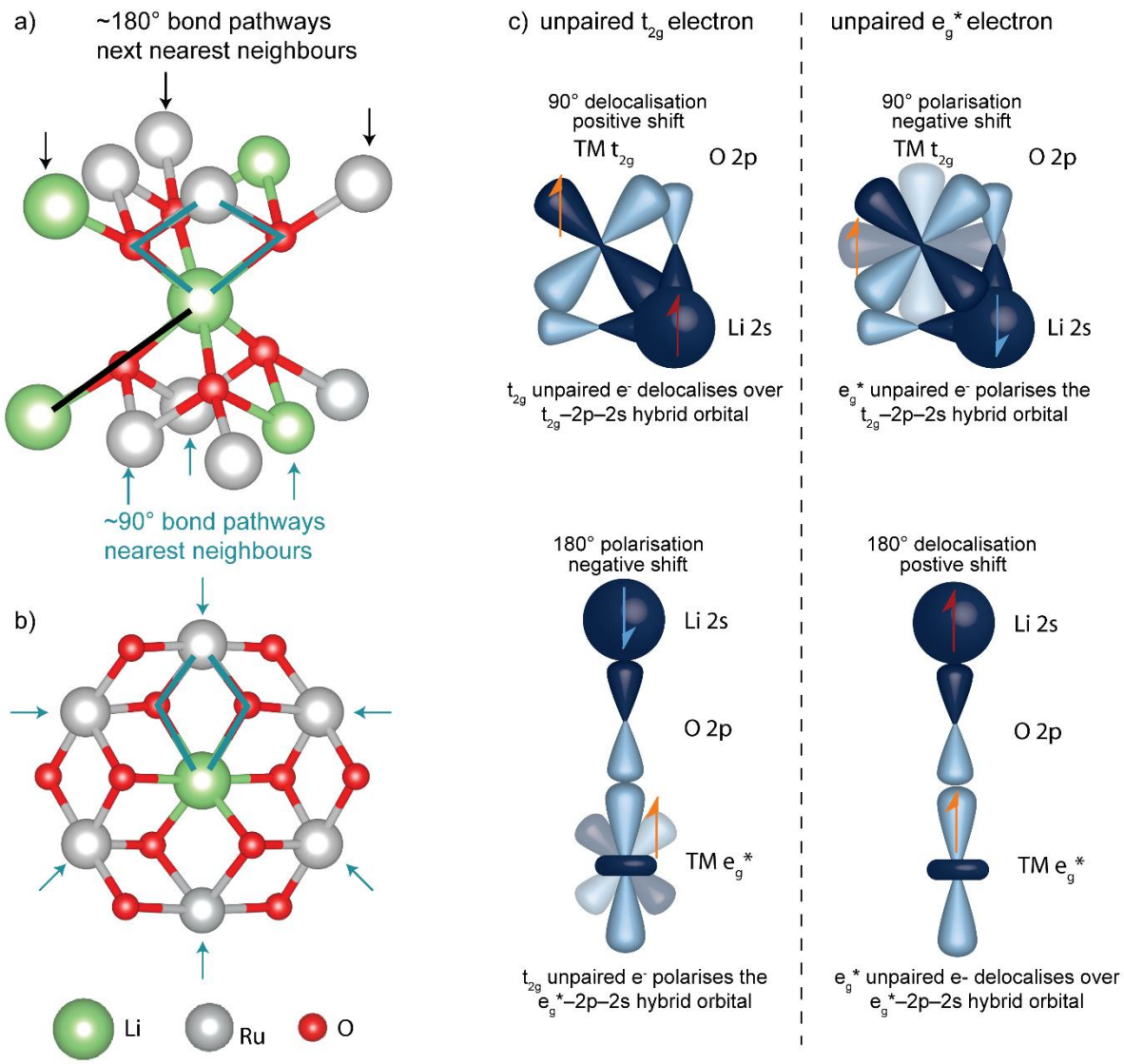

Figure 1.16 a) Illustration of the coordination environment of a Li-layer Li in Li_2RuO_3. There are 6 nearest neighbours (3 above and 3 below) which can transfer unpaired spin density to Li via Ru–O–Li 90° bonds (blue arrows). There are 6 next nearest neighbours (3 above and 3 below) which can transfer unpaired spin density to Li via Ru–O–Li 180° bonds (black arrows). The 90° interactions from within the Li layer can generally be ignored as these neighbours are Li-only. b) Illustration of the coordination environment for a TM-layer site in Li_2RuO_3, there are 6 next nearest neighbours which can transfer unpaired spin density to Li via Ru–O–Li 90° bonds (blue arrows). c) Cartoon representations for TM–O–Li spin transfer. Left-hand side shows the expected spin transfer for a TM with unpaired spin(s) in it's e_g* orbitals; the right-hand side shows the expected spin transfer for a TM with unpaired spin(s) in it's t_{2g} orbitals. The TM electron spins are shown in orange with positive induced spin density in red and negative induced spin shown in blue.

Whilst Li has been discussed above, in this work ^{7}Li, ^{59}Co, ^{27}Al and ^{17}O are all studied and considered using the bond pathway approach. The theoretical basis for these less well studied nuclei is less well defined. In the Li case, the Li contribution to the TM–

O–Li hybrid orbitals is from the 2s orbital so it can interact with the nucleus directly. The situation is more complicated for O (2p), Al (3p) or Co (3d and 4s). For Al and O, which have no significant contribution to the valence states from s-orbitals, unpaired spin density transfer to the p-orbitals cannot interact with the nucleus via a direct contact interaction, however spin density in the valence states will induce a polarisation of the closed-shell core s-orbital electrons. This is analogous to the core-polarisation Knight shift in metallic compounds. It has been shown that the hyperfine field induced at the nucleus, by the Pauli spin density, from the 2p and 3p states is positive (of the same sign) but negative (and of the opposite sign) from 3d states and above.[164] This means that the bond pathway interactions for Al (3p) and O (2p) should still result in shifts of the same sign as in Li. This also implies that for Co, spin transfer to the 3d states should give rise to, via a core polarisation mechanism, some spin density at the nucleus of the opposite sign as is expected for Li. However, for Co, spin density can also be transferred to the nucleus through a direct contact interaction via it's 4s states, which should result in unpaired spin density at the nucleus of the same sign as expected for Li. This later, direct contact, mechanism seems to dominate for Co as calculated fermi contact shifts (Table 2.2), display broadly the same sign and size of shift as would be predicted for Li and Figure 1.16. Ultimately, first principles calculations are invaluable in these complex cases, as even if the absolute magnitude of the shifts is not correct, the sign of the calculated unpaired spin density transfer can help rationalise the observed spectra.

1.9.2 Random Solution Models

If the exact coordination environment is known, then using either calculated or experimentally determined shifts it is possible to compute the expected shift by simply summing the contributions of each bond pathway. For example, Li_2MnO_3 with TM-layer perfect honeycomb ordering (Figure 1.7) would show a single Li-layer resonance corresponding to:

$$4Mn_{90}^{4+} + 2Li_{90}^{+} + 4Mn_{180}^{4+} + 2Li_{180}^{+} \quad (1.16)$$

Using bond pathway contributions determined experimentally,[162] the expected shift is:

$$4 \times 250 + 2 \times 0 + 4 \times -60 + 2 \times 0 = 760ppm \quad (1.17)$$

In reality, Li_2MnO_3 has 2 Li-layer sites (2c and 4h) which have slightly different shifts due to small differences in bond angle and bond length, however to a first approximation the shift from the bond pathway approach is correct.

If the TM-layer is not perfectly ordered, which is the case for most mixed TM $LiTMO_2$, then the number of combinations of neighbours for both sites in the Li-layer and the TM-layer can become too large to consider site by site. Interpretation of the NMR spectra can be very challenging in this case and it can be useful to utilise the additive nature of the Fermi-contact shift to generate model spectra. The simplest and most general model is to assume a "random solution" of cations in the TM-layer. Below is NCA is used as an example.

To calculate the NMR spectrum of a Li-layer Li, that would result for a random solution of cations, all combinations of the 12 neighbours (6 90° and 6 180°) that determine the shift are computed. Then each combination is assigned a probability based on its stoichiometry. The calculation of the probability can be done using the multinomial formula:

$$P = \left(\frac{n!}{n_{Ni}! \times n_{Co}! \times n_{Al}!}\right) \times (p_{Ni}{}^{n_{Ni}} \times p_{Co}{}^{n_{Co}} \times p_{Al}{}^{n_{Al}}) \quad (1.18)$$

Where n is the total number of atoms for a given coordination environment, n_{Ni}, $n_{Co}$and n_{Al} are the number of Ni, Co and Al atoms for the combination and p_{Ni}, $p_{Al}$and p_{Co} are the probability of finding Ni, Co or Al, determined by their stoichiometry, in that environment. This formula is applied to every combination of 6 180° neighbours and every combination of 6 90° neighbours, and the results multiplied together to give the overall probability of the full 12 neighbour combination. A Gaussian peak can then be

calculated for each environment, with the height of the peak (a) given by the probability, the peak centre (b) determined by the corresponding shift, the width (80ppm in this work) (c) which should reflect the intrinsic peak width if the site were isolated, and x stepped in defined increments (in this work 1 ppm):

$$f(x) = ae^{-\frac{(x-b)^2}{2c^2}} \tag{1.19}$$

The Gaussian functions of all environments can then be summed together to give an approximate NMR spectrum for comparison with the experimental spectrum.

1.9.3 Li Motion

Li ion conduction is a key factor in electrode performance as Li ions must be able to reach the electrolyte easily for the cell to function well. It is therefore desirable to have low barrier to Li hopping in the electrode in order to promote good Li conduction. Fast Li motion affects the NMR lineshapes that are observed. Below, the example of symmetrical two site exchange, which is an oversimplification but provides a useful framework for understanding motional effects, is considered.

The effect of motion on the NMR spectrum for symmetrical two site exchange depends on two factors: the frequency separation of the sites (Ω_Δ) and the exchange frequency (k). If the Ω_Δ and (k) are of similar orders of magnitude then the sample is in said to be in the "intermediate exchange" regime.[165] Within this regime there are two sub-regimes which depend on the relative magnitudes of Ω_Δ and k. If $k < |\Omega_\Delta/2|$ then the sample is in the "slow intermediate exchange" regime and if $k < |\Omega_\Delta/2|$ then the sample is in the "fast intermediate exchange" regime. For the "slow intermediate exchange" regime, when the nuclei exchange, they experience different precession frequency which induces a phase shift, the accumulation of which leads to enhanced transverse (T_2) relaxation and broadening of the spectrum. This enhanced T_2 relaxation will lead to reduced signal intensity for Hahn-echo experiments. This is "motional broadening". For

the "fast intermediate exchange" regime the hopping becomes fast enough that the nuclei have no time to acquire a phase shift between hops and effectively experience an average procession frequency. Under these conditions an average shift is observed and the lineshape becomes narrower as the hopping frequency increases. This is called "motional narrowing".[165]

In real systems there are hundreds of Li environments (784 possible Li environments in NCA for example) therefore it is necessary to have an expedient method of calculating the effects of exchange on our lineshapes. Norris' formula,[166] which allows rapid computation of the lineshape can be used, although several assumptions must be taken into account. Firstly the hopping rate between all sites must be the same, secondly all sites are assumed to participate in the hopping and thirdly a value for the native linewidth (full width at half maximum in Hz) of a non-exchanging, non-overlapping site ($\nu_{1/2,no\text{-}exch}$) for all the sites must be chosen. With this the lineshape (L_{hop}) can be calculated.[26]

$$L_{hop} = \frac{-i\sum_j\sum_k F_{jk}(\nu)}{1 + k_{ex}\sum_j\sum_k F_{jk}(\nu)} \cdot \frac{1}{\omega_{Li}10^{-6}} \tag{1.20}$$

Where k_{ex} is the exchange frequency, ω_{Li} is the Larmor frequency which converts the lineshape onto a ppm scale and $\sum_j\sum_k F_{jk}(\nu)$ is the sum for all environments of $F_{jk}(\nu)$ which describes the lineshape contribution for each environment.

$$F_{jk}(\nu) = \frac{P_{jk}}{i(\nu - \nu_{jk}) - \nu_{\frac{1}{2},no\text{-}exch} - k_{ex}} \tag{1.21}$$

Where P_{jk} is the probability for a given environment and ν_{jk} is the corresponding shift (ppm) The values calculated in the random solution can be converted by this formula into a distribution which accounts for motional narrowing and values of k_{ex} can be estimated.

1.9.4 Variable Offset Cumulative Spectra (VOCS)

Paramagnetic and quadrupolar spin interactions can be extremely large and can give rise to spectra where the width of the line shapes are larger than the excitation widths of the pulses. Whilst various strategies have been employed to record so called "ultra-wideline" NMR spectra, the most applicable to fast relaxing systems (such as paramagnetic battery materials) is frequency stepped measurements.[167] To record a frequency stepped spectrum multiple individual spectra are recorded at different offset frequencies and then summed together to give an overall spectrum. In early work this was achieved by sweeping the magnet with a fixed offset frequency,[168–170] however for most modern pulsed NMR hardware it is generally more convenient to step the offset frequencies and leave the B_0 field unchanged to achieve the same goal. The spectra that result from this stepped offset acquisition and summation are called variable offset cumulative spectra (VOCS). It was shown by Tong that for Hahn-echo experiments on a static sample, the VOCS experiment can capture the theoretical spectra, were uniform broad excitation possible, provided that the frequency separation between the offsets is not too large.[171] In this work all VOCS spectra were recorded using Hahn-echo experiments so the size of the frequency step that is appropriate is determined by the π refocussing pulse which has the lowest field strength. The summation of all the sub spectra to create the correct overall spectrum relies on the correct phasing of each sub spectrum; for extremely broad signals this can be challenging. The application of a window function to each sub spectrum, such that the only the central part of the excitation width is retained, whilst the remainder is set to zero can help alleviate this issue. Defining a value x as

$$x = (\omega - \omega_0)/\omega_1 \tag{1.22}$$

Where ω_0 is the carrier frequency, ω is the frequency of any point on the spectrum and ω_1 is the excitation frequency, Tong showed that the everything but central part can be filtered out by setting the intensity to zero when $|x| \geq 1.73$.[171] As well as helping to

alleviate the challenge of phasing a VOCS, application of the window function removes noise that would otherwise retained in the final spectrum. Pell et al. demonstrated that under MAS, VOCS can produce the theoretical broadband spectrum with the correct sideband intensities.[172] One disadvantage of performing frequency stepped experiments is the long time they take acquire and also the need for the experimenter to constantly retune the probe, this later drawback can be ameliorated through the use of automated tuning and matching systems, for example a tuning robot.[173]

1.10 Motivation and Outline of Thesis

The development of high capacity Li-ion batteries essential for the next generation of EV technology. In additional to high capacities a reduction in cost and toxicity, through adoption of low-Co or preferably Co free materials, is desirable. New avenues in battery materials particularly Li-excess materials, which have high capacities and can be Co free, have the desired high capacities and low costs, however there are many challenges blocking their implementation such as high first charge capacity loss, poor rate capability and voltage fading. Greater understanding of the redox processes which give rise to their anomalously high capacities is required if these processes are to be harnessed without the draw backs that they seem to engender. Long-range and local structure changes are intimately tied high voltage degradation and redox processes. A better understanding of these changes, their causes and their effects (positive and negative) is needed in order to aid rational materials design. Ultimately some local structure changes may be required in order to produce the highest capacities but to what degree these changes can be borne by the materials, without critical impacts on performance remains to be seen.

In order to further these understandings, extensions to the utilisation of current structural probes must be developed. Solid state NMR is one of the most important local structure techniques, but the study, of many nuclei in battery materials, has been

neglected owing to the challenges inherent in measuring spectra of, for example, ^{17}O, ^{59}Co and ^{27}Al, in paramagnetic materials. Additionally, model compounds are often invoked in order to study some aspect of electrode operation whilst excluding other factors which may complicate the picture considerably. This has been a fruitful approach but care needs to be taken when evaluating model compounds as their behaviour is rarely as simple as would be desirable.

The goal of this work is to leverage existing NMR techniques to study "exotic" nuclei in battery materials and by doing so gain insight into both the chemistry of the battery systems and lay new foundations for future use of less common NMR nuclei in battery materials.

In Chapter 2, the widely used commercial battery material NCA ($LiNi_{0.8}Co_{0.15}Al_{0.05}O_2$) is investigated using ^{7}Li, ^{17}O, ^{59}Co and ^{27}Al NMR. The Jahn-Teller behaviour of the pristine material is characterised using this multinuclear approach. The Li dynamics on discharge are probed using variable temperature ^{7}Li NMR. Finally, the redox mechanisms are considered and the unusual behaviour of the ^{59}Co NMR is assigned.

In Chapter 3, Li_2RuO_3, often employed as model compound, is studied in detail. ^{7}Li and ^{17}O NMR investigations, supported by neutron diffraction and magnetometry, demonstrate the significant effect of Ru–Ru dimerisation on the local and electronic structure, which is commonly neglected by battery studies. The ^{7}Li and ^{17}O NMR spectra are recorded and assigned at room temperature and through the dimer-solid to dimer-liquid phase transition. Assignments of the ^{17}O NMR required careful consideration of the O coordination and an extension of the commonly applied bond pathway approach.

In Chapter 4 the work of Chapter 3 is extended to delithiated Li_xRuO_3. The long-range structural changes, observed by in-situ diffraction, are correlated with the changes in the NMR spectra. The observation of ^{17}O NMR throughout the charging process is one

of the first studies of it's kind and in conjunction with the ^{7}Li NMR reveals information about the electronic and local structure not obtainable by any other technique.

Chapter 2: Multinuclear NMR Investigations of Distortions, Li-mobility and Redox Phenomena in NCA

2.1 Abstract

$Li(Ni_{0.80}Co_{0.15}Al_{0.05})O_2$ is an industrially important cathode material and is likely to become even more so in the coming decade. Many aspects of its local structure both in the pristine material and on cycling are not well characterised, owing to the complexity inherent in a layered rocksalt material with a disordered transition metal layer containing Ni, Co and Al, as well as the Jahn-Teller (JT) activity of Ni^{3+}. In this work, in addition to the commonly utilised ^{7}Li NMR, the TM layer is examined directly, by exploiting the NMR active ^{59}Co and ^{27}Al nuclei and the anion framework of the material studied via ^{17}O NMR of isotopically enriched samples. Through these complimentary probes the JT ordering in the pristine material is characterised, showing that, whilst the JT distortions are averaged on the NMR timescale, the arrangements in which the JT axes coordinate with one another, make up greater proportion of the averaged structure. On discharging there is a sharp increase in Li dynamics and at the onset of fast Li motion, evidence of heterogeneous delithiation is observed. Such heterogeneity may eventually give rise to "sluggish" and "active" populations of Li on multiple cycles, a well-known degradation pathway. Finally, the redox mechanisms of NCA are examined. The unexpected behaviour observed in ^{59}Co NMR on delithiation is explained by invoking the paramagnetic contribution to the chemical shift and the change in energy separation of the t_{2g} and e_g* levels in Co at the end of charge, providing information about the Co^{3+} electronic structure and a framework for the interpretation of ^{59}Co shifts in future studies.

2.2 Introduction

NCA ($Li(Ni_{0.80}Co_{0.15}Al_{0.05})O_2$) is one of the premier commercial Li-ion battery cathode materials. Understanding why it is such a good cathode material can help guide the design and understanding of the next generation of materials. In addition, there is a still a gap between the theoretical and practical performance of NCA, which may be reduced with greater understanding of its degradation mechanisms. Some aspects of NCA have been very well studied; as discussed in section 1.2.4, NCA overcomes many of the challenges associated with single TM layered transition metal oxide cathode by virtue of its mixed TM layer. The lack of long-range ordering or segregation in the TM layer of NCA plays a role in the suppression of Li/vacancy orderings and stacking sequence changes, as the lack of TM layer order reduces the thermodynamic driving forces for these long-range, cooperative processes. Still many aspects of NCA's behaviour on charge are not well characterised. The role Al plays in increasing the thermal and cycling stability is not clear, migration into tetrahedral sites at the end of charge and prevention of Ni migration has been proposed.[174,175] Although there are clearly long range effects that are supressed by a mixed TM-layer, the relatively low stoichiometry of Al and Co have a disproportionate effect on the cycling performance. The relatively low concentrations of "defect" atoms required to produce these effects suggests that there may be strong local order effects to be accounted for.

The long-range structure of pristine NCA is relatively straightforward. It has the α-$NaFeO_2$ structure type with the Li and the TMs arranged in layer and the rhombohedral space group $R\bar{3}m$. The local structure is much more complex as NCA has a disordered TM-layer the single crystallographic site can have hundreds of possible combinations of nearest and next nearest neighbours. As detailed in section 1.7 the NMR spectra of species containing paramagnetic ions are generally dominated by the effects of these ions namely, the large Fermi-contact shifts and the broadening caused by electron-nuclear dipolar coupling. In pristine NCA these effects come from the d^7

($t_{2g}^6 e_g^{*1}$) Ni^{3+}. As Ni^{3+} is a JT-ion its octahedra will distort (Figure 1.4), with two elongated bonds along one axis and four remaining bonds shortened. The JT distortion lifts the degeneracy of the e_g orbitals and hence the unpaired electrons are contained in the orbital along the long axis (d_{z^2}). As the Fermi-contact shift depends on the through bond transfer of electron density to the NMR active nucleus' s-orbitals (section 1.7.1), whether the Ni^{3+} is bonded to the species in question via a JT lengthened or shortened bond greatly affects its shift contribution. In NCA, as in $LiNiO_2$, no cooperative, static JT distortion is observed.[33–35]

In this chapter both pristine and delithiated NCA are investigated using a multinuclear NMR approach. First the pristine material is investigated the local structure and JT behaviour are discussed in detail, particularly with respect to the effect the JT dynamics have on the NMR spectroscopy. Then, the dynamics of the Li on delithiation and its impact on the cycling behaviour are highlighted. Finally, the complex redox behaviour of NCA on delithiation is discussed in the context of new information gained through the use of challenging and unconventional NMR nuclei.

All calculations presented were performed by Dr Ieuan D. Seymour. Calculations were carried out in the code CRYSTAL using hybrid functionals B3-LYP with 20% and 35% Hartree-Fock exchange referred to in the text were necessary as HYB20 and HYB35 respectively. Further computational details can be found elsewhere.[176]

The code for modelling the fast Li-ion motion utilising Norris' formula was written by Dr Katharina Märker.

The code used to filter each sub-spectrum in the VOCS was written by Dr Erlendur Jónsson.

The NCA precursor for ^{17}O samples were prepared by Dr Brian May. They were layered double hydroxides prepared by a hydrothermal route described elsewhere.[177]

2.3 Experimental

2.3.1 Materials and Synthesis

For the pristine ^{7}Li, ^{27}Al and ^{59}Co NMR study, NCA ($Li(Ni_{0.8}Co_{0.15}Al_{0.05})O_2$), from TODA America (NAT-1050), was used as received and is henceforth referred to as TODA-NCA. The cycled and variable temperature ^{7}Li NMR was performed on the same TODA America (NAT-1050) NCA but as the material had been stored outside a glovebox for a significant period, the material was calcined at 800°C for 4hrs (5°Cmin^{-1} heating rate, cooled by switching off the heating elements) to remove surface species—sample henceforth referred to as HT-TODA-NCA.[178] Refinements of lab X-ray diffraction showed that HT-TODA-NCA has slightly higher Ni-Li anti-site disorder (5%) compared to the as received TODA-NCA (1%) (Table 2.1). To enable ^{17}O NMR measurements, NCA samples were enriched in the I=5/2 NMR active nucleus ^{17}O. A previously successful strategy for performing such enrichments in Li_2MnO_3 and Li_2RuO_3 has been to heat the synthesised material under a $^{17}O_2$ enriched atmosphere.[101,179] The TODA-NCA has a primary particle size between 300 nm and 1 μm and a spherical secondary particle morphology with a radius <10 μm,[180] therefore NCA particles with a smaller particle size were desired to facilitate uniform enrichment and to maximise O-exchange. The NCA hydroxide precursors were heated at 400°C for 4hrs (5°Cmin^{-1} heating rate, cooled by switched off the heating elements) to form oxides. These were annealed at 800°C for 1h and 700°C for 12h (5°Cmin^{-1} heating rate, cooled by switching off the heating elements). The results of this synthesis yielded a phase pure NCA powder, henceforth referred to as "primary synthesis NCA". This was subsequently enriched via secondary annealing step in a static O_2 (70% ^{17}O NUKEM Isotopes) environment at ~320 kPa at 800°C for 12 h (5°Cmin^{-1} heating rate, cooled by switched off the heating elements). Both the NCA resulting from the primary synthesis and the enrichment were confirmed to be phase pure with anti-site disorder of 4.6%

and 10.6% respectively (section 2.4.1), determined from Rietveld refinement using X-ray diffraction data. Attempts to perform an enrichment during the primary synthesis (i.e. annealing the NCA and Li oxides at 700°C for 12hrs and then 800°C 1hr in the ^{17}O atmosphere) resulted in significantly high anti-site disorder >20%. The enrichments were performed with sample masses ~80mg and with a $^{17}O_2$ volume of 12-15cm^3. Although small particle size NCA was used to perform the enrichment step, it is possible that the enrichment of the sample is not uniform, for example it might be expected that the surface would exchange more O during the annealing step. In order to test this and probe any changes in surface structure induced by the $^{17}O_2$ annealing step, focused ion beam secondary ion mass spectrometry (FIB-SIMS) measurements would be valuable. This would enable depth profiling of the isotopic composition of the NCA particles.

2.3.2 Diffraction

Powder diffraction was collected on a Panalytical Empyrean diffractometer using CuKα radiation to check the purity and the anti-site disorder in the materials. Simple Rietveld refinements were performed using the TOPAS program;[181] the peak shape and diffractometer constants were set using a Si standard.

2.3.3 NMR Methods

^{7}Li NMR was conducted at 4.7 T using a Bruker 1.3 mm MAS probe at 60kHz MAS frequency. The spectra presented are rotor-synchronised Hahn-echo experiments with the echo delay equal to one rotor period unless otherwise noted. Spin lattice T_1 relaxation was measured by a saturation recovery experiment to be ~5 ms for the bulk NCA Li signal. Recycle delays were set to be five times the T_1 value (40 ms) for quantitative acquisition. Where presented, T_2 was measured using a series of Hahn-echoes with incrementing numbers of rotor periods as the echo delay and fitting the intensities using an exponential decay function. ^{7}Li spectra were referenced to 1M

LiCl in D_2O at 0ppm or solid Li_2CO_3 at 0ppm. Temperature calibration was performed *ex situ* using the ^{207}Pb shift of $Pb(NO_3)_2$ as an NMR thermometer[182]. Although ^{7}Li is a spin I=3/2 nucleus, due its low nuclear quadrupole moment, it was treated as a pseudo-I=1/2 nucleus.

^{17}O NMR was conducted at 11.7 T using a Bruker 1.3 mm MAS probe at 60kHz MAS frequency. Due to the extremely broad line shapes, the ^{17}O spectra were recorded as variable offset cumulative spectra (VOCS) composed of several individual rotor-synchronised Hahn echo spectra, summed together to give the full spectrum. As ^{17}O is a spin I=5/2 nucleus, a $\pi/2$ pulse, optimised on the reference compound (0.1M $KCo(CN)_6$ in D_2O) was divided by 3 to give a shorter effective $\pi/2$ pulse which will be approximately quantitative for all signals regardless of quadrupolar coupling (section 1.8.1). The rf-field strength of the effective $\pi/2$ pulses (0.71 μs at 100 W) is 350kHz which equates to ~5200ppm at 11.7T. For an excitation of 90% for the effective π-pulse a spacing of 1.6 times this value is possible, however a flat excitation profile for the full width of the spectrum is possible if the VOCs experiments are much closer together hence the spectra were spaced 2500 ppm apart from each other. The frequency range covered, number of experiments and experimental duration accompany the spectra. T_1 relaxation was only explicitly measured for the sharp 0ppm component (due to the long acquisition times required for the broad component) and was ~30ms, the broad component at high shift was assumed to be much shorter as the intensity of this broad component did not change when the recycle delay was shortened from 100 ms to 5 ms. Due to the long spectral acquisition times, individual slices of the VOCS were recorded with a recycle delay of 5ms except for the slices around 0ppm in the cycled sample which used a recycle delay of 100 ms. This compromise allows the observation of both the fast and slow relaxing components of the spectra in a semi-quantitative fashion without making the acquisition times impractically long. The VOCS were collected with the aid of an automatic tuning/matching robot.[173] ^{17}O spectra were referenced to

the secondary reference CeO_2 at 877ppm or H_2O at 0ppm. A filtering script was applied to each sub-spectrum of the VOCS as described in section 1.9.4.

^{27}Al NMR was conducted at 4.7 T using a Bruker 1.3 mm MAS probe. ^{27}Al is a spin I=5/2 nucleus $\pi/2$ pulse, optimised on the reference compound ($AlF_{3(s)}$ at -17 ppm) was divided by 3 to give a shorter effective $\pi/2$ pulse which will be quantitative for all signals regardless of quadrupolar coupling (section 1.8.1). Recycle delays of 0.1 s were used which is quantitative for the paramagnetically shifted Al signal (T_1s on the order of μs)[183] but not for the diamagnetic signals.

^{59}Co NMR was conducted at 4.7 T and 16.4 T using a Bruker 1.3 mm MAS probe. ^{59}Co is a spin I=7/2 nucleus $\pi/2$ pulse, optimised on the reference compound (0.5 m $K_3[Co(CN)_6]$ in D_2O) was divided by 4 to give a shorter effective $\pi/2$ pulse which will be quantitative for all signals regardless of quadrupolar coupling (section 1.8.1). Saturation recovery measurements for the pristine material were performed and a single component fit for the entire distribution of shifts was used and gave a $T_1 = 1$ms. Recycle delays of 2 ms were used for the cycled samples to minimise acquisition times. For the pristine material recycle delays of 10ms were used.

2.3.4 Electrode Preparation and Electrochemistry

Cathodes for NMR characterisation were produced by grinding by hand, with an agate pestle and mortar, the sample, Super P carbon (Timcal) and Kynar Flex® (Polyvinylidene Fluoride PVDF) in a ratio 80:10:10 by mass for 20 minutes until well mixed. N-methyl-2-pyrrolidone (NMP) was added to form a slurry which was transferred onto aluminum foil and spread using a 150 μm doctor-blade. The films were dried under vacuum at 100°C overnight. Cathodes were punched to a diameter of 1.11 cm giving a surface area of 0.97 cm^3 and mass loadings in the range 6-8 mg. Coin cells were made in an argon filled glovebox with H_2O level < 0.1 ppm and O_2 level $= 0.3$ ppm. Cathodes were placed on steel current collectors (0.5 mm) and separated from

the counter electrode by glass fiber soaked with electrolyte. The anode was a lithium foil (Sigma Aldrich, 99.9 %), and backed with a steel current collector. The entire assembly was compressed by a steel wave spring and crimped. The electrolyte used was 1M $LiPF_6$ in a 1:1 ratio of ethylene carbonate and dimethyl carbonate (EC:DMC, Sigma Aldrich).

All potentials are with respect to Li/Li^+. Currents were set at C-rate C/20 based on the active mass loading of each cell and according to the theoretical 0.8 Li capacity i.e. corresponding to the removal of the full 0.8 Li per formula unit ($247.6mAhg^{-1}$) . Measurements were carried out on a Bio-Logic or an Arbin potentiostat. Once charged, cells for NMR were deconstructed in the same glovebox, the cathodes rinsed with DMC solution (99.9 % Sigma Aldrich) and dried under vacuum for 30 minutes. The cathode material was scraped off the foil and packed into 1.3 mm zirconia rotors with Vespel caps for NMR analysis.

2.4 Part 1: Characterisation of Pristine NCA

While the long-range structure of pristine NCA is well characterised, the local arrangements in the TM-layer are not well understood. The presence JT distortions, caused by the Ni^{3+} ions, has generally not been considered as they have little effect on the long-range structure and on the NMR timescale, they may be considered dynamically averaged. In this section, the basic characterisation of the samples used for both the study of pristine NCA and NCA on delithiation will be review and then the NMR spectra of pristine NCA will be considered in detail.

2.4.1 Diffraction

Preliminary materials characterisation was carried out on all the NCA samples using XRD. Rietveld refinements were performed by the following procedure: Using peak shapes and instrument parameters refined using Si standards the lattice parameters

and scale factor were allow to vary to obtain the correct peak positions. Then size and strain parameters were allowed to refine to obtain more accurate peak shapes for the specific sample. Next, the Ni occupation of the Li-layer was then accounted for by refining the Li-layer (3a) site as a split position between Li/Ni with the total occupancy constrained to be one; Li occupying Ni sites was not considered. Finally, the O z parameter was allowed to refine. The other occupancies were fixed at the values expected from the stoichiometry and the thermal parameters were treated isotropically and were fixed at 0.6Å^2. The results of these refinements are displayed in Table 2.1 and in Figure 2.1. The samples were confirmed to be pure by XRD, although the anti-site disorder, characterised by the (003)/(104) peak ratio, varied somewhat. The precise quantification of the this antisite disorder is limited to some extent by data quality. Analysis of SQUID magnetometry might provide corroborating evidence to help better quantify the amount of the Ni^{2+} in the Li-layer, as defects of this type introduce strong antiferromagnetic order between the TM-layers.[44]

2.4.2 Electrochemistry

Typical electrochemical voltage curves for each of the NCA samples are shown in Figure 2.2. TODA-NCA and HT-TODA-NCA show quite typical voltage curves for NCA, although the high voltage features are slightly different. The HT-TODA-NCA may already have a more densified surface due to the additional annealing step which may be the reason for the difference. The ^{17}O-NCA shows poorer performance. There is a low voltage process before the plateau is reached which is unexpected and unaccounted for. The voltage plateau occurs at an overpotential >0.2V. The source of this overpotential may be due to the additional Ni in the Li layer which is expected to impede the kinetics. It is challenging to produce homogeneous films with very small batches of cathode material and hence poor-quality cathodes may also factor into the difference between the ^{17}O-NCA sample and the other NCAs. Additionally, ^{17}O-NCA

has much smaller particles and this may exacerbate issues arising from surface impurity species and transformations.

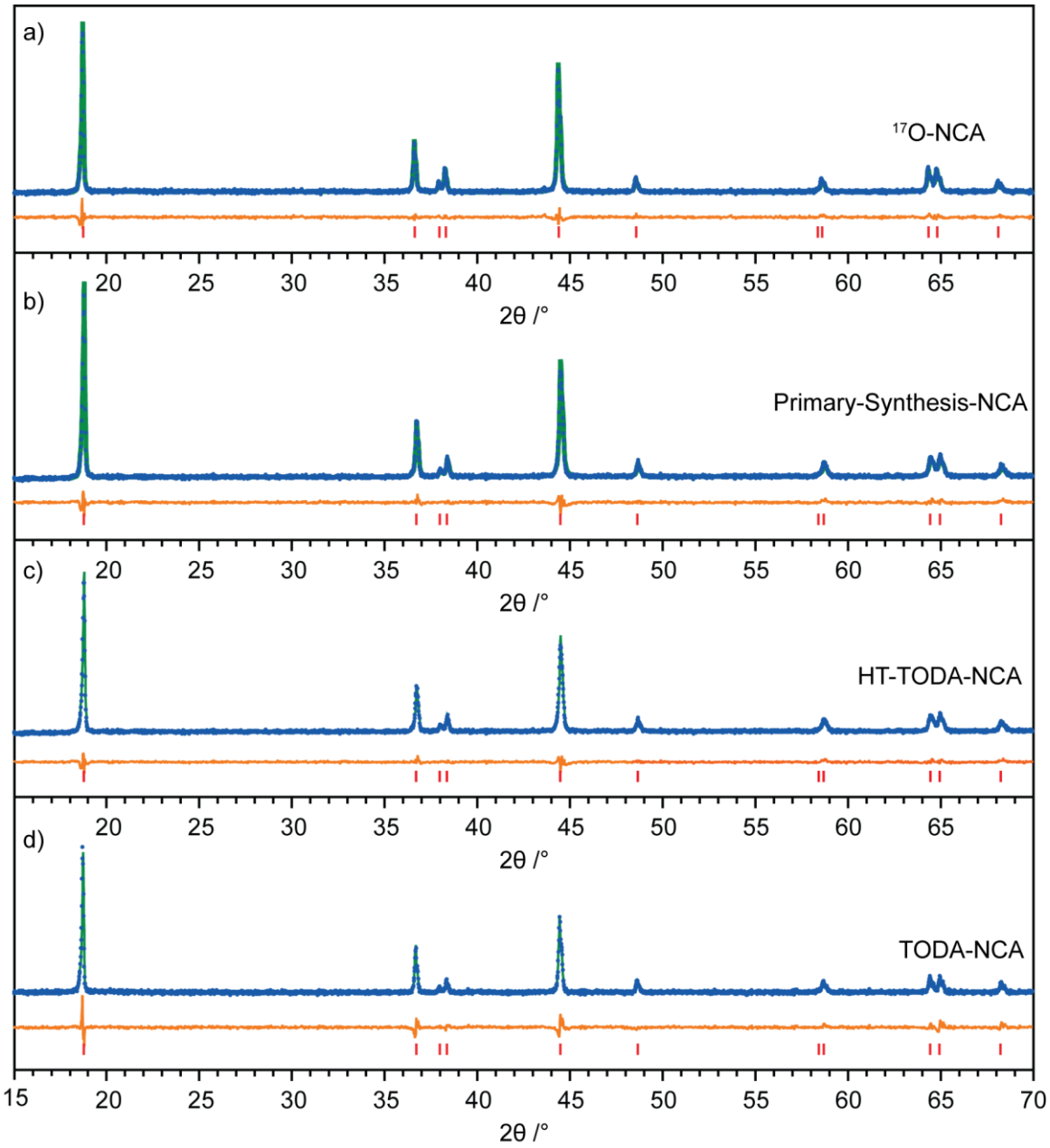

Figure 2.1 Diffraction patterns of the NCA samples in this work. The refined parameters are reported in Table 2.1. The experimental pattern is shown in blue, the model is in green, the difference is shown in orange and the tick marks in red show the positions of the peaks predicted by the $R\bar{3}m$ space group.

Table 2.1 Refined crystallographic parameters of the different NCA samples used refined against the $R\bar{3}m$ space group.

Sample Name	Ni on Li sites/%	a/Å	c/Å	O z-coordinate	R_{wp}
TODA-NCA	1.21(3)	2.86555(5)	14.2006(3)	0.2573(3)	5.263
HT-TODA-NCA	4.98(2)	2.86740(4)	14.1907(6)	0.2563(2)	3.441
Primary -NCA	4.62(2)	2.86704(4)	14.1980(2)	0.2567(1)	3.382
^{17}O-NCA	10.62(2)	2.87265(5)	14.2056(5)	0.257(2)	3.370

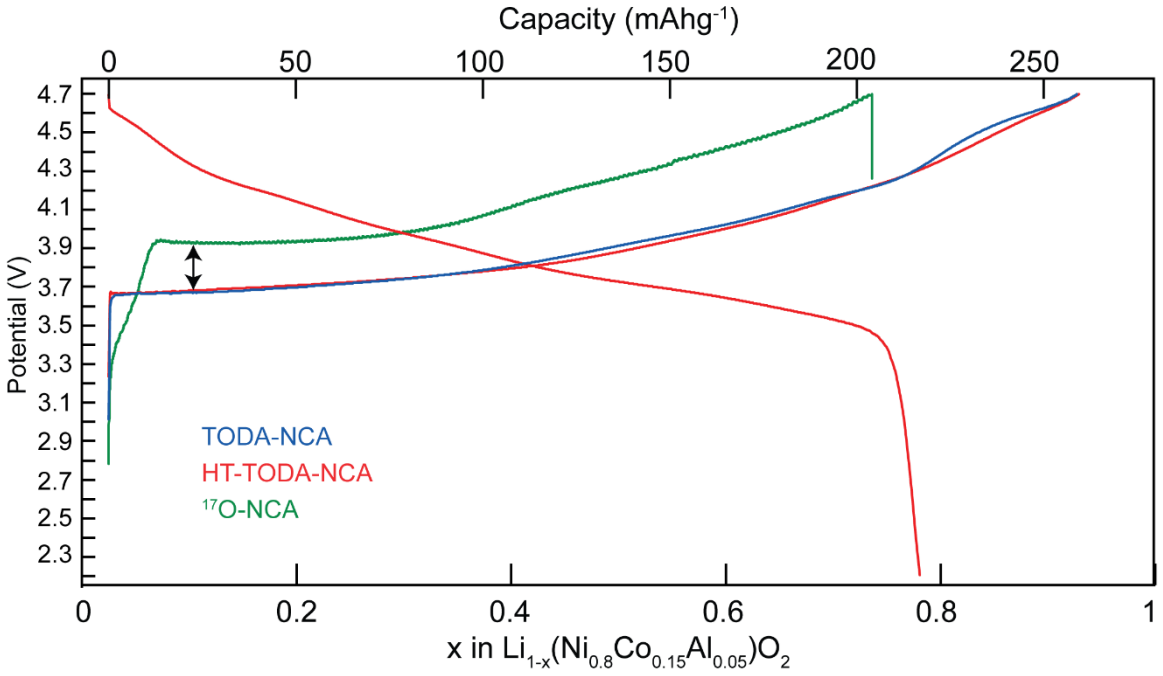

Figure 2.2 Typical electrochemical charging curves for each of the NCA samples. The first HT-TODA-NCA (red) discharge curve is also shown. The TODA-NCA (blue) shows the typical electrochemical profile of NCA. The HT-TODA-NCA shows similar voltage vs capacity behaviour but lacks the feature at high voltage observed in the TODA-NCA. ^{17}O-NCA (green) shows significantly poorer performance. In the initial part of charge there is a low voltage process which is not expected for NCA. Additionally, there is a large >0.2V overpotential (black arrow) once the plateau is reached. The sawtooth pattern observed is due unusually large to temperature fluctuations due to external temperature control issues. This effect is generally more prominent in samples where increasing the temperature and therefore the kinetics will lead to a reduction in the overpotential.

2.4.3 ^{7}Li NMR

The ^{7}Li NMR for each of the NCA samples in this work are shown in Figure 2.3. The NCA ^{7}Li spectra show a broad peak centred around 560 ppm spanning from ~100-900 ppm and the sidebands resulting from these resonances, as well as small diamagnetic peak at 0ppm, which is assigned to Li surface species and other diamagnetic impurities. The patterns are similar although the HT-TODA-NCA shows a slightly broader pattern with a lower peak position at ~550 ppm. The broadness of the pattern is a result of the range of local Li environments that are present in NCA. Each of these individual resonances are not resolved due to their broadening by the electron-nuclear dipolar coupling and short T_2s. The line shape is asymmetric a gradual tail off from the peak towards 0 ppm and a sharper drop on the high shift side. In addition, the TODA-NCA and ^{17}O-NCA have a more prominent shoulder at ~660 ppm.

2.4.4 ^{7}Li NMR Discussion

As discussed above, the Fermi-contact shift that results from a Ni^{3+}–O–Li, for both 90° and 180° pathways, depends strongly on whether the Ni^{3+}–O bonds involved are JT lengthened or JT shortened. The 90° bond pathways can be split into δ_{SL}—the Fermi-contact contribution for a 90° pathway which goes via one lengthened and one shortened JT bond—and δ_{SS}— the Fermi-contact contribution for a 90° pathway which goes via two JT shortened bonds. The δ_{SL} pathway goes via a polarisation mechanism in which the Ni–O, $3d_{z^2}$–$2p_z$ orbital polarises the Li–O $2p_{x/y}$–2s orbitals imparting a positive shift. The δ_{SS} pathway goes via a similar mechanism of polarisation of Li–O by Ni–O, however the $3d_{x^2-y^2}$ orbitals, which would usually contain unpaired electrons, are effectively unoccupied due to the JT distortion and the shift is consequently smaller. The 180° bond pathways can be split into δ_L—the Fermi-contact contribution for a 180° pathway which goes via a lengthened JT bond—and δ_S— the Fermi-contact contribution for a 180° pathway which goes via a JT shortened bond.

In this case both δ_L and δ_S would be expected to go via a delocalisation mechanism giving positive shifts (section 1.7.1), as the e_g* electron from Ni^{3+} can delocalise over the (Ni^{3+}–O–Li) e_g*–2p–2s hybrid orbital and induce positive spin density at the Li nucleus. For δ_L, the e_g* orbital is the elongated, half occupied d_{z^2} orbital so the shift is large, for δ_L, the e_g* orbital is the shortened, empty $d_{x^2-y^2}$ orbital so the shift is much smaller.

A random solution model spectrum was constructed, as described in section 1.9.2, for comparison with the ^{7}Li NMR spectra. Previous studies have shown using bond pathway contributions for Ni^{3+} that represent a dynamically averaged shift can reproduce the Li spectrum reasonably well.[176] This simplifies the generation of the model and only the number of Ni^{3+} neighbours is needed to generate the shift for each environment. The dynamically averaged shifts ($\delta_{90°}$ and $\delta_{180°}$) are given by:

$$\delta_{180°} = (2\delta_S + \delta_L)/3 \tag{2.1}$$

and

$$\delta_{90°} = (\delta_{SS} + 2\delta_{SL})/3 \tag{2.2}$$

This approach was also adopted in this work, with bond pathways for Ni^{3+} set at −15 and 125 ppm for 90° and 180° respectively, based on the previous study;[176] all other species (Li^+ and Co^{3+}) assumed to contribute 0 shift. The spectrum that resulted from this random solution modelling is shown alongside the experimental spectra in Figure 2.3.

The model reproduces the lineshape reasonably well, however there is clear deviation at ~660 ppm where a shoulder is observed in the experimental spectrum. This high shift feature is at the shift expected for Li with 6Ni 180° and 6Ni 90° neighbours. and suggests that these $LiNiO_2$-like environments occur with a higher probability that the

random solution model predicts. This may indicate that the diamagnetic TM ions (Co^{3+} and Al^{3+}) tend to be accommodated in pairs or small clusters.

The slightly lower centre of mass and peak position for the HT-TODA-NCA vs TODA-NCA and ^{17}O-NCA indicates that its average Ni oxidation state may be slightly higher than the ideal 3+. This could be caused by loss of Li from the surface due to the additional annealing step, accompanied by densification of the surface into NiO like domains. The Ni^{2+} needed to form this surface layer could be formed by disproportionation of Ni^{3+} into Ni^{2+} on the surface and Ni^{4+} in the bulk. Another factor could be the susceptibility which, in the case of increased Ni occupation of Li sites, is expected to become more antiferromagnetic as the Ni–O–Ni 180° exchange pathways are antiferromagnetic, and lead to lower NMR shifts; interestingly the ^{17}O-NCA, which also has higher antisite disorder than the TODA-NCA does not exhibit a lower shift. An alternate explanation is temperature differences between the samples which were recorded at "room temperature" which equates to approximately 55°C for 60kHz MAS. The difference in the prominence of the 660 ppm shoulder suggests that there are genuine but small local structure differences. Interestingly the ^{17}O-NCA and the TODA-NCA which have very different Ni-Li mixing (~11% and ~1.5% respectively) have very similar Li NMR spectra. Likely because Ni^{2+} in the Li-layer only has 90° nearest neighbour type bond pathways to the Li and these are relatively small. Alternatively, the antisite disorder observed by diffraction could be due to domains with very high antisite disorder on the surface; these domains would be Li poor and might not be highly visible in the ^{7}Li NMR. The bulks of the structure, which is visible could then be similar to the TODA-NCA.

The presence of Ni^{2+} in the Li-layer, is likely charge compensated, as outlined in section 1.2.2, by the creation of Ni^{2+} in the TM-layer and loss of Li: effectively $1Ni^{3+}$ and $1Li^{+}$ are replaced by $2Ni^{2+}$. This hypothesis is supported by the lack of isotropic ^{7}Li signals at negative shift, which would be expected for Li in the TM layer—they have only 90°

Ni neighbours which induce negative shifts. Ni^{2+} in TM-layer will induce very similar effects as Ni^{3+} in the NMR spectra; the principal difference being the lack of JT distortion and slightly higher magnitude of the shifts. Ni^{2+} in Li-layer sites would induce small negative shifts (ca. -30ppm)[162] in adjacent Li ions.

The small peak observed at 0ppm is assigned to diamagnetic impurity species, particularly γ-$LiAlO_2$ which has been reported in these materials previously[176] and is known to form on NMC-type cathodes when Al doping is attempted.[183] This hypothesis is supported by the ^{27}Al NMR in which a diamagnetic component is also observed. However, it is not clear whether lithium surrounded by only diamagnetic species (i.e. Li–6Al/Co environments) within the NCA structure itself could be responsible for this peak. This could be ascertained using T_1 relaxation measurements as Li in an entirely diamagnetic matrix will typically have T_1 relaxation times on the order of 100 s (for example ca. 130 s for Li_2CO_3),[184] whereas if there are paramagnetic centres in the vicinity these relaxation times are likely to be lower by an order of magnitude. An example for this is $LiCoO_2$: poorly stoichiometric LCO typically has ^7Li T_1 relaxation times of ca. 3 s but highly stoichiometric LCO has T_1 relaxation time of ca. 18 s.[30]

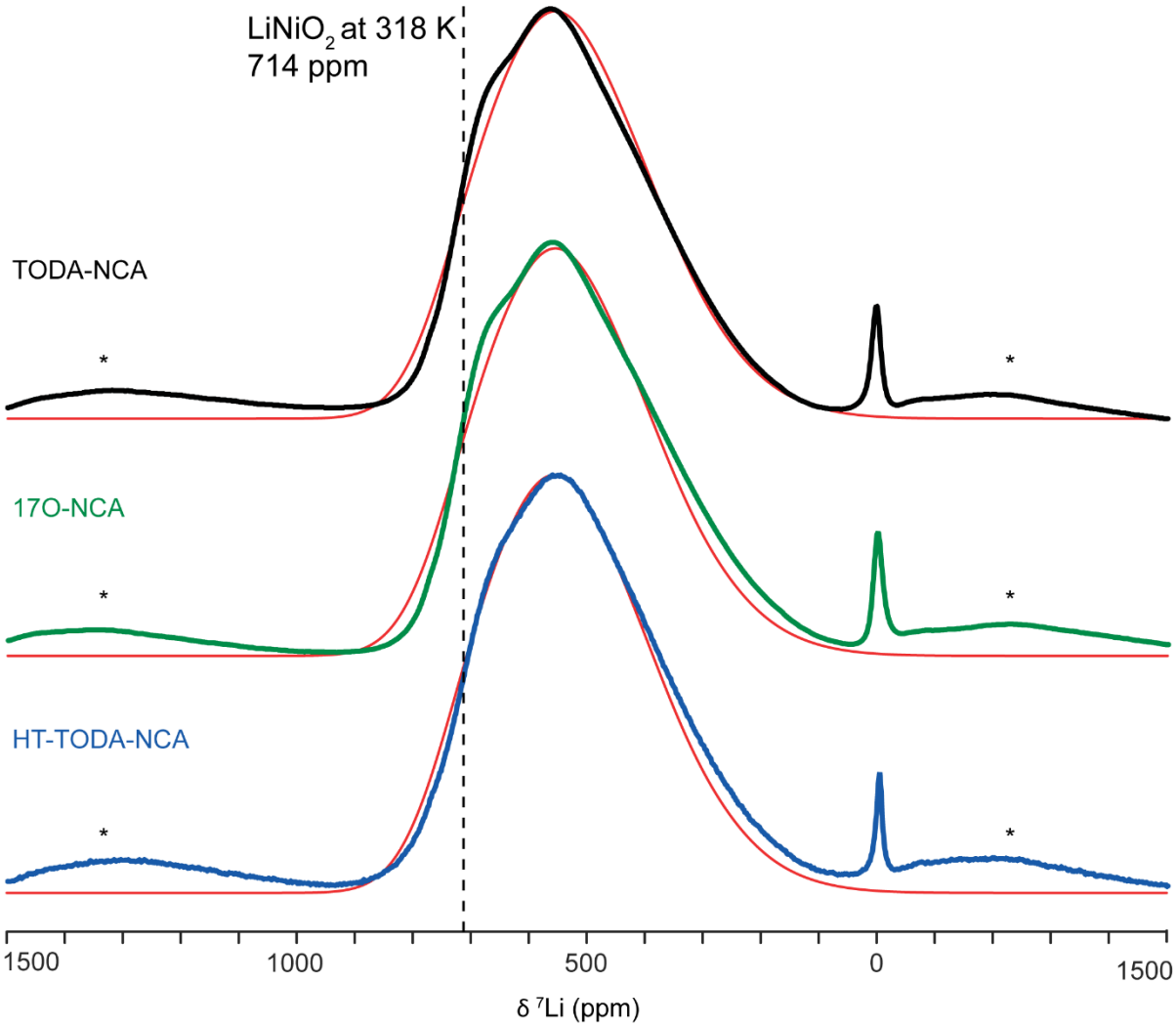

Figure 2.3 ^{7}Li NMR spectra of NCA samples at 4.7 T and 60kHz MAS. The experimental patterns are shown in black (TODA-NCA), green (^{17}O-NCA) and blue (HT-TODA-NCA). A calculated spectrum derived from a random solution model—i.e. one that assumes the TM-layer has no local ordering—is shown in red. Spinning sidebands are indicated with asterisks. The peak at 0ppm, assigned to diamagnetic impurities such as Li_2CO_3 and γ-$LiAlO_2$, is not included in the model. The isotropic resonance of $LiNiO_2$ is reported as 714 ppm at 318 K which is marked on the spectrum.[185] The temperature of these 60kHz MAS spectra is ~328 K which may explain why the "$LiNiO_2$-like" environment occurs at lower shift.

2.4.5 ^{27}Al NMR

The ^{27}Al NMR spectrum for pristine TODA-NCA is shown in Figure 2.4a. The spectrum is composed of two distinct regions. As in the ^{7}Li NMR spectra, there is a small diamagnetic peak around 0 ppm. Typical diamagnetic chemical shifts for octahedrally coordinated Al species are 0-10 ppm with tetrahedrally coordinated Al around 50-80 ppm.[186] The peaks in this region are assigned to diamagnetic Al species, mostly likely octahedrally coordinated Al from γ-$LiAlO_2$.[176] The paramagnetic region is at a negative shift—all the Al associated within the structure is expected to produce signal in this region. DFT calculated shift contributions from a previous study[176] can be used to estimate the shift from each Al–xNi environment. The ^{27}Al spectrum is most intense at the most negative (most shifted) end of the paramagnetic region and it has been suggested that this indicates that the most highly shift local ordering (Al–6Ni) is the preferred Al coordination.[183] This is at odds with other experimental data (and the Li NMR) which do not support strong local ordering or nano-domains.[176] Another proposed assignment of the spectrum speculates that there is a preference for the Ni^{3+} JT axes to point towards the Al sites[176]—this will be discussed in more detail along with the Co NMR in section 2.4.7.

2.4.6 ^{59}Co NMR

The ^{59}Co NMR spectrum for pristine TODA-NCA is shown in Figure 2.4b. Whilst the very large shifts observed for ^{59}Co in NCA might initially appear to be due to very large positive paramagnetic Fermi-contact shifts, the greater part of the magnitude of the signal is due to chemical shift; the ^{59}Co NMR shift for $LiCoO_2$, which can be considered a diamagnetic analogue to NCA, is ~14000ppm. If the position of the diamagnetic region is recalibrated to 14000ppm (rather than 0 ppm which is intuitively expected) then the observed shift range of ~13000-11000 ppm is ascribed to negative Fermi-contact shifts originating from Ni^{3+}. The wedge-like lineshape observed for the

isotropic resonances is similar to that observed for ^{27}Al, with the most intense part of the spectrum (at 11600 ppm) furthest from the diamagnetic region.

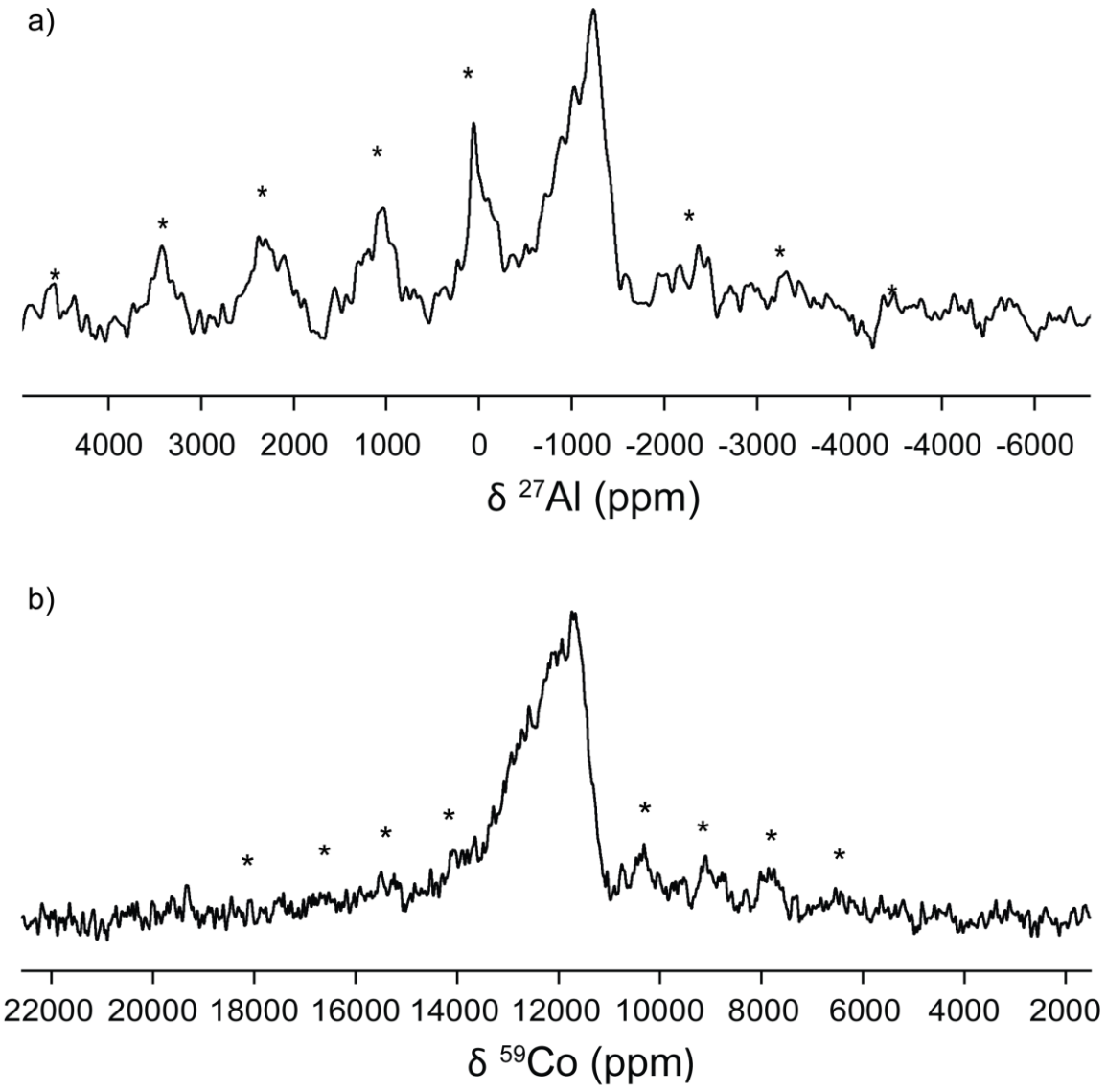

Figure 2.4 ^{27}Al (a) and ^{59}Co (b) MAS NMR spectra for pristine TODA-NCA. a) The isotropic resonances between 0 and −1200 ppm give a wedge-like lineshape. The sharp resonance at 0 ppm is associated with diamagnetic Al surface species. b) Isotropic resonances between ca. 11600 and 13600 ppm give a similar wedge-like profile as observed in (a). Spinning sidebands are marked with asterisks.

2.4.7 Discussion of ^{27}Al and ^{59}Co NMR of Pristine NCA

Al and Co occupy the same crystallographic sites and therefore their spectra offer two complementary probes to understand the distribution of Ni^{3+} and its JT distortion in the presence of the Co and Al "defect" sites. In the spectra for both nuclei the wedge-like lineshapes (Figure 2.4) suggest the most common local environments are those which give rise to large negative shifts. Al/Co lie within the TM layer and therefore they only have six TM 90° nearest neighbours (in contrast to Li which has six TM 90° nearest neighbours and six TM 180° next nearest neighbours). Each 90° Ni^{3+} bond pathway is mediated via two Ni–O–Al/Co bonds and the shift contribution of each Ni^{3+} is strongly dependent on whether one of the Ni–O–Al/Co pathways go via a JT lengthened bond (δ_{SL}) or whether both Ni–O–Al/Co are short (δ_{SS}). DFT calculations for an Al doped into a $LiNiO_2$ lattice predict the δ_{SS} bond pathway gives small positive shifts, whereas the δ_{SL} pathway gives large negative shifts (ca. −300 ppm). [176] As expected, similar calculations performed for Co and Al show the similar behaviour (Table 2.2).

Table 2.2 Comparison of DFT calculated values for δ_{SS} and δ_{SL} bond pathways for ^{27}Al and ^{59}Co using the code CRYSTAL with B3LYP functional containing 20% Hartree-Fock exchange

Type of Bond Pathway	Calculated ^{27}Al NMR shift (ppm) (HYB20)[1]	Calculated ^{59}Co NMR shift (ppm) (HYB20)[2]
δ_{SS}	11	16
δ_{SL}	-336	-587
Dynamic Average $(2\delta_{SL} + \delta_{SS})/3$	-220	-386

[1] Values are taken from reference [176]

[2] Values from DFT calculations performed by Ieuan D. Seymour

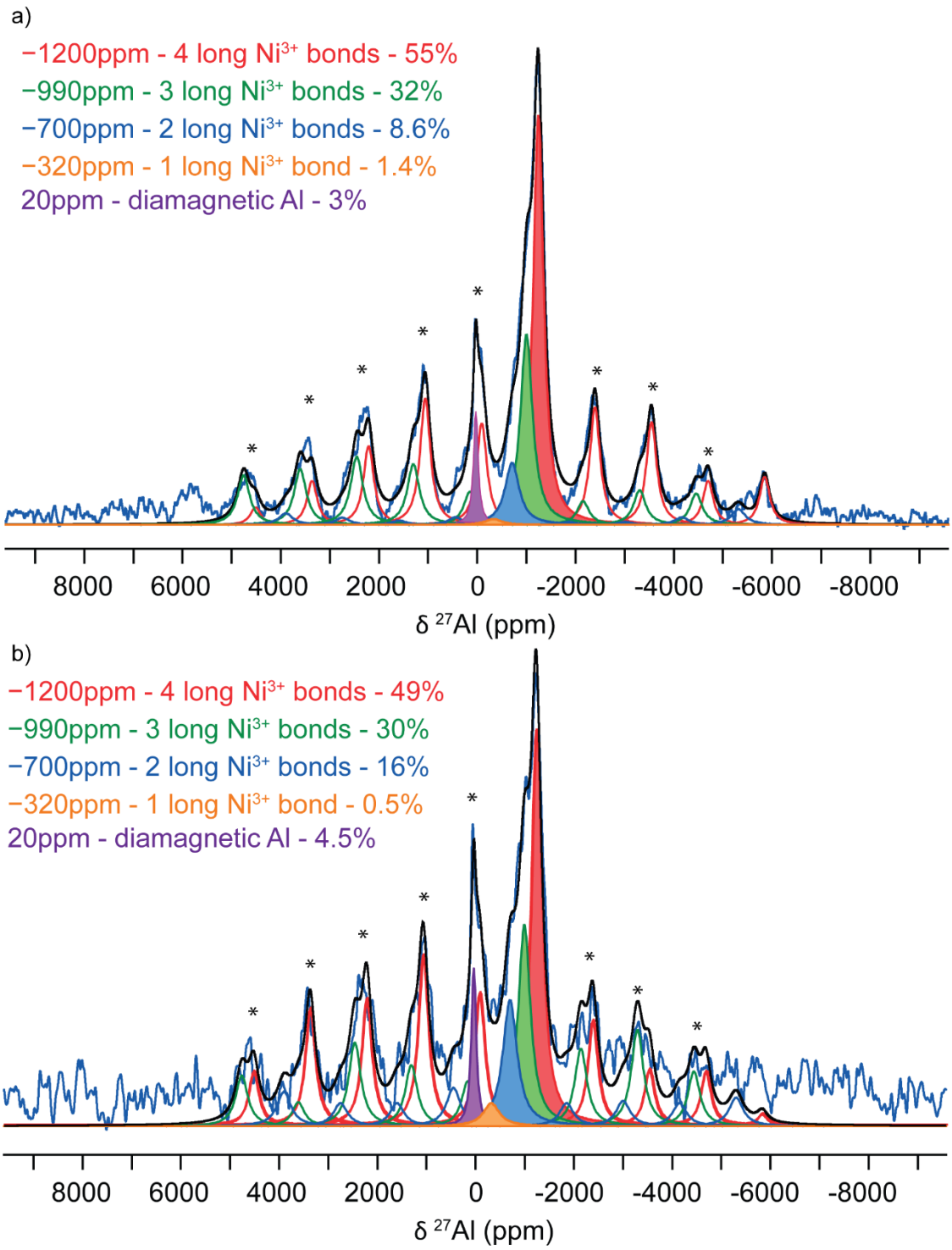

Figure 2.5 ^{27}Al NMR spectrum of TODA NCA at 4.7 T and 60 kHz MAS frequency. a) shows the spectrum recorded using a $\pi/2$ pulse optimised on AlF_3. In the $\pi/2$ experiment, the peak at the highest shift, assigned to environments with $4\delta_{SL}$ bond pathways, is enhanced. b) shows the spectra recorded a shorter $\pi/6$ pulse. This leads to quantitative spectrum although the S/N ratio is reduced. For both spectra the deconvolution of the spectrum was done using the DMfit software.[187] The fitted isotropic resonances are shown in filled colour whilst their corresponding sidebands are shown by the outlined peaks.

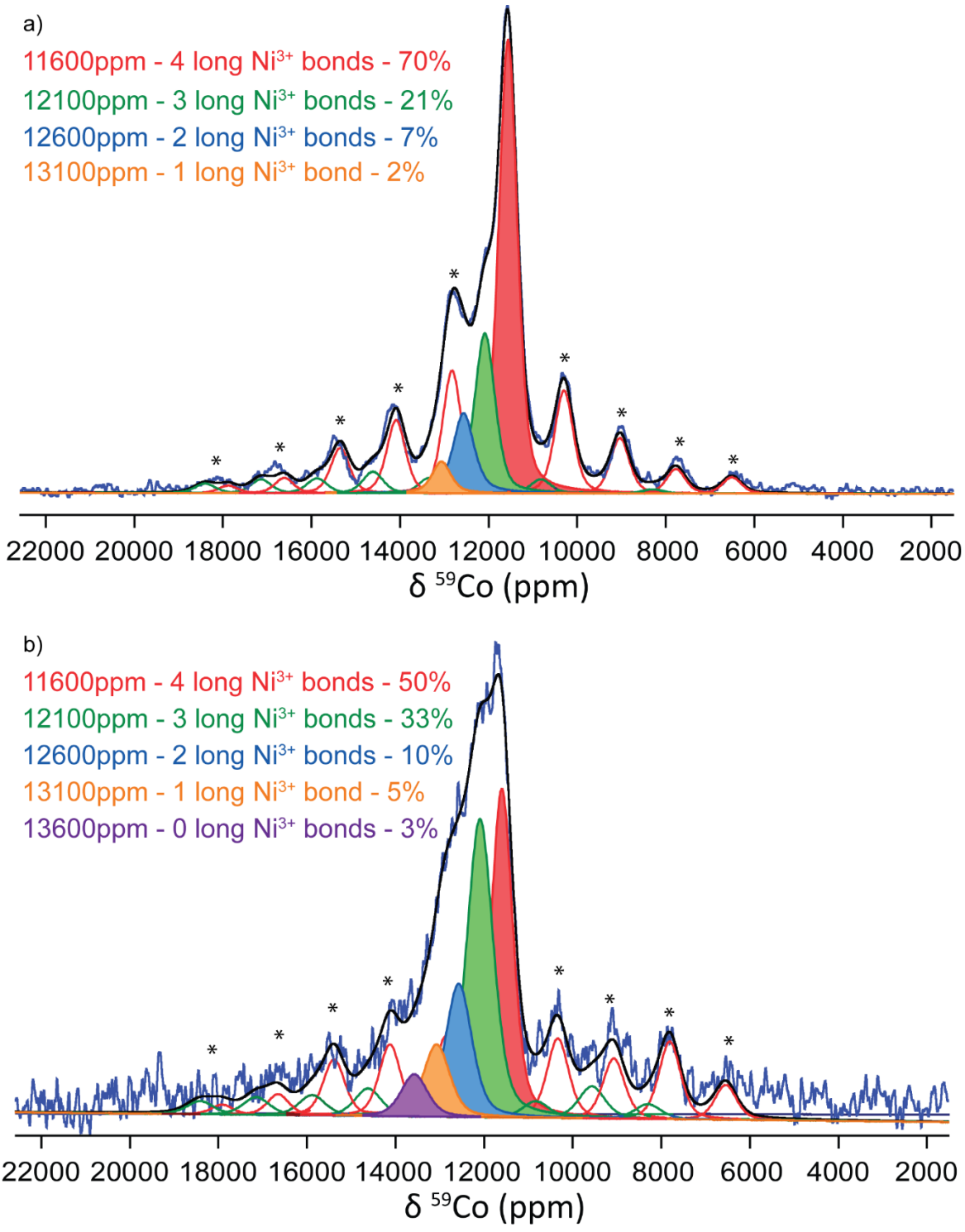

Figure 2.6 ^{59}Co NMR spectra for TODA-NCA at 4.7T and 60kHz MAS frequency. a) shows the spectrum recorded using a $\pi/2$ pulse optimised on 0.1 M $K_3[Co(CN)_6]$ in D_2O. The use of a longer pulse leads to an enhancement of the signals from environments with lower quadrupolar coupling constants (C_q). In the $\pi/2$ experiment, the peak at lowest shift, assigned to environments with $4\delta_{SL}$ bond pathways, is enhanced. b) shows the spectra recorded a short $\pi/8$ pulse. This leads to quantitative spectrum although the S/N ratio is reduced. For both spectra the deconvolution of the spectrum was done using the DMfit software.[187] The fitted isotropic resonances are shown in filled colour whilst their corresponding sidebands are shown by the outlined peaks.

For both ^{59}Co and ^{27}Al, the magnitude of the negative δ_{SL} is so much larger than δ_{SS}, that the shift of a given environment does not necessarily reflect the number of Ni neighbours, but rather the number of δ_{SL} bond pathways it experiences. The most intense parts of the spectra occur at ca. −1200 ppm and ca. 11600 ppm for Al and Co respectively, which are extremely close to the values predicted by the calculations for 4 δ_{SL} bond pathways (−1344 ppm and 1652 ppm respectively). These shifts could be the result of Al/Co surrounded by 4,5 or 6 Ni nearest neighbours (Figure 2.7).

With the caveat that a static, cooperative JT distortion does not occur for NCA, and that on the "NMR timescale" (10s of μs) the JT axes are in flux, it is worth considering which local coordinations are likely to be thermodynamically favourable and therefore make up a larger part of the average structure sampled in the NMR spectra. By considering how defect atoms can be accommodated in an ordered array of JT bonds, a picture of these favourable local environments can be built up.

One striking absence from both the ^{27}Al and ^{59}Co spectra is the lack of peaks at even lower shifts, resulting from Al/Co with 5 or 6 δ_{SL} bond pathways. Such environments should be possible for 5/6Ni neighbour environments. Doping a single defect into either a layered $LiMnO_2$-like structure (section 1.2.3)[48,49] or into a zig-zag ordered structure,[176] results in a defect environment with $4\delta_{SL}$ bond pathways (Figure 2.7a). This configuration causes the minimum disruption to the Ni^{3+} JT array. Reorientation of JT long axes such that there are $5\delta_{SL}$ pathways (Figure 2.7b) disrupts the pairwise coupling of JT axes between adjacent Ni^{3+} ions. Such pairwise couplings are predicted by first principle calculations to be stabilising.[188] Similarly for a single defect reducing the number of δ_{SL} bond pathways below 4 requires distortion of the Ni^{3+} pairing and the creation of O sites which must be highly distorted. This argument suggests that for a defect atom surrounded by 6Ni neighbours, the most energetically favourable configuration will have $4\delta_{SL}$ (and $24\delta_{SS}$) pathways.

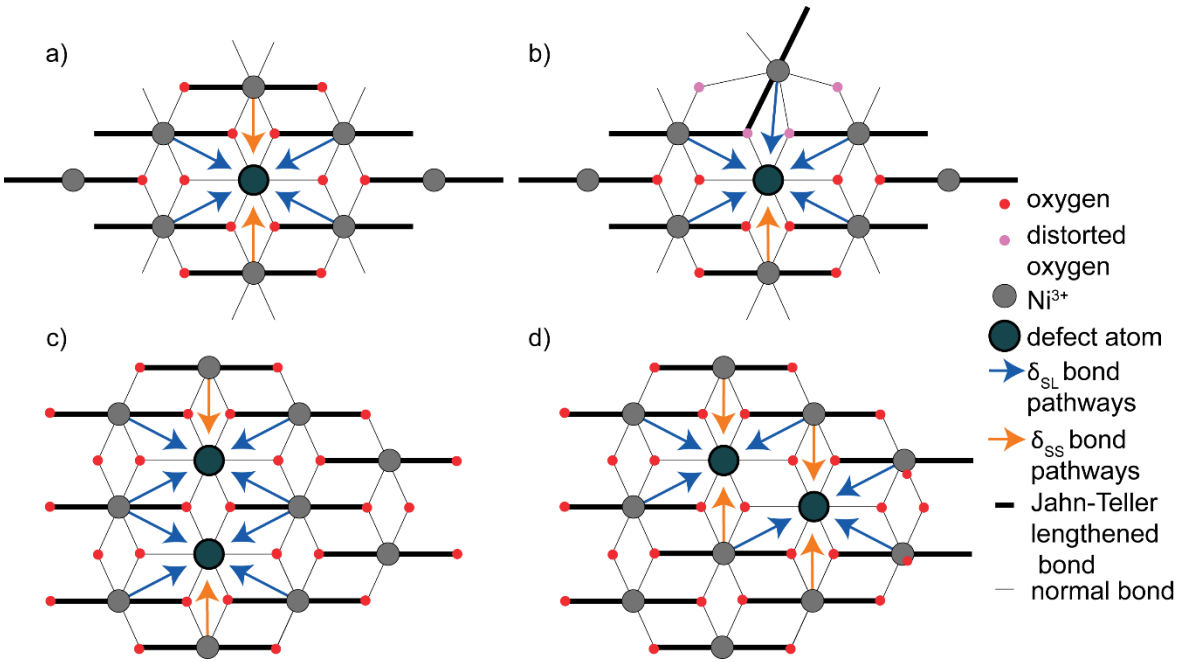

Figure 2.7 Schematic representation of introduction of defect atoms into a cooperatively distorted JT lattice (layered $LiMnO_2$-like). a) shows the $4\delta_{SL}2\delta_{SS}$ bond pathway environment that would be expected for the introduction of one defect atom. b) Illustrates the distortion that must occur for a $5\delta_{SL}1\delta_{SS}$ bond pathway environment to occur. Disrupted oxygen ions are shown in pink. c) and d) show the possible organisation of two defect sites (i.e. an Al or Co sites with only 5Ni ions). c) demonstrates the $4\delta_{SL}1\delta_{SS}$ coordination and d) the $3\delta_{SL}2\delta_{SS}$ coordination showing how both may be coordinated without large disruption of the Ni-Ni JT interactions. Ni atoms are show in grey, defect atoms in blue, oxygen in red, highly disrupted oxygen in green, bonds are shown by black lines with thick black lines representing the long JT axes for each Ni, δ_{SL} bond pathways are shown by blue arrows and δ_{SS} bond pathways by orange arrows.

The case of defect atoms surrounded by 4/5 Ni^{3+} is slightly more complex. Two adjacent defect atoms (creating two 5Ni neighbour sites) can be arranged, without disrupting the Ni^{3+} array, to create two local environments one with $4\delta_{SL}$ and one with $3\delta_{SL}$ (Figure 2.7c-d). Similarly, there are five arrangements of three defect atoms which can give a $4Ni^{3+}$ neighbour environment with $4\delta_{SL}$, $3\delta_{SL}$(×2) or $2\delta_{SL}$(×2). Without knowing the energetic preference, or additionally in the case of three or more defects, the preferred clustering geometry, it is not possible to say which are the lowest energy environments. However, it is clear there isn't a strong preference for defect atoms surrounded by 4/5 Ni^{3+} to have $4\delta_{SL}$ pathways, as this would result in 90% of the signal occurring at −1200 ppm and 11600ppm for Al and Co respectively, which is not

observed experimentally (Table 2.3). If it is assumed that all the arrangements that cause minimal distortion of the JT axes are equally probable, then the random solution probabilities of each number of Ni neighbours can be converted into an expected distribution of $4\delta_{SL}$, $3\delta_{SL}$ and $\leq 2\delta_{SL}$ environments (Table 2.4). There is excellent agreement between this model and the integrated intensities of both the ^{59}Co and ^{27}Al NMR spectra (Table 2.3).

Whilst this model cannot separate the specific local environments and clustering's which make up the thermodynamic minima in the JT orientation energy surface, it does demonstrate that the energy surface is far from flat. On average the JT distortion adopts a kind of pseudo-ordered state were local defects are accommodated by coordination environments which resemble those expected for a totally ordered JT array, these low energy states can easily interconvert and do so on the timescale much faster than that of the NMR experiments.

The integrated intensities of the NMR spectra change, particularly in the case of ^{59}Co, depending on the pulse length used. The use of the $\pi/2$ pulse, optimised on a non-quadrupolar reference, exploits the differences in nutation behaviour for environments with different quadrupolar coupling constants (C_Q), enhancing those signals with smaller electric field gradient anisotropy (Figure 2.5a and Figure 2.6a) . In this case, the highly shifted peaks at -1200 ppm and 11600 ppm, for Al and Co respectively, increase in intensity. This supports the assignment that these peaks are at least partly caused by the more symmetric Al/Co-6Ni type environments. The larger enhancement for ^{59}Co stems from its larger nuclear quadrupole moment (Q) compared to ^{27}Al (0.42 b vs 0.15 b)

Table 2.3 Results of fitting the ^{27}Al and ^{59}Co NMR spectra of pristine TODA-NCA.

Assignment of Peak	^{27}Al			^{59}Co		
	Shift (ppm)	Relative Integration (%)		Shift (ppm)	Relative Integration (%)	
		Quadrupolar ($\pi/6$)	Non-Quadrupolar ($\pi/2$)		Quadrupolar ($\pi/6$)	Non-Quadrupolar ($\pi/2$)
$4\delta_{SL}$	−1200	49	55	11600	50	70
$3\delta_{SL}$	−990	30	32	12100	33	21
$2\delta_{SL}$	−700	16	8.6	12600	10	7
$1\delta_{SL}$	−320	0.5	1.4	13100	5	2
$0\delta_{SL}$	0	4.5	3.0	13600	3	0

Table 2.4 Probability distribution for Ni coordination of "defect atoms" in NCA and the combination of these probabilities with the fraction of configurations which give rise to different bond pathways as described in the text, giving a prediction of the fractions for the fitted NMR spectra.

Number of Ni neighbours	Random solution probability	Possible δ_{SS} and δ_{SL} configurations	Expected fraction of environments	Bond pathway configuration	Predicted fraction of NMR signal
6	0.2621	$4\delta_{SL}2\delta_{SS}$	1	$4\delta_{SL}$	0.51
5	0.3932	$4\delta_{SL}1\delta_{SS}$	$\frac{1}{2}$	$3\delta_{SL}$	0.29
		$3\delta_{SL}2\delta_{SS}$	$\frac{1}{2}$	$\leq 2\delta_{SL}$	0.20
4	0.2458	$4\delta_{SL}0\delta_{SS}$	1/5		
		$3\delta_{SL}1\delta_{SS}$	2/5		
		$2\delta_{SL}0\delta_{SS}$	2/5		

2.4.8 ^{17}O NMR of NCA

The ^{17}O NMR spectrum for pristine ^{17}O enriched 17O-NCA is shown in (Figure 2.8) and is centred around 12000 ppm. The spectrum is extremely broad >30000 ppm and was therefore recorded as a VOCS (section 1.9.4). As with the other spectra obtained from NCA, the ^{17}O NMR spectrum represents many possible O local environments each with different shifts. In addition, the O are bonded directly to the paramagnetic species (Ni^{3+}), which leads to extremely large shifts and strong electron-nuclear dipolar coupling.

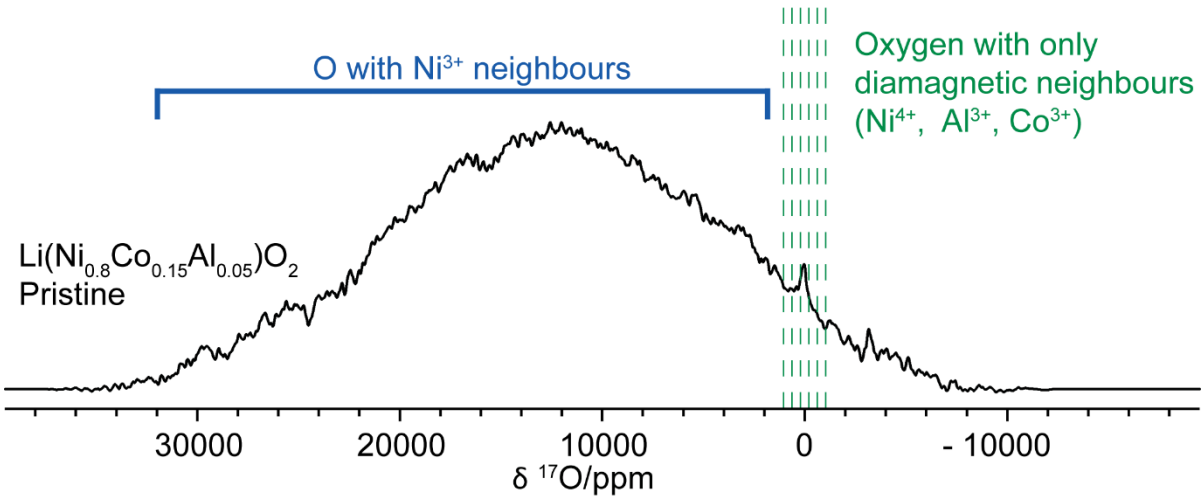

Figure 2.8 ^{17}O NMR spectra for TODA-NCA at 11.7T and 60kHz MAS frequency. The pristine spectrum was recorded at variable offsets between −5000 and 30000 ppm with a spacing of 2500 ppm. Total acquisition time was 38.5h. The expected regions for paramagnetic signal (blue) and diamagnetic signal (green) are highlighted

The small peak at ~0 ppm is consistent with some diamagnetic impurities as observed in the Al and Li NMR most likely γ-$LiAlO_2$ or Al_2O_3 but also O environments surrounded by defects: O is more likely to have no paramagnetic neighbours in the bulk structure as it only has 3TM neighbours as compared to 6 for Al/Co or 12 for Li in the ideal layered structure. The NMR spectrum is not quantitative for these diamagnetic environments, as the long recycle delays required to prevent saturation of the diamagnetic signals would have prevented acquisition of the paramagnetic (sample) spectrum in a practical timeframe.

In order to help rationalise this spectrum Fermi-contact shifts were calculated for $LiNiO_2$ using DFT (HYB20). A $LiNiO_2$ cell with the $LiCoO_2$ $R\bar{3}m$ structure was relaxed and formed a distorted structure in which the JT axis are arranged in a zig-zag arrangement. Naturally this cooperative distortion is not representative of a dynamically averaged JT distortion, but it can offer some insight into the effect of the JT distortion on the O bond pathways.

As with the ^{7}Li, ^{27}Al, ^{59}Co bond pathways, the bond pathways for ^{17}O depend strongly on whether the interaction goes via the JT lengthened or JT shortened bond. Ni^{3+}–O

via a long JT axis (δ_L) gives a shift of ~9500 ppm compared to a much more modest bond pathway contribution for Ni^{3+}–O via a short JT axis (δ_S) of ~1800 ppm. In a JT ordered array of Ni^{3+} ions, each O always has $1\delta_L$ and $2\delta_S$ Ni–O pathways giving a total shift of 13100 ppm. JT fluctuations could create an O environment with two (or three) lengthened bonds pointing towards it, however it would be highly distorted and would likely be high in energy (similar to the $5\delta_{SL}$ case in the ^{27}Al and ^{59}Co case). Such a configuration is more likely to be a transition state between lower energy JT orderings. Therefore, the average O environment resulting from JT fluctuations is likely to be heavily weighted towards the JT ordered environment (i.e. $1\delta_L$ and $2\delta_S$ Ni–O pathways), if there are no defects atoms nearby. The expected shift for a dynamic JT distortion is therefore likely to be very close to the shift calculated for the JT ordered $LiNiO_2$ structure. There may be some deviations due to differences in bond lengths in a dynamic vs static structure. In $LiNi_{0.8}Co_{0.15}Al_{0.05}O_2$ the random solution probability of an O having 3Ni neighbours is ~51%.

For O near 1 defect atom, which make up 38% O in a random solution model, if the JT distortion were static, the shift would be either $1\delta_L$ and $1\delta_S$ (11300 ppm) or $2\delta_S$ (3600 ppm). Due to the JT dynamics, the shift for O near 1 defect atom is most likely somewhere between these two values. The dynamically averaged shift for Ni^{3+} ($(\delta_L + 2\delta_S)/3$) is ~4360 ppm, which gives an estimate of 8700 ppm. For the same reasons discussed for the 0-defect atom case, a configuration with $2\delta_L$ is unlikely to make up a significant proportion of the average structure. O with only 1Ni neighbour accounts for ~10% of the O in a random solution and would be expected to have a shift of ca. 4360 ppm.

The calculated shifts are in reasonable agreement with the observed spectrum; however, the spectrum is extremely broad and lacks the clear features corresponding to O with 1,2 and 3 Ni neighbours that might be expected. The are several factors which play into this broadness. The first is the e-n dipolar interaction, which is likely to be

extremely large given the proximity of the O to the Ni^{3+} paramagnetic centres. This interaction can be averaged under MAS if the spinning frequency is fast enough, however in this case the e-n dipolar interaction is too large to be significantly averaged even at 60kHz MAS frequency, so a manifold of spinning sidebands is expected for each site. Similarly, the quadrupolar interaction may not be fully averaged under MAS so may also contribute to the spinning sideband manifolds. Anisotropic bulk magnetic susceptibility (ABMS) effects will also play a role. Particles with non-zero susceptibility (NCA for example) induce an nonuniform field in nearby particles, which leads to broadening of the NMR spectrum.[189] The isotropic part of this effect can be averaged by MAS but the anisotropic part cannot, which leads to highly distorted spinning sideband manifolds.[190] The T_2s for O in NCA are likely to be extremely short due to the paramagnetic relaxation effect, which leads to inherently broadened resonances for individual sites, regardless of the other sources of broadening. Therefore, although there are fewer possible O configurations in NCA than for the other nuclei studied in this work (10 for O vs 784 for Li), each of these will give rise to an extremely broad isotropic resonance and a manifold of spinning sidebands (caused by poorly averaged e-n dipolar and quadrupolar interactions) whose intensities and widths will be effected by ABMS effects causing further broadening. The overlap of the isotropic resonances and sideband manifolds of each of these sites gives rise to the broad spectrum observed. The centre of mass of the spectrum is at approximately the shift anticipated by the DFT calculations and despite the lack of resolved peaks is in good agreement with the assignments for ^{7}Li, ^{27}Al and ^{59}Co.

2.5 Part 2: NCA on Delithiation

On cycling, large electronic and structural changes take place due to the deintercalation of Li. The changes to the long-range structure, oxidation states, surface transformations etc. have been extensively studied in NCA and analogous materials as outlined in section 1.2. Firstly, the ^{7}Li NMR spectra on cycling are presented. NMR is a can

provide a sensitive probe for examining the mobility of ions. Secondly, the ^{27}Al, ^{59}Co and ^{17}O NMR are considered in order to probe the local structure changes and the redox mechanisms.

2.5.1 Delithiated NCA – ^{7}Li NMR

Upon initial delithiation, until 0.18 Li removed per formula unit (x=0.82), the broad distribution shifts towards zero. This is expected and is a result of the oxidation of paramagnetic Ni^{3+} into diamagnetic Ni^{4+}. Oxidation of diamagnetic (low spin d^6) Co^{3+} to paramagnetic Co^{4+} appears to occur simultaneously (further discussion section 2.6.3),[63] but does not seem to have a significant effect on the ^{7}Li NMR spectrum. DFT calculated shifts for Co^{4+}–O–Li in a small $LiNi_{1/3}Co_{1/3}Al_{1/3}O_2$ super cell are relatively small: 51 ppm and 5 ppm for nearest neighbours (90°) and next nearest neighbours (180°) respectively. In addition, Co^{4+} is often assumed to cause such rapid relaxation in nearby Li that its effects cannot be observed clearly[29]. Upon further delithiation the ^{7}Li NMR spectrum sharpens considerably, as well as continuing to decrease in average shift. This sharpening of the Li resonances has been observed in NCA in previous studies[180] but was not commented upon. In the closely related material, NMC811, it has been attributed an increase in Li mobility after small amount of Li is removed from the structure[26]. In the case where Li hops from site to site, at a frequency faster than the timescale of the NMR experiment, a time-averaged signal will be observed. Narrower than expected lineshapes, could also indicate a Li ordering scheme, however examination of NMR spectra recorded at variable temperature (VT) indicates that this is not the case. As the temperature is increased the lineshapes become sharper (Figure 2.10). An increase in temperature should give rise to faster Li motion and hence a sharper resonance, whereas a Li ordering of some kind might be expected to be disrupted at higher temperatures giving the opposite trend.

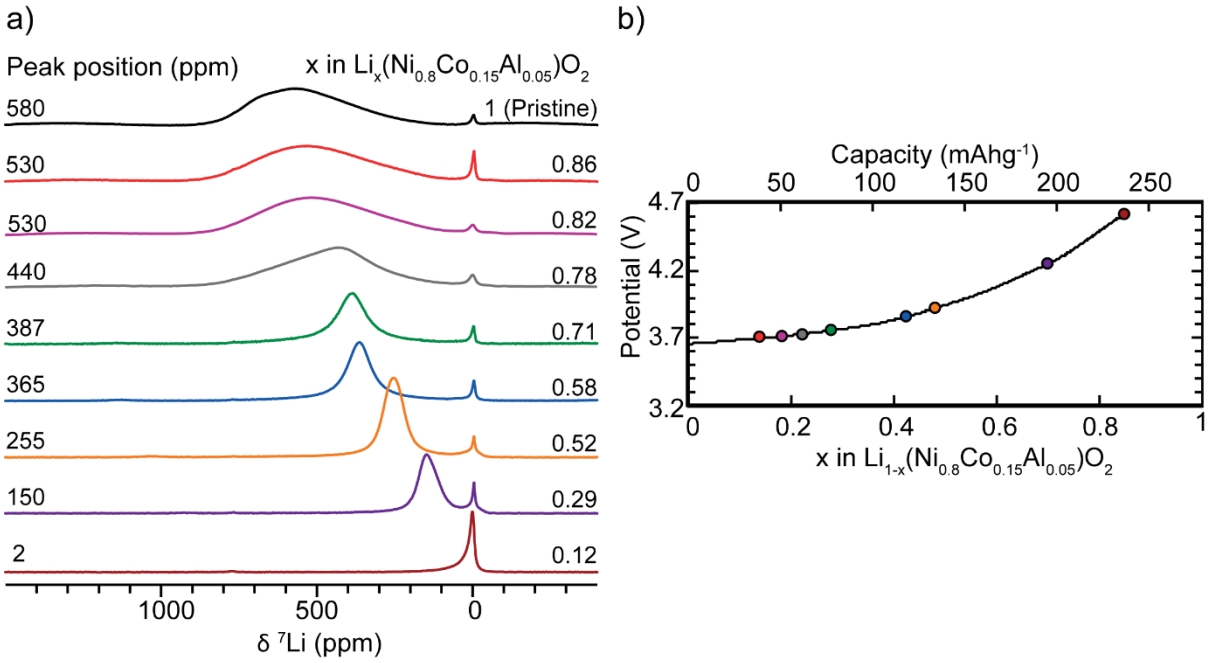

Figure 2.9 a) ^{7}Li NMR spectra of ex-situ NCA samples at various state of charge. The position of the most intense point is labelled on the left side. The degree of delithiation (calculated from to the total charge transferred for each according to the electrochemistry) is indicated by the value of x on the right-hand side, which refers to the expected change in Li stoichiometry per formula unit: $Li_{1-x}Ni_{0.8}Co_{0.15}Al_{0.05}O_2$. b) Electrochemical profile of NCA on first charge. States of charge that electrodes where charge to for ex-situ NMR are highlighted with coloured markers.

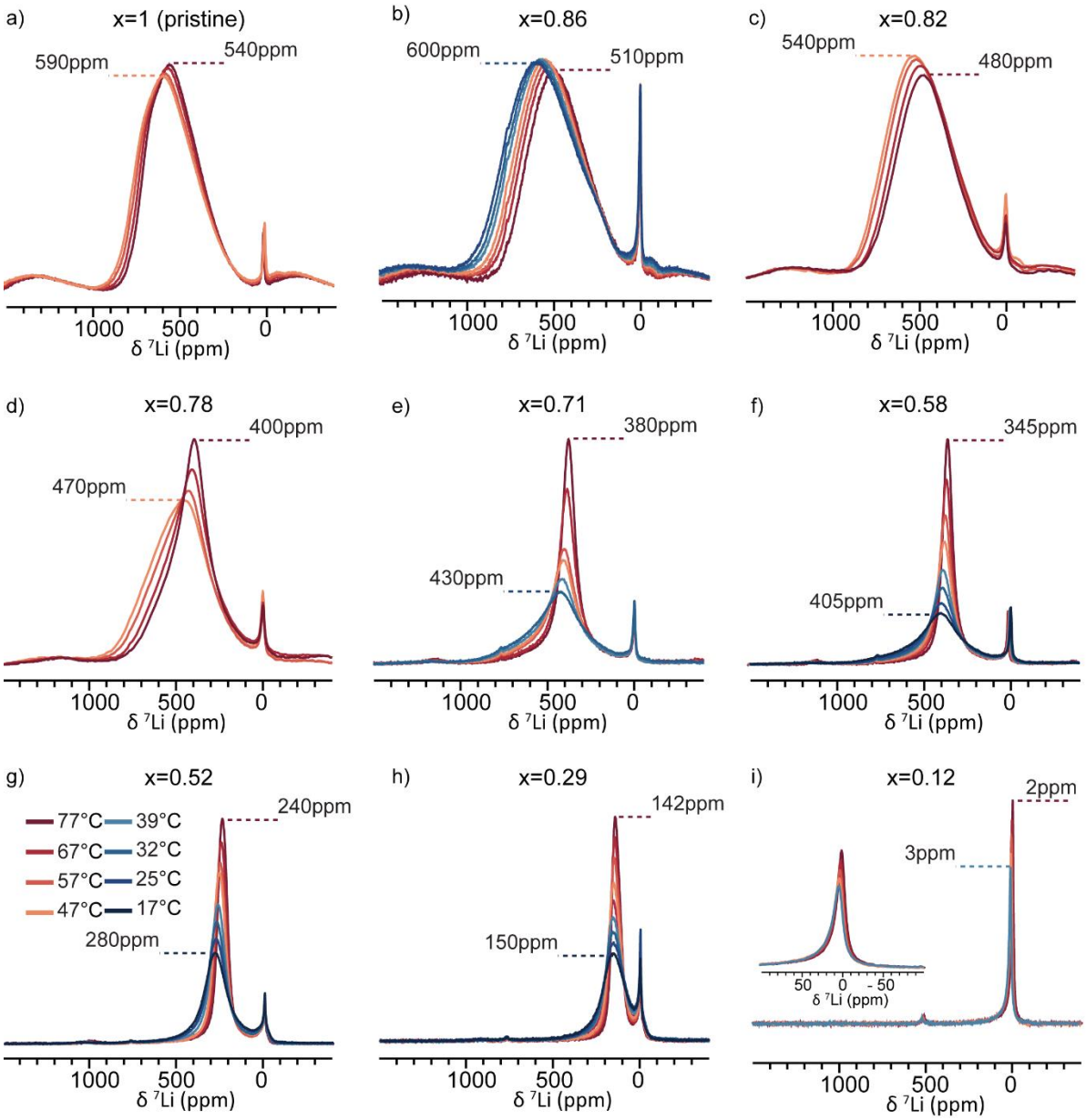

Figure 2.10 ^{7}Li spectra of NCA at various states of delithiation and temperatures. x denotes the amount of Li removed per formula unit calculated from the electrochemistry. The spectra shown in a) and b) remain relatively unchanged by temperature variation. The spectra in c),d),e) and f) have sharper lineshapes at higher temperature indicating the Li motion is enhanced by higher temperature. All the shifts (which derive from the paramagnetic centres) are expected to have Curie-Weiss like dependence hence the resonances move to lower shifts at higher temperatures in all the samples. Within each panel, spectra are displayed without scaling, between panels the spectra are normalised arbitrarily so that the most intense spectra all have the same maximum intensity for ease of comparison.

2.5.2 Modeling the ^{7}Li Spectra

As stated in section 2.4.4, a simple probabilistic approach can be used to model the spectra of pristine NCA. However, once the NCA enters the fast Li motion regime, the broad spectrum predicted by the statistical model becomes insufficient. In order to model the lineshape of the mobile Li the calculated probabilities and shifts were converted into chemical exchange lineshapes using Norris' formula as outlined previously (section 1.9.3)[26,166]. In order to make use of this convenient formula the native linewidth for a single, non-overlapping, non-exchanging, Li environment ($\nu_{1/2,no\text{-}exch}$) must be determined, in addition, $\nu_{1/2,no\text{-}exch}$is assumed to be the same for every Li environment. As $\nu_{1/2,no\text{-}exch}$ cannot be measured in this case a sensible approximation must be used. The linewidth of another paramagnetic compound, without multiple Li environments could be used to estimate $\nu_{1/2,no\text{-}exch}$, however, any paramagnetic compound will have a linewidth induced by temperature gradients in the rotor and even a seemingly ideal reference like layered $LiNiO_2$ has a dynamically averaged JT distortion which may lead to broadening. Layered $LiMnO_2$, could be a good reference, however as well as containing a different paramagnetic ion its static, cooperative JT distortion will give rise to a large electron-nuclear dipolar anisotropy, again broadening the signal. The linewidth of the 0ppm diamagnetic peak, present in all the samples in this work, are 1000-2000Hz; these peaks are likely a composite of several different diamagnetic Li environments but provide a reasonable reference point. Considering this using a $\nu_{1/2,no\text{-}exch}$ in the region of 1000Hz is reasonable. For an upper bound, the sharpest peak modelled in this work (x=0.51 at 77°C), which has a linewidth of ~5000Hz cannot be modelled with a $\nu_{1/2,no\text{-}exch}$ greater than 2300Hz, even if an infinite of the hopping rate is chosen. From these considerations, values of 500, 1000 and 1500Hz were used to calculate hopping rates to illustrate the trends in Li mobility in NCA (Figure 2.11). The lineshapes calculated using $\nu_{1/2,no\text{-}exch}$ = 1000Hz are compared with the experimental spectra in Figure 2.12.

The mobility increases sharply between x=0.82 and x=0.71. The hopping rates derived from the $\nu_{1/2,no\text{-}exch}$=1000Hz give hopping rates on the order of 70kHz which, if converted into a diffusion coefficient using the Einstein-Smoluchowski relation (assuming a two dimensional random walk and a Li-Li site distance of 2.865Å) the diffusion coefficient $D_{li} = 1.4 \times 10^{-11}$cm^{2}s^{-1} similar to conductivities derived from other methods[191–193]. While a quantitative evaluation of the diffusion coefficient for each SOC is not possible the qualitative assessment that the Li mobility increases dramatically between x=0.82 and x=0.71 is robust and our model reproduces diffusion coefficients consistent with those measured previously.

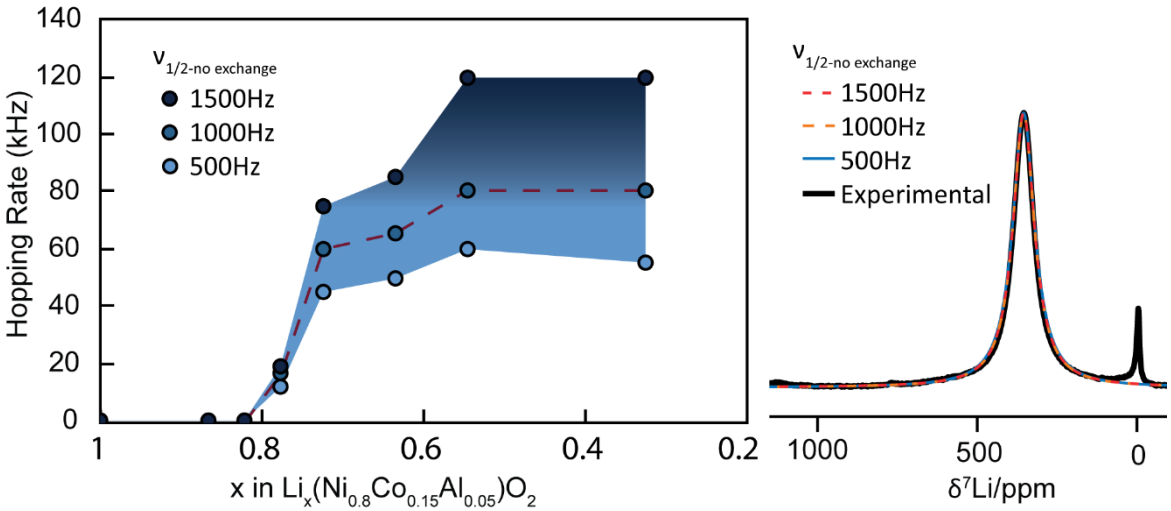

Figure 2.11 Calculated hopping rates are plotted for the SOCs tested. The blue markers indicate values obtained for each of the proposed values for $\nu_{1/2,no\text{-}exch}$. The shading indicates the range of possible hopping rates inferred from our modelling of the spectral lineshapes. The red dotted line is a guide for the eye, highlighting the trend in the case $\nu_{1/2-,no\text{-}exch}$ =1000Hz, highlighting the increase and subsequent plateau of the diffusion coefficient. An example spectrum (x=0.45) is shown on the right, superimposed on the experimental data are the model spectra obtained for the three different values of $\nu_{1/2-,no\text{-}exch}$.

The onset of the fast Li motion is not complete throughout the sample by either x=0.78 or x=0.71 (Figure 2.12d and e). The overall fit, particularly in the case of x=0.78 is poor. The model shown in Figure 2.12 assumes that the average Ni oxidation state is the same in each population; the poor fit for the samples with significant populations of both mobile and non-mobile Li indicates this is a poor assumption.

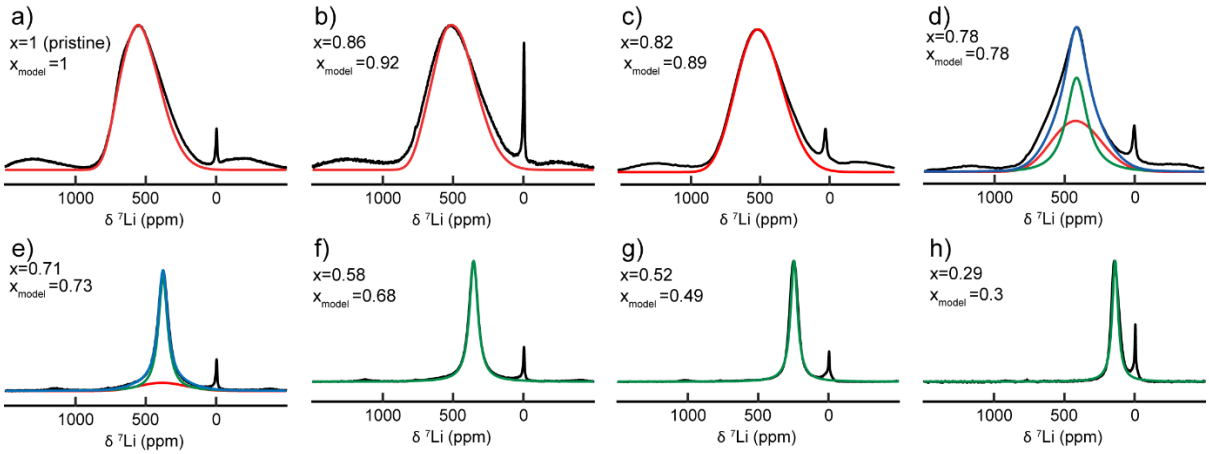

Figure 2.12 Comparisons between modelled and experimental NCA spectra recorded at 67°C. The spectra modelled using a random solution, with no averaging caused by fast motion are shown in red. The spectra in which there is fast Li mobility have been modelled using the fast motion lineshapes described in the text. In the case where both types of Li are present the sum of the two components is shown in blue. All the fast motion lineshapes shown assume that $\nu_{1/2,no\text{-}exch}$=1000Hz.

2.5.3 Analysis of Non-Mobile vs Mobile Li

The presence of mobile and non-mobile Li is clearest for the x = 0.78 sample so it will be analysed further (Figure 2.13). As discussed in section 1.9.3, motion with a hopping frequency which is similar in magnitude to the frequency difference of the sites results in enhanced transverse (T_2) relaxation (Figure 2.14). The enhanced T_2 relaxation for the mobile component of the signal can be exploited to effectively filter the spectra by increasing the number of rotor periods between excitation, refocussing and acquisition in the Hahn-echo experiment. This allows the non-mobile Li to be observed exclusively, for accurate fitting. This filtering unambiguously reveals that the centre of mass of non-mobile Li peak occurs at higher chemical shift than the mobile component. The non-mobile component has an almost identical centre of mass as the x = 0.82 spectrum (560ppm vs 530ppm at 47°C), suggesting this population of Li is virtually unchanged despite change in overall delithiation. By contrast, the mobile Li signal moves to lower shifts as expected. The difference in the centres of mass indicates that there are two distinct populations within the electrode that have different average Ni oxidation states and levels of lithiation.

Using the T_2 filtered experiments to fix the peak position and width of the non-mobile component, conventional Hahn-echo experiments can be fit to find the signal integration corresponding to each population. This integrated intensity can be scaled to reflect the T_2 difference of the mobile and non-mobile Li (which are not observed to change significantly over the temperature range measured). The results of this analysis are shown in Figure 2.13. Very little change in integration of the mobile vs non-mobile signal is observed between 47°C and 77°C. In addition the change in the position of the peaks is similar and they don't migrate towards the same centre of mass, as would be expected if the Ni oxidation state was homogenised.

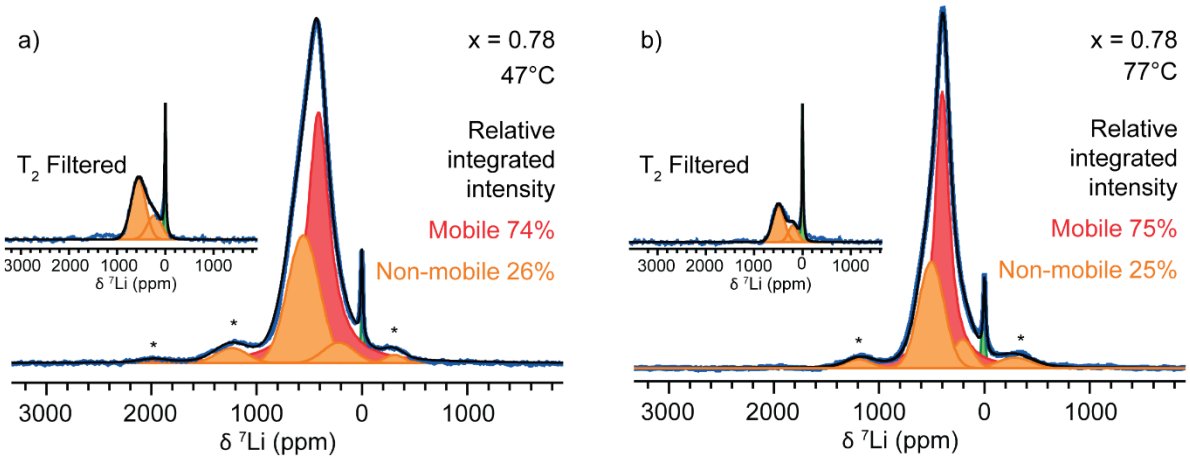

Figure 2.13 ^{7}Li NMR spectra for HT-TODA-NCA sample electrochemically charged to x = 0.78 ($Li_xNi_{0.8}Co_{0.15}Al_{0.05}O_2$) at 47°C (a) and 77°C (b). Inset show the T_2 filtered experiments recorded with Hahn-echo delays τ = 267μs, from which the non-mobile (orange) lineshape was determined. The normal Hahn-echo experiments (τ = 16.6μs) have been fit using these lineshapes, their spinning sidebands (marked with *) and a single Lorentzian peak (red) for the mobile Li signal. Calculated integrated intensity scaled by T_2 (~0.04ms and 0.2ms for mobile and non-mobile Li respectively) are displayed on the spectra

The different Li regimes may exist in different crystalites, i.e some crystalites are more higly delithiated and have mobile Li and some are less delithiated and the Li is still in a non-mobile regime. Alternatively the two populations might be present within the same particle. The resilience of the mobile and non-mobile populations on heating suggests that they cannot easily interconvert. It is unlikely that at moderate temperatures (77° C), and in the absence of electrolyte, that the two Li populations could interconvert if they were not within the same crystalite. The persistence of non-

mobile Li at 77°C could also be because the barriers to Li mobility are too large to be overcome despite the increase in temperature.

The heterogeniety might be caused by the build up of surface contaminants, which can impede the electronic and ionic transport of the crystalites and are unlikely to be evenly distributed on all crystalites, due to storage conditions of the material.[194] The HT-TODA-NCA used in this work was stored in an Ar glovebox which should prevent large scale build up of Li_2CO_3 and $LiHCO_3$, and was annealed at 800°C for 4 hrs in order to remove any species formed due to spikes in H_2O and O_2 levels in the glovebox during the period of storage.[178] However, some surface species may still be present or densification of the surface may introduce similar differences in ionic and electronic transport between particles. It is clear that, beyond a threshold of delithiation, further delithiation becomes kinetically facile and that before this threshold is reached Li mobility is relatively slow. This kinetic limitation close to x=0 is evident in the first cycle capacity loss is observed in all NCA particles (Coulombic efficiency of around 88% on cycling between 4.7-2.7V are typical). Furthermore, this capacity loss can be ameliorated by either cycling at elevated temperature (60°C) or adding a potentiostatic step to the discharge, suggesting a kinetic origin.[195,196] A similar loss in capacity is observed regardless of the upper cut off voltage on first charge suggesting that it is an intrinsic kinetic limitation of the pristine material, rather than a high voltage degradation process,[196] such as surface transformations which impede Li diffusion or shrinkage of the Li slab caused by Ni/Li antisite disorder.[115,197]

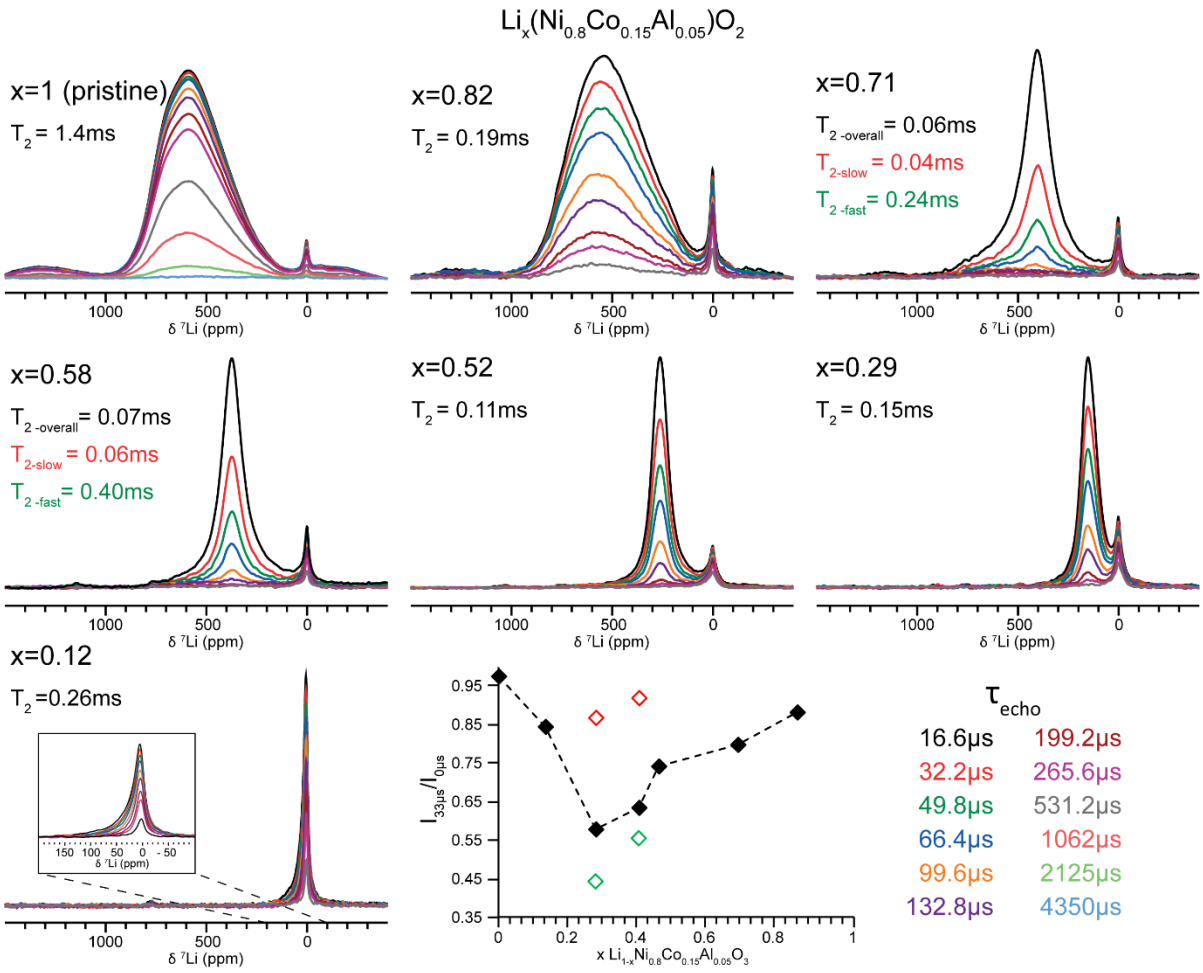

Figure 2.14 ^{7}Li NMR spectra for HT-TODA-NCA samples at various states of charge with variable echo delays. the T2s for each sample are listed. In the cases where mobile and non-mobile Li coexist, the T2s for each were calculated. The ratio of the intensity observed after the minimum echo delay ($I_{33\mu s}$) versus the theoretical intensity at 0 echo delay ($I_{0\mu s}$) is plotted, in the case where 2 T2s were modelled both are plotted. This plot shows the trend in the T2s with shorter T2 giving lower $I_{33\mu s}/I_{0\mu s}$ values. In the non-mobile Li samples (pristine and x=0.86) and the non-mobile components of the mixed samples (x=0.71 and x=0.58, red) remain long whereas the mobile Li signal have much shorter T2s due to the Li motion.

2.5.4 Discussion—Li Mobility and Reaction Heterogeniety

The mobility of Li in the lattice will be affected by both the physical and electronic structure. DFT calculations have shown that Li hopping between two octahedral sites occurs preferentially via the intermediate tetrahedral site.[57] Occupation of the intermediate tetrahedral site is much more favourable if each of the other two Li sites it shares faces with are vacant, therefore this "divacancy" mechanism is impeded at

high Li concentration. The identity and charge state of the TM ion which shares a face with the tetrahedral site will affect its site energy.[92,198] Finally the size of the Li-slab also affects the Li mobility.[198] Naturally, as Li is removed from the lattice, each of these factors will change. The increased availability of the of vacancies and the increase in Li slab size upon initial delithiation explain the observed rise in mobility. The increase in the number of Ni^{4+} and Co^{4+} ions in lattice could lead to a decrease in mobility as the activation barrier to hop to their adjacent sites will be increased, however the presence of low valent ions such a Co^{3+} (still present at the end of charge, see section 2.6.3) may help provide a network of low energy sites that help alleviate these effects. DFT calculations on Al^{3+} doped into a $LiCoO_2$ supercell indicated that, despite the very similar ionic radii for Co^{3+}/Al^{3+}, the tetrahedral Li site coordinated by Al^{3+} has a higher site energy, due to the poorer shielding from the adjacent TM layer offered by the O coordinated by Al^{3+}.[198] For this reason it is unlikely the Al offers much in terms of improving Li^+ mobility. The region of mixed fast/slow motion is in a relatively flat part of the voltage profile, so the difference in potential required to remove additional Li from delithiated particle vs removing Li from a less delithiated, but more kinetically impeded particle will not be large.

It is a consistent observation that, the average Ni oxidation state implied by the NMR shift of the mobile Li is closer to 3+ than that expected from the electrochemistry. The model employed in this work assumes that Co and Ni are oxidised simultaneously however a sequential oxidation process has been reported.[64,199] If Ni and Co are assumed to oxidise sequentially, then the lag between NMR and electrochemistry becomes even more significant, even if calculated Co^{4+} shifts (which are small in magnitude) are added to the model. As will be discussed later (section 2.6.3) the ^{59}Co NMR strongly implies Co oxidation from the start of charge, although not necessarily what fraction of the charge compensation comes from Co^{3+} versus Ni^{3+}. Despite the nominally lower voltage of the Ni^{3+} redox couple, in a TM-layer disordered compound each TM experiences a slightly different inductive effect from its neighbours and will have a

different redox potential than its single TM analogue. The model of fast motion Li assumes that all sites in the lattice have the same probability of being occupied however as discussed above, this is not likely. The observed lag in the NMR-implied Ni oxidation state, strongly suggests the mobile Li spends a greater proportion of close to Ni^{3+} than Ni^{4+}. Not surprising given higher energy of sites near Ni^{4+}. A wrinkle in this interpretation is that the largest shift contribution for Li is from Ni^{3+} δ_{nnn} (Ni^{3+}–O–Li 180°) pathways, which means an unexpectedly higher shift could be caused by the Li spending more time with Ni^{3+} as its next nearest (180°) neighbour. The observed lag could be linked to the JT distortion of Ni^{3+}, as the fast motion model assumes that the JT distortion is perfectly averaged, however the JT axes may have a preferential orientation with respect to Li, as observed for the ^{59}Co and ^{27}Al spectra.

Kinetic limitations and reaction heterogeneity will have a negative impact on the performance of the cathode. If the heterogeneity occurs between particles then, if capacity loss due to under-utilised particles is to be avoided, overpotentials will be required to activate the sluggish particles. If there is heterogeneous reaction within individual particles, then strains will be introduced, and energy will be required to propagate the two-phase boundary through the particle leading to increased impedance. In the worst case such strains could induce primary particle fracture. Whilst differences in surface structure and adsorbed species cannot be ruled out as a cause entirely, the complex behaviour of the Ni^{3+} JT bonding observed in pristine NCA may hold the key understanding its intrinsic kinetic limitations. As discussed in section 2.4.7, the dynamic JT distortion in NCA is far from random and seems to prefer local orderings that allow favourable interactions between adjacent Ni^{3+} ions. The creation of Li vacancies and the reduction in the concentration of Ni^{3+} will change the energy landscape for the JT axes; energetically favourable configurations may shift away from pairwise interactions of Ni^{3+} ions and towards coordination of vacancy sites for example. This change in the low energy configurations of the JT bonds may play a role in improving the mobility.

2.6 Cycled NCA—^{59}Co, ^{27}Al and ^{17}O NMR

NMR spectra of TODA-NCA upon delithiation are shown in Figure 2.16 and Figure 2.17 for ^{27}Al and ^{59}Co respectively. Additionally, ^{17}O NMR VOCS for pristine and charged ^{17}O-NCA are shown in Figure 2.15. For all nuclei measured in the pristine material, the distribution of shifts was assigned by considering first the number of Ni^{3+} neighbours and, for ^{59}Co and ^{27}Al, combining this with likely JT orderings to deconvolute the observed NMR lineshape. In all cases, the presence of Ni^{3+} neighbours determine centre of mass of the shift. As Ni^{3+} is oxidised a similar shift trend is expected for the ^{59}Co, ^{27}Al and ^{17}O as was observed for ^{7}Li, i.e. a shift toward the diamagnetic region as delithiation proceeds.

2.6.1 ^{17}O NMR—Cycled NCA

The ^{17}O VOCS spectrum from an electrode charged to 4.7 V ($204mAhg^{-1}$ ~ $Li_{0.27}(Ni_{0.80}Co_{0.15}Al_{0.05})O_2$) is shown in comparison to the spectrum obtained for the pristine material in Figure 2.15. The electrochemical profile for ^{17}O-NCA (Figure 2.2) shows larger overpotentials than typically observed for TODA-NCA or HT-TODA-NCA. This accounts for the relatively low electrochemical capacity extracted despite the high cut off voltage. The greater overpotentials are most likely caused by the increase in Li/Ni mixing in the Li-layer as well as the presence of surface species. Despite these differences, the Li content estimated from the electrochemistry is qualitatively in agreement with the ^{7}Li NMR shift of this sample, lying intermediate between the shifts observed for the HT-TODA-NCA samples with 0.29 and 0.12 Li per formula unit (inset Figure 2.15). At this SOC most of the Ni will have been oxidised to 4+. The ^{17}O spectrum shows an increase in signal around 0 ppm and a loss of signal in the paramagnetic region. This is the anticipated change and supports assignment of the broad ~12000 ppm peak in the pristine VOCS to O with a varying number of Ni^{3+} neighbours (principally $3Ni^{3+}$). The loss of the highly shifted O signal is consistent the

majority of the Ni^{3+} being oxidised, although the remaining broad signal indicates that some paramagnetic species remain in the lattice: likely a mix of Co^{4+} and Ni^{3+}.

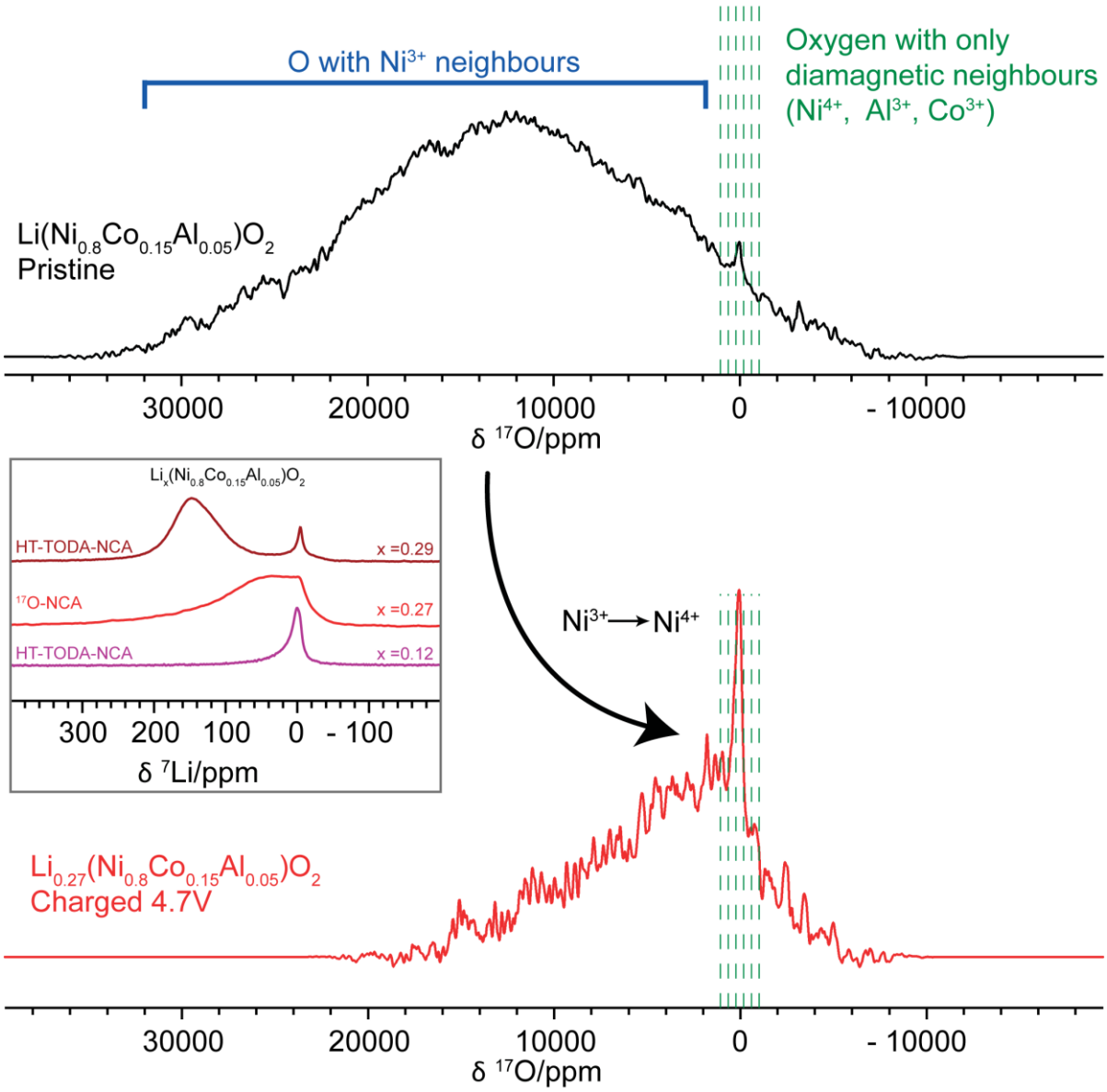

Figure 2.15 ^{17}O NMR spectra of pristine and charge ^{17}O-NCA. The charged sample, which has 0.18Li per formula unit, shows an increase of signal in the diamagnetic region consistent with oxidation of Ni^{3+}→Ni^{4+}. Some paramagnetic signal remains at lower shift which may be due to Co^{4+}, residual Ni^{3+} or unpaired electron spins which are not explained by a strict ionic redox model. The inset shows a comparison of the charge ^{17}O-NCA sample with two HT-TODA-NCA samples demonstrating that shift of the ^{17}O-NCA is around the expected value and qualitatively confirming its SOC.

2.6.2 ^{27}Al NMR—Cycled NCA

The ^{27}Al NMR spectra show the expected trend of a gain in signal in the diamagnetic region at the expense of the paramagnetic sites. The spectra we recorded with short recycle delays (0.1s) in order to maximise any paramagnetic signals and are not quantitative in the diamagnetic region. Despite this biasing of the spectra no paramagnetic Al sites are observed at high states of charge in contrast to the ^{17}O VOCS. It has been proposed that at the end of charge Al migrate into tetrahedral sites in the Li layer in Al containing $LiTMO_2$, particularly in the case where Al is coordinated by 6Co.[61] Whilst such environments are statistically unlikely to occur in NCA there may still be migration of Al into tetrahedral sites. The ^{27}Al shift for tetrahedral Al in a diamagnetic site is ~70 ppm.[200] No clear evidence for a peak at this shift was observed in the majority of samples, although there is definitely signal above 0 ppm particularly for the 0.16 sample, which, given possibility of 2nd order quadrupole shifts at low fields and the low signal to noise ratios, is not inconsistent with tetrahedral sites. For an NCA sample charged to 4.8V and then potentiostatically charged until the expended capacity was 270 $mAhg^{-1}$, the peak moved to higher ppm, with a shoulder at ~73 ppm. This change was only visible when a non-quadrupolar $\pi/2$ pulse was used (Figure 2.16 bottom). This observation supports the hypothesis that some Al migrates into the TM layer at the end of charge. The peak is only clearly observed in the sample which is potentiostatically charged suggesting this migration occurs at the highest levels of delithiation. Additionally, most of the signal remains in octahedral environments—notably the "tetrahedral" signal can only be observed clearly using $\pi/2$ pulse experiments implying a lower EFG anisotropy for this environment. A more detailed study would be required to quantify the relative amounts of each of the Al environments at the end of charge.

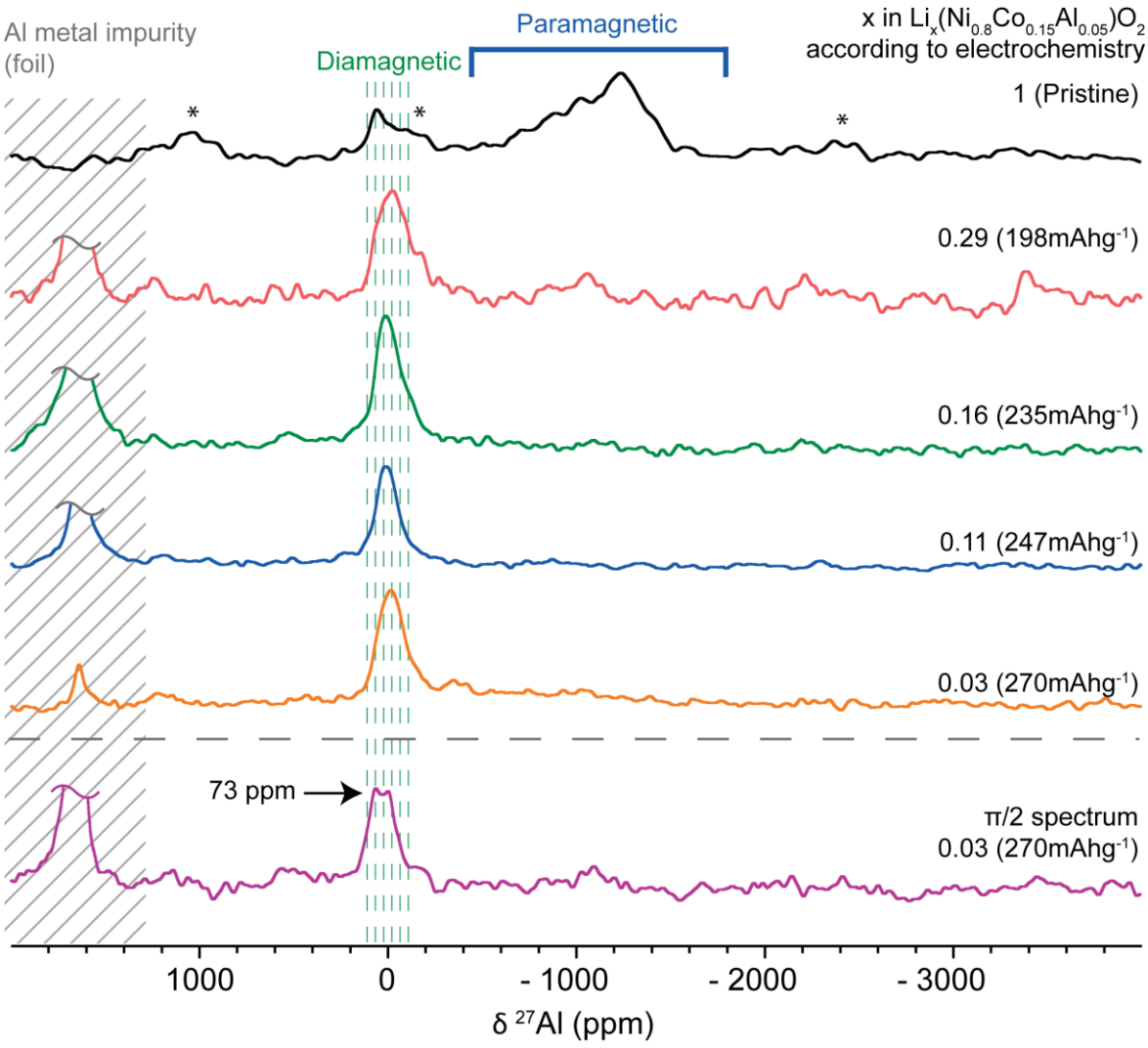

Figure 2.16 ^{27}Al NMR spectra for TODA-NCA recorded at 4.70T and 60kHz MAS frequency a various states of charge. Shift regions for paramagnetic (blue), diamagnetic (green) and impurity metal (grey) are indicated. All spectra except the bottom spectrum are recorded with π/6 pulses used as the effective π/2 pulse to quantitatively excite all signals. The bottom spectrum was recorded with a π/2 pulse as optimised for AlF_3(s).

2.6.3 ^{59}Co NMR—Cycled NCA

Most of the ^{59}Co spectra of cycled NCA, were recorded at higher fields than the pristine spectra discussed previously. The spectra of cycled ^{59}Co samples, which contain less observable Co^{3+} near the end of charge, could be acquired much more quickly at 16.4 T. Additionally, the electric field gradients at the nucleus are expected to become larger as the charge state of the adjacent ions is changed and Li is removed, hence a higher

field is desirable (section 1.8). This has the unfortunate effect of increasing the broadening due to the e-n dipolar coupling. As the observable ^{59}Co signal decreases in intensity, wide sweeps using variable offsets were performed to ascertain whether the signal became significantly broader, or whether new signals could have emerged; between -1000ppm and 30000ppm no new signals were observed

The ^{59}Co spectra are scaled by mass and scans and their integrated intensities (in relation to the pristine material) are also listed (Figure 2.17). There is a loss of signal with delithiation although even at the end of charge some ^{59}Co signal remains (35%). In the pristine material the Co^{3+} is diamagnetic and hence observable by NMR. The ^{59}Co NMR signal is not expected to be observable for Co^{4+}; Since Co^{4+} is itself paramagnetic, the effective spin transfer will be extremely large, hence extremely rapid relaxation will be induced, causing a loss of signal. It is likely that the signal loss in the ^{59}Co spectrum on delithiation is as a result of $Co^{3+} \rightarrow Co^{4+}$ oxidation. It is possible that the loss of signal is due to faster T_2 relaxation during the echo delay for the more delithiated samples; the spectra are recorded as Hahn-echoes to reduce probe ringing and background. Whilst, in the cycled ^{7}Li NMR the T_2 relaxation was enhanced on delithiation, this was an effect of the increased Li motion. In the case of Co/Al/O the T_2s would be expected to increase as the sample becomes less paramagnetic overall due to Ni^{3+} oxidation. This possibility warrants further investigation.

The change in peak position for the ^{59}Co spectra is more challenging to rationalise. At the nominal composition x = 0.91, the peak shifts towards the diamagnetic region (14000 ppm) as expected. However, once the composition reaches x = 0.56, the peak returns to approximately the shift of the pristine material (ca. 12000 ppm). Between compositions x = 0.56 and x = 0.29 the Co NMR barely changes with only a small loss in signal and virtually no peak shift observed. Finally, upon delithation to the end of charge the remaining Co signal is shifted further from the expected diamagnetic region with a peak position ~11500 ppm. The nominal composition in this case is -0.08, i.e.,

the nominal electrochemical capacity corresponds to the removal of more lithium than implied by the stoichiometry of the sample, assuming 100% coulombic efficiency. The cells for ^{59}Co NMR were cycled at C/50 in order to ensure low overpotentials, hence some of the erroneous capacity observed for the highly delithiated sample can be attributed to electrolyte decomposition, and its true Li stoichiometry can be assumed to be at or close to the maximum delithiation assuming Al^{3+} is electrochemically incative of x = 0.05.

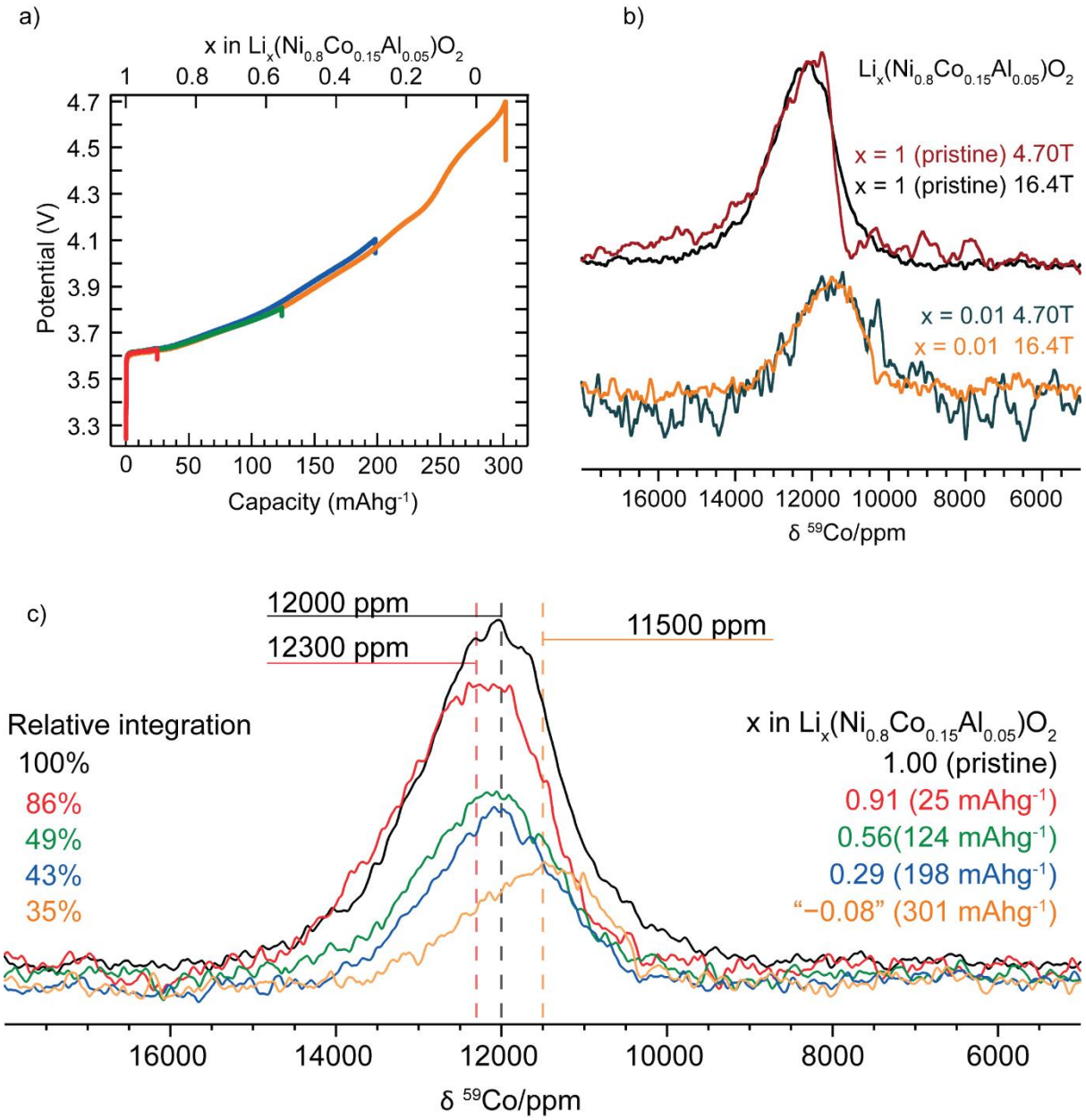

Figure 2.17 a) Voltage curve showing states of charge sampled for the ^{59}Co NMR study. b) ^{59}Co spectra for pristine and cycled TODA-NCA at 4.70 and 16.4 T demonstrating the lack of a significant 2nd order quadrupolar shift for either sample. C) ^{59}Co spectrum for TODA-NCA at various points of charge with labels indicating the relative integration and the Li remaining per formula unit (derived from electrochemistry) in each case.

This unanticipated shift in the ^{59}Co resonances is intriguing, particularly as similar behaviour is not observed in the ^{27}Al, ^{17}O or ^{7}Li. One possible factor could be a large shift caused by the 2nd order quadrupolar interaction, however this can be ruled out as the no change in peak position is observed for the pristine sample or a sample at the end of charge at different field strengths (Figure 2.17b). A second possibility is that,

for the portion of Co^{3+} that remains, whilst the hyperfine shift from Ni^{3+} is lost a new shift from paramagnetic Co^{4+} arises. This is also not likely, as the shifts from Co^{4+}–O–Co^{3+} arise from unpaired spins in the t_{2g} orbitals, the dominant shift interaction (which would occur via a delocalisation mechanism) would be the 90° interaction and it would be expected to be positive, contrary to the observed shift. The 180° Co^{4+}–O–Co^{3+} shift is expected to be negative but cannot explain the shift as, without significant Co^{4+} migration to the Li-layer, Co^{3+} can have no Co^{4+} 180° neighbours.

The peak which remains at the end of charge is on the highly shifted end of the pristine Co spectrum and in the pristine material fits the shift assigned for Co with $4\delta_{SL}$ Ni^{3+} pathways (11600 ppm). This raises the possibility that at the end of charge, the remaining Co^{3+} is still coordinated by Ni^{3+} and specially via δ_{SL} pathways. If in the pristine material a Co^{3+} surrounded by $4\delta_{SL}$ pathways, for example Co-6Ni, were particularly energetically favourable, possibly due to favourable JT ordering accommodated by the Co^{3+}, then such a region could be more difficult to oxidise and could lead to a region that remains largely 3+. This is also seems unlikely, as if the Co NMR is quantitative and 35% of the Co is in these domains, 18-27% of the Ni in the sample would be required to remain 3+ (depending on whether the stable domain requires 4, 5 or 6Ni^{3+} ions to form). Additionally, this hypothesis is not supported by the O NMR where the O coordination expected for this type of domain is absent (i.e. O with one long JT bond to Ni^{3+} and two other bonds); 9-14% of the O should be in this environment. Although it is true that, if such, essentially static, JT domains existed then the ^{17}O signal may be shifted or unobservable due to the large EFG anisotropy that a static JT arrangement would create. The lack of evidence for Ni^{3+} in either the ^{27}Al or ^{7}Li NMR spectra is also convincing evidence against this hypothesis—it is hard to imagine 3+ domains making up significant proportion of the TM layer not interacting with either ^{7}Li or ^{27}Al.

One very interesting property of ^{59}Co NMR is the extremely large chemical shift range observed for diamagnetic ^{59}Co complexes. The source of these large chemical shifts is the so-called paramagnetic contribution to the diamagnetic chemical shift. This shift is derived from the mixing of symmetry-allowed, low lying excited states with the ground state and should not be confused with the paramagnetic Fermi-contact shift.[201] The size of this chemical shift will increase if the energy difference between the ground state and the lowest lying excited states decreases. As the ground state of Co^{3+} is low spin d^6 $t_{2g}^6 e_g^{*0}$ and the low-lying excited states have the configuration $t_{2g}^5 e_g^{*1}$, for Co^{3+} energy difference is simply the crystal field splitting energy (Δ). In Co^{3+} complexes the paramagnetic chemical shift is lowest for strong field ligands, such as CN^-, which increase Δ,[202] hence $K_3Co(CN)_6$, which is the primary reference for ^{59}Co resonates at much lower shift (0 ppm) than does $LiCoO_2$ ~14000 ppm) (Figure 2.18).

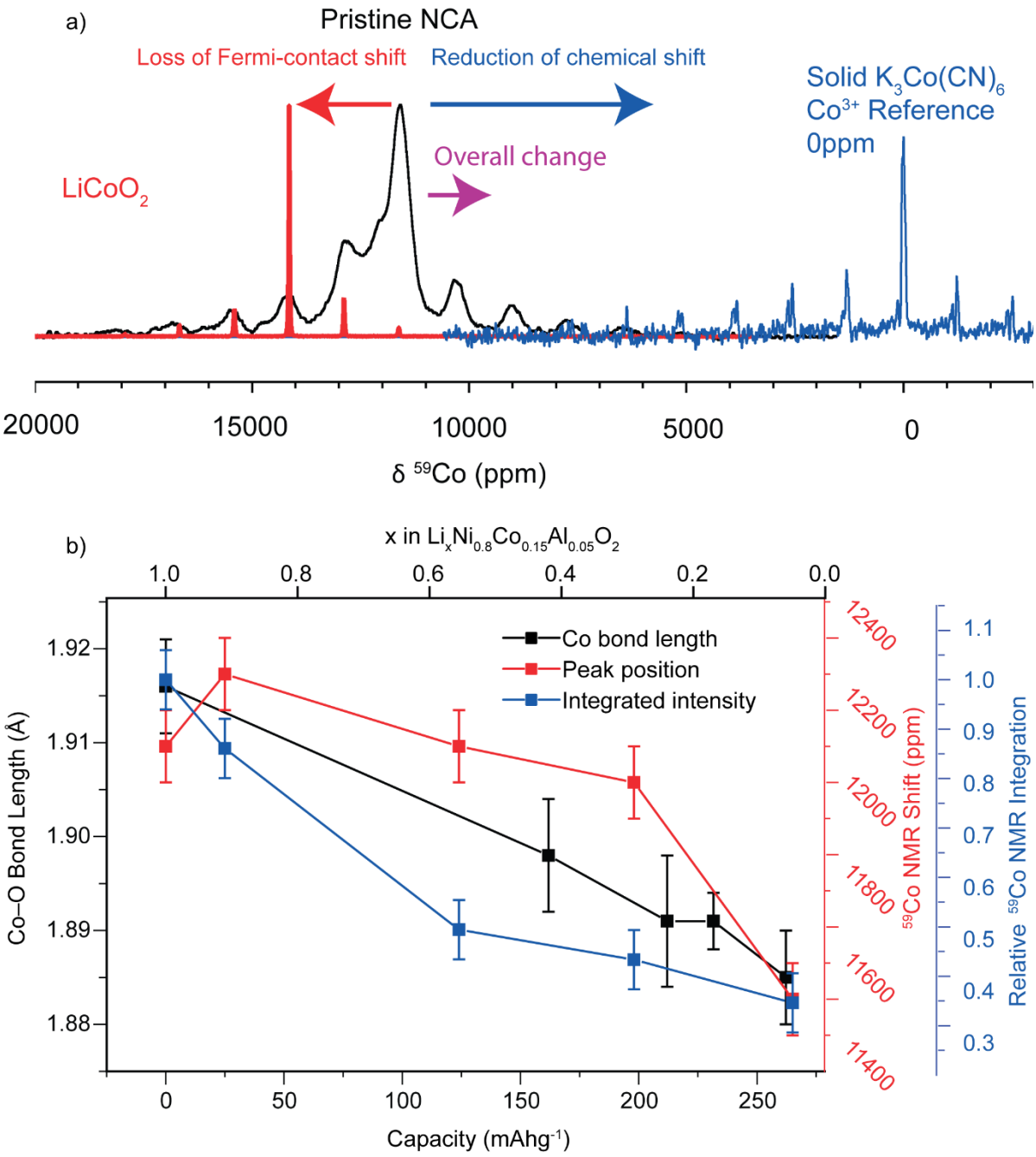

Figure 2.18 a) Illustration of the shift ranges for $LiCoO_2$ (red), pristine NCA (black) and solid $K_3Co(CN)_6$ (blue). The loss of NCA's Fermi-contact shift is expected to move it towards the $LiCoO_2$ shift region, whilst the reduction in the chemical shift due to increasing Δ is expected to move it towards the $K_3Co(CN)_6$ region. The overall change is a slight shift to lower ppm (purple). b) comparison of the evolution of Co–O bond length, ^{59}Co NMR shift and ^{59}Co integrated intensity versus the SOC of TODA-NCA. Co–O bond lengths derived from EXAFS and taken from ref.[63]

In NCA or $LiCoO_2$ the energy separation, Δ, is between the non-bonding Co t_{2g} states and the Co–O antibonding e_g^* orbitals (Figure 1.4a). As discussed previously, for

$LiCoO_2$, (section 1.2.1) the Co K-edge spectrum does not show the same continuous edge shift observed for Ni and Mn complexes.[65,66,203] However, the $L_{II,III}$-edge XANES, which are sensitive to transitions from 2p→3d do show a shift to higher energy.[67] As no edge shift is seen in the K-edge spectra, the changes in the $L_{II,III}$-edge spectra are most likely not simply due to an increase in the oxidation state of the Co ion. Rather, the energy gap between the 2p and 3d states has increased as the vacant 3d states (e_g^* orbitals) are pushed up in energy. This rise in the energy of the e_g^* states is caused by a lowering in energy of the Co–O e_g bonding states due to increasing hybridisation. L-edge XANES show a similar trend.[63] Increasing hybridisation of the Co^{3+}–O states should, as observed in the L-edge- XANES, result in an increase in Δ and hence a reduction in the paramagnetic chemical shift. The change in peak position for the ^{59}Co spectrum is therefore dependent on two principal factors: loss of the Ni^{3+} negative Fermi-contact shifts (principally via δ_{SL} bond pathways) and the reduction in positive, chemical shift caused by an increasing energy separation of the t_{2g} and e_g^* levels in Co due to increased Co–O hybridisation. The ^{59}Co NMR must be understood in the context of complementary techniques such as L-edge XANES, EXAFS and XRD, all of which offer information about the Co–O bond lengths and hybridisation.

During the initial period of discharge, from x = 1 to x = 0.91, signal is lost, which suggests Co is oxidised from the beginning. The peak position moves slightly towards higher shifts, which indicates that initially the loss of Fermi-contact shift outweighs the loss of chemical shift. In the next part of the charge x = 0.91 to x = 0.6 more Co and Ni are oxidised, and more Co signal is lost. In this part of the charge the loss of Fermi contact shift is dominated by the effects of the changing chemical shift of the residual Co^{3+} ions that remain in the structure. The period of charge from x = 0.60 to x = 0.36 sees very little change in the intensity of the Co spectrum perhaps indicating that the change in the Co oxidation state has ceased temporarily. At the same time the shift does not change either indicating a balance between the changes due to the

Fermi-contact and chemical shifts. From the x = 0.6 to x = 0.91 more Co signal is lost and the change in the peak position indicates the change of the chemical shift outweighs the change in the Fermi-contact shift contribution.

This non-monotonic behaviour is somewhat challenging to interpret however there is no reason to assume the evolution of Fermi-contact and chemical shift contributions are monotonic either. Whilst, the majority of L-edge XANES edge shift occurs before x = 0.24, EXAFS data show that the Co–O bond length changes continually with large change between x = 1 and x = 0.42, a period between 0.42 and 0.17 where the change is fairly small and finally a period between 0.17 and 0.06 where the change is faster again.[63] This is in reasonable agreement with the observed change in the Co shift (Figure 2.18). Another possible origin of discrepancy between the XANES data and the ^{59}Co NMR is that in the ^{59}Co NMR, signal is only observed for Co^{3+} whereas XANES measures the signals regardless of its formal oxidation states. The formation of Co^{4+} is likely to drive a shortening of the Co–O bond lengths due to its higher charge. By contrast, Co^{3+} is more likely to have its bond length and hybridisation changes forced upon it by the changes in the lattice, as a result of the loss of Li and the changes in oxidation of other ions. This may create a lag between the changes observed in the XANES and the NMR. As discussed in section 2.4.7, the majority of the Fermi-contact shift on Co comes via δ_{SL} bond pathways which depend on the orientation of the Ni^{3+} long JT axes. The JT distortions in NCA are dynamic, however as discussed previously, the more thermodynamically favourable arrangements will make up more of the average ordering which is probed on the NMR timescale. The loss of the Fermi-contact shift may not be monotonic, for example the balance of Ni^{3+}/Ni^{4+} may reach a critical point during charge, at which the pseudo-ordering of the JT axes is be lost and the average shift experienced by Co^{3+} changes dramatically. A sudden change in Fermi-contact shift, accompanied by a relatively small change in the chemical shift, is one possible explanation for the relatively static Co peak position between x = 0.6 and x = 0.36. The sharp change at the end of charge is accompanied by reduction in the Co–O bond

length (as observed in EXAFS) however there is also the collapse of the c-lattice which leads to an even more compressed TM–O layer. This may introduce strains around Co^{3+} which remains in the lattice (35% of the NMR signal) which compress its octahedra and help drive the sharp change in peak position from x = 0.36 to x = 0.01. More measurements of both the ^{59}Co NMR and the Co XANES are required if more mechanistic detail is to be uncovered.

Recently, evidence has emerged of the "RIXS feature", commonly observed in O-redox materials, for highly charged NCA.[63] The ^{59}Co NMR support this observation, as plainly Co signal is observed where, if conventional cationic redox is assumed, all Co should be 4+. Whilst the RIXS feature has been used by many authors as a "fingerprint" of O redox there is no prevailing interpretation about the mechanism of O redox which would give rise to such a feature. Unfortunately, there is not sufficient resolution in our ^{17}O spectra to observe or rule out the possibility of O–O dimers for example. Recent work has suggested that migration of TM species is a prerequisite for O redox. ^{27}Al NMR in highly delithiated samples, tentatively suggest that some Al occupies tetrahedral sites at the end of charge and may be the required migrating species. In principal either Ni^{4+} or Co^{4+} could also migrate; although for reasons of crystal field stabilisation, this is unlikely. The Co^{3+} observed at the end of charge in this study cannot be the migrating species, as if it were in tetrahedral sites it would not remain diamagnetic. By the same logic, Co^{3+} in tetrahedral sites cannot be ruled out entirely as it would not be observable by NMR, however generally in NCA, Ni is considered the more likely migrating species.[204] The good cyclability demonstrated by NCA suggests that "true" anionic redox, characterised by greater than TM-expected capacity and large change in voltage profile after 1st charge, does not occur in NCA, however the presence of Co^{3+} at the end of charge and new observation of the O-redox RIXS feature is intriguing. The Co^{3+}, observed at the end of charge, acts essentially a spectator ion, as apart from the change in energy separation of its t_{2g} states and e_g^*

states it remains largely unaffected by the charging process. The role that it plays in any unconventional redox processes remains to be determined.

2.7 Conclusion

A multinuclear NMR approach has been used to understand the local structure of pristine and electrochemically charged NCA. The use of challenging and unconventional nuclei (^{59}Co and ^{17}O) has allowed the JT distortion in pristine NCA to be characterised: whilst the JT distortions are dynamically disordered, the NMR supports a model of thermodynamically favoured arrangements, which make up a greater part of the average structure. ^{7}Li NMR has been used to support these conclusions and to provide insight into the mobility of Li on charge. Rapid Li motion occurs in the HT-TODA-NCA sample from x=0.78 onwards. Using T_2 filtered experiments, non-uniform delithiation has been observed and it has been demonstrated that this inhomogeneity survives moderate heating of the delithiated powders. The Li mobility study provides insights into the inherent kinetic limitations observed in NCA.[196,205,206]

The charging mechanisms of NCA determined from the ^{7}Li NMR study are complemented by ^{17}O, ^{27}Al, and ^{59}Co NMR. The use of ^{59}Co NMR in a paramagnetic battery material is, to the authors knowledge, entirely novel and through the use of this probe new insights into the unusual redox behaviour present in NCA have been demonstrated. The earliest sampled state of charge (x=0.92) shows that some Co^{3+} has been oxidised demonstrating that both Ni and Co are oxidised simultaneously from the beginning of charge. The ^{59}Co NMR provides a unique probe for Co^{3+} ions and highlights that 30% of the Co^{3+} ions remain at the end of charge, in stark contrast to the conventional viewpoint: that all the Co should be in the 4+ oxidation state at the end of charge. The ^{59}Co NMR shifts have been assigned using complementary information from published XANES and EXAFS data and show that the energy gap between the Co t_{2g} states and the Co–O antibonding e_g^* states increases during the

charging process.[63] The Co^{3+} that remains visible in the ^{59}Co NMR spectra is intriguing evidence of the unconventional redox that occurs in $LiNi_{0.8}Co_{0.15}Al_{0.05}O_2$. Charge compensation by rehybridisation of the Co–O molecular orbitals, with no change in the Co effective nuclear charge has long been hypothesised in $LiCoO_2$.[67] Due to the ambiguity in interpreting Co XAS data (both K and $L_{II,III}$-edge spectra) this theory could not be confirmed, however the ^{59}Co NMR demonstrates without doubt that Co^{3+} is present at the end of charge in clear support of this theory. In addition to the well-established "rehybridisation" hypothesis,,[68,207] recent studies have revealed the same "RIXS feature" in NCA, as that which is commonly presented as evidence of anionic redox in the Li-excess materials.[63] The appearance of this "feature" (discussed in more detail in section 1.5.3) in NCA at the end of charge demands that either: the theories which link it inextricably to the Li-excess family of materials (and their many singular properties) be revised and accept that the "feature" could be the result of a rehybridisation process; or that charge compensation in NCA must be revaluated and the possibility of "anionic redox" in NCA, along with all the current ideas about stabilisation of oxidised oxygen (section 1.5.2), be considered for this apparently conventional material.

In order to understand the role O plays in the redox chemistry of layered cathodes, model compounds can be used. Li_2RuO_3 is one such compound and its structural and redox chemistry will be investigated in detail in the next two chapters.

Chapter 3: Characterizing the Structure and Phase Transition of Li_2RuO_3 using Variable Temperature ^{17}O and ^{7}Li NMR Spectroscopy

3.1 Abstract

Li-excess lithium-ion battery cathode materials and the role that reversible anionic redox may play in their high capacities, have generated significant interest, motivating studies of the oxygen local structure. Li_2RuO_3 is an intriguing Li-excess model compound, which is studied here by local (^{7}Li and ^{17}O MAS NMR) and long-range (X-ray and neutron diffraction) structural probes. Li_2RuO_3 is often reported as adopting the $C2/m$ or the $C/2c$ space group, which ignores the important role that Ru–Ru dimerization plays in controlling its properties. ^{17}O NMR reveals four oxygen sites confirming the room temperature $P2_1/m$ structure proposed by Miura, Y.; Yasui, Y.; Sato, M.; Igawa, N.; Kakurai, K. *J. Phys. Soc. Japan* 2007, *76*, 033705. Through the rationalisation of the ^{17}O NMR shifts, at room temperature and through the phase transition (>260°C), detailed information concerning the electronic structure and locations of the unpaired electrons in this compound is revealed.

3.2 Introduction

Since 2001, the use of Li-excess cathodes materials, in which some of the TM sites are occupied by Li, have been a potential avenue to push the capacity of the traditional

layered rocksalts even further[73,75]. Exchanging TM and Li ought to reduce the number of sites available for redox during Li removal, however many Li-excess materials have shown the ability to deintercalate more Li than expected if only TM oxidation is considered. The hypothesis that O participates reversibly in the redox reaction has now been extensively studied in these materials, and related model compounds: in $Li_{1.2}Mn_{0.54}Co_{0.13}Ni_{0.13}O_2$, $Li_2Ru_{0.75}Sn_{0.25}O_3$ and $Li_{1.3}Mn_{0.4}Nb_{0.3}O_2$ for example[78,122,132]. The proposed redox process in these cases is distinct from the electronic processes observed on O as a result of O-TM hybridization, which cannot increase the capacity beyond the expected TM redox[135].

While the exact mechanism for oxygen redox may depend on the type of cathode material in question, three main mechanisms are reported. In one case the oxidation of O is accompanied by a shortening of the O–O interatomic distances leading to stabilization by the formation of peroxo-like species.[132,138,208] The second, which is proposed to occur in the case in which strong, directional hybridization of O–TM prevents rotation of the O p orbitals towards one another, is localized hole formation on oxygen.[121,123,209] The third, is characterised by metal migration which leads to the formation undercoordinated O atoms; these can be stabilised by either short O–O bond formation or M–O rehybridization, forming a bond with a bond order greater than one.[136,140] Owing to the difficulty in directly observing the O redox phenomenon, along with the complexity of structures of many Li-excess compounds,[85,87,109,210,211] model compounds, that simplify the redox processes are essential to understanding the functioning of these materials. Li_2RuO_3, which may be written as $Li(Li_{1/3}Ru_{2/3})O_2$ to emphasize the layered structure and analogy to $LiCoO_2$, is one such model system. However, the anionic redox properties of this material cannot be fully rationalized without a full understanding of the local crystallographic and electronic structures of the starting material. This is the aim of this chapter.

As discussed briefly in section 1.4, the structure of Li_2RuO_3 is often incorrectly reported as having the $C2/c$ or $C2/m$ space group, due to earlier reports.[79,125,129] The correct structure was first reported by Miura et al.[212] and has the same, familiar O3 type stacking honeycomb TM layer order present in the $C2/c$ and the $C2/m$ structure (Figure 3.1b), however the $P2_1/m$ space group accommodates an "armchair" configuration of Ru–Ru dimers (Figure 3.1a). At room temperature, the Ru^{4+} lattice comprises an ordered array of dimers, Li_2RuO_3 forming a valence bond crystal (VBC)[213,214] (Figure 1b). This dimerisation of the low spin $4d^4$ (S = 1) ion leads to the quenching of at least one of the unpaired spins on each Ru^{4+} and a concomitant reduction in the magnetic susceptibility[212,215]. At ~270 °C Li_2RuO_3 exhibits a phase transition, evidence from a pair distribution function (PDF) analysis study show that, although dimers remain above the transitions, the dimers are disordered within the lattice and thermal fluctuations drive dynamics between different dimer pairs; this is termed a resonating valence bond (RVB) state.[214,215] As well as being an interesting phenomenon from the perspective of the solid state physics, probing the dimer-solid to dimer-liquid transition may offer insights in to the changes that occur on cycling.

Neutron diffraction measurements were performed by Dr Kent J. Griffith.

Computational details and discussion are included here as the methodology and assumptions made in the computations are pertinent to the rest of the discussion, however all calculations presented were performed by Dr Ieuan D. Seymour and not the author.

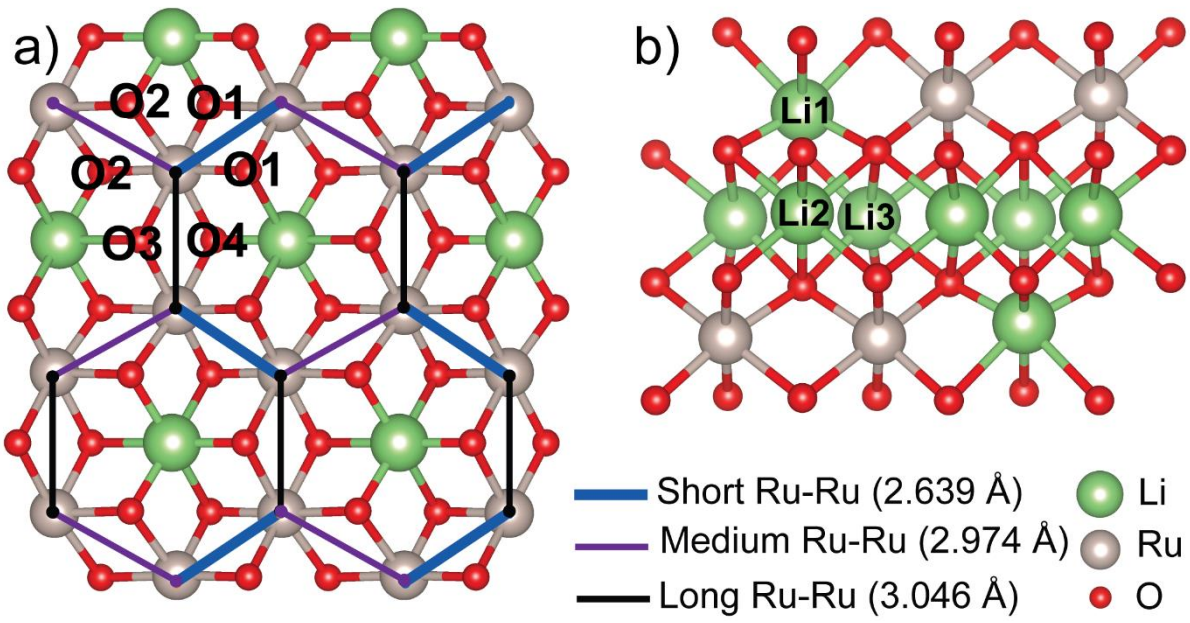

Figure 3.1 Schematic representation of (a) the "honeycomb" Ru layer and (b) the layered structure of Li_2RuO_3. The crystallographic O sites are labelled to show their position relative to the Ru dimers and the Li sites are shown in the position within the layers.

3.3 Experimental

3.3.1 Materials and Synthesis

Li_2RuO_3 was synthesized by solid state methods. Li_2CO_3 (Sigma Aldrich 99.997%, 10% excess) and RuO_2 (Alfa Aesar 99.9%, dried at 500 °C overnight) were ground together and heated to 600 °C for 12 hrs, then cold-pressed into pellets and heated further to 900 °C for 12 hrs and then to 1000 °C for 12 h with intermediate grinding. To record the ^{17}O NMR spectra, samples were enriched in the I = 5/2 NMR active nucleus ^{17}O, by heating the hand-ground precursors materials in a static O_2 (70% ^{17}O NUKEM Isotopes) environment at ~380 kPa at 1000 °C for 24 hrs.

3.3.2 NMR Methods

Room temperature ^7Li NMR was conducted at 4.7 T using a Bruker 1.3 mm MAS probe at an MAS frequency of 60 kHz. The spectra presented are rotor-synchronised Hahn echo experiments with the echo delay equal to one rotor period. T_1 relaxation

was measured to be ~330 ms (48 ppm) and ~480 ms (28 ppm) using inversion recovery and saturation recovery experiments; recycle delays were set to be five times the largest T_1 value for quantitative acquisition.

Room temperature ^{17}O NMR was conducted at 11.7 T using a Bruker 1.3 mm MAS probe at an MAS frequency of 60 kHz. The spectra presented are rotor-synchronised Hahn echo experiments with the echo delay equal to one rotor period. T_1 relaxation was measured to be ~100 ms (1070 ppm), ~10 ms (740 ppm), ~160 ms (580 ppm) and 250 ms (200 ppm) using saturation recovery experiments and recycle delays were set to be five times the largest T_1 value for quantitative acquisition.

^{17}O variable temperature NMR was performed at 16.4 T using a Bruker 4 mm probe at an MAS frequency of 14 kHz. The spectra presented are rotor-synchronised Hahn echo experiments with the echo delay equal to one rotor period. The value of T_1 from room temperature experiments were used once the T_1 was confirmed to decrease with increasing temperature. Due to the challenge of safely spinning the samples at high temperatures, the recycle delays were set to 0.75 s for the single acquisition experiments to provide better signal-to-noise more quickly. The VOCS experiments were carried out with shorter delays as many spectra needed to be recorded at each temperature; delays of 5 ms were used, which is roughly equal to the T_1 beyond the phase transition. Temperature calibration was performed *ex situ* using the ^{207}Pb shift of $Pb(NO_3)_2$ as an NMR thermometer with very similar bearing and drive pressures[182]. A calibration curve was made to translate the thermocouple temperatures to sample temperatures.

^{7}Li variable temperature NMR was performed at 9.4 T using a Bruker 7 mm laser probe at an MAS frequency of 4 kHz. The spectra presented are rotor-synchronised Hahn echo experiments with the echo delay equal to one rotor period. A recycle delay of 5 s was used. The sample was heated using a CO_2 laser which shines onto the rotor. KBr was ground into the sample to assist spinning and as an *in situ* thermometer using the ^{79}Br shift as described by Thurber and Tycko[216].

3.3.3 Diffraction Methods

Powder x-ray diffraction patterns were recorded on a Panalytical Empyrean diffractometer emitting Cu Kα (1.540598 Å + 1.544426 Å, 1:1 ratio) radiation. Scans were recorded from 5-86° 2ϑ in steps of 0.017° 2ϑ. Constant-wavelength neutron scattering measurements were performed on SPODI, the high-resolution neutron diffraction beamline at MLZ in Garching, Germany. Li_2RuO_3 was packed under air into a 10 mm diameter cylindrical sample holder made of vanadium. Rietveld refinements were performed using GSAS-II[217]. Neutron diffraction experiments were carried out at room temperature at 1.5483 Å and 2.536 Å with Ge(551) and Ge(331) monochromator crystals, respectively. The shorter wavelength provided a larger Q-range; the longer wavelength provided higher resolution. The coherent neutron scattering lengths of ^{7}Li, Ru, and O are –2.22, 7.03, and 5.803 fm, respectively, affording better visibility (vs. X-rays) of the light atoms in the presence of ruthenium.

3.3.4 Magnetic Measurement Methods

The DC magnetisation of Li_2RuO_3 was measured using a Quantum Design SQUID (MPMS 3) in a magnetic field of 100 Oe between 2–400K under both field-cooled (FC) and zero-field-cooled (ZFC) conditions. Diamagnetic contributions to the susceptibility from ion cores in Li_2RuO_3, were subtracted.[218].

3.3.5 Density Functional Theory Calculations

In this study, solid-state density functional theory (DFT) calculations were performed using the augmented planewave plus local orbital APW+lo[219,220] method in ELK[221], a full-potential linearized augmented plane wave (FP-LAPW) code. An APW+lo approach in ELK was chosen in the current study over an all-electron LCAO approach, as adopted in previous studies by some authors,[222–224] as a thoroughly tested all-electron Gaussian basis set for Ru was not available. Similar linear augmented plane wave (LAPW) approach in the WIEN2k code[225] has recently been successfully used to

calculate the ^{7}Li and ^{31}P Fermi contact shifts in a range of Li transition metal phosphate compounds.[226,227]

Three DFT optimised Li_2RuO_3 structures ($P2_1/m$, $C2/m$ dimerized, $C2/m$ un-dimerized) from the previous work of Kimber et al.[215] were used in the current study without further structural optimisation. Spin polarised DFT calculations using the Perdew−Burke−Ernzerhof (PBE) exchange–correlation functional[228,229] with ferromagnetic spin alignment were used to evaluate the wavefunction of the Li_2RuO_3 structures and calculate the unpaired spin density at the nuclear position $\rho(0)$. In the ELK code, $\rho(0)$ is integrated within a sphere around the nucleus defined by its Thomson radius.[230] Thomson radii of 8.46 and 22.86 fm were used for Li and O respectively. Muffin tin radii of 1.800 a_0, 2.101 a_0 and 1.624 a_0 were used for Li, Ru and O, respectively. The number of augmented planewaves was set by the parameter $R|\boldsymbol{G}+\boldsymbol{k}|_{\max}= 8$, where R is the average muffin tin radius and G are the reciprocal-lattice vectors. The Brillouin zone of the $P2_1/m$, $C2/m$ dimerized, $C2/m$ un-dimerized unit cell structures were sampled with applied crystal symmetry using evenly spaced k point meshes of 10×9×5, 10×10×9 and 11×11×9. In all calculations, polarisation of the core was enabled. Convergence of the energy and unpaired spin density at the nuclear position was checked with respect to the k-point density, $R|\boldsymbol{G}+\boldsymbol{k}|_{\max}$ and muffin tin radii.

It has recently been shown that the use of hybrid functionals or a Hubbard U correction (DFT+U), results in a breaking of the Ru–Ru dimers, which favours a magnetic state in which each Ru site has a spin of approximately S=1.[231,232] This structure is similar to the un-dimerised $C2/m$ structure. Although the self-interaction error in standard DFT is known to cause overly delocalised wavefunctions, in the current system, standard DFT produces results in dimerised structures that are consistent with powder neutron diffraction. Standard DFT was therefore used for the calculation of the Fermi

contact shifts in this work instead of hybrid functionals which have been adopted in previous studies.[222–224]

3.4 Results and Discussion

3.4.1 Diffraction

In order to verify the phase purity of the samples, simple refinements were performed on a lab diffractometer. These confirmed that no impurity phase was present, with exception of the ^{17}O enriched sample, which contained ~4% RuO_2 by weight. The non-enriched sample was additionally characterised by neutron diffraction in order to verify the presence of lower intensity reflection that confirm Miura's dimerised structure.[212] A neutron refinement was performed. A reasonable fit was achieved but the fit to the lower Q reflections (fig pink box) was poor. Previous studies, in which many synthesis procedures for Li_2RuO_3 were screened, show that there is a strong correlation between synthesis procedures and ordering/disordering of the dimers. The peak widths of reflections with an a-lattice component, i.e. (hkl) where $h \neq 0$, were particularly sensitive to the synthesis conditions as the dimerisation is principally in the a direction (Figure 3.5a), whilst the c-lattice peaks, (001) for example, are less affected.[233] An additional finding was that with longer heating times the a-lattice parameter decreased, driving the ratio $\sqrt{3}a/b$ further from one—the value expected for an undistorted $R\bar{3}m$-like TM layer.[233] The a-lattice parameters for the enriched and non-enriched samples were refined to be 4.9333(7)Å and 4.9372(2)Å respectively with $\sqrt{3}a/b$ ratios of 0.9742 and 0.9739 respectively. These values are close to those reported by Jimenez-Segura et al. for similar synthesis conditions and confirm that the Li_2RuO_3 samples used in this work are representative.[233]

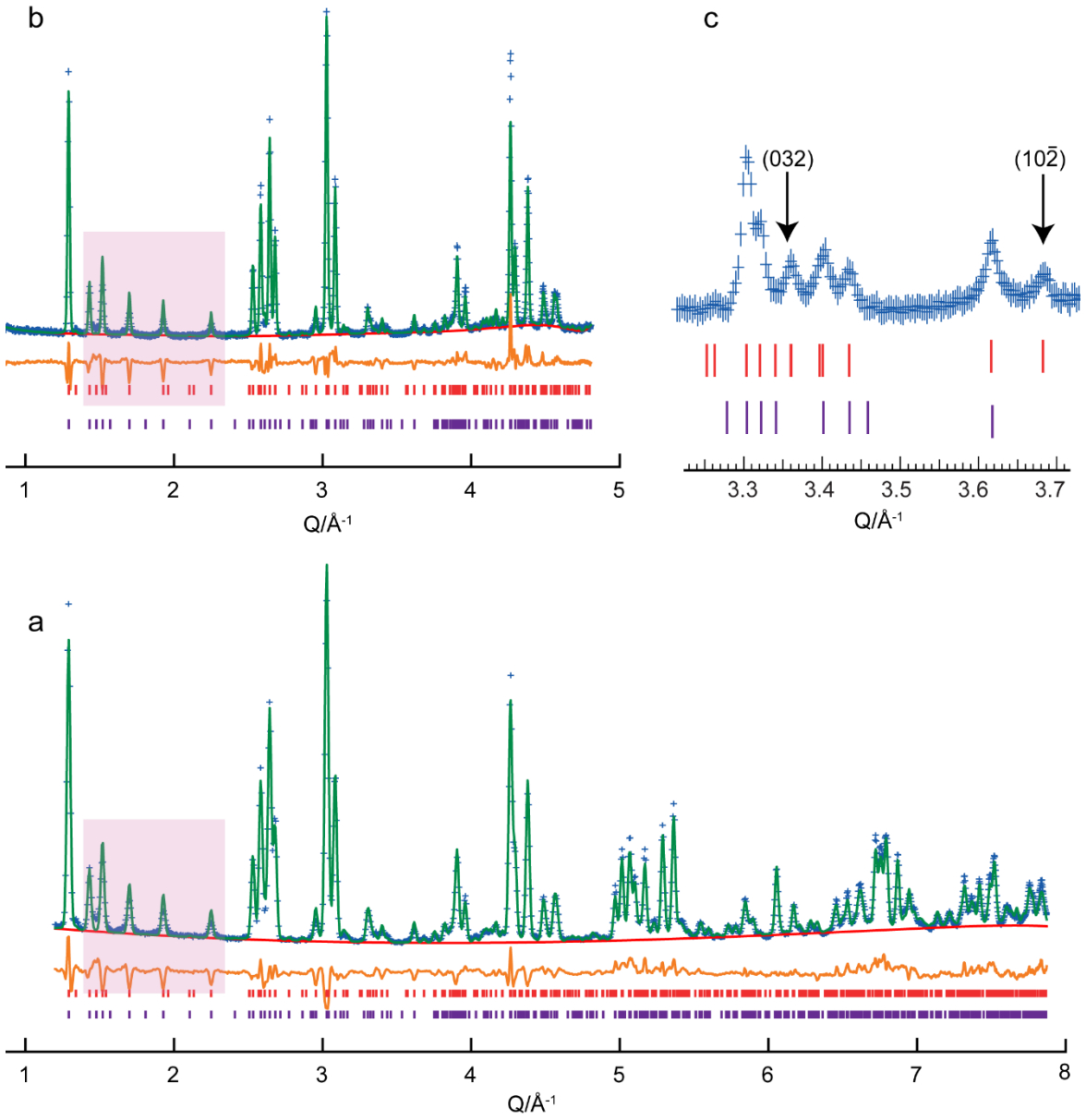

Figure S2.1: Neutron and X-ray diffraction Rietveld co-refinements using $P21/m$ space group. Data recorded at (a) 1.5483 Å and (b) 2.536 Å with curves representing the data (blue), the fit (green), and difference (orange). The tick marks beneath the spectra represent the $P21/m$ space group (red) and the $C2/m$ space group (purple). (c) highlights the reflections missed by the $C2/m$ space group but fitted in the $P21/m$ case as observed by Miura et al.[212] Refined Lattice parameters for Li_2RuO_3 a = 4.937(2) Å, b=8.7768(3) Å, c=5.894(3) Å and β=124.39(5)°.

3.4.2 Magnetic Susceptibility

Field cooled (FC) and zero field cooled (ZFC) susceptibilities were recorded for Li_2RuO_3 (Figure 3.2). Susceptibility (χ) vs T and $1/\chi$ vs T were plotted in order to determine the Curie constant and the Weiss temperature for the sample in the region 100–300 K. There is a kink in both the FC and ZFC curves at 92 K. This is most likely due to a magnetic transition. Above 300 K the susceptibility begins to increase as the transition approaches, therefore this region was excluded from the fitting. The $1/\chi$ vs T plot was fitted in the defined temperature range by minimising the total least squares difference between the experimental data and a curve calculated using the equation $\chi = \chi_0 + \frac{C}{T-\theta}$. The parameters χ_0 (a temperature-independent susceptibility), C (the Curie constant) and θ (the Weiss temperature) were allowed to vary to achieve the best fit and the results are displayed in Table 3.1.

Table 3.1 Calculated magnetic parameters from fitting region between 100-300 K using $\chi = \chi_0 + \frac{C}{T-\theta}$

Parameter	Value (FC)	Value (ZFC)
Curie Constant/K emu mol^{-1}	0.023	0.016
Weiss Constant/K	0	23.8
χ_0 /emu mol^{-1}	0.00056	0.00057
Estimated Moment/ μ_B	0.43	0.36

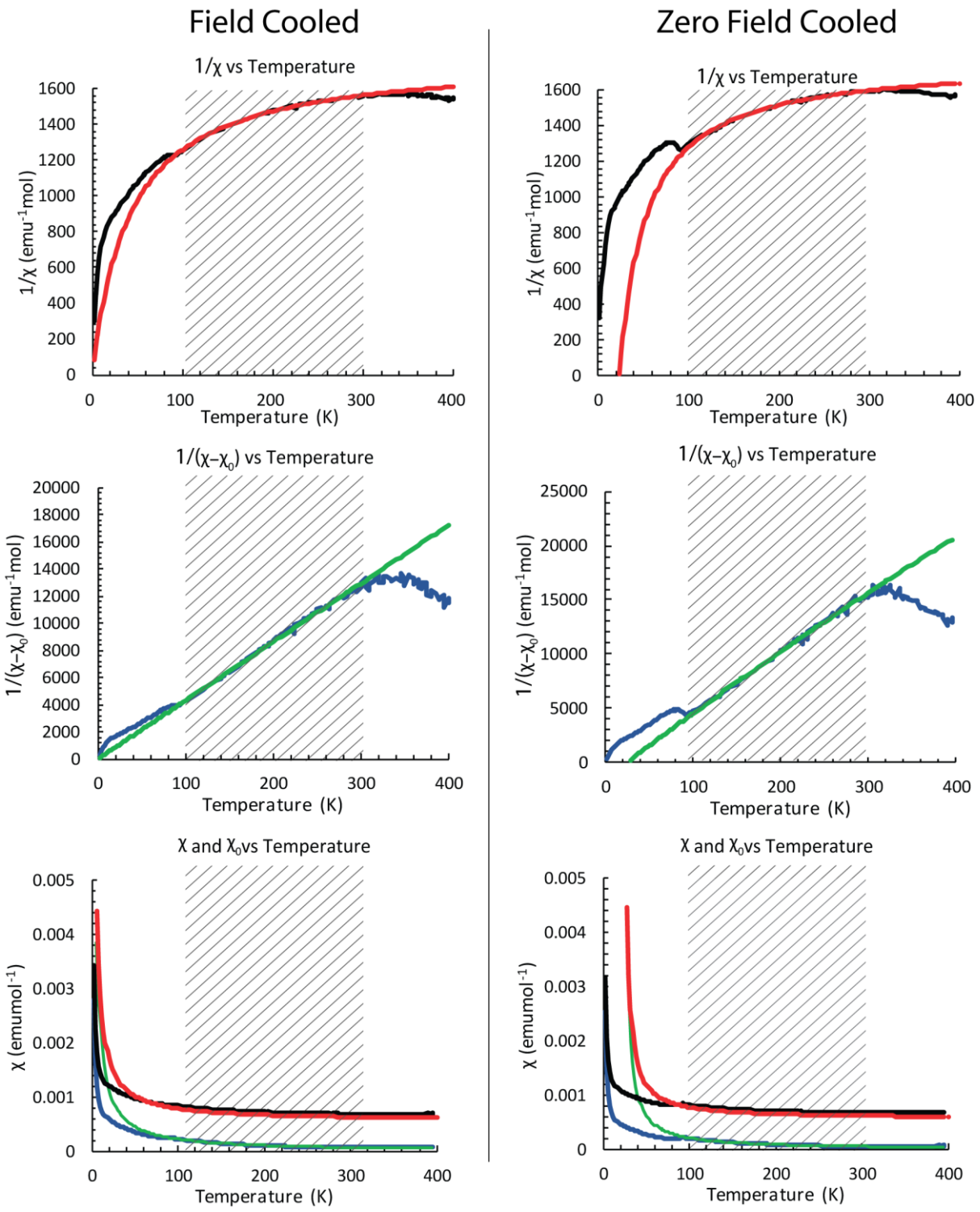

Figure 3.2 Field-cooled and zero-field-cooled molar susceptibility (χ) inverse molar susceptibly vs T plots and the same plots with the temperature independent susceptibility (χ_0, calculated a described in the text) for Li_2RuO_3. The raw data are shown in black and corresponding fit to the data is shown in red. The susceptibility after subtraction of the temperature independent susceptibility ($\chi-\chi_0$) are shown in blue and the corresponding fit to the data in green. The shaded area shows the region that was refined against in the fit.

An effective magnetic moment, μ_{eff}, at room temperature of 0.43 μ_B was determined from the FC measurement, consistent with previous studies and confirming that the number of unpaired electrons per Ru^{4+} ion is far fewer than expected for a low-spin d^4 (S = 1) transition metal[79,212,232]. The origin of this magnetic behaviour is the long-range dimerisation of the Ru which gives a distorted Ru layer (Figure 3.1a). The value of μ_{eff} is even lower than that expected for a S=1/2 ion using the spin only formula ($1.73\mu_B$) consistent with spin-orbit coupling and/or partial coupling of both unpaired electrons.

3.4.3 Electrochemical Characterisation

The efficacy of the material as a Li-ion cathode was tested to ensure that the material performed comparably with literature reports and to observe any changes between the sample enriched in ^{17}O and the sample synthesised by a more conventional method. Charge discharge curves for galvanostatic cycling are shown in Figure 3.3. The capacities and first charge capacity loss are typical of Li-excess materials and are consistent with previously reported results for Li_2RuO_3.[127] The enriched sample shows a slightly lower initial plateau than the regular sample, additionally the capacity on first charge was slightly lower. The lower capacity may be a result of a slightly lower than expected weight fraction of Li_2RuO_3 as the enriched sample contains ca. 4 wt% RuO_2 (which is electrochemically inactive), additionally there is typically more variability in electrode produced in very small batches, as was the case for the enriched material, which may lead to some additional loss. The different voltage profile may be caused in part by to the slower rate at which the enriched material was cycled (C/40 vs C/20 with respect to 1 Li removal). There may also be some effect of the degree of dimer ordering in the pristine material. It has been shown that longer and hotter annealing processes yield a material with greater dimer ordering which might be expected to alter the voltage required for Li extraction.[233] This is a little surprising as, as discussed in section 3.4.1, the $\sqrt{3}a/b$ ratio is similar for both materials. The effects

of an anneal in O_2 gas are not well characterised and may warrant further investigation. The evidence from the diffraction and ^{7}Li NMR, which are extremely similar for both materials indicate that the electrochemical differences between the materials may due to surface and particle size differences, rather than differences in the bulk structure.

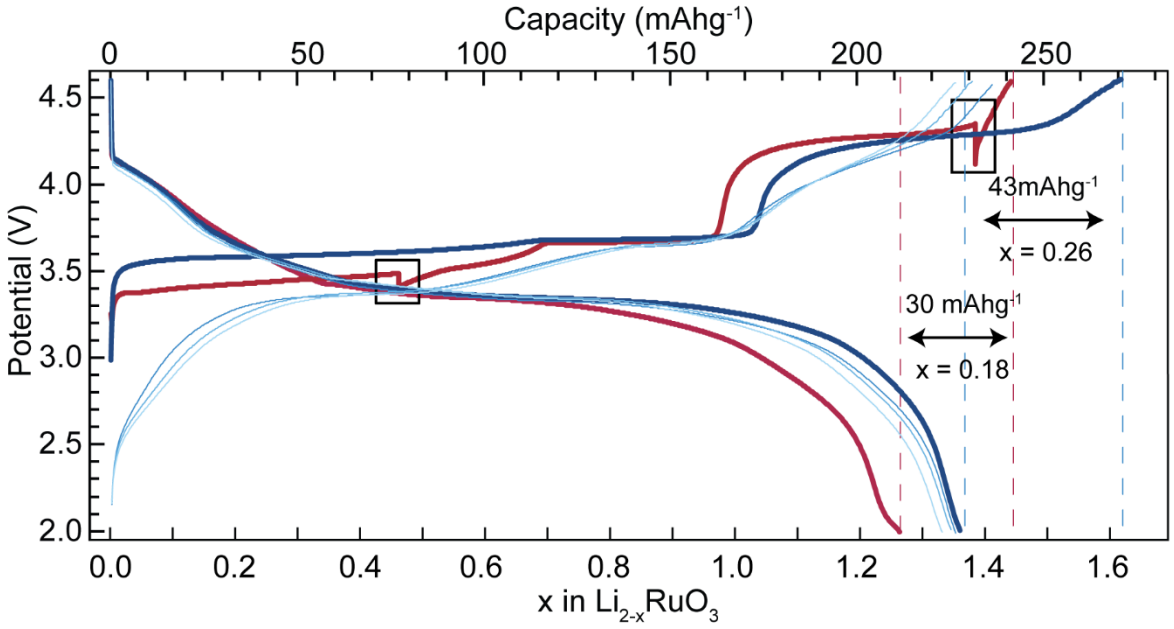

Figure 3.3 Galvanostatic cycling curves for Li_2RuO_3. The red curve shows the charge-discharge profile for the first cycle of the Li_2RuO_3 sample enriched in ^{17}O at a rate of C/40 (with respect to the removal of 1 Li per formula unit). The thick blue curve shows the charge-discharge profile for the first cycle of the Li_2RuO_3 sample synthesised in air as described in section 3.3.1 ^{17}O at a rate of C/20 (with respect to the removal of 1 Li per formula unit); subsequent cycles are shown by the thin and progressively lighter blue lines. During the cycling of the enriched sample cycling was interrupted twice by power outages, these interruptions are highlighted by black boxes.

3.4.4 Room Temperature NMR Spectroscopy:

The room temperature magic angle spinning (MAS) (60kHz) ^{7}Li spectrum was collected and, as observed in previous studies, there are two main resonances centred around 27ppm and one at 47ppm[234,235] (Figure 3.4a). These environments can be modelled with three peaks in a 2:1:1 ratio. The $P2_1/m$ structure has three Li sites in the asymmetric unit: Li1 (2e) in the Ru-layer and Li2 (2e) and Li3 (4f) sites in the Li-layer (Figure 3.1b). The peaks at 25ppm and 31ppm are assigned to Li2 and Li3 based on their similar shifts (they are both Li-layer sites) and their integrated

intensities, which match what is expected from the crystal structure. The 47ppm peak is assigned to the structurally distinct Li1 site which lies in the Ru-layer.

As the paramagnetic (Fermi-contact interaction) contributions to the ^{6,7}Li NMR shift are relatively large, it is reasonable to assume that they are the dominant contributions to the total shift. The overall Fermi-contact interaction can often be understood using a bond pathway approach where the Fermi-contact shift is considered additive: the shift of a site being the sum of all the individual nearest neighbour and next nearest neighbour contributions. This methodology is well established for Li, particularly in the case of octahedral Li, where the sign and size of the shift can be predicted by consideration of the orbital occupation and the Li-O-M bond angle.[152,155]. Regardless of the effect of the dimerization, for Ru^{4+} with localized electrons the expected shift for a 90 ° Ru–Li–O pathway is positive whereas for a 180 ° Ru–Li–O pathway it is expected to be negative[155]. Li1 has only 90 ° pathways to Ru^{4+} whereas Li2 and Li3 have both, therefore it is reasonable to assign the more positive shift to Li1.

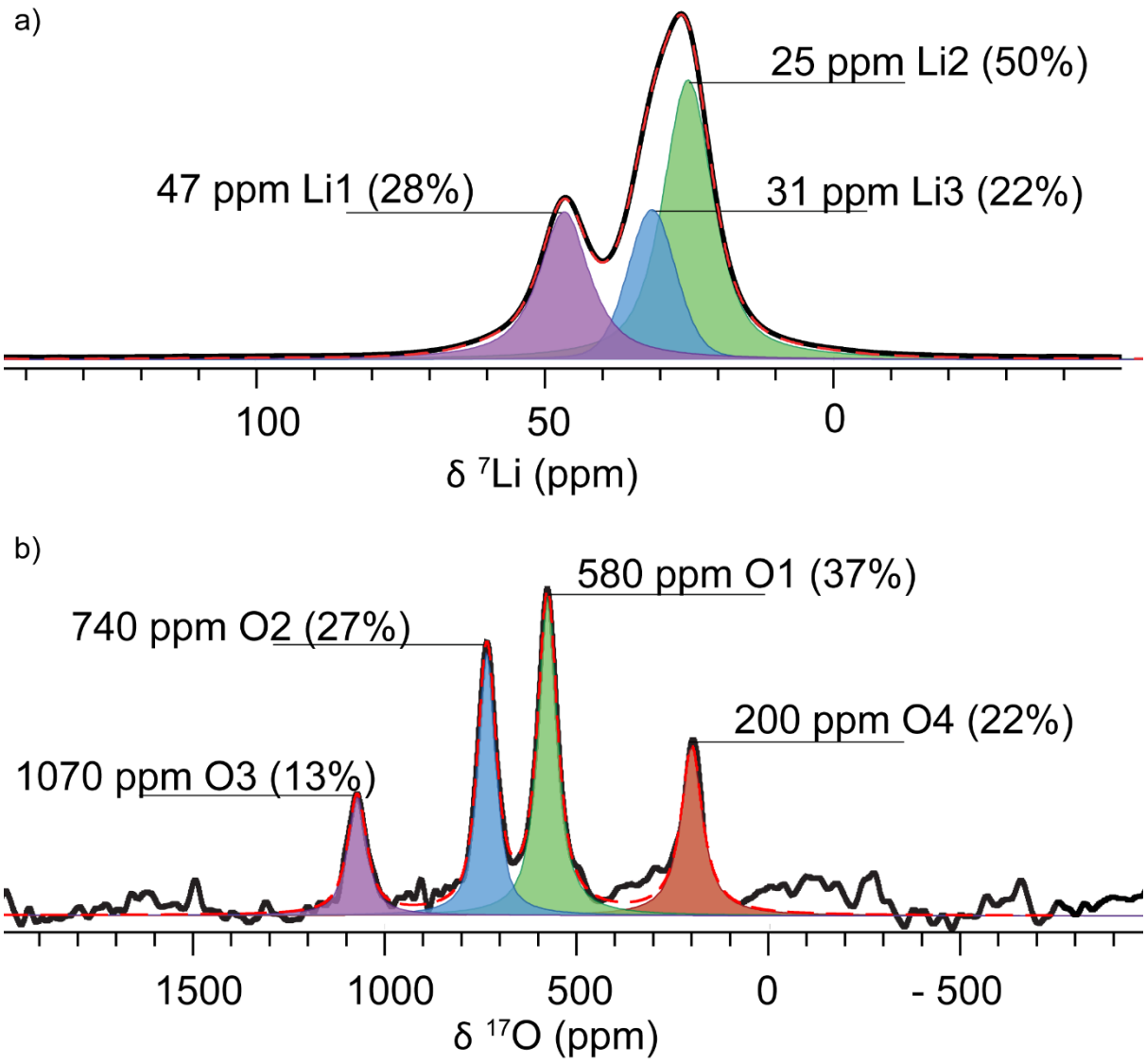

Figure 3.4 ^{7}Li MAS NMR (a) and ^{17}O MAS NMR spectrum (b) of Li_2RuO_3 at room temperature. Peaks fitted and labelled with their shift, assigned site and relative integrated intensity (in brackets). Experimental spectra are in black. Fit to the data is shown by the red dashed line.

The observed ^{7}Li shifts (and corresponding bond pathway contributions) are noticeably lower than those caused by the (S=3/2) Mn^{4+} ions in the structurally related material Li_2MnO_3, which are on the order of 750 and 1500ppm for the Li and TM layers respectively.[100] This is consistent with a reduction in the number of unpaired spins in Ru^{4+} due to dimerization, as discussed in greater detail below, and the lower magnetic susceptibility of Li_2RuO_3: for Li_2MnO_3 the effective magnetic moment is close to the spin only value of 3.85 μ_B (3.56 μ_B and 3.43 μ_B for in plane and out of plane moments

respectively[236]) much larger than the measured effective moment for Li_2RuO_3 of 0.43 μ_B.

The ^{17}O NMR spectrum of ^{17}O-enriched Li_2RuO_3 displays 4 distinct O shifts at 200, 580, 740 and 1070ppm (Figure 3.4b). The ratio of these shifts is approximately 1:2:2:1, which is in line with the expectation from the $P21/m$ crystal structure which contains four oxygen sites (Figure 3.1a). This is in contrast to the $C2/c$ and $C2/m$ structures which contain only 3 O sites with an expected ratio of 1:1:1. ~4% RuO_2 was observed by XRD in the enriched sample but was not observed in the NMR spectrum of this sample, presumably because of its low concentration. The ^{17}O NMR shift of RuO_2 is known (917ppm)[237] and the RuO_2 impurity can be observed in samples with a greater weight percentage of RuO_2 .

3.4.5 First Principles Calculations

In order to assign the ^7Li and ^{17}O NMR resonances of Li_2RuO_3 and provide further insight into the electronic structure and magnetic properties, first principles calculations were performed. The DFT optimized $P2_1/m$ structure previously reported by Kimber et al. [215] was first used to calculate the unpaired spin density at the nuclear positions of ^7Li and ^{17}O. In addition to this structure, in which the dimers are arranged in an "armchair" configuration, spin densities that result from the previously reported[215] $C2/m$ (parallel) dimer structure and un-dimerized $C2/m$ (uniform) structure were also calculated for comparison (Figure S5.2). As discussed by Kimber et al. calculations with the $P2_1/m$ structure lead to a 0 K structure with an unpaired spin density corresponding to approximately S = $\frac{1}{2}$; the density of states plots qualitatively reproduce the MO diagram shown in Figure 3.6c but with close-to-equal occupation of the π^* and δ^* orbitals imply quasidegeneracy of these orbitals.

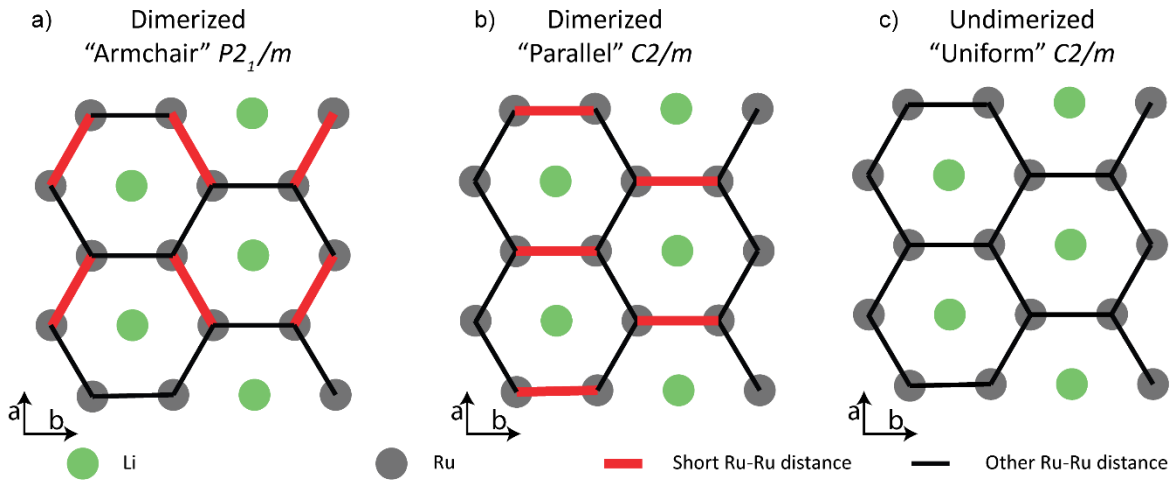

Figure 3.5 Schematic representation of the Ru layer in the three different calculated structures. a) The "armchair"-like ordering of the Ru–Ru short bonds (dimers) with the $P2_1/m$ unit cell, b) another possible ordering with the dimers arranged "parallel" to one another with the C2/m unit cell and c) an undimerized "uniform" C2/m structure.

As detailed in previous reports[222,223,227] the Fermi contact NMR shift, δ_{iso}, is related to the hyperfine coupling constant A_{iso}, by:

$$\delta_{iso} = \frac{10^6 A_{iso} \Phi(\mathrm{T})}{2h\nu_0} \tag{3.1}$$

Where ν_0 is the Larmor frequency, h is Planck's constant and $\Phi(\mathrm{T})$ is a temperature dependent scaling factor (discussed further below). A_{iso} is related to the unpaired spin density at the nuclear position, $\rho(0)$, by:

$$A_{iso} = \frac{2}{3S}\mu_0\mu_B\mu_N g_e g_I \rho(0) \tag{3.2}$$

Where μ_0, μ_B, μ_N, g_e and g_I are the vacuum permeability, Bohr magneton, nuclear magneton, free electron g factor and nuclear g factor and S is the formal electron spin, respectively. If the magnetic susceptibility adopts Curie–Weiss behaviour, the temperature-dependent scaling factor, $\Phi(\mathrm{T})$, in Equation (3.1 is given by:

$$\Phi(\mathrm{T}) = \frac{B_0\mu_{eff}^2}{3k_B g_e \mu_B (T-\theta)} \tag{3.3}$$

Where B_0 is the external NMR field and T is the temperature. μ_{eff} and θ are the effective magnetic moment and Weiss constant, respectively, determined from magnetic susceptibility measurements.[222] The unpaired spin density, $\rho(0)$, can be directly computed with nominally 0 K DFT calculations in the ferromagnetic state and scaled into the paramagnetic regime of experimental NMR measurements using equations 3.1-3.3.

It is necessary to calculate a scaling factor in order to derive an ambient temperature Fermi contact shift, from the calculated unpaired spin densities of the 0K structure, which correspond to a perfect ferromagnetic alignment of all the unpaired spins. In most cases, the ferromagnetic ground state predicted by DFT has formal spin that is simply determined by the oxidation state of the TM ions. Here, however, due to the dimerization this is no longer trivial. As stated above, the calculated 0K structure has S=1/2 per Ru^{4+}, whereas the experimental effective moment suggests S<1/2. The experimental effective magnetic moment is used here to scale the 0K unpaired spin density (equation 3.3) in order to account for this. The unpaired spin densities, calculated Fermi-contact shifts and experimental shifts are compared in Table 3.2

3.4.6 Discussion of Room Temperature Experimental NMR Shifts

In the case of Li, each calculated structure gives unpaired spin densities, which qualitatively reproduce the experimental spectrum and the relative sizes of the shifts. The Li1 site in the $Li_{1/3}Ru_{2/3}$ layer has essentially twice the unpaired spin density of the Li2 and Li3 sites in the Li layer and the multiplicities of these sites give the observed peak ratios. The calculated unpaired spin densities are much lower for either of the dimerized structures, the fit being better for the $P2_1/m$ vs. $C2/m$ structure (which predicts a larger difference between the Li2 and Li3 shifts than seen experimentally). However, the Li NMR results do not unambiguously prove that the structure is dimerised.

In contrast, the calculated oxygen shifts can offer more insight. The magnitude of the unpaired spin density at the nuclear position of the four O sites (Table 1) in the $P2_1/m$ structure is $\rho_{O4} \leq \rho_{O1} \leq \rho_{O2} \leq \rho_{O3}$, which is in good agreement with the observed ^{17}O NMR spectrum, where we observe four peaks with the expected 1:2:2:1 intensity ratio. Both the $C2/m$ structures only have two O sites and thus only two ^{17}O resonances would be expected. Although the Fermi-contact interaction generally dominates the NMR shifts of paramagnetic solids, there will also be a contribution from the chemical shift, which could be significant in the case of ^{17}O, particularly in this system where S<1/2: the ^{17}O resonances of Li_2TiO_3, which is isostructural to undimerized Li_2RuO_3, and Li_2MnO_3, has large ^{17}O chemical shifts of 372.3 and 409.8 ppm.[238] Thus, while the large differences between the observed Li_2RuO_3 resonances are ascribed to the differences in the Fermi-contact shifts, the systematic under prediction of the experimental shifts in the DFT calculations is ascribed at least in part to the chemical shift, which on the basis of the Li_2TiO_3 shifts may contribute as much as 400 ppm to the overall shift. There is another more subtle point: on initial inspection it may appear that the magnitudes of the ^{17}O spin densities of the $C2/m$ S=1 non-dimerized structure, which are approximately double the $P2_1/m$ spin densities, might yield shifts closer to the experimental shifts. This ignores the scaling factor ($\Phi(T)$) needed to convert the 0K structure to the room temperature Fermi-contact shift. If the predicted effective magnetic moment that arises from the S = 1 $C2/m$ structure is accounted for, this leads to predicted shifts that are much larger than the observed shifts. A similar phenomenon is responsible for the much larger Fermi contact shifts seen for the S = 3/2 Li_2MnO_3 material. The previously reported spin densities for Li_2MnO_3 (calculated using hybrid functionals rather than standard DFT)[101] are actually smaller (3.7-14.2$\times 10^{-3}\rho(0)$) than those calculated for Li_2RuO_3, highlighting the important role that the reduced susceptibility plays in the comparatively small NMR shifts of Li_2RuO_3.

Table 3.2 Unpaired spin density at the ^{7}Li and ^{17}O nuclear positions from DFT calculations for the various proposed Li_2RuO_3 structures. The calculated room temperature shift for the $P2_1/m$ structure (obtained assuming the experimentally determined magnetic susceptibilities) is compared with the experimental NMR shift values.

	Unpaired Nuclear Spin Density $1 \times 10^{-3}\rho(0)$ $(1/a_0^3)$			Calculated Fermi-contact Shift (ppm)	Observed Shift (ppm)*
Site	$P2_1/m$ (armchair)	$C2/m$ (parallel)	$C2/m$ (uniform)	$P2_1/m$ (armchair)	
Li1	3.14 (2e)	2.18 (2a)	7.23 (2a)	23	47
Li2	1.48 (4f)	0.93 (4h)	4.32 (4h)	11	25
Li3	1.71 (2e)	1.47 (2d)	4.54(2d)	13	31
O1	26.4 (4f)	33.6(8j)	76.9 (8j)	197	580
O2	47.6 (4f)	49.9 (4i)	70.3 (4i)	355	740
O3	69.9(2e)	-	-	521	1070
O4	9.4 (2e)	-	-	70	200

*Observed shift includes contributions from both the Fermi-contact and chemical shifts.

Further insight into the causes of the different spin densities and Fermi contact shifts of the four resonances can be obtained by analyzing the structure and Ru–O/Ru–Ru bonding in more detail. The unpaired electrons in the low-spin d^4 Ru^{4+} ions are found in the t_{2g} symmetry orbitals; these valence electrons are normally considered non-bonding in an octahedral complex but within the $P2_1/m$ dimerized structure form covalent bonds along the Ru-Ru short distances (Figure 3.6a), the strong σ type overlap between the d_{xy} orbitals being the main driver for dimerization. This d_{xy}–d_{xy} hybridisation was calculated by Kimber et al. to cause a large bonding-antibonding split of >2 eV.[215] This strong interaction effectively removes two unpaired electrons from the Ru–Ru pair leaving six electrons to populate the remaining orbitals. By forming appropriate linear combinations of the other t_{2g} orbitals (d_{xz} and d_{yz}) π and δ type overlaps are also possible (Figure 3.6c and d). If the energy gap between the π* and δ* orbitals were large enough to overcome the electron pairing energy, an S = 0 ground state would be formed with filled π, δ and π* and empty δ* orbitals. DFT calculations by other authors suggest that the π* and δ* orbitals are in fact very close in energy so that they can be considered quasidegenerate[239]. This would lead to a

ground state with one unpaired electron per Ru^{4+} with the unpaired electrons primarily contained in the π* and δ* antibonding orbitals of the Ru–Ru bond. The effective magnetic moment of 0.43 μB indicates that the average number of unpaired spins may be lower than one with a degree of electron pairing in the π* orbital; nonetheless, the unpaired spins will still reside in the π* and δ* orbitals.

In an undistorted octahedron the spin transfer expected from a t_{2g} orbital to the M–O–Li pathway is symmetric and positive (Figure 3.6f)[155], however due to the dimerization and lifting of the degeneracy of the t_{2g} orbitals, the t_{2g} spin transfer pathway, is different for each of the Ru–O bonds and not all the t_{2g} orbitals contribute equally to the spin transfer. By analogy with bonds formed in C–C molecules, the π* and δ* orbitals, which contain the most unpaired electron density, comprise lobes which mostly point away from the Ru–Ru dimers. The spatial extent of the π* and δ* orbitals is largest for the oxygen that are in the plane of and pointing away from the Ru–Ru dimer i.e. "outward" pathways (Figure 3.6h). Following the hypothesis that more effective overlap with the O 2p orbitals will lead to larger induced shifts, the shift caused by each pathway should increase in magnitude from smallest to largest: inward, axial, outward (Figure 3.6). As the d_{xy} orbital forms the σ bond of the dimer it does not contribute significantly to the hyperfine shift as the electrons it contains will be paired. This σ bond is extremely energetically favourable and therefore for the purpose of rationalising the spin transfer and the NMR spectra the d_{xy} orbitals can be considered inactive.

Each oxygen site has two Ru neighbours and for each Ru neighbour each oxygen has two p orbitals of the correct symmetry to form p–d π pathways. By examining the connectivity of the four sites (Table 3.3) and considering their relative intensities it is possible to rationalize the magnitude of each of the observed shifts. O3 is a 2e Wyckoff site with the most outwards pathways (Table 3.3) and so is assigned to the peak at 1070ppm. O2 has the next most outwards pathways and is a 4f site, consistent with

the greater intensity of the 740ppm peak. The second 4f site (O1) is assigned to the 580ppm peak and finally O4 is assigned to the 200ppm peak. These assignments are consistent with the DFT calculations. The contribution of polarisation of the O(2p)–Ru(eg*) hybrid orbital should contribute a small negative shift (section 1.7.1), however the shifts arising from delocalisation are typically larger and this polarisation mechanism is likely to be the same for all O regardless of their geometry.

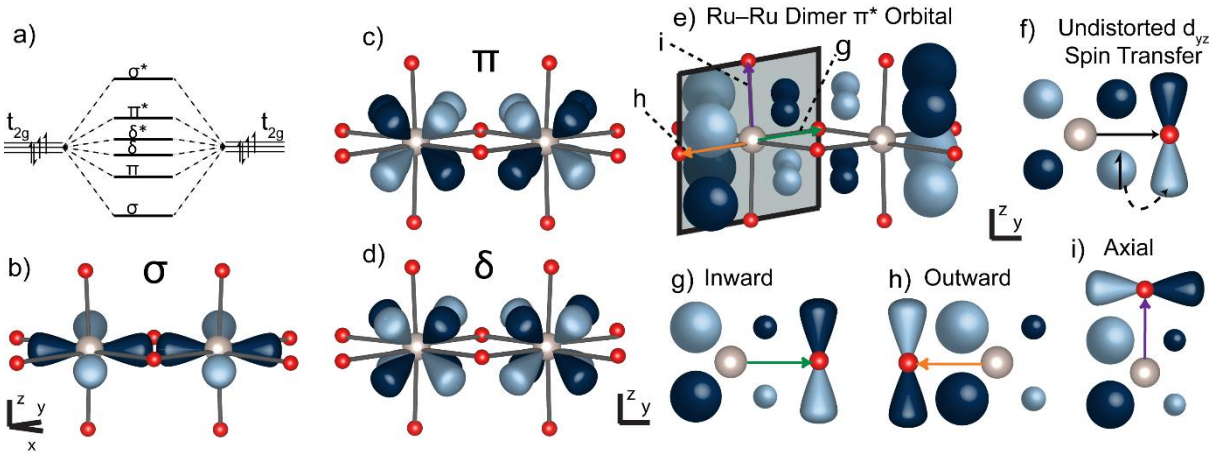

Figure 3.6 (a) Cartoon showing the energy levels expected for a Ru–Ru dimer. (b) The strong σ-type overlap between the d_{xy} orbitals. (c) The π type bonding that is possible by the in-phase overlap of the π symmetry combination of the d_{xz} and d_{yz} orbitals. (d) The δ type bonding that is possible by the in-phase overlap of the δ symmetry linear combination of the d_{xz} and d_{yz} orbitals; out of phase combinations give rise to the σ*, π* and δ* molecular orbitals. (e) Visualisation of the π* orbital showing the distortion of the paramagnetic electron's wavefunctions; the δ* orbital is not shown but would have qualitatively identical shape. (f) Schematic of spin transfer from an undistorted partially occupied t_{2g} d orbital to the O 2p orbital: The M and O orbitals are of the correct symmetry to form a spin orbital and hence the polarisation of the t_{2g} electron is transferred to the whole M–O pathway giving a positive shift. (g), (h) and (i) show the effect of the distortion on the spin transfer pathways for each of the possible Ru–O bonds around the dimer. Each of (g), (h) and (i) are labelled on (e), in order to show their position relative to the dimer axis.

Table 3.3 Number of each type of O-Ru bond pathways for each O site.

Site	Wyckoff Symbol	Observed Shift (ppm)	Number of d–p π-Type Overlaps			
			Outwards	Axial	Inwards	Inactive
O1	4f	580	0	0	2	2
O2	4f	740	1	2	0	1
O3	2e	1070	2	0	0	2
O4	2e	200	0	4	0	0

3.5 Variable Temperature NMR Studies

The phase transition in Li_2RuO_3 can be probed using variable temperature NMR. In the case of both the ^7Li and ^{17}O NMR spectra, the peaks move to higher shifts on increasing the temperature; this is contrary to what is normally observed for Fermi-contact shifts of paramagnetic systems in the Curie-Weiss regime, where a decrease in shift with temperature is generally seen. In the initial stage of heating, this can be ascribed to the increase in the number of unpaired spins before the phase transition due to thermal fluctuations and the increased occupations of higher energy δ^* states; in the magnetometry data the susceptibility rises slightly above 300K (Figure 3.2). Above the phase transition the sharp rise in the susceptibility is accompanied by a sharp increase in the size of the observed shifts as expected[212].

In the case of ^7Li (Figure 3.7), the signal is lost as the critical temperature (of the phase transition) is reached. This is attributed to fluctuations, either electronic or magnetic, on the NMR timescale that occur at the onset of the phase transition and which cause very rapid spin-spin (T_2) and/or spin-lattice (T_1) relaxation such that coherence is lost during the echo delay. A similar loss of ^7Li signal has been observed in partially delithiated $LiCoO_2$ and low Ni/Mn content NMCs before they undergo their metal-insulator transitions (MIT).[29,161] In Li_2RuO_3, as the critical temperature is approached and the dimers increasingly break up, more localised and unpaired 4d t_{2g} electrons are formed. Rapid nuclear relaxation is caused by slow electronic relaxation times (T_{1e}s) of these unpaired electrons on a timescale similar to that of the electron-nuclear coupling. As the temperature increases, the fluctuations increase, the T_{1e}s decrease, (the system becomes increasingly paramagnetic) and the nuclear relaxation times increase, and Li signal is again observed. Unfortunately, due to hardware constraints, the MAS frequency attainable at very high temperatures is quite low, which hinders

unambiguous assignment of the isotropic resonances. On the basis of the high temperature structure reported by Miura et al.[126] which has three Li sites which are broadly similar to the room temperature structure, our tentative assignment is that two similar resonances occur at ~135ppm (Li in the Li layer) and a second broader resonance is present from 300-500ppm (Li in the TM layer). Figure 3.8a shows the spectrum of Li_2RuO_3 at 410 °C for 4 kHz and 3.5 kHz MAS frequencies. The peak at 135 ppm is static despite the change in MAS frequency. It is expected that the isotropic resonance should occur at the centre of gravity of the pattern however it does not. The entire spectrum lies within the excitation width of the pulse meaning it is unlike another unresolved resonance is responsible for this. For this reason and the fact that the crystal structure always contains two distinct types of Li sites (Li layer and Ru layer sites) it is expected that there is another resonance which occurs under the sidebands of the main resonance between 300–500ppm but that this is broader and not observed clearly.

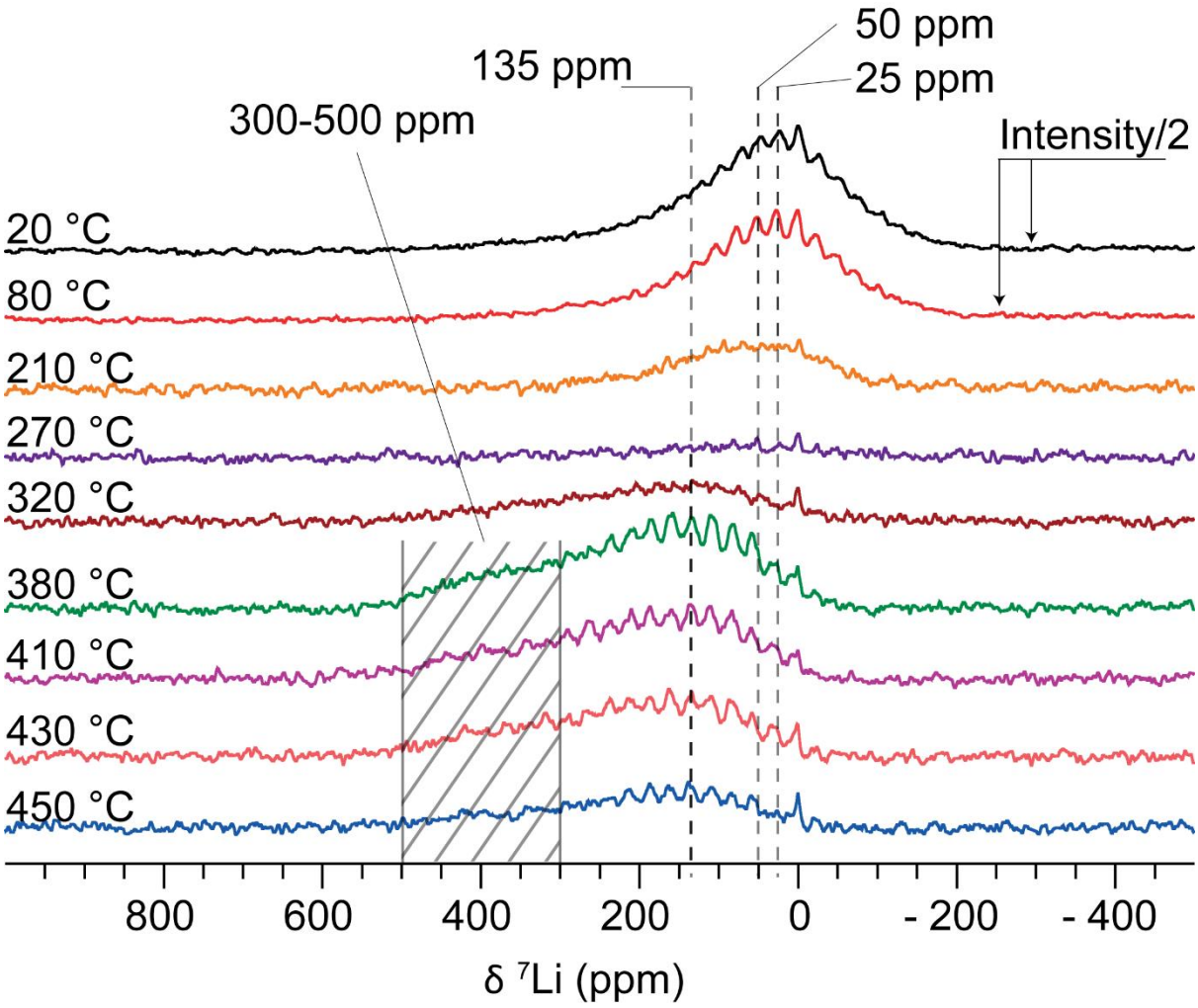

Figure 3.7 High temperature ^{7}Li NMR spectra of Li_2RuO_3. Isotropic resonances are indicated with their shifts; the additional peaks are spinning sidebands. The hashed area indicates the region in which the second peak in the high temperature spectra is expected but for which no sharp resonance is observed.

Although broadening of the ^{17}O resonances is seen at the phase transition and above, they never vanish completely and the spectra were more easily acquired and tracked through the phase transition (Figure 3.9). Using variable offset cumulative spectra (VOCS) collected with an automatic tuning/matching robot[173], the full bandwidth of the spectrum of the more strongly paramagnetic oxygen can be captured. At 220°C, before the onset of the phase transition there are two isotropic ^{17}O resonances at ~1180ppm and ~820ppm. These evolve steadily to 1500ppm and 1100ppm respectively, at 260°C. These intermediate temperature spectra are more typical of paramagnetic O

and the broadening points to a loss in the distinct identities of the O sites as the phase transition approaches along with broadening due to increased T_{1e}s of the Ru 4d electrons. Above the phase transition, the resonances shift further to ~2300ppm and ~2150ppm and broad manifold of well resolved spinning sidebands are observed. Although the calculated un-dimerized 'uniform' structure is not a good representation of the true high temperature structure, which is an intrinsically dynamic system in which short Ru–Ru distances persist, it can give some insight into the assignment of the high temperature NMR. Without calculating the shifts, qualitative comparison of the unpaired spin densities suggest that the peaks can be assigned to the two oxygen sites with Wyckoff positions 8j (~2300ppm) and 4i (~2150ppm) in the high temperature $C/2m$ structure. This is in agreement with the relative magnitudes of the shifts for 8j and 4i sites in Li_2MnO_3.[101] The presence of only two resonances suggests that the average local structure experienced by the O is consistent with the $C/2m$ structure and that the dimerisation above the transition is dynamically averaged on the NMR time scale.

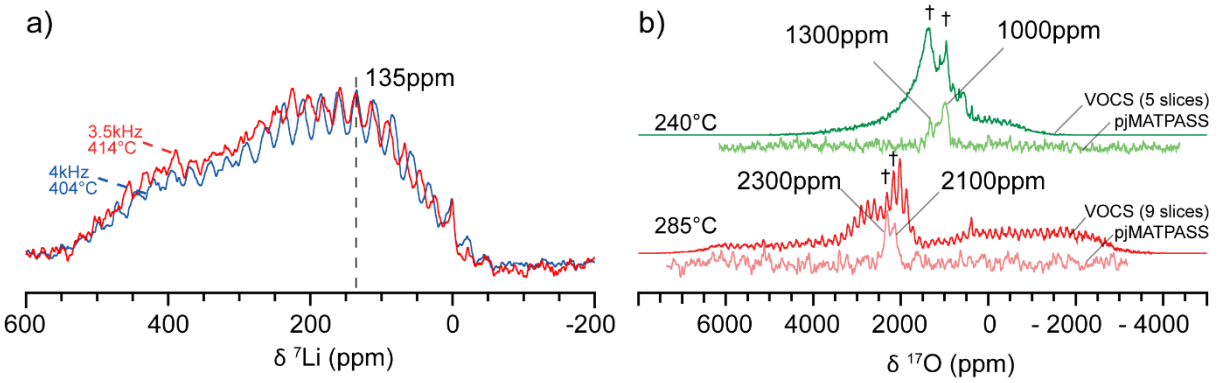

Figure 3.8 Spectra aiding the assignment of the isotropic resonances at high temperature. a) ^{7}Li NMR spectra recorded at ~410 °C for Li_2RuO_3 at 3.5 kHz (red) and 4 kHz (blue). The only clearly unchanged resonance is the one at 135 ppm. The recorded temperatures for each spectrum immediately before ^{7}Li acquisition were 404 °C and 414 °C for 4 kHz and 3.5 kHz, respectively. b) Comparison of isotropic resonances from pj-MATPASS experiments shown with the full VOCS spectra for the high temperature ^{17}O NMR experiments. Isotropic resonances are indicated with daggers and the shifts of the pj-MATPASS peaks indicated.

The more significant broadening seen for ^{7}Li rather than ^{17}O is tentatively ascribed to the orientation of the t_{2g} orbitals which point directly towards Li but not towards O, allowing a direct overlap with the Li 2s orbitals. Interestingly the 740ppm peak (O2) has the shortest spin-lattice relaxation (T_1) (10ms vs ~200ms for the other sites) at room temperature and has a steeper rise in shift with temperature. The reason for this may lie in the nature of the thermal fluctuations that lead to the phase transition. Each O site has only one $Ru(t_{2g})$–$O(2p)$–$Ru(t_{2g})$ connection which plays a role in the magnetic interactions between the Ru^{4+} ions, O2 joins the strongly bonded and spin paired σ orbital of one Ru^{4+} to partially spin unpaired π* and δ* orbitals on a second Ru^{4+}, whereas the other O sites link orbitals with the same occupation (i.e. σ↔σ and π*/δ*↔π*/δ*). This unique connectivity may cause O2 to be more sensitive to an

increase in the number of unpaired spins and changes in their electronic relaxation times, induced by the thermal excitations.

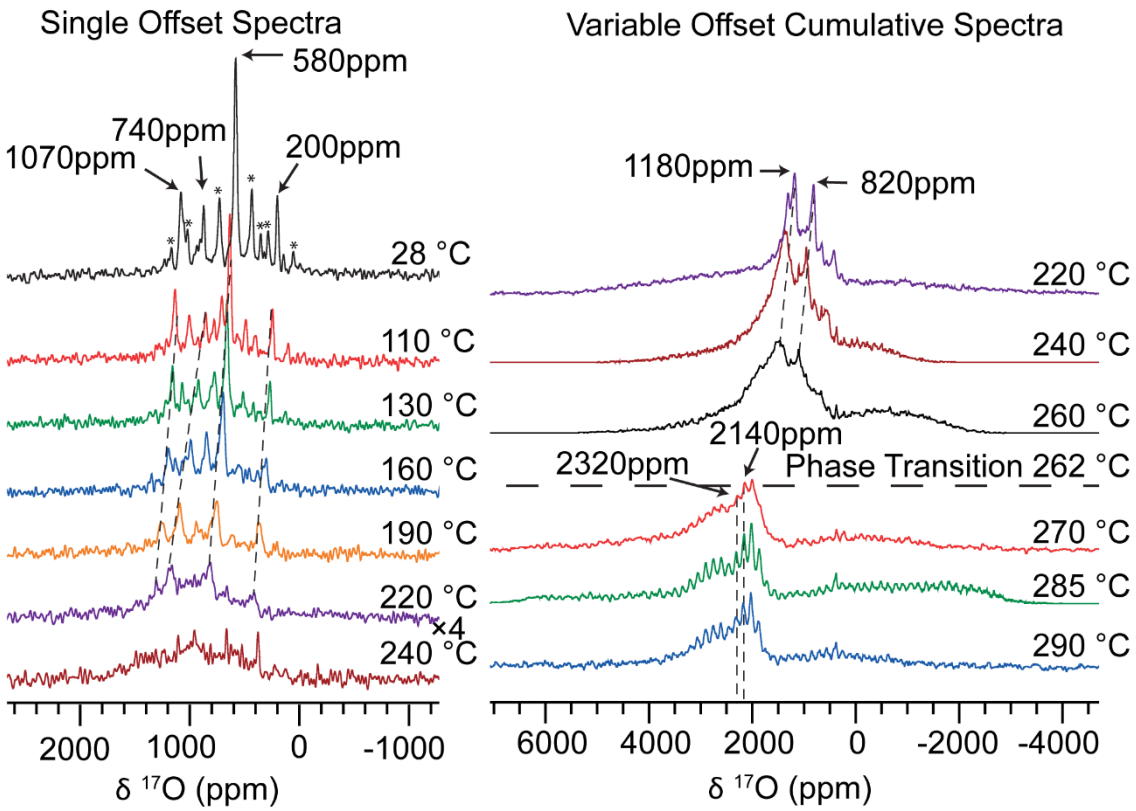

Figure 3.9 High temperature MAS NMR ^{17}O spectra of Li_2RuO_3. Isotropic resonances and their evolution with temperature are labelled with dashed lines. Other peaks are spinning sidebands. Single offset spectra are recorded with a quantitative recycle delay (75 ms). The T_1 is reduced as the temperature rises so the variable offset spectra were recorded using a shorter but still quantitative recycled delay (5ms).

3.6 Conclusions

In summary, the nature of the local structure and phase transition in Li_2RuO_3 have been determined from ^7Li and ^{17}O NMR supported by density functional theory, bonding analysis, and neutron diffraction. These data confirm that the room temperature structure contains four distinct O sites; this is in good agreement with the previously reported but often overlooked $P2_1/m$ structure and our DFT computed shifts. The size of the O hyperfine shifts can be rationalized when the Ru dimerization

is accounted for: bond pathway analysis, well established for the analysis of the spectra of paramagnetic battery materials,[155] must be extended to account for the complicated local structure. Careful analysis of both the spin densities and magnetic susceptibilities is required in order to make accurate predictions of hyperfine shifts. The much larger hyperfine shifts observed above the transition temperature for both nuclei show that the unpaired electron density expected on Ru^{4+} is largely quenched in the room temperature structure. Of note, by comparing the experimental and DFT-derived results we show that although the unpaired spin densities seen for Li_2RuO_3—even in the dimerized state—are larger than those of the related material Li_2MnO_3, despite the smaller number of unpaired spins, the susceptibility of Li_2MnO_3 results in a noticeably larger hyperfine shifts at room temperature.

It is common practice to use NMR shifts derived from model compounds such as Li_2RuO_3 to help rationalize spectra of other compounds of interest for example Sn doped and delithiated Li_2RuO_3.[234] Here we demonstrated that the room temperature structure of pristine Li_2RuO_3 may not always be the most appropriate model compound with which to help rationalize the NMR spectra of Ru^{4+} substituted materials: a more careful analysis of how substitution affects long range ordering is required. The high temperature phase may provide a more appropriate model for this type of analysis and we hope that the shifts observed here will prove useful in interpreting spectra from other systems and samples relevant to understanding the electrochemical functioning of these materials. The extension of the highly versatile bond pathway approach to rationalize the NMR shifts of ^{17}O is a significant step towards using this challenging nucleus effectively to understand delithiated Li-ion battery cathodes, which is a development that is highly anticipated by the battery community. The results highlight that TM-TM interactions should not be ignored in the case of 4d and 5d TM containing compounds, particularly in the case of anionic redox cathode materials, as their effects on the oxygen lattice are non-trivial. The insights gained about pristine

Li_2RuO_3 and the tools developed to help interpret the by ^{17}O and ^{7}Li NMR spectra will be extended, in the next chapter, to study Li_2RuO_3 on delithiation.

Chapter 4: Electronic and Local Structure Changes of Li_2RuO_3 on Delithiation Using ^{17}O and ^{7}Li NMR Spectroscopy

4.1 Abstract

Li_2RuO_3 is a key model compound in the study of Li-excess materials and their anionic redox processes. The demonstration of reversibility of these anionic processes has motivated many studies with the hopes of opening new frontiers for high capacity cathode design. The complex electronic and structural behaviour of Li_2RuO_3 on discharge, is intrinsically tied to its operation as cathode material. Using a multinuclear (^{7}Li and ^{17}O) NMR approach, with complimentary diffraction and magnetic characterisation, details of these subtle behaviours are revealed. The dimerisation, which plays a crucial role in the pristine material, is shown to be largely preserved throughout the charging. Using variable temperature measurements and comparisons to Li_2RuO_3 above and below its dimer-solid to dimer-liquid transition, the observed spectra can be characterised as arising from an electronic structure in which the majority of electrons are spin paired and where unpaired spins can be thermally excited.

4.2 Introduction

Li_2RuO_3 is an important model compound for understanding the Li-excess family of materials. As discussed in the previous chapter, the properties of the pristine material are more complex than is generally assumed. A similar approach to that used in Chapter 3 has been adopted in order to probe the changes that occur on electrochemical

cycling. Whilst Li_2RuO_3, with its single $Ru^{4/5+}$ redox couple and well-defined honeycomb TM ordering, is an attractive model compound, the Ru–Ru interactions and the series of two phase reactions it undergoes on first charge make it behaviour more challenging to interpret

Previous authors have shown that on the first charge Li_2RuO_3, exhibits three plateaus each indicative of a two-phase reaction. There are three phases present during delithiation. Naturally the first is the pristine material (phase 1) discussed in detail in Chapter 3. Phase 2 is reported to form with the approximate composition $Li_{1.4}RuO_3$ and is structurally similar to phase 1, with the same space group and only small differences in the lattice parameters (Table 4.1).[129] The total slab height—i.e. the distance between the O ions on either side of 1 TM and 1 Li layer (Figure 4.1)—increases slightly in line with the increased layer separation generally observed for layered Li ion battery materials on initial delithiation.[64]). The second plateau, which occurs at ca. 3.67 V, corresponds to a second two-phase reaction in which phase 2 is transformed into phase 3. The composition of phase 3 has been estimated to be $Li_{0.9}RuO_3$.[129] This is a more dramatic transition with literature reports suggesting the formation of an $R\bar{3}$ phase and involving a rearrangement of the O sublattice, with a transformation from cubic close packed (ccp) to a hexagonal close packed (hcp) arrangement (Figure 4.1).[128,129,240] After this, delithiation continues via a solid solution type reaction until the end of charge with a final composition down to around x = 0.2, in the most delithiated examples.[240,241]

The redox behaviour of Li_2RuO_3 and particularly its Sn and Mn substituted analogues has been studied extensively. During the initial period of charge, steady evolution of the Ru K-edge XANES is indicative of $Ru^{4+} \rightarrow Ru^{5+}$ oxidation, in both Li_2RuO_3 and its Mn and Sn substituted analogues.[127,132,240] The capacity beyond this point ($>168mAhg^{-1}$ or 1 Li per formula unit for Li_2RuO_3) has been attributed to O activity. For $Li_2Ru_{0.5}Sn_{0.5}O_3$ XPS supports the $Ru^{4/5+}$ oxidation during the low region (the $Ru3d_{5/2}$

binding energy increases by −0.7 eV up to 4V), upon charging to through the high voltage region, the binding energy shifts back slightly.[132] Similar behaviour was observed for Li_2RuO_3 via in-situ Ru K-edge XANES, in which the edge shows an initial shift towards higher energy, during $Ru^{4+/5+}$ region of the charge, but then shifts partially back towards the original position during the high voltage region of charge.[127] A mechanism in which Ru is oxidised to Ru^{6+} and then is reduced via the cleavage of a Ru–O bond to form a peroxo/superoxo-like species was proposed and may explain these observations;[132] these proposals have motivated NMR studies to help understand these phenomena.

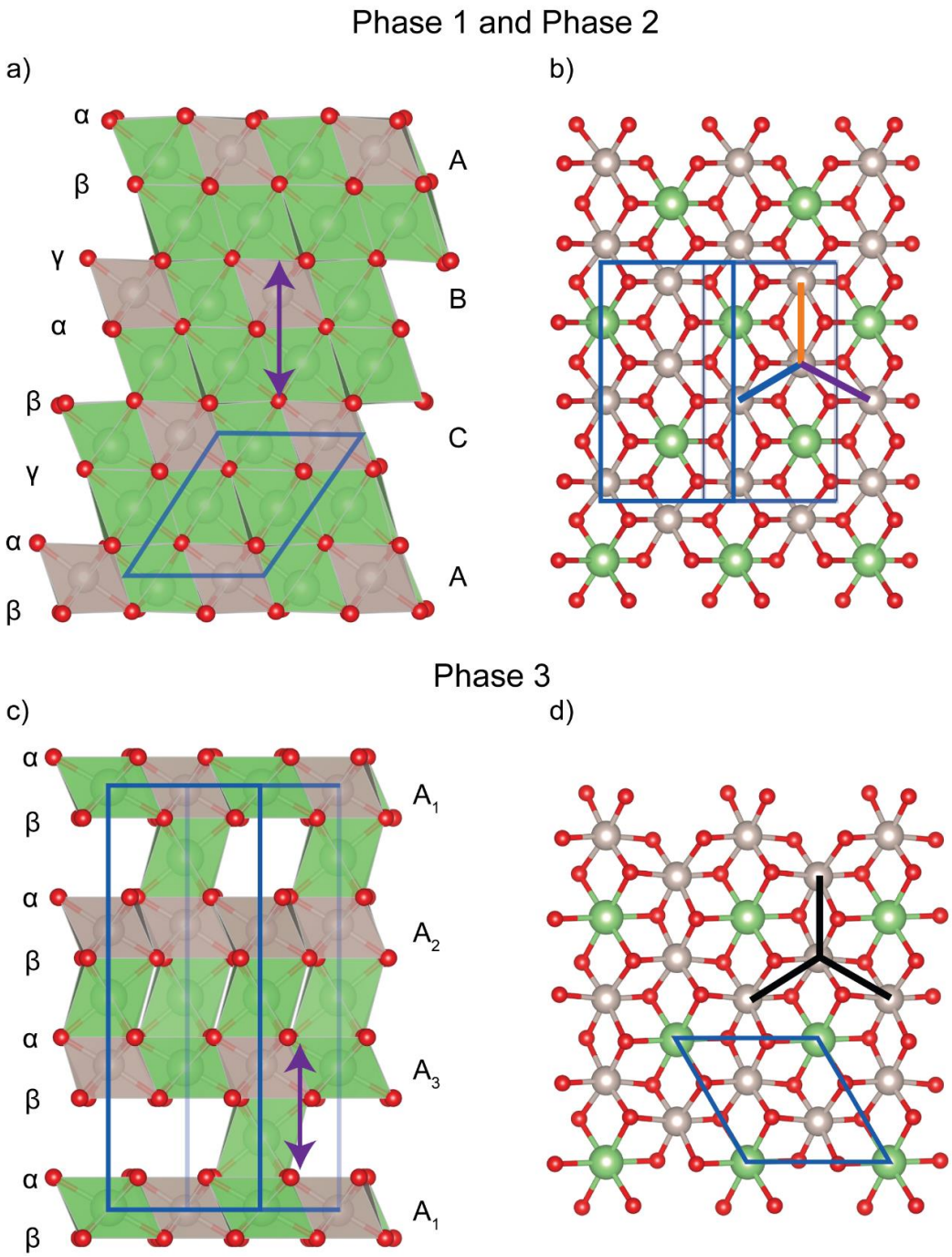

Figure 4.1 Structures of Li_xRuO_3 phases. a) View parallel to layers for phases 1 and 2 (space group $P2_1/m$) showing the O3 type stacking of both the cations (A,B,C) and the oxygen lattice (α,β,γ). The oxygens form a cubic close packed (ccp) array. b) View perpendicular to the TM-layer for phases 1 and 2, three distinct Ru–Ru distances are present, short (blue), medium (purple) and long (orange). c) the $R\bar{3}$ ilmenite-like structure of phase 3 as reported by Kobayashi et al.[124] shown perpendicular to the cation layers. The stacking of the oxygen transforms to a hexagonal close packed (hcp) array (α,β) with effectively O1 stacking. The TM stacking has be denoted A_1, A_2, A_3 as, although the cation layers lie directly above one another, because of the honeycomb ordering, the honeycomb layers repeat after 3 layers. d) TM layer view for phase 3, due to the trigonal symmetry, only a single Ru–Ru distance is possible. Unit cell are shown in blue. The combined slab distance referred to in the text and in table Table 4.1 is shown in purple and allows easy comparison of the size of the layers regardless of the unit cell.

Naturally, changes in coordination geometry of Ru are expected on oxidation. During the period of charge associated with $Ru^{4+/5+}$ oxidation—up to 168mAhg^{-1} or x = 1—the series of two-phase reactions defines the structural changes that occur. The pristine material, referred to as phase 1, has be extensively characterised in the previous chapter (Chapter 3) and will not be revisited in detail, however its salient properties must be highlighted with respect to phase 2 and phase 3, notably the dimerisation of Ru. Analysis of the Ru K-edge EXAFS, during the low voltage region, show that the average Ru–O distance shrinks continuously as expected for $Ru^{4/5+}$ oxidation (from ca. 2.04Å in the pristine material to ca. 1.96Å for phase 3).[127] In addition, a reduction in the Debye-Waller factor accompanies the transformation from phase 2 to phase 3 indicating a more uniform Ru–O bond length as this phase is formed.[127] As well as disparate Ru–O bond lengths, the pristine material also features robust Ru–Ru dimerisation which distorts the unit cell, on initial delithiation to phase 2 the distortion caused by this dimerisation is eased, as observed in the ratio $\sqrt{3}a/b$ which becomes closer to one for phase 2 and indicates the TM-layer is less distorted and more similar to that expected for an undistorted $R\bar{3}m$ material like $LiCoO_2$.[128,242] Magnetic measurements performed on chemically delithiated Li_2RuO_3 indicate that the Ru–Ru dimers persist in phase 2.[128] As well as magnetic moments lower than expected if isolated Ru^{4+} or Ru^{5+} unpaired spins were present, phase 2 exhibits a dimer-solid to dimer-liquid transition similar to pristine Li_2RuO_3, indicating that the reduced susceptibilities are due to dimerisation and not delocalisation.[128] Principal component analysis of K-edge Ru XAS data for $Li_2Ru_{0.75}Sn_{0.25}O_3$ demonstrated that, even in the Sn doped case, distinct short and long Ru–M distances could be identified and persist throughout the low voltage region.[243]

The low voltage region, which is characterised by Ru oxidation, ends with the formation of phase 3, which is less well understood than phases 1 and 2. As well as the required

rearrangement of the O lattice, the formation of phase 3 also brings about a large reduction in layer spacing as characterised by the movement of the most intense diffraction peak to higher angle and lower d-spacings.[129] The decrease in combined slab height from phase 2 to phase 3 is ca. 4.8%,[124,128] This is smaller than the c lattice parameter shrinkage observed in $LiCoO_2$ upon its transformation, at higher states of charge, from a monoclinic cell with O3 TM stacking to the hybrid H1-3 structure (.ca 5.6%) but is still very significant.[244] c-lattice parameter collapse is observed in many layered Li compounds, although in mutli-transition metal $LiTMO_2$s the change is continuous as they exhibit solid solution behaviour. Charge transfer from the O^{2-} ions, on to the TM centres, as the TM ions become highly charged, and subsequent reduction in the repulsion between TM-layers, has been proposed to cause this collapse in NMC811.[245] In the H1-3 phase of $LiCoO_2$, alternating Li-layers are completely delithiated and the TM-slabs above and below these layers slide creating O1 stacking. In that case, the completely delithiated layers are highly contracted and account for the large c-lattice collapse.[246] The proposed ilmenite structure features partially delithiation of all layers, rather than inhomogeneous delithiation of certain layers.

Table 4.1 Table showing values lattice parameters and structural information for Li_2RuO_3 phases on delithiation as reported. The compositions derived in this work are also noted

Phase Name		Phase 1	Phase 2	Phase 3
Space Group		$P2_1/m$	$P2_1/m$	$R\bar{3}$
Reported Composition		Li_2RuO_3	$Li_{1.4}RuO_3$	$Li_{0.9}RuO_3$
Lattice Parameters	a /Å	4.9372	4.9668	5.0865
	b /Å	8.7808	8.6349	5.0865
	c /Å	5.8974	5.8978	14.0233
	β / °	124.4	123.98	-
Volume per Ru /Å^3		52.74	52.44	52.37
Ru-Ru Bond length	Long	3.025	2.995	-
	Medium	2.966	2.987	-
	Short	2.680	2.645	-
	Average	2.890	2.876	2.951
TM Slab Height		2.272	2.283	2.029
Li Slab Height		2.594	2.607	2.646
Combined Slab Height		4.864	4.890	4.674
Reference		[179]	[128]	[129]
Composition (this work)		Li_2RuO_3	$Li_{1.3}RuO_3$	$Li_{0.95}RuO_3$

Magnetic susceptibility studies for phase 3, conducted on chemically delithiated samples, show nearly temperature independent magnetic susceptibilities; this, in conjunction with an observed drop in the resistivity suggests Pauli paramagnetism may be the origin of the magnetism in this phase.[247] The trigonal $R\bar{3}$ unit cell precludes ordered (long-range) Ru–Ru dimerisation and alongside the magnetic measurements, which suggest Ru^{5+} t_{2g} electrons are delocalised suggests that dimerisation may be lost on the formation of phase 3. XAS analysis, support this as once the high voltage plateau is accessed, short Ru–M distances were not required to fit the EXAFS.[243]

During the high voltage plateau no significant evolution of peak positions is observed, while the reflections are gradually broadened, suggesting an increase in disorder.[127] Additionally pre-edge features, which are initially weak in the pristine material and during the initial phase of delithiation, become more pronounced during the high voltage plateau; these features are associated with transitions from the 1s to the 4d, which are formally dipole-forbidden for Ru in perfect octahedral coordination, suggest

the Ru environment becomes less centrosymmetric so that the 4d and 5p states are able to mix.[127] The broadening observed in the diffraction remains on discharging indicating the irreversibility of this process.[240]

In this chapter ^{7}Li and ^{17}O NMR spectroscopy will be used in order to probe the electronic and local structure changes in Li_2RuO_3 on cycling. Each of the phase transitions in the low voltage region and the changes that occur during the high voltage plateau will be investigated in order to help understand the electronic and structural processes that occur through charging.

4.3 Experimental

Li_2RuO_3 was synthesised as described in the previous chapter (Chapter 3). Cathodes for NMR characterisation were produced by grinding by hand, with an agate pestle and mortar, the active material, Super P carbon (Timcal) and Kynar Flex® (Polyvinylidene Fluoride PVDF) in a ratio 80:10:10 by mass for 20 minutes until well mixed. N-methyl-2-pyrrolidone (NMP) was added to form a slurry which was transferred onto aluminum foil and spread using a 150 μm doctor-blade. The films were dried under vacuum at 100°C overnight. Cathodes were punched to a diameter of 1.11 cm giving a surface area of 0.97 cm^3 and mass weightings in the range 5-10 mg. Coin cells were made in an argon filled glovebox with H_2O level < 0.1 ppm and O_2 level $=$ 0.3 ppm. Cathodes were placed on steel current collectors (0.5 mm) and separated from the counter electrode by glass fiber soaked with electrolyte. The anode was a lithium foil (Sigma Aldrich, 99.9 %), and backed with a steel current collector. The entire assembly was compressed by a steel wave spring and crimped. The electrolyte used was 1M $LiPF_6$ in a 1:1 ratio of ethylene carbonate and dimethyl carbonate (EC:DMC, Sigma Aldrich).

All potentials are with respect to Li/Li^+. Currents were set at C-rate C/40 based on the active mass loading of each cell and according to the theoretical 1 Li capacity i.e.

corresponding to the removal of the full 1 Li per formula unit ($168.6 mAhg^{-1}$). Measurements were carried out on a Bio-Logic potentiostat. Once charged, cells for NMR were deconstructed in the same glovebox, the cathodes rinsed with DMC solution (99.9 % Sigma Aldrich) and dried under vacuum for 30 minutes. The cathode material was scraped off the foil and packed into 1.3 mm zirconia rotors with Vespel caps for NMR analysis.

^{7}Li NMR was conducted at 4.7 T using a Bruker 1.3 mm MAS probe at 60 kHz MAS frequency. The spectra presented are rotor-synchronised Hahn echo experiments with the echo delay equal to one rotor period unless otherwise noted. ^{7}Li T_1s for pristine Li_2RuO_3 were measured to be ~330 ms (48 ppm) and ~480 ms (28 ppm) using inversion recovery experiments. For the cycled samples, for which T_1 was always measured to be lower, a recycle delay of 2s was used unless noted. ^{7}Li spectra were referenced to 1M LiCl in D_2O at 0 ppm or solid Li_2CO_3 at 0 ppm. Temperature calibration was performed *ex situ* using the ^{207}Pb shift of $Pb(NO_3)_2$ as an NMR thermometer[182]. A calibration curve was made to translate the thermocouple temperatures to sample temperatures. Although ^{7}Li is a spin I=3/2 nucleus, due its low nuclear quadrupole moment it was treated as a pseudo-I=1/2 nucleus.

^{17}O NMR was conducted at 11.7 T or 16.4 T using a Bruker 1.3 mm MAS probe at a MAS frequency of 60 kHz. The 11.7 T spectra are presented where available and 16.4 T spectra are clearly marked. Very little difference was observed between spectra recorded at the two fields. The spectra presented are rotor-synchronised Hahn-echo experiments with the echo delay equal to one rotor period. T_1 relaxation was measured to be ~100 ms (1070 ppm), ~10 ms (740 ppm), ~160 ms (580 ppm) and 250 ms (200 ppm) using saturation recovery experiments. As with ^{7}Li, the ^{17}O T_1s on charging were measured to be shorter than this (longest was ca. 100ms for ca. 200 ppm peak); a pragmatic approach was adopted and a recycle delay of 0.6 s was used for effectively "quantitative" experiments which allowed efficient acquisition, without supressing the

slower relaxing components of the signal. Shorter recycle delays were used in some cases and this is noted with the spectra. As detailed in section 1.8.1, in order to produce a spectrum which is quantitative between all environments, regardless of quadrupolar coupling constant (C_Q), a shorter pulse than optimised for the reference compound must be used. In this work ^{17}O spectra were recorded a with π/6 $\left(\frac{\pi}{2I+1}\right)$ pulses as the "effective π/2" pulses.

Variable temperature (VT) ^{6}Li and ^{17}O NMR spectra for pristine Li_2RuO_3 were acquired at 16.4 T using a Bruker 4 mm probe at a MAS frequency of 14 kHz. Further information about these spectra is available in the previous chapter (section 3.3.2).

Powder diffraction for characterization of the materials and for in-situ measurements was collected on a Panalytical Empyrean diffractometer using CuKα radiation and with a Bragg-Brentano geometry. Rietveld refinements were performed using the TOPAS program. For the in-situ refinements, a sample displacement parameter was refined to account for the displacement of the film from the optimised position and then fixed, no other instrumental parameters were varied. Le Bail fits were used to obtain reasonable lattice parameters for each of the three phases. Significant preferred orientation in the (001) direction was present and hence a correction for this was refined for the pristine material and then fixed and applied to all phases. During the sequential Rietveld refinement, only lattice parameters and weight percentage were allowed to refine and the results of the previous pattern were used as the input for the next refinement. The electrochemical charging was performed at C/20 (with respect to 1Li extraction) and 188 patterns were recorded between 15-60° 2ϑ with a scan time of 607s (total duration 31h 40m).

Magnetic susceptibility measurements were carried out on a Quantum Design Magnetic Properties Measurement System (MPMS) with a Superconducting Quantum Interference Device (SQUID) magnetometer. FC and ZFC susceptibility were measured in a field of 100 Oe in the temperature range 2 – 300 K. Cathodes for these experiments

were made as self-supporting PTFE films by mixing the active material, carbon super P (Timcal) and PTFE in a 75:20:5 ratio. These were then rolled into thin films using a glass rod and then processed as described previously. In order to avoid ferromagnetic contamination, non-metallic tools were used when possible. Mass loadings for these cells were ca. 16 mg. Diamagnetic contributions to the susceptibility from ion cores in Li_2RuO_3, the PTFE binder and carbon were subtracted.[218]

4.4 Results and Discussion

4.4.1 In-situ X-ray Diffraction

In-situ XRD was performed in order to probe the evolution of Li_2RuO_3 through delithiation. The lower voltage region consists of two two-phase regions, followed by a single-phase region at high voltage, during which the reflections broaden and shift slightly (Figure 4.2). These observations are in-line with observations from previous reports.[127,129] Sequential Rietveld refinements were performed in order to quantify the phase fractions; the results of these refinements are compared with voltage profile in Figure 4.3. The refinements show that phase 1 is completely transformed, and phase 2 is maximised at x = 1.3, this suggests the composition for this phase is $Li_{1.3}RuO_3$, The conversion of phase 2 to phase 3 is complete by x = 0.95, which implies an initial composition for phase three of $Li_{0.95}RuO_3$. These compositions are the same as or very similar to those proposed by Kobayashi et al.[247]

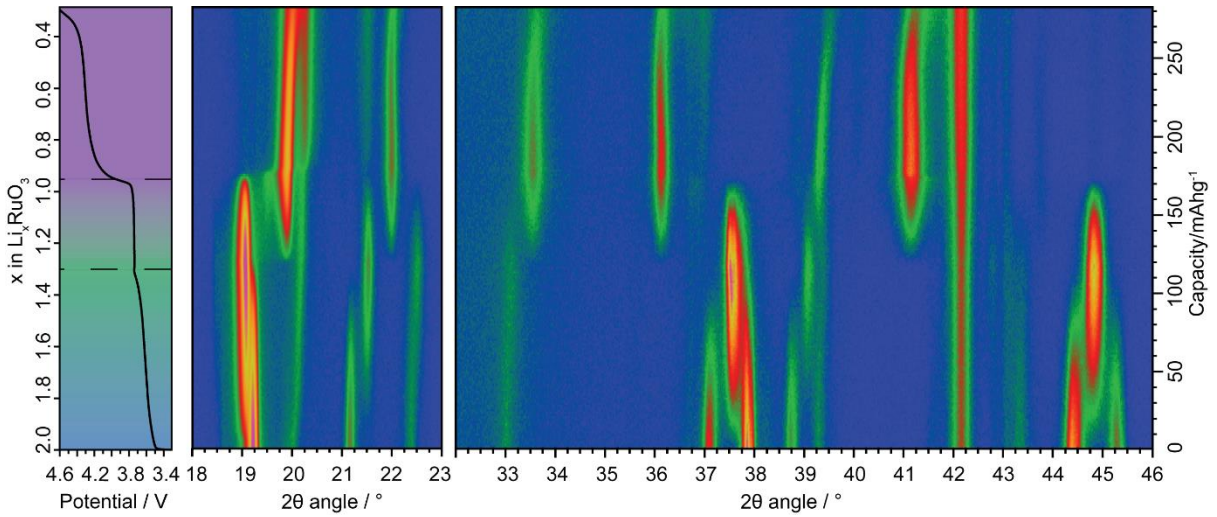

Figure 4.2 In-situ XRD for Li_2RuO_3 conducted at rate of C/20. The leftmost panel shows the corresponding electrochemistry highlighting the correlation of the two-phase behaviour with electrochemical plateaus in the low voltage region. The middle and right panels show the in-situ diffraction data as a contour map with lighter colours indicating greater intensity. The middle panel shows a zoomed in region highlighting the change in the "layer spacing" peak i.e. the reflection that arises due to the d-spacing between the layers the (001) reflection for phases 1 and 2 ($P2_1/m$) and (003) for phase 3 ($R\bar{3}$); the contour plot for this is the square root of the intensity to allow the other reflections to be observed as well. The rightmost panel shows the evolution of the other peaks. The y axes are common between all panels.

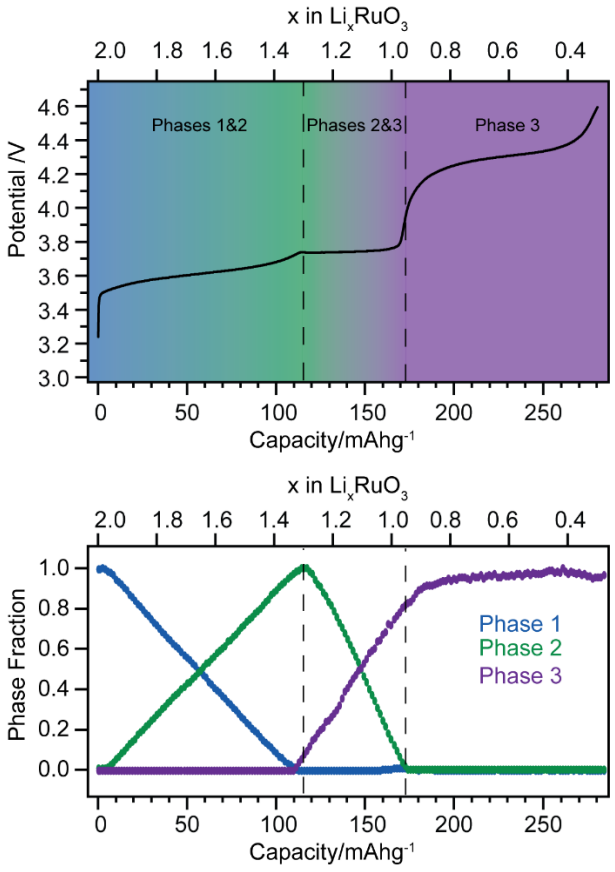

Figure 4.3 In-situ electrochemistry and refined phase fraction of each of the delithiated phases of Li_2RuO_3. Phase 2 maximises at x = 1.3 (115 $mAhg^{-1}$) and disappears by x = 0.95 (158 $mAhg^{-1}$) at which point phase 3 is at a maximum. These regions are highlighted by the shading of the electrochemistry. Blue corresponds to the phase1, green to phase 2 and purple to phase 3.

The phase fractions refined from this *in-situ* measurement have been used in order to estimate the composition of the samples for the SQUID magnetometry and for the NMR measurements which are both *ex-situ* measurements. The *in-situ* diffraction captures the instantaneous "kinetic" structure, which may relax in the time which elapses between cycling and the *ex-situ* measurements. This may create a disconnect between the composition expected on the basis of the *in-situ* measurement and the actual composition measured by NMR or SQUID magnetometry.

4.4.2 Magnetic Measurements

Squid magnetometry was performed on the pristine material and ex-situ samples cycled to different states of charge (Figure 4.4). Three samples were prepared x = 1.5 x = 0.9 and x = 0.8. In order to determine the fraction of each phase for the samples, Rietveld refinements of XRD were performed and are noted in Figure 4.4. The x = 0.8 sample is essentially only phase 3, whilst the x = 1.5 is mostly phase 2. The x = 0.9 sample is a roughly even mixture of phases 2 and 3, this unexpected as in the in-situ diffraction, at the same state of charge, only phase 3 is present. The difference may due to the relaxation of the sample during the time period between cycling and measurement. The magnetic susceptibility samples are also briefly exposed to air when they are transferred from the glovebox to the magnetometer—although contact is minimised as much as possible by sealing the sample with parafilm—this may also contribute to this difference. Susceptibilities are of a similar order of magnitude as in the pristine material.

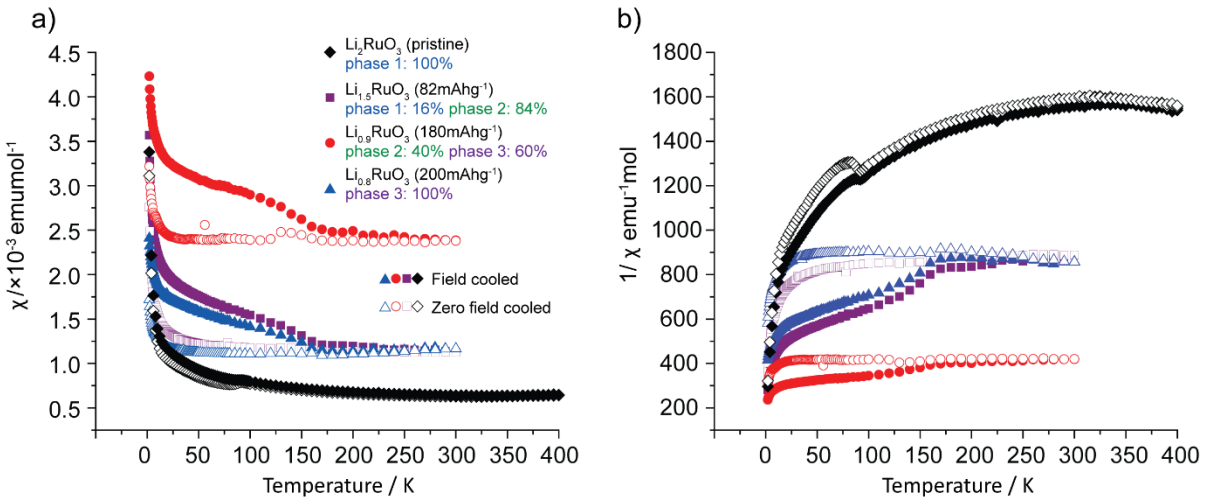

Figure 4.4 SQUID magnetometry data recorded for 4 samples of Li_2RuO_3. a) Temperature vs χ plot for 4 samples: Pristine Li_2RuO_3 (black diamonds), $Li_{1.5}RuO_3$ (purple squares), $Li_{0.9}RuO_3$ (red circles) and $Li_{0.8}RuO_3$ (blue triangles). Field cooled and zero field cooled data are shown with filled and open symbols respectively. b) 1/T vs χ plots for the same data highlighting the non-Curie-Weiss behaviour exhibited in the charge samples.

In order to extract an effective magnetic moment (μ_{eff}) for each sample, 1/ χ vs T plot was fit for the full temperature range measured (2-300 K) by minimising the total least squares difference between the experimental data and a curve calculated using the equation:

$$\chi = \chi_0 + \frac{C}{T - \theta} \tag{4.1}$$

The parameters χ_0 (a temperature-independent susceptibility), C (the Curie constant) and θ (the Weiss temperature) were allowed to vary, the results of this fitting is show in Table 4.2 and the fits to the data in Figure 4.5. Another strategy that has been successfully employed for the fitting the low temperature magnetic behaviour of structures with clustered metal centres, for example GaV_2O_4 and AlV_2O_4,[248,249] has been to utilise a so called "spin gap term" in addition to the Curie-Weiss term in order to model the thermal excitation of spins into the triplet state:

$$\chi = \frac{C}{T-\theta} + \frac{D}{T\left[1+\frac{1}{3}\exp\left(\frac{E_g}{k_B T}\right)\right]} \tag{4.2}$$

Where E_g is the energy gap that characterises the energy required to excite the bonding cluster into the triplet state. It the case of Li_2RuO_3 no isolated Ru^{4+} atoms are expected so the Curie-Weiss term might be superfluous and temperature independent term that accounts for interactions between the dimers introduced, so the susceptibility might have the form:

$$\chi = \chi_0 + \frac{D}{T\left[1+\frac{1}{3}\exp\left(\frac{E_g}{k_B T}\right)\right]} \tag{4.3}$$

Attempts to fit the data using this model yielded very small values of E_g such that the Boltzmann term became equal to 1 and D then became a proxy to the Curie constant (C) from the original Curie-Weiss + χ_0 model in equation.

Table 4.2 Magnetic parameters for cycled Li_2RuO_3 samples $Li_{1.5}RuO_3$, $Li_{0.9}RuO_3$ and $Li_{0.8}RuO_3$ modelled using $\chi = \chi_0 + \frac{C}{T-\theta}$.

Parameter	$Li_{1.5}RuO_3$	$Li_{0.9}RuO_3$	$Li_{0.8}RuO_3$
Fraction Phase 1	16	0	0
Fraction Phase 2	84	40	0
Fraction Phase 3	0	60	100
Curie Constant/K emu mol-1	0.0011	0.0024	0.0011
Weiss Constant/K	0.0018	0.0021	0.0049
χ0 /emu mol-1	-0.75	-0.32	-1.30
Estimated Moment/ μB	0.12	0.13	0.20

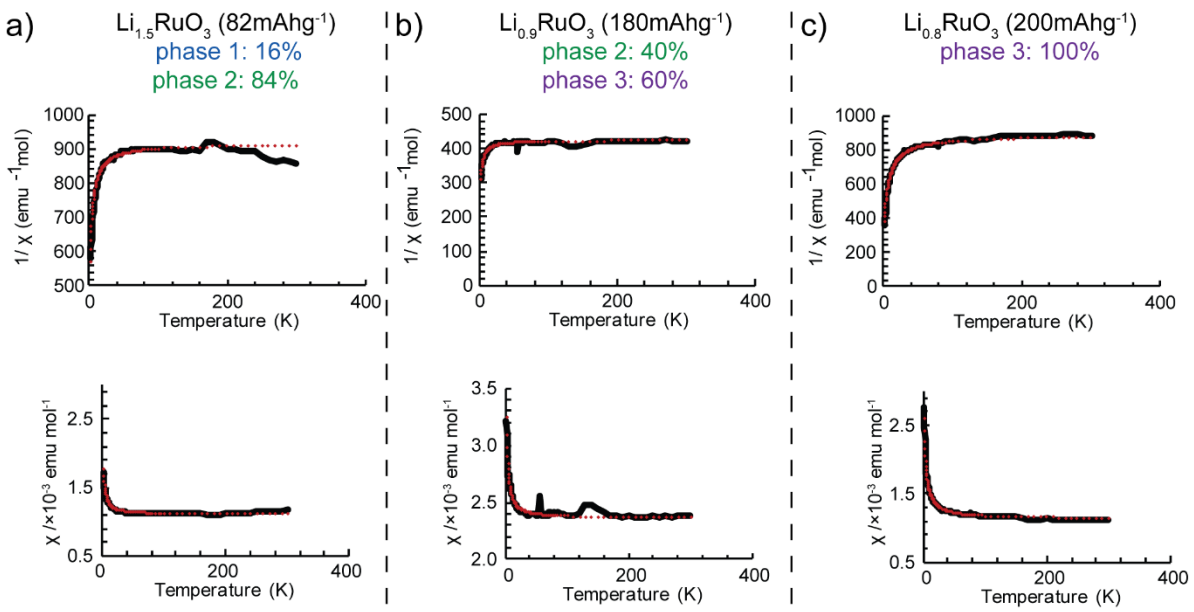

Figure 4.5 Fits to zero-field-cooled molar susceptibility and inverse molar susceptibly vs T plots for $Li_{1.5}RuO_3$ (a), $Li_{0.9}RuO_3$ (b) and $Li_{0.8}RuO_3$ (c) modelled using $\chi = \chi_0 + \frac{C}{T-\theta}$. The experimental data are shown in black and the fit to the data is shown in red.

4.4.3 ^{7}Li and ^{17}O NMR from Phase 1 to Phase 2

The change in the Li and O environments on delithiation was investigated by ^{7}Li and ^{17}O NMR spectroscopy. The data are presented for each phase transition separately in order to focus on each of the three phases on delithiation. First the transition from phase 1 to phase 2 is investigated (Figure 4.6 and Figure 4.7). Phase 1 and phase 2 are broadly similar, both have the $P2_1/m$ space group and dimerised Ru. On minimal delithiation (x=1.90 and x =1.75) , the ^{7}Li NMR spectra display virtually no change in shift, although the signal intensity decreases, and the peaks become broader. In the middle of the transformation (x = 1.62, x = 1.50 and x =1.40) the signal intensity is significantly lower—far lower than the reduction in Li content can account for—while the peak positions again match those of phase 1. The absence of new peaks (leaving aside the peak which appears at 0 ppm which is assigned to diamagnetic surface species) is striking, as from the in-situ diffraction the weight percentage of each phase should be equal at x =1.62. When the data is scaled up multiple times, new peaks are observed

at slightly higher shift (55-95 ppm Figure 4.6, pink box). Finally, for x = 1.24, at which point the sample has been entirely converted to phase 2 (and a very small amount of phase 3), three sharp resonances are observed, in line with the three Li sites in the literature structure for phase 2. The occupancies of these sites is not commented upon by previous authors owing to the insensitivity of x-ray diffraction to Li.[128,247] The intensity of the spectra recovers such that the total integrated Li intensity of this sample is greater than the value expected considering the level of delithiation—87% relative to the pristine material compared to the expectation 62%. This suggests a return to an ordered regime. The most highly shifted peak occurs at 52 ppm, very close to the 47 ppm peak assigned to Li in the Ru layers. The two remaining resonances occur at lower shifts at 11.5 ppm and 3.2 ppm respectively.

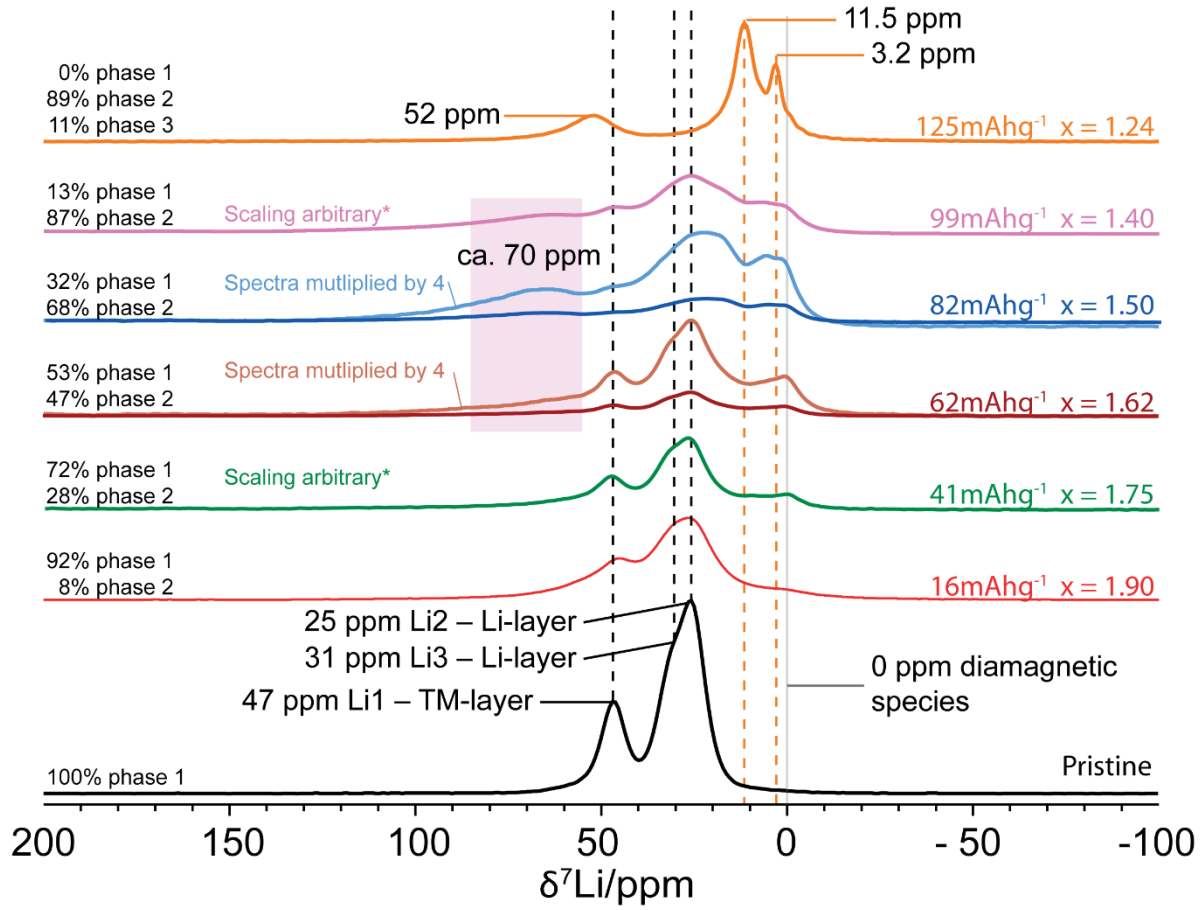

Figure 4.6 ^{7}Li NMR during the first plateau during which time phase1 is converted into phase 2. The states of charge of the spectra are noted on the right-hand side. The spectra have been scaled by mass and number of scans so that they are quantitatively comparable, excepting the x = 1.75 (green) and x = 1.40 (pink) samples. The positions of the peaks in the pristine material are labelled with their assignments and the black dashed line are a guide for the eye. Similarly, the peaks of the x = 1.24 sample, which corresponds to almost pure phase 2, are labelled. A 0 ppm peak, which is observed most prominently in the scaled-up spectra, is assigned to diamagnetic surface species. The pink box highlights the resonances from the more paramagnetic Li environments that appear in the middle spectra. Approximate phase fractions derived from the Rietveld refinements of the in-situ XRD data at equivalent states of charge are displayed on the left-hand side of the spectra.

During the same period of delithiation the ^{17}O NMR exhibits some similarities (Figure 4.7a). On initial charging to x = 1.75 the spectrum is broadened, and shoulder peaks appear. The total integrated intensity drops, similar to that observed in the Li spectrum, although the poor signal to noise ratios for some of the ^{17}O spectra prevent precise quantification. On further charging to x = 1.40 the shifts for the peaks remain

approximately similar but the ratio changes significantly. The 740 ppm peak, which was assigned to O2 in the pristine material is the only unobscured peak remaining from phase 1, the other peaks from phase 1 lying underneath resonances that result from phase 2. The ratio of phase 1: phase 2 in this sample is ca. 1:9. At x = 1.12 phase 1 has been entirely converted and although it is ca. 60% phase 2 and 40% phase 3, this is the first sample without any phase 1. The 740 ppm peak vanishes as expected and a lineshape similar to the x = 1.40 sample results, although the peaks are less sharp, probably due to the mixture of phase 2 and phase 3 resonances.

In addition to the measurements performed with a long recycle delay, which ought to be quantitative for all signals with respect to saturation, spectra with shorter recycle delays were recorded in order to favour signals with faster relaxation. If new resonances emerge, with significantly different relaxation behaviour—i.e. much shorter T_1 and T_2 relaxation constants—then their shorter T_2s may prevent their observation during "quantitative" experiments, particularly if they are very broad, as coherence is lost during the echo delay. Single pulse experiments can be used, however for these samples the high number of scans and the poor signal to noise ratios precludes this, as the background signals and bassline distortion obscure the sample data. Additionally, shorter recycle delay experiments allow more scans to be completed in the same timeframe allowing the acquisition of spectra with greater signal to noise ratios, in which broad resonances are more likely to be observable. Finally, such measurements give an idea of the relaxation behaviour of the resonances without explicit measurement (which is very time consuming for ^{17}O). The results are shown in Figure 4.7c. The pristine material and the x = 1.75 sample are similar and underline that the 740 ppm peak, assigned to O2, has considerably shorter T_1 relaxation (the other peaks are saturated by the short recycle delay experiments). The two samples with a majority of phase 2 (x = 1.40 and x = 1.12) show the cluster of resonances 750-1050 ppm do not decrease in intensity despite the reduced recycle delay whilst the peaks around 230 ppm are lost. Approximate T_1 values for these peaks were recorded and were ca. 30 ms and

ca. 100 ms for 750-1050 ppm and ca. 230ppm respectively, which reflect this observation. Interestingly no new resonances were observed at either higher or lower shift ranges in either these experiments, or when extremely short (0.005s) recycle delay were used in variable offset cumulative spectrum (VOCS) experiments sweeping from −1000-3000 ppm. Figure 4.7b shows the ^{7}Li NMR spectra which correspond to the ^{17}O NMR samples and show how the two spectra evolve in tandem.

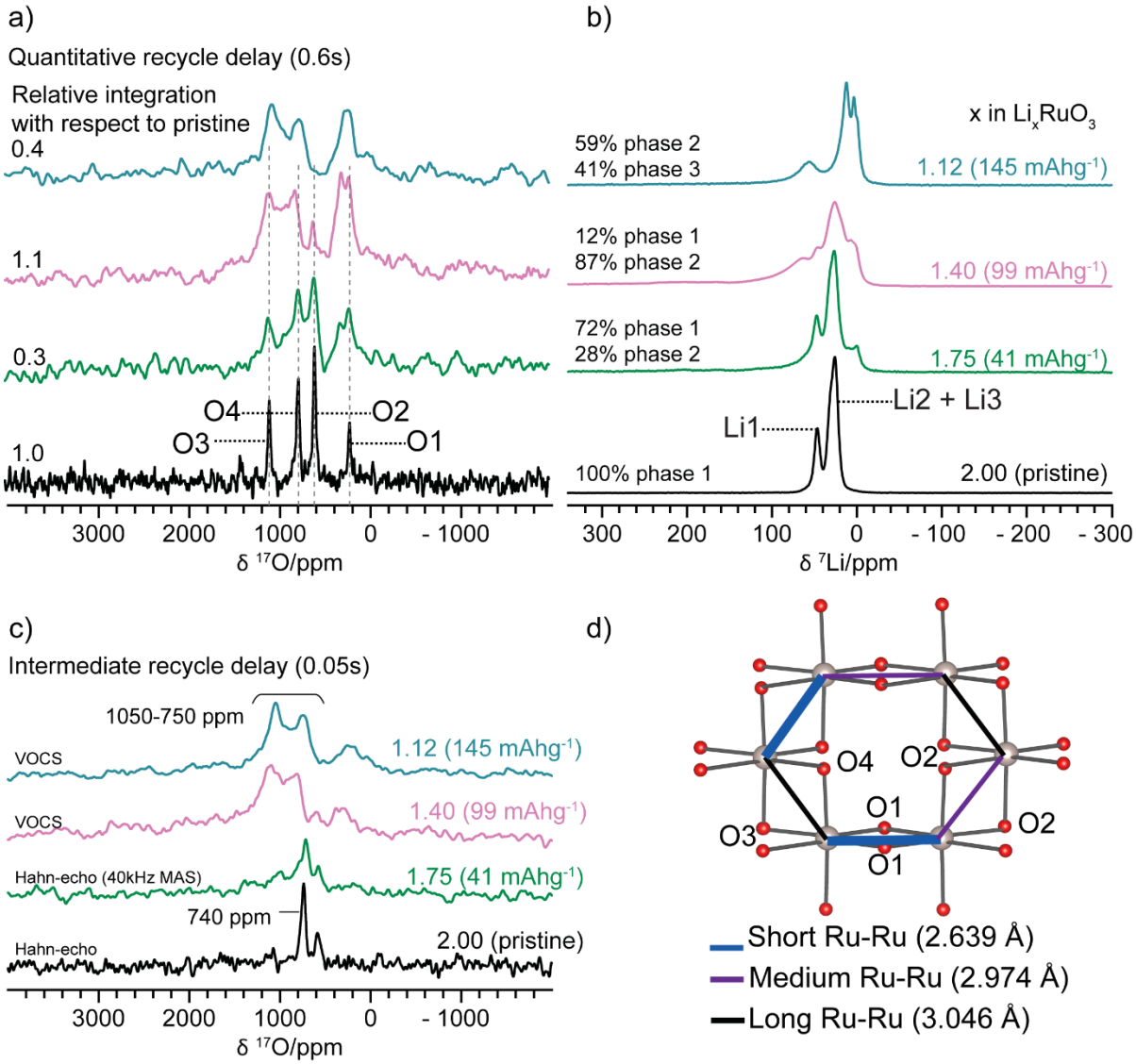

Figure 4.7 ^{17}O NMR spectra recorded for ^{17}O enriched samples of Li_2RuO_3 at various states of delithiation highlighting the two phase region between phases 1 and 2. a) Shows the spectra recorded using a recycle delay, determined to be quantitative for the discharged material (longest T_1 measured for peak .ca 200 ppm was 100 ms). b) shows the ^{7}Li NMR spectra of the same samples c) intermediate recycle delay experiments. d) a schematic view of the O sites in the pristine Li_2RuO_3. Approximate phase fractions derived from the Rietveld refinements of the in-situ XRD data at equivalent states of charge are above the corresponding Li spectra and are equivalent for the O spectra.

4.4.4 Phase 1 to Phase 2 – Discussion

In both the ^{17}O and ^{7}Li NMR the shift ranges observed for phases 1 and 2 are very similar, perhaps unsurprisingly considering their structural similarity. The pristine phase peaks are visible to some extent whenever some amount of phase 1 remains. The lack of change in position of these phase 1 peaks, suggests that the Ru–Ru order of phase 1 is virtually unchanged and implies that the newly formed Ru^{5+} is accommodated by phase 2. A narrow solid-solution regime may exist for phase 1 such that the broadening of the resonances, observed during the initial period of charge (until x = 1.75), and the loss of signal intensity may be due to a small amount of Ru^{5+} formed in phase 1 giving rise to electronic fluctuations and increased Li mobility due to a small increase in Li vacancy concentration. Alternatively, the observed changes could be caused by distortions in the local structure of phase 1 due to strain produced by the nucleation of phase 2.

In the mixed phase 1: phase 2 regime the ^{7}Li signal is almost completely lost (x = 1.42 – 1.62) whereas the ^{17}O signal at in that region (x = 1.62) is largely retained. A similar loss of $^{6/7}Li$ signal, without loss of ^{17}O signal is observed in the VT NMR spectra for pristine Li_2RuO_3 for moderately high temperatures—i.e. at temperatures lower than the onset of the dimer-solid to dimer-liquid transition at ca. 250°C (Figure 4.8). In addition, the new peaks observed at ca. 70 ppm for ^{7}Li and between 750-1050 ppm for ^{17}O match the shift ranges observed for the pristine material between 161-216°C indicating the origin of these shifts and signal loss behaviour may be similar. The changes in the moderately high temperature NMR were ascribed to an increase in the number of unpaired electrons as the phase transition approaches. The loss of Li signal was attributed to electronic fluctuations which induce rapid relaxation; a more pronounced effect is observed in the Li spectra as the t_{2g} orbitals, which are expected to contain the unpaired spins for both Ru^{4+} and Ru^{5+}, point directly at the Li 2s orbitals. Phase 2 must consist of a mixture of Ru^{4+} and Ru^{5+} and whilst eventually an

ordered array of dimers may arise, during the initial formation a similar regime to the moderate high temperature Li_2RuO_3, in which excitations drive up the number of unpaired electrons despite dimerisation, is most likely.

Once phase 1 is eliminated, phase 2 appears to adopt a more ordered arrangement. The low magnetic moments measured for phase 2 in this work (ca. $0.12\mu_B$), and previously reported ($0.06\mu_B$), magnetic data,[128] imply formation of dimers with S = 0: i.e. Ru^{4+}–Ru^{4+} and Ru^{5+}–Ru^{5+} rather than Ru^{4+}–Ru^{5+} which would give rise to unpaired electrons (Figure 4.9). The composition $Li_{1.3}RuO_3$ implies a Ru^{4+}:Ru^{5+} ratio of 3:7 but is extremely close to $Li_{1.33}RuO_3$ with an implied Ru^{4+}:Ru^{5+} ratio of 1:2, neither of these can be accommodated by a single unit cell (which contains only 4 Ru atoms). In the diffraction in this work, no superstructure, indicating long range charge ordering was observed, however previous performed on a chemically delithiated sample, with composition $Li_{1.27}RuO_3$, did observed some superstructure which could be caused by such a charge ordering, although no super-cell was proposed.[128]

Once phase 1 is completely consumed, three sharp resonances are observed in the ^7Li NMR, consistent with the crystallographic structure proposed by Jimenez-Segura et al.[128] The higher shift peak is assigned as the Li in the TM-layer, for the same reasons in the pristine material (i.e. Only 90° Li–O–Ru bond pathways which are expected to be positive), whilst the other two peaks correspond to the 4f and 2e sites in the Li-layer. The observed ratio of these peaks is approximately 1:2:1 (Figure 4.6 x = 1.24) which is the ratio expected if the occupancy of each crystallographic sites is identical. While equal delithiation from each site might be considered quite unlikely, given the very different coordination environments for the TM-layer and Li-layer sites, similar behaviour is observed in the $Li[Li_{1/3-2x/3}Ni_xMn_{2/3-x/3)}]O_2$ family of materials, where Li is extracted from both the Li and TM layer sites at similar rates at for the early stages of charge.[65,95,111] Another possibility is that the spectrum is not quantitative, however the measured T_2s for the Li in the TM-layer and Li in the Li-layer (taken together) are

ca. 1 ms and ca. 1.5 ms respectively which would lead to 3% and 2% intensity loss during the echo delay respectively; the T_1s are also similar for each site: ca. 200ms. Therefore, writing the composition implied by the NMR results for phase 2 ($Li_{1.3}RuO_3$) notation gives: $Li_{0.65}[Li_{0.21}Ru_{2/3}]O_2$. This analysis assumes that the structure derived from diffraction, which is mainly sensitive to Ru positions, is correct and that no new Li coordination environments emerge, for example tetrahedral sites. Additionaly, the sharpness of the Li peaks implies that the Li is highly ordered which may be due to a coordination of the occupied and vacant Li sites with the charge of the dimers.

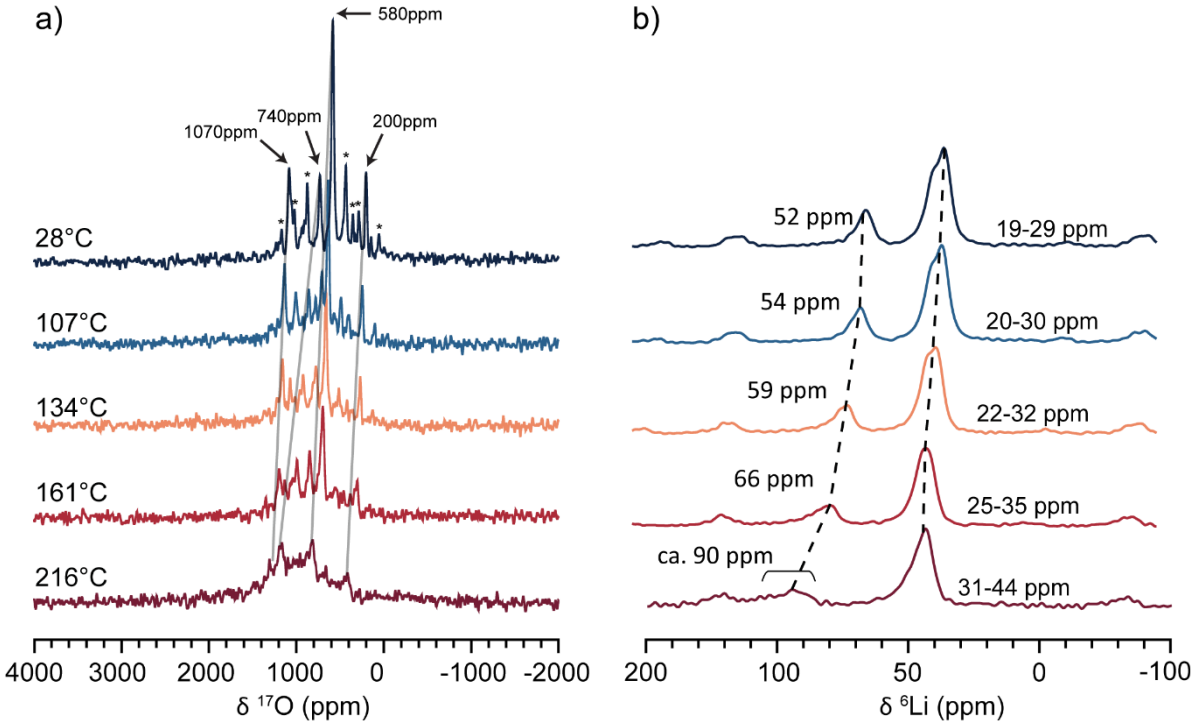

Figure 4.8 Moderate temperature VT NMR spectra of Li_2RuO_3 recorded at 16.4 T and 14 kHz MAS. a) ^{17}O spectra show a migration to a broad group of resonances between 200-1500 ppm. b) ^{7}Li spectra showing a change across the temperature range of ca. 40 ppm for the TM-layer Li and ca. 10 ppm for the Li-layer signals. The difference in the Li peak positions is possible due a second order quadrupole shift (due to the field change but expected to very small for $^{6/7}Li$) and/or the effects of narrowing of lines due to using ^{6}Li not ^{7}Li

The ^{17}O NMR spectra for the majority phase 2 samples (x = 1.4 and x = 1.12) show that while the shift range for the two phases is similar, phase 2 has broader resonances. This may be due to the larger number of discreet O environments, as whilst in phase 2 there are still only 4 crystallographic sites, the mixture of Ru^{4+} and Ru^{5+} neighbours

will split these into many more. The similar shifts observed can be rationalised by considering the model for Fermi-contact shifts derived from Ru^{4+} dimers, presented in the previous chapter (section 3.4.6). In the case of Ru^{4+}–Ru^{4+} each dimer contains 8 electrons and in the dimer, assuming the energy difference between the π* and δ* orbitals is greater than the energy required to pair two electrons, S = 0 and the HOMO is the δ* orbital (Figure 4.9c). Excitation would create unpaired electrons in the π* and δ* orbitals resulting in a state with $S = \frac{1}{2}$ per Ru (Figure 4.9b). In the case of Ru^{5+} the arrangement of electrons is nearly identical, but the HOMO is the δ orbital and an excitation would produce unpaired spins in the δ and δ* orbitals (Figure 4.9d). In the previous chapter it was argued, on the basis of the shape of the π* and δ* orbitals (mostly pointing away from the Ru dimer, Figure 4.10d), that the position of the O atoms relative to the dimer gave rise to the distinct shifts observed. The expectation that unpaired spins for a Ru^{5+} dimer will lie in the δ* orbital should result in similar shifts, however as δ orbitals are bonding, they have a different shape; Rather than the majority of their unpaired electron density pointing away from the dimer, most is localised between the Ru^{5+} atoms (Figure 4.10c). This may explain the observation of a larger group of resonances at high shift, which are show evidence of short relaxation times (as their intensity is not lost with shorter recycle delay experiments) as more of the oxygen environments (for example O1, the interdimer oxygen) are exposed to more unpaired spin density. The possibility of Ru^{4+}– Ru^{5+} dimers has been discussed by other authors and was dismissed on the basis that such an arrangement would necessarily result in an unpaired electron which is not consistent with the low moments observed.[128] Ru^{4+}– Ru^{5+} dimers might exist as an excited state or as a transition state if the dimer ordering were to fluctuate.

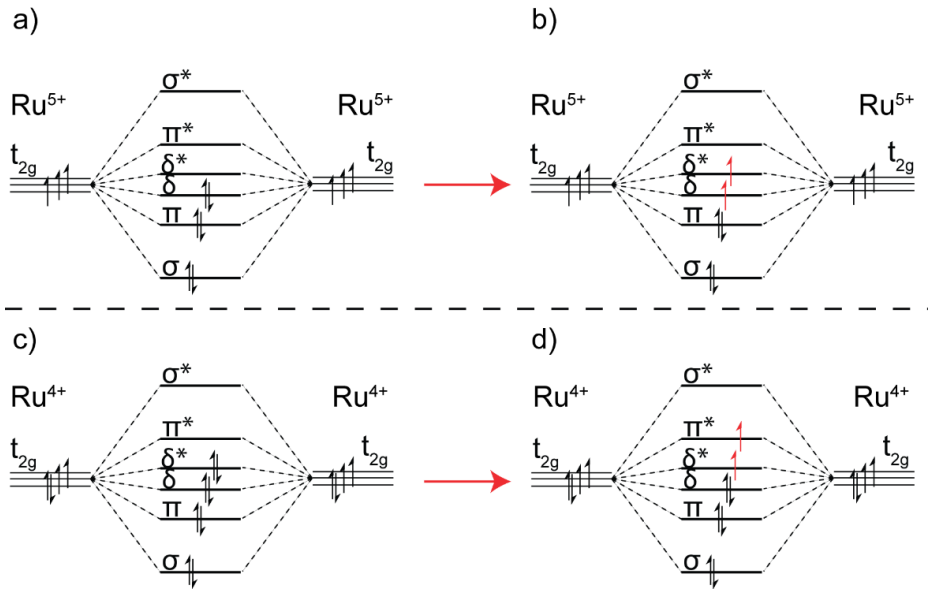

Figure 4.9 Molecular orbital diagrams for Ru^{5+} (a and b) and Ru^{4+} (c and d) dimers. The left-hand side shows the low energy configuration, if the energy required to pair two electrons is less than the energy difference between the δ and δ* (a) or δ* and π* (c). The right-hand side show the location of unpaired spins (red) on excitation.

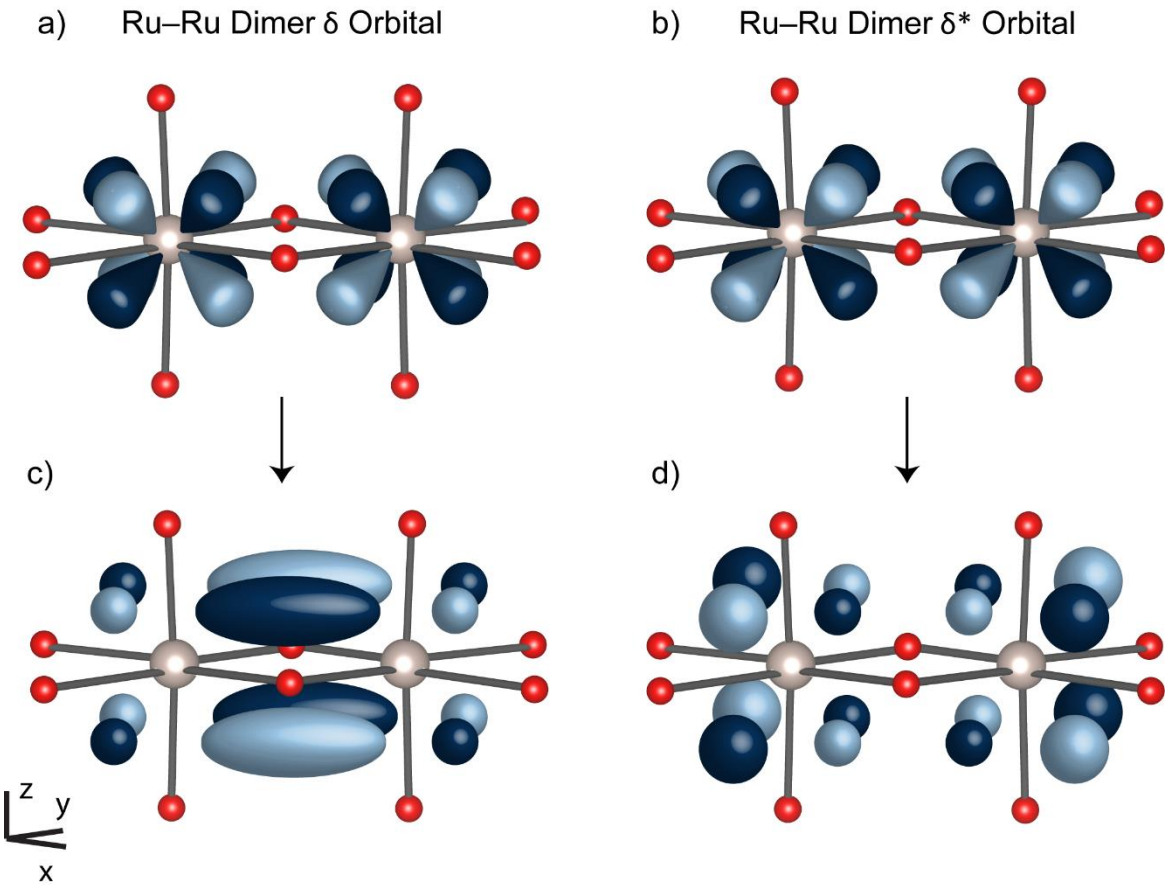

Figure 4.10 Cartoon illustration of the shape of δ and δ* orbitals expected to be the location of unpaired spin density in "excited" Ru^{5+}–Ru^{5+} dimers. The dimer axis is between the two Ru atoms (grey) in the xy-plane. a) and b) show the δ symmetry combination of the d_{xz} and d_{yz} orbitals arranged to either give an in phase bonding overlap (a) or an anti-phase anti-bonding overlap (b). c) shows the expected shape of the δ bonding orbital which has significant density along the dimer axis. d) shows antibonding δ* combination for which the spin density most points away from the dimer

4.4.5 ^{7}Li and ^{17}O NMR from Phase 2 to Phase 3

The second phase transition occurs between phases 2 and 3 in a narrower electrochemical window (ca. $0.95<x<1.3$) and results in a sharp change in layer spacing (Table 1.1). The ^{7}Li NMR spectra during this transition display similar trends as in the transition between phases 1 and 2 (Figure 4.11). Initially ($x = 1.12$) the only peaks visible are those which correspond to the parent phase (phase 2) even though phase 3 should composed roughly 41% of the sample at this state of charge. Upon further delithiation to $x = 1.08$, there is almost no Li signal at all and even scaling the spectrum up by a factor of 32, the spectrum is dominated by a peak at 0ppm which is attributed to diamagnetic surface species. Finally charging the material so that only phase 3 is present ($x = 0.80$) results in a spectrum which resembles a broadened and slightly shifted version of the phase 2 spectrum ($x = 1.24$). The 75 ppm peak may be fit with a single Lorentzian, whilst the peak centred around 16 ppm requires at least two, which are considered together, as they represent similar environments and would be hard to separate accurately, as they overlap both with each other, and with the 0 ppm diamagnetic peak. Fitting the spectrum in this way suggests ca. 50% Li signal from each part of the spectrum and considering the overlap of the diamagnetic peak with the ca. 16 ppm peaks, this group of resonances is likely slightly overestimated. The T_2 measured for these two groups of resonances are ca. 0.5 ms and 0.7 ms for the 75 ppm and 16 ppm respectively which will not affect the observed intensities significantly. On further charging the peaks broaden further and move to higher shifts.

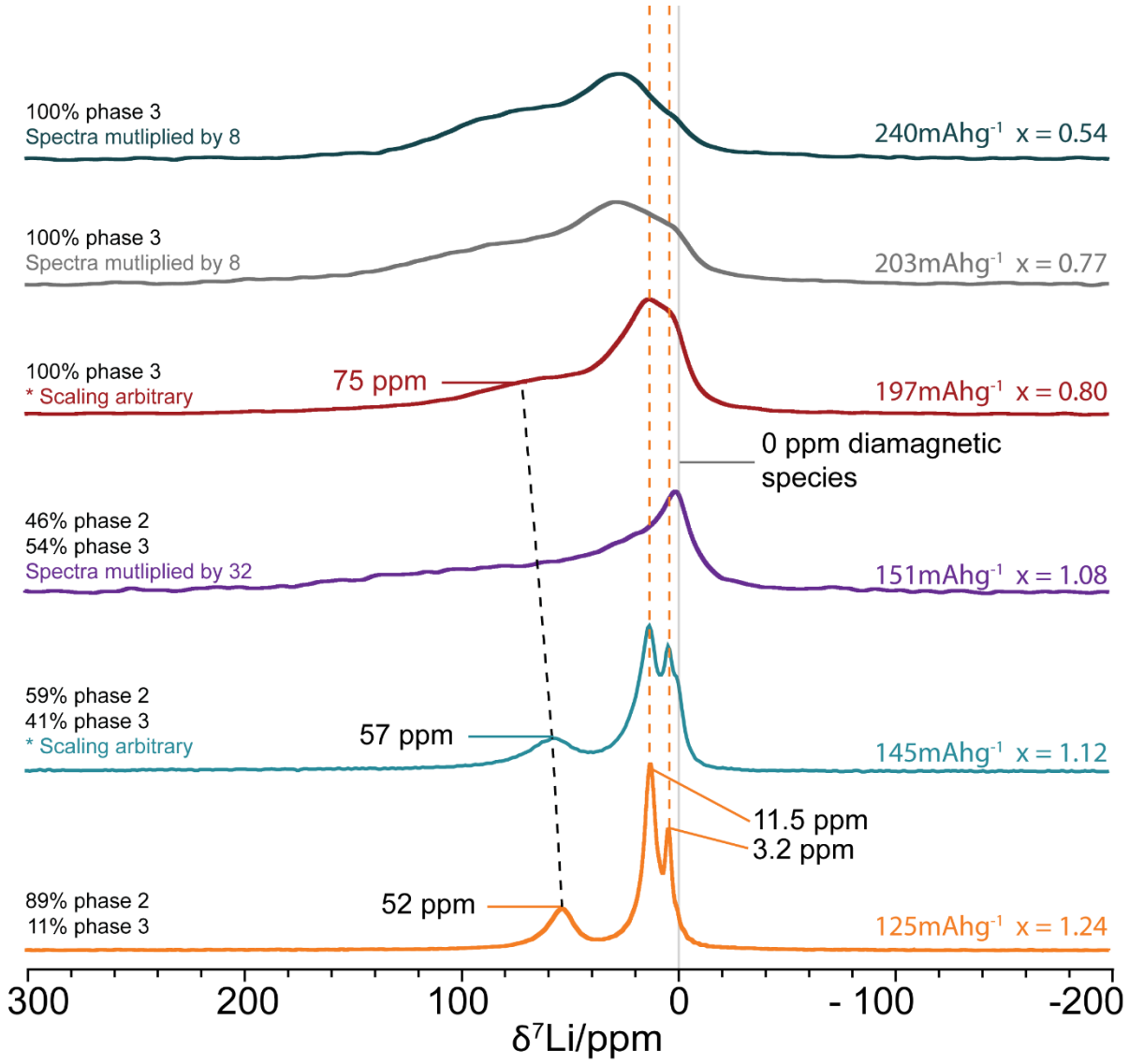

Figure 4.11 ^{7}Li NMR during the second part of the low voltage region, during which time phase 2 is converted into phase 3; this is followed by the high voltage plateau. The states of charge of the spectra are noted on the right-hand side. The spectra have been scaled by mass and number of scans so that they are quantitatively comparable, excepting the x = 1.12 (teal) and x = 0.80 (brown) samples. The black dashed line is a guide for the eye showing the evolution of the TM-layer Li peak. A grey line marks 0ppm, resonances at this shift are assigned to diamagnetic surface species. Approximate phase fractions derived from the Rietveld refinements of the in-situ XRD data at equivalent states of charge are displayed on the left-hand side of the spectra.

The ^{17}O NMR also shows broadening and a loss of signal on formation of phase 3 (Figure 4.12). The x = 0.51 sample shows significantly different peak positions in the quantitative recycle delay experiments (Figure 4.12a), however the intermediate recycle delay experiments reveal a spectrum resembles the x = 0.60 spectrum but moved to higher shift. This indicates that the signal observed in the intermediate recycled delay

spectrum has shorter relaxation time constants (T_1 and T_2) than both the signal observed in the long recycle delay experiments and the signal observed in the previous sample. Finally, experiments with extremely short recycle delays (0.005s) were carried out in order to enhance signal to noise ratios for the highly charged samples and also to apply an effective T_1 filter (Figure 4.12c). This experiment revealed that a significant spinning sideband manifold emerges for the x = 0.51 sample but that the same change does not occur for either the x =1.40 (ca. 87% phase 2 and 13% phase 1) or x = 0.60 (100% phase 3) samples.

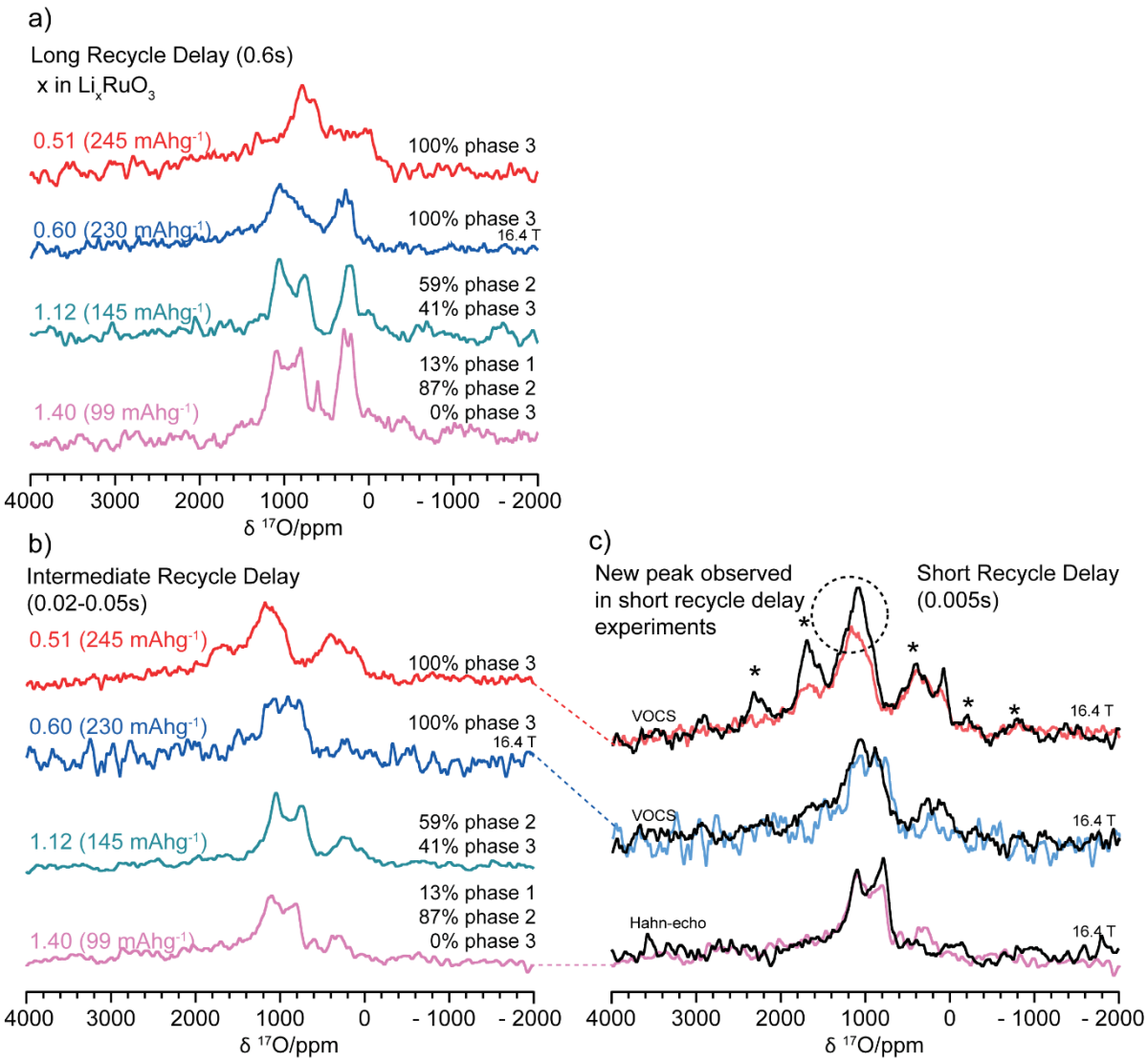

Figure 4.12 ^{17}O NMR on formation and charging of phase 3. a) Spectra recorded with quantitative (0.6 s) recycle delay. b) spectra recorded with an intermediate recycle delay (0.02-0.05 s) analogous to delays used for the post dimer-liquid transition in pristine Li_2RuO_3. These experiments were recorded as VOCS between 3000 and -1000 ppm but no shifts similar to the high temperature pristine experiments were observed. c) Spectra recorded with extremely short recycle delays are shown (in black) overlaid over their intermediate recycle delay analogues (coloured). The x = 0.51 sample displays prominent spinning sidebands which are marked by asterisks. Some spectra in this figure were recorded at 16.4 T rather than 11.7 T or by VOCS rather than by single Hahn-echo experiments; these differences are noted above the spectra. Approximate phase fractions derived from the Rietveld refinements of the in-situ XRD data at equivalent states of charge are displayed with their corresponding spectra.

4.4.6 ^{7}Li and ^{17}O NMR from Phase 2 to Phase 3 –Discussion

The general appearance of the NMR spectra on the initial formation of phase 3 (up to x = 0.80) is remarkably similar to spectra of both phases 1 and 2, particularly considering the large difference in layer spacing. The relatively small effect that this

quite dramatic structural transformation has on the NMR spectra indicates that it is not accompanied by wholesale changes in the electronic structure of the Ru layers, which tend to dominate the NMR spectra. The similarity of the electronic structure between phase 3 and phases 1 and 2 can be observed clearly in VT NMR experiments (Figure 4.13). The migration of the peaks, for both the mixed phase 1 and 2 sample (x = 1.40) and the sample for phase 3 on initial formation (x = 0.8), towards higher shifts as the temperature increases is the opposite trend as expected for a normal paramagnetic sample and is identical to the trend observed for phase 1 (Figure 4.8b). In the pristine case this behaviour was attributed to a thermally driven increase in the number of excited dimer states (Figure 4.9c) and hence an increase in the average number of unpaired spins. Such a thermally activated increase in unpaired spins would explain the observed behaviour for phase 2 and 3, at least on their formation.

Continued charging of phase 3, along the high voltage plateau gives rise to significant changes; in both ^{7}Li and ^{17}O NMR spectra, the peaks become broader and move to higher shifts. The broadening could be caused by several factors: electronic fluctuations, structural disorder and distortions and—in the case of ^{7}Li—mobility. The diffraction results from this study, as well as diffraction and XAS data from other authors,[127,240,243] indicate an increase in structural disorder during this plateau, which the broadening of the NMR spectra support, although the other factors may play a role as well. The Ru oxidation state for phase 3 is known to be Ru^{5+} and if it were undimerised very large shifts, due to the Fermi contact interaction, of even greater magnitude than those observed for ^{7}Li and ^{17}O in the post dimer-liquid transition spectra (Figure 3.7 and Figure 3.9) would be expected—i.e. 135 ppm and ca. 400 ppm for Li in the TM and Li layers respectively and ca. 2200 ppm for O. No such peaks were observed in frequency stepped experiments demonstrating that, even in phase 3 at the end of charge, the number of unpaired spins is relatively low.

The temperature dependence of the ^{7}Li spectrum at the end of charge (x = 0.55) is interesting. The high shift end of the spectrum increases in intensity on heating. This may be an effect of motion. As discussed previously (section 1.9.3), Li exchange with a similar frequency to the frequency separation of the exchanging sites, will give rise to enhanced T_2 relaxation, increasing the rate of hopping, such that each Li experiences an averaged field during the delay period of the echo, rather than several discrete fields, will ease the effects of this T_2 enhancement and give rise to a motionally narrowed, average signal, which may be occurring in this case. The temperature dependence of this peak, which appears to move to slightly higher shift on increasing temperature is somewhat ambiguous as a new peak growing in, at higher shift, which could be the cause of the increase in intensity, might result in apparent increase in shift of the original peaks. This is significant as it has been proposed that, on the basis of susceptibility and resistivity measurements, the $R\bar{3}$ phase is close to metallic and exhibits Pauli-paramagnetism.[247] The NMR shifts resulting from Pauli-paramagnetism (Knight shifts) do not generally display strong temperature dependence as the Pauli paramagnetic susceptibility is largely temperature independent, however in the case where the sample becomes more metallic with heating an increase could occur. For this reason and due the slightly ambiguous temperature dependence of the x = 0.55 sample, Pauli-paramagnetism cannot be ruled out in this case.

What seems clear is that on the formation of phase 3, the electronic structure is similar to phases 1 and 2 which strongly suggest the Li remains dimerised and that the dimers must be ordered in some way as no shifts similar to those observed above the dimer-liquid transition in pristine Li_2RuO_3 were observed. This contradicts $R\bar{3}$ structure,[124] which cannot accommodate different Ru–Ru distances and suggests the space group of this sample may have lower symmetry. Detailed diffraction studies are needed to confirm this. By the end of charge significant changes has occurred. The ^{17}O NMR may ultimately be a more sensitive probe as it is never lost from the lattice and occupies the same sites, relative to the Ru throughout. The presence of an oxygen signal with

much more prominent spinning sideband manifold indicates an increase in one of the anisotropic interactions the O experiences; either the quadrupolar interaction or the electron-nuclear dipolar interaction, although a combination of both seems likely. Despite this change the low shifts, which never increase to similar levels seen for the post-dimer liquid transition Li_2RuO_3 sample, strongly imply that even at the end of the charge the Ru is still, for the most part, dimerised.

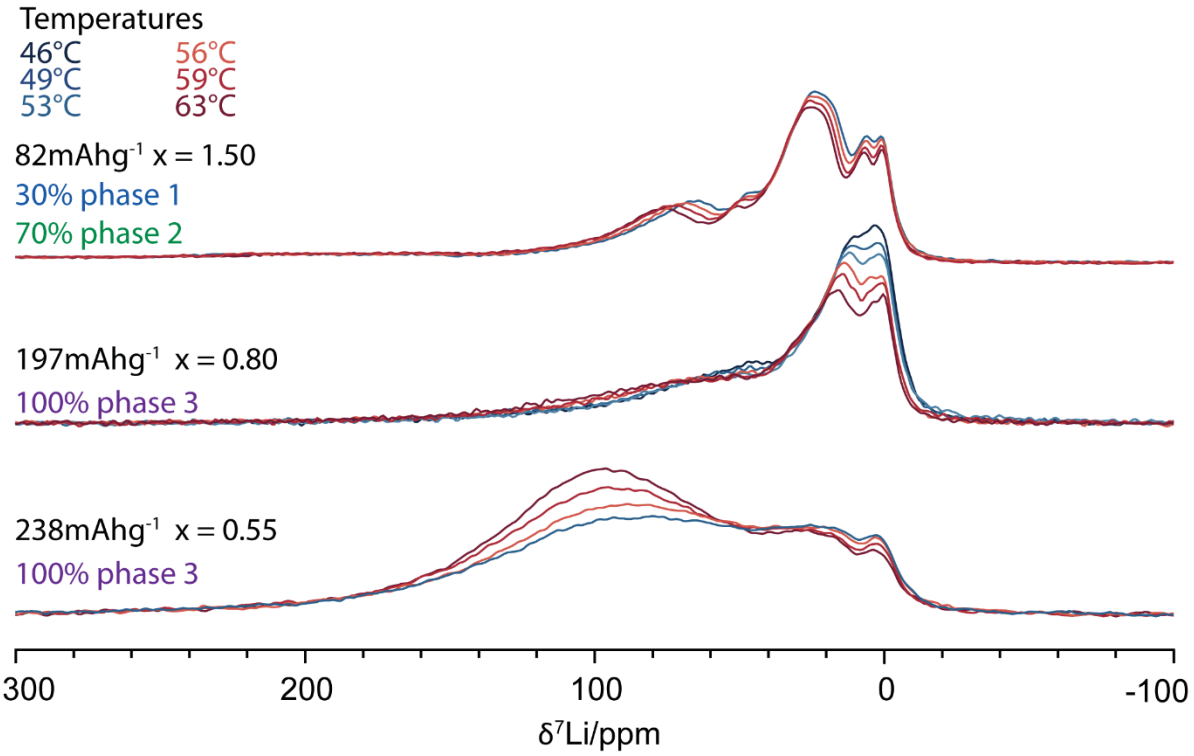

Figure 4.13 VT ^{7}Li NMR recorded at 60 kHZ MAS and 4.7 T. Temperature, composition and state of charge information is given in the figure.

Dimerisation is not the only possible ordering: The dimerisation in Li_2RuO_3 is particularly robust, as exemplified by the persistence of short Ru–Ru distances through the phase transition. However other orbital orderings are known for so called "213" compounds.[250] A model, in which electron motion is restricted to an individual TM_6 hexagon, but in which the electrons are delocalised within the hexagon is well established for related Ru and Ir compounds, particularly for $SrRu_2O_6$.[251] This motif, termed a "quasi-molecular orbital" (QMO) seems to prevail in systems where the electron delocalisation between TM sites is dominated by d–p hoping, rather than the

direct d–d hoping which seems to dominate for Li_2RuO_3 and gives rise to the metal-metal dimerisation. The exact nature of the electronic structure in $Li_{2-x}RuO_3$ is not clear. The low susceptibilities and small NMR shifts indicate the number of unpaired spins is low, however the lack of certainty about the exact structure (both long and short range) makes it impossible to say whether short Ru–Ru distances remain and therefore whether or not direct d–d interactions continue to dominate the orbital ordering. Even the preservation of the honeycomb ordering in the Ru-layer is not certain and migration of Ru (as is implied by some theories of O-redox)[136,140] might result in more extended clusters, such as the trimers observed for $LiVO_2$ or another unexpected ordering.[252] PDF measurements of delithiated samples would be invaluable in order to help ascertain not just the local structure but also the nature of the electron delocalisation. Without additional information, the continued dimerisation of the Ru is the most likely explanation for the observed magnetic properties and NMR spectra.

The prevailing explanation for the extraordinary capacity displayed by Li-excess materials is O redox and by the end of charge a significant amount of O redox must have occurred. For $Li_2Ir_{1-y}Sn_yO_3$, it has been suggested that the pure Li_2IrO_3 phase does not exhibit any oxygen redox and the large capacities exhibited are due to the oxidation of Ir to >5+.[140] Whilst it is possible that the electrochemical activity in Li_2RuO_3 is due entirely to Ru oxidation both the Ru XAS measurements and the observed electrochemical hysteresis both suggest O redox is the origin. As detailed in section 1.5.2, various mechanisms have been proposed to explain this phenomenon. One possibility is formation of peroxo-like O-dimers, which has proposed for various 4d/5d TM Li-excess materials,[130,138,243] The formation of these ca. 2.5Å O–O dimers is proposed to distort the RuO_6 octahedra, which can be accommodated due to the vacant Li TM-layer sites.[127,243,253] An alternate explanation is migration of TM metals into the Li-layer, leaving undercoordinated O atoms which can then either rehybridise a remaining coordinated TM ion, or pair with another undercoordinated O atom to form a short (ca. 1.5Å) O-dimer.[136,140] Indeed, computational study of Li_2RuO_3 have

suggested a cation migrated version of the $R\bar{3}$ structure is the thermodynamically stable structure at the end of charge.[241] If migration occurs, the rehybridization of dangling O electrons onto Ru seems likely as the formation of short O–O dimers was only predicted for Sn coordinated O atoms in the $Li_2Ir_{1-y}Sn_yO_3$ study.[140]

The effect on the NMR spectra of either of these processes should be significant. A key factor in both mechanisms is the loss of Li from the TM layers which, according to our tentative assignment does not occur completely on the formation of phase 3. Due to the uncertainty surrounding the electronic structure of phase 3 at the end of charge, it is difficult to make an assignment of the Li spectra on the basis of the observed shifts, however apparent Li mobility in the VT NMR is more likely for Li in the Li layers. Observations for other Li-excess materials show that in similar compounds, all the Li leaves the TM-layers by the end of charge.[65,95,111] If O–O dimers form in the material then it should result in extremely large quadrupolar coupling constants (C_Q), as was observed for Li-air discharge product Li_2O_2 (lithium peroxide), which displayed C_Q = ca. 18 MHz.[254,255] However, the long O dimers that are proposed to form in the "peroxo" mechanism have significantly longer O–O distances (ca. 2.5Å)[138] compared to the Li_2O_2 (ca. 1.28Å) and might result in smaller electric field gradients at the nucleus and consequently lower C_Q values. If Ru migration followed by the formation an O–Ru bond with a bond order >1, the shorter Ru–O distance as well as the loss a coordinating Ru ion will certainly change the electric field gradient (and thus C_Q) and the electron-nuclear dipolar interaction at the O nucleus, as well as the asymmetry of both, which could account for the growth of the spinning sideband manifold. The loss a Ru from the dimer matrix must surely perturb any Ru-dimer order that exists for phase 3 leading to an increase in unpaired spin density and therefore larger Fermi-contact shifts and electron nuclear dipolar interactions. Previous theoretical work suggests that Ru migration is thermodynamically favourable,[241] however in that work the Ru was undimerised and a limited number of arrangements were considered—i.e. no hybrid H1-

3 type stackings or tetrahedral Li environments, particularly "dumbbell defects" with tetrahedral Li coordinated around a vacancy in the TM layer (Li_{tet}–V–Li_{tet}), which have long been theorised to be thermodynamically stable and kinetically able to form at the end of charge in Li-excess materials.[58,94,256,257] Additional theoretical work which takes these possible structures into account and can account for the Ru–Ru dimers, which may persist unto the end of charge, would be extremely valuable. Whilst the NMR results cannot conclusively determine which mechanism occurs, indeed some combination of both may be occurring, the changes observed in both ^{7}Li and ^{17}O NMR which are steady and continuous, rather than dramatic and abrupt, suggest that until the very end of charge, much of the local and electronic structure remains relatively unchanged.

4.5 Conclusion

The complex delithiation behaviour of Li_2RuO_3 has been studied in order to unpick the long-range, local and electronic structure changes that it undergoes. ^{7}Li and ^{17}O NMR have been systematically applied and through their interpretation new information about this important model compound has been revealed.

During the low voltage, "conventional" redox portion of the charge process, it is shown that phase 2 is formed. This phase is broadly similar to the pristine material, despite the mixed $Ru^{4+/5+}$ oxidation state. ^{7}Li NMR demonstrates that Li is removed from both the Li and the TM layers on the formation of phase 2. The composition of phase 2 refined ($Li_{1.3}RuO_3$) is extremely close to $Li_{1.33}RuO_3$, which would imply an average Ru oxidation of 4.67+ or a Ru^{5+}:Ru^{4+} ratio of 2:1, and it is possible to imagine that this neat charge-stoichiometry might lend itself to an ordered array of Ru^{4+} and Ru^{5+}. Both phase 1 and phase 2 seem able to accommodate some degree of non-stoichiometry. During their 2-phase coexistence, there is a loss of signal, in the ^{7}Li NMR in particular. A similar signal loss is associated with the approach of the phase transition and a rise

in the electronic fluctuations, in the pristine material. This suggests similar disturbance of the Ru–Ru dimer ordering in both phases during this period.

Phase 3, on initial formation, is also somewhat similar to phases 1 and 2 in terms of its NMR spectra, despite the large structural changes that occur, indicate that on formation of phase 3, Ru is likely still dimerised. This hypothesis is supported by the temperature dependence of the ^{7}Li NMR shifts, which suggest a temperature activated increase in unpaired spin density for phases 1 and 2 and for phase 3 on initial formation.

During the high voltage region. Evidence of disordering is observed in both the ^{17}O and ^{7}Li NMR spectra. By the end of charge, the observation of an increase in Li signal upon heating, which suggest Li motion, indicates that the remaining Li is likely in the Li-layer, as motion in these sites seems more plausible. The more highly shifted peaks and the emergence of a stronger spinning sideband manifold at the end of charge for ^{17}O show a change in the electronic structure of some O has occurred. Considering the state of charge at which this change is observed ($Li_{0.55}RuO_3$)—if it is assumed all the capacity expended beyond the $Ru^{4/5+}$ redox couple is compensated by oxygen redox—this suggests a composition of approximately $Li_{0.55}Ru^{5+}O^{2-}_{2.5}O^{-1}_{0.5}$. If this O oxidation is compensated by Ru migration (making for the moment the assumption that Ru migrates as 5+) followed by "ligand-metal charge transfer", via the mechanism proposed for $Li_2Ir_{1-x}Sn_xO_3$ by Hong et al.[140] (i.e. formation of TM–O bonds with a bond order >1) each migrating ion accounts, on average 4e$^-$, which implies ca. $1/8Ru^{5+}$ must migrate. If it is assumed that Ru^{5+} is unlikely to occupy octahedral Li-layer sites due to its small ionic size (0.565Å) and high charge, then the possibility that Ru^{5+} is re-reduced back to 4+ or else occupies tetrahedral dumbbell sites must be considered. Such a reduction might explain the shifting back towards lower Ru oxidation observed by other authors in the XAS measurements.[127,258]

One striking absence from the NMR studies, both ^{7}Li and ^{17}O is a shift corresponding to either and oxidised O ion itself, or a Li shifted by an oxidised O ion (which would

have an unpaired electron). It is possible such a signal may not be observable—likely in the case of an isolated O^- ion—or may overlap with the other signals—possible in the case of Li shifted by O^-—however, the lack of both seems to condemn the idea of an isolated O^- ion. As stated above, the "ligand-metal charge transfer" hypothesis predicts a significant population of O ions, presumably still formally O^{2-} owing to their rehybridisation with Ru, which should be observable in our measurement—it has been established that signals from ions participating in M–O rehybridisation can be observed in the ^{59}Co studies detailed in Chapter 2. These environments might be expected to have significantly different C_q values than the other sites and may have moderately different chemical shifts. This may be the origin of the more paramagnetic peak observed at the very end of charge.

Ultimately more work, both computational and experimental is required if the redox mechanism at the end of charge is to be determined, but the results of this study are sufficient to discard some hypotheses, namely the formation of O^- ions. This work presents strong evidence that the role dimers play in Li_2RuO_3 is felt throughout the charge and the effects they have need to be considered seriously in the future, in the interpretation of the experimental results and particularly in theoretical calculations.

Chapter 5: Conclusions and Future Work

The principal objective of this work was to build upon the well-established NMR methodology for studying battery materials by expanding the range of nuclei considered to include more "exotic" species such as ^{59}Co and ^{17}O. By using these relatively under-exploited probes it was hoped that new insights into battery cathodes with significance either as industrially relevant materials (NCA) or as model compounds for the anionic redox phenomena (Li_2RuO_3).

From the perspective of method development, ^{17}O NMR has been employed in very few paramagnetic systems before. Li_2MnO_3 was the first study of a paramagnetic Li-ion cathode material,[101] paramagnetic oxygen NMR was employed to study the oxygen ion conductor $La_2NiO_{4+\delta}$,[259] and very recently it was employed in the study of $LiCoO_2$ on 1st charge.[103] The ^{17}O study of Li_2RuO_3 presented Chapter 4 of this work is the first study of ^{17}O NMR on delithiated samples, in which the signals for ^{17}O are observable at all states of charge. This has enabled their evolution to be tracked for the first time. The bond pathway approach which has allow intuitive interpretation of Li NMR spectra in paramagnetic materials, particularly $LiTMO_2$ materials,[155,163] has been utilised and extended in Chapter 3 by combining the results of first principals calculations with experimental spectra and consideration of the coordination geometry of each O site. This is a significant step in the journey of ^{17}O NMR for paramagnetic materials and demonstrates, if an appropriate system is chosen, ^{17}O spectra can be obtained on electrochemical cycling and useful scientific insight obtained. Although on delithiation ^{59}Co NMR has been studied before, notably for $LiCoO_2$,[103] no signals at the end of charge have been reported. In $LiCoO_2$ the sharp diamagnetic signal at ca. 14400 ppm is gradually lost, presumably due to conversion of observable Co^{3+} into $Co^{4+}$and the subsequent metal-insulator-transiton.[103] The presence of Co^{3+} at the end of charge for NCA (Chapter 2) was unanticipated but is not inexplicable, as it has long been mooted that the electrochemical behaviour of Co is not as simple as $Co^{3+}\rightarrow Co^{4+}$,

due to its weak K-edge XANES shift.[67] Co exhibits strong hybridisation with O, so in systems where no metal insulator transition is present, even if the Co is "oxidised fully"—that is Li is extracted such that an oxidation change of Co from 3+ to 4+ is expected and no "O-redox" features are observed—then ^{59}Co signal may be observable. This signal may offer some insight into the band structure of the material as the quantity of Co^{3+} and therefore, the quantity of the Co–O hybrid states which are oxidised, may be established. A valuable extension to this work would be perform complete relaxometry measurements on the ^{59}Co NMR samples and careful quantification measurements, as this would allow these insights to be gained for NCA.

For other Co containing compounds such as NMC ($LiNi_XMn_YCo_ZO_2$) some preliminary work has already been conducted, although the presence of the additional Mn^{4+} Fermi-contact shifts broaden the spectra further, thus measurements, which require VOCS to record in full, are much more time consuming. Another good extension to this work would be the study of a largely diamagnetic compound, possibly $LiAl_xCo_yO_2$, in which the effects of the changing Fermi-contact shift and the changing paramagnetic chemical shift could be separated. For such a study complimentary K and L-edge XANES would be extremely valuable.

For NCA, in addition to the above, a clearer picture has been built up of the characteristics of the TM layer—that is JT distortions are dynamic but that the average structure reflects orderings around the "defect atoms" which are in line with what would be expected for an ordered array of dimers. The increase in Li motion, which has recently been observed in NMC811[26] and which may play a role in the development of reaction heterogeneity and degradation, has been demonstrated.[205,206]

For the Li_2RuO_3, the characterisation of the pristine and cycled materials has enabled a complete picture of the NMR of the material to be built up. Recording *ex-situ* XRD, SQUID magnetometry and NMR on the pure phases as they form and at the very end of charge would be a valuable extension of the work and would facilitate the assignment

of the NMR spectra and characterisation of both the local and electronic structure. The high temperature VT NMR of the pristine material establish what NMR characteristics should be observed for dimer-liquid Ru^{4+}. The shifts from these experiments are themselves, far smaller than would be expected for isolated $Ru^{4/5+}$ ions and therefore the fact that, on charging, the NMR shifts don't exceed or even come close to these values, suggests strongly that the dimerisation is preserved until the very end of charge. This is a significant finding and one that could not have been revealed by ^{7}Li NMR alone, which becomes a less useful probe as the Li concentration decreases. The study of the doped phases of Li_2RuO_3, particularly the Sn doped phase, which only introduces diamagnetic Sn^{4+} (itself potential another NMR probe) and may change the mechanism of oxidised O stabilisation (Sn^{4+} migration rather than Ru^{4+}), would be interesting further work in this area.

In order to truly understand current Li-ion battery cathodes and to design the next generation of materials, their charge compensation mechanism—arguably their most essential attribute—must be understood. In this work, it has been shown that even for one of the most industrially popular cathodes (NCA), the models used at present fail to capture the precise nature of the Co oxidation. Through the study of Li_2RuO_3 it has been shown how challenging it can be to unpick the electronic structure of even a so-called model compound, particularly on delithiation. The question of what the precise nature of anionic redox is remains hotly contested.

Part of the difficulty of finding an acceptable mechanism for anionic redox lies in fact that all explanations are somewhat unpalatable and require some willing suspension of disbelief. Yet, no neat, chemically intuitive theory has been or, in the author's opinion, will be forthcoming. Turning our attention critically to each of the main hypotheses discussed in section 1.5.2:

I. "Peroxo-like" species formation: The observed RIXs features are not consistent calculated RIXs, either for O–O bond distances predicted by calculation (.ca

1.9 Å for LR-NMC),[136] or observed by HAADF-STEM (for Li_2IrO_3).[138] These species would give rise to a RIXs feature at lower absorption energies (<529 eV).[136] The observed 531 eV feature is more consistent with the shorter bond distances in molecular O_2 (1.20 Å)[260] or Li_2O_2 (1.49 Å).[145,261]

II. Isolated hole states on O^-: These defy chemical intuition and although examples of such from the field of high T superconductivity have been cited,[133,262] in these cases the hole states on O are generally understood to delocalise across 4 of the O ions coordinating a Cu^{2+} and that it combines with electron spin on Cu^{2+} to form a spin singlet. [263] This is a far cry from an isolated O^- ion and suggests these species will likely be stabilised through covalency if they form.

III. Transition metal migration followed by charge ligand-metal charge transfer: It is the author's opinion that this the most compelling theory to date, as in addition to explaining the extra capacity, it deals neatly with the characteristic attributes of O-redox (voltage fade, 1st cycle irreversibility etc.). It is also relatively easy to point to diffraction studies which show TM metal migration in Li-excess compounds.[136,140] Yet it is not a perfect explanation. TM migration is known to occur at high voltage (particularly on the surface)[114] so the evidence from diffraction is not conclusive. Furthermore, the ambiguity about how the resultant oxidised O species are stabilised creates an obstacle to experimental verification.[140]

Of course, owing to the difficultly of explaining the anionic redox phenomenon, many alternative explanations are being proposed continuously for example:

I. Oxidation to of TM ions to higher oxidations states, specifically in the Mn containing materials Mn^{4+} in octahedral sites, migrating to tetrahedral sites as Mn^{7+}.[110]

II. Formation of O_2-like species (O–O distance, ca. 1.21 Å) which are coordinated by Mn^{4+} via a short Mn–O bond (ca. 2.2 Å) giving a Mn–η1–O_2 moiety contained within the crystal structure.[261]

Both these theories have the advantage of a clear signature that might be experimentally detected, Mn^{7+} for the former and an O_2 species coordinated by 1 Mn in the latter and time will tell whether such experimental evidence will be forthcoming.

Throughout the discussion of the myriad explanation of why and how anionic redox occurs, it should be clear that many of the theories outlined are not mutually exclusive. Ultimately an extremely challenging problem, such as anionic redox, is good for the field of battery science, as it has spurred the development and extension of many existing techniques. On a small scale, it is not dissimilar to the space race, where many innovations borne out of rigorous constraints and requirements, found their way into other arenas afterwards. So too developments made in the pursuit of unravelling anion redox, will have applications in studying redox processes in other materials, as well as in science in general. It is my hope that the techniques used in this work, will find other hands to carry them forward and that paramagnetic NMR of "exotic" nuclei will continue to see use, not just the field of battery materials, but also in any field where their application might provide new insight.

References

1 T. Yamahira, H. Kato and M. Anzai, *J. Power Sources*, 1996, 63, 303.

2 D. MacKay, *Sustainable Energy – without the hot air*, UIT Cambridge Ltd., Cambridge, 1st edn., 2008.

3 House of Commons Business Energy and Industrial Strategy and Committee, 2018, 65.

4 J. Macdonald, *Bloom. New Energy Financ.*, 2016, 1–2.

5 R. A. Huggins, *Advanced Batteries Materials Science Aspects*, Springer US, LaVergne, 1st edn., 2008.

6 J. B. Goodenough and Y. Kim, *Chem. Mater.*, 2010, 22, 587–603.

7 J. Xiao, W. Xu, D. Wang, D. Choi, W. Wang, X. Li, G. L. Graff, J. Liu and J.-G. Zhang, *J. Electrochem. Soc.*, 2010, 157, A1047.

8 A. R. Armstrong, M. Holzapfel, P. Novák, C. S. Johnson, S. H. Kang, M. M. Thackeray and P. G. Bruce, *J. Am. Chem. Soc.*, 2006, 128, 8694–8698.

9 K. Mizushima, P. C. Jones, P. J. Wiseman and J. B. Goodenough, *Solid State Ionics*, 1981, 3–4, 171–174.

10 J. Lee, A. Urban, X. Li, D. Su, G. Hautier and G. Ceder, *Science (80-.).*, 2014, 343, 519–522.

11 R. Wang, X. Li, L. Liu, J. Lee, D. H. Seo, S. H. Bo, A. Urban and G. Ceder, *Electrochem. commun.*, 2015, 60, 70–73.

12 N. Twu, X. Li, A. Urban, M. Balasubramanian, J. Lee, L. Liu and G. Ceder, *Nano Lett.*, 2015, 15, 596–602.

13 R. Chen, S. Ren, M. Knapp, D. Wang, R. Witter, M. Fichtner and H. Hahn,

Adv. Energy Mater., 2015, 5, 1–7.

14 N. Yabuuchi, K. Yoshii, S.-T. Myung, I. Nakai and S. Komaba, *J. Am. Chem. Soc.*, 2011, 133, 4404–4419.

15 N. Yabuuchi, *Chem. Lett.*, 2016, 46, 412–422.

16 A. Abdellahi, A. Urban, S. Dacek and G. Ceder, *Chem. Mater.*, 2016, 28, 3659–3665.

17 M. S. Whittingham, *Chem. Rev.*, 2004, 104, 4271–4301.

18 E. Plichta, M. Salomon, S. Slane, M. Uchiyama, D. Chua and W. B. Ebner, *J. Power Sources*, 1987, 21, 25–31.

19 C. Delmas, C. Fouassier and P. Hagenmuller, *Phys. B+C*, 1980, 99, 81–85.

20 W. Li, J. Reimers and J. Dahn, *Solid State Ionics*, 1993, 67, 123–130.

21 A. Van der Ven, M. K. Aydinol, G. Ceder, G. Kresse and J. Hafner, *Phys. Rev. B*, 1998, 58, 2975–2987.

22 Z. Chen, Z. Lu and J. R. Dahn, *J. Electrochem. Soc.*, 2002, 149, A1604.

23 R. Yazami, Y. Ozawa, H. Gabrisch and B. Fultz, *Electrochim. Acta*, 2004, 50, 385–390.

24 A. Yano, M. Shikano, A. Ueda, H. Sakaebe and Z. Ogumi, *J. Electrochem. Soc.*, 2017, 164, A6116–A6122.

25 M. Ma, N. A. Chernova, B. H. Toby, P. Y. Zavalij and M. S. Whittingham, *J. Power Sources*, 2007, 165, 517–534.

26 K. Märker, P. J. Reeves, C. Xu, K. J. Griffith and C. P. Grey, *Chem. Mater.*, 2019, 31, 2545–2554.

27 M. K. Aydinol, A. F. Kohan, G. Ceder and K. C. and J. Joannopoulos, 1997, 56,

1–12.

28 M. Aykol, S. Kim and C. Wolverton, *J. Phys. Chem. C*, 2015, 119, 19053–19058.

29 M. Ménétrier, I. Saadoune, S. Levasseur and C. Delmas, *J. Mater. Chem.*, 1999, 9, 1135–1140.

30 M. Ménétrier, D. Carlier, M. Blangero and C. Delmas, 2008, 8–11.

31 A. Manthiram, J. C. Knight, S.-T. Myung, S.-M. Oh and Y.-K. Sun, *Adv. Energy Mater.*, 2016, 6, 1501010.

32 S. Laubach, S. Laubach, P. C. Schmidt, D. Ensling, S. Schmid, W. Jaegermann, A. Thißen, K. Nikolowskid and H. Ehrenberge, *Phys. Chem. Chem. Phys.*, 2009, 11, 3010.

33 A. Rougier, C. Delmas and A. V. Chadwick, *Solid State Commun.*, 1995, 94, 123–127.

34 I. Nakai, K. Takahashi, Y. Shiraishi, T. Nakagome, F. Izumi, Y. Ishii, F. Nishikawa and T. Konishi, *J. Power Sources*, 1997, 68, 536–539.

35 R. Stoyanova, E. Zhecheva and C. Friebel, *J. Phys. Chem. Solids*, 1993, 54, 9–13.

36 C. Delmas, M. Ménétrier, L. Croguennec, I. Saadoune, A. Rougier, C. Pouillerie, G. Prado, M. Grüne and L. Fournès, *Electrochim. Acta*, 1999, 45, 243–253.

37 C. Liang, F. Kong, R. C. Longo, C. Zhang, Y. Nie, Y. Zheng and K. Cho, *J. Mater. Chem. A*, 2017, 5, 25303–25313.

38 C. Pouillerie, E. Suard and C. Delmas, *J. Solid State Chem.*, 2001, 158, 187–197.

39 S. H. R. J. Gummow, M. M. Thackeray, W. I. F. David, *Mater. Res. Bull.*, 1992, 27, 327–337.

40 X. Xiang and W. Li, *Electrochim. Acta*, 2014, 133, 422–427.

41 T. A. Arunkumar, Y. Wu and A. Manthiram, *Chem. Mater.*, 2007, 19, 3067–3073.

42 J. Morales, C. Pérez-Vicente and J. L. Tirado, *Mater. Res. Bull.*, 1990, 25, 623–630.

43 T. Ohzuku, A. Ueda and M. Nagayama, *J. Electrochem. Soc.*, 1993, 140, 1862.

44 N. A. Chernova, G. M. Nolis, F. O. Omenya, H. Zhou, Z. Li and M. S. Whittingham, *J. Mater. Chem.*, 2011, 21, 9865–9875.

45 N. A. Chernova, M. Ma, J. Xiao, M. S. Whittingham, J. Breger and C. P. Grey, *Chem. Mater.*, 2007, 19, 4682–4693.

46 A. Rougier, C. Delmas and G. Chouteau, *J. Phys. Chem. Solids*, 1996, 57, 1101–1103.

47 K. Yamaura, M. Takano, A. Hirano and R. Kanno, *J. Solid State Chem.*, 1996, 127, 109–118.

48 F. Capitaine, P. Gravereau and C. Delmas, *Solid State Ionics*, 1996, 89, 197–202.

49 P. G. Bruce, a. R. Armstrong and R. L. Gitzendanner, *J. Mater. Chem.*, 1999, 9, 193–198.

50 M. M. Thackeray, *Prog. Solid State Chem.*, 1997, 25, 1–71.

51 J. R. Dahn, E. W. Fuller, M. Obrovac and U. von Sacken, *Solid State Ionics*, 1994, 69, 265–270.

52 S. Choi and A. Manthiram, *J. Electrochem. Soc.*, 2002, 149, A162.

53 M. G. S. R. Thomas, W. I. F. David, J. B. Goodenough and P. Groves, *Mater. Res. Bull.*, 1985, 20, 1137–1146.

54 C. Wolverton and A. Zunger, *J. Electrochem. Soc.*, 1998, 145, 2424.

55 L. Wang, T. Maxisch and G. Ceder, *Chem. Mater.*, 2007, 19, 543–552.

56 a Van Der Ven and G. Ceder, *Electrochem. Solid-State Lett.*, 2000, 3, 301–304.

57 A. Van der Ven and G. Ceder, *J. Power Sources*, 2001, 97–98, 529–531.

58 J. Reed, G. Ceder and a. Van Der Ven, *Electrochem. Solid-State Lett.*, 2001, 4, A78.

59 J. Reed and G. Ceder, *Chem. Rev.*, 2004, 104, 4513–4534.

60 A. Rougier, I. Saadoune, P. Gravereau, P. Willmann and C. Delmas, *Solid State Ionics*, 2003, 90, 83–90.

61 N. V. Faenza, N. Pereira, D. M. Halat, J. Vinckeviciute, L. Bruce, M. D. Radin, P. Mukherjee, F. Badway, A. Halajko, F. Cosandey, C. P. Grey, A. Van Der Ven and G. G. Amatucci, *Chem. Mater.*, 2018, 30, 7545–7574.

62 I. Saadoune, M. Ménétrier and C. Delmas, *J. Mater. Chem.*, 1997, 7, 2505–2511.

63 Z. W. Lebens-Higgins, N. V. Faenza, M. D. Radin, H. Liu, S. Sallis, J. Rana, J. Vinckeviciute, P. J. Reeves, M. J. Zuba, F. Badway, N. Pereira, K. W. Chapman, T.-L. Lee, T. Wu, C. P. Grey, B. C. Melot, A. Van Der Ven, G. G. Amatucci, W. Yang and L. F. J. Piper, *Mater. Horizons*, , DOI:10.1039/c9mh00765b.

64 M. D. Radin, S. Hy, M. Sina, C. Fang, H. Liu, J. Vinckeviciute, M. Zhang, M. S. Whittingham, Y. S. Meng and A. Van der Ven, *Adv. Energy Mater.*, 2017, 7, 1602888.

65 W.-S. Yoon, Y. Paik, X.-Q. Yang, M. Balasubramanian, J. McBreen and C. P. Grey, *Electrochem. Solid-State Lett.*, 2002, 5, A263.

66 S. J. Hwang, H. S. Park and J. H. Choy, in *Solid State Ionics*, 2002.

67 W.-S. Yoon, K.-B. Kim, M.-G. Kim, M.-K. Lee, H.-J. Shin, J.-M. Lee, J.-S. Lee and C.-H. Yo, *J. Phys. Chem. B*, 2002, 106, 2526–2532.

68 R. Qiao, J. Liu, K. Kourtakis, M. G. Roelofs, D. L. Peterson, J. P. Duff, D. T. Deibler, L. A. Wray and W. Yang, *J. Power Sources*, 2017, 360, 294–300.

69 W.-S. Yoon, C. P. Grey, M. Balasubramanian, X.-Q. Yang, D. a. Fischer and J. McBreen, *Electrochem. Solid-State Lett.*, 2004, 7, A53.

70 W. Yoon, M. Balasubramanian, K. Y. Chung, X. Yang, J. Mcbreen, C. P. Grey and D. A. Fischer, 2005, 17479–17487.

71 S. Hwang, W. Chang, S. M. Kim, D. Su, D. H. Kim, J. Y. Lee, K. Y. Chung and E. A. Stach, *Chem. Mater.*, 2014, 26, 1084–1092.

72 F. Lin, I. M. Markus, D. Nordlund, T.-C. Weng, M. D. Asta, H. L. Xin and M. M. Doeff, *Nat. Commun.*, 2014, 5, 1–9.

73 Z. Lu, D. D. MacNeil and J. R. Dahn, *Electrochem. Solid-State Lett.*, 2001, 4, A191.

74 Z. Lu, D. D. MacNeil and J. R. Dahn, *Electrochem. Solid-State Lett.*, 2001, 4, A191.

75 T. Ohzuku and Y. Makimura, *Chem. Lett.*, 2001, 2, 744–745.

76 Z. Lu, L. Y. Beaulieu, R. a. Donaberger, C. L. Thomas and J. R. Dahn, *J. Electrochem. Soc.*, 2002, 149, A778.

77 J. R. Croy, D. Kim, M. Balasubramanian, K. Gallagher, S.-H. Kang and M. M. Thackeray, *J. Electrochem. Soc.*, 2012, 159, A781.

78 N. Yabuuchi, M. Takeuchi, M. Nakayama, H. Shiiba, M. Ogawa, K. Nakayama, T. Ohta, D. Endo, T. Ozaki, T. Inamasu, K. Sato and S. Komaba, *Proc. Natl. Acad. Sci. U. S. A.*, 2015, 112, 7650–5.

79 A. C. W. P. James and J. B. Goodenough, 1988, 294, 287–294.

80 M. J. O'Malley, H. Verweij and P. M. Woodward, *J. Solid State Chem.*, 2008,

181, 1803–1809.

81 P. Strobel and B. Lambert-Andron, *J. Solid State Chem.*, 1988, 75, 90–98.

82 V. Massarotti, M. Bini, D. Capsoni, a. Altomare and a. G. G. Moliterni, *J. Appl. Crystallogr.*, 1997, 30, 123–127.

83 B. Ammundsen and J. Paulsen, *Adv. Mater.*, 2001, 13, 943–956.

84 C. Zhan, T. Wu, J. Lu and K. Amine, *Energy Environ. Sci.*, 2018, 11, 243–257.

85 Z. Lu, Z. Chen and J. R. Dahn, *Chem. Mater.*, 2003, 15, 3214–3220.

86 H. Kobayashi, H. Sakaebe, H. Kageyama, K. Tatsumi, Y. Arachi and T. Kamiyama, *J. Mater. Chem.*, 2003, 13, 590–595.

87 Z. Lu, L. Y. Beaulieu, R. a. Donaberger, C. L. Thomas and J. R. Dahn, *J. Electrochem. Soc.*, 2002, 149, A778.

88 Y. S. Meng, G. Ceder, C. P. Grey, W. Yoon, M. Jiang and J. Bre, *Powder Diffr.*, 2006, 2, 2404–2412.

89 M. S. Islam, R. A. Davies and J. D. Gale, *Chem. Mater.*, 2003, 15, 4280–4286.

90 W. S. Yoon, S. Iannopollo, C. P. Grey, D. Carlier, J. Gorman, J. Reed and G. Ceder, *Electrochem. Solid State Lett.*, 2004, 7, A167–A171.

91 Z. Lu and J. R. Dahn, *J. Electrochem. Soc.*, 2002, 149, A815.

92 K. Kang, Y. S. Meng, J. Bréger, C. P. Grey and G. Ceder, *Science (80-.).*, 2006, 311, 977–980.

93 J. Breger, K. Kang, J. Cabana, G. Ceder and C. P. Grey, *J. Mater. Chem.*, 2007, 17, 3167.

94 C. P. Grey, W.-S. Yoon, J. Reed and G. Ceder, *Electrochem. Solid-State Lett.*, 2004, 7, A290.

95 W.-S. Yoon, N. Kim, X.-Q. Yang, J. McBreen and C. P. Grey, *J. Power Sources*, 2003, 119–121, 649–653.

96 J. Bréger, N. Dupré, P. J. Chupas, P. L. Lee, T. Proffen, J. B. Parise and C. P. Grey, *J. Am. Chem. Soc.*, 2005, 127, 7529–7537.

97 R. Shunmugasundaram, R. S. Arumugam and J. R. Dahn, *J. Electrochem. Soc.*, 2016, 163, A1394–A1400.

98 A. Boulineau, L. Croguennec, C. Delmas and F. Weill, *Chem. Mater.*, 2009, 21, 4216–4222.

99 M. D. Radin, J. Alvarado, Y. Shirley Meng and A. Van der Ven, *Nano Lett.*, 2017, 17, 7789–7795.

100 J. Bréger, M. Jiang, N. Dupré, Y. S. Meng, Y. Shao-Horn, G. Ceder and C. P. Grey, *J. Solid State Chem.*, 2005, 178, 2575–2585.

101 I. D. Seymour, D. S. Middlemiss, D. M. Halat, N. M. Trease, A. J. Pell and C. P. Grey, *J. Am. Chem. Soc.*, 2016, 138, 9405–9408.

102 F. Dogan, J. R. Croy, M. Balasubramanian, M. D. Slater, H. Iddir, C. S. Johnson, J. T. Vaughey and B. Key, *J. Electrochem. Soc.*, 2014, 162, A235–A243.

103 F. Geng, M. Shen, B. Hu, Y. Liu, L. Zeng and B. Hu, *Chem. Commun.*, 2019, 7550–7553.

104 M. M. Thackeray, S.-H. Kang, C. S. Johnson, J. T. Vaughey, R. Benedek and S. A. Hackney, *J. Mater. Chem.*, 2007, 17, 3112.

105 C. S. Johnson, N. Li, C. Lefief and M. M. Thackeray, *Electrochem. commun.*, 2007, 9, 787–795.

106 C. S. Johnson, N. Li, C. Lefief, J. T. Vaughey and M. M. Thackeray, *Chem. Mater.*, 2008, 20, 6095–6106.

107 M. M. Thackeray, S.-H. Kang, C. S. Johnson, J. T. Vaughey and S. A. Hackney, *Electrochem. commun.*, 2006, 8, 1531–1538.

108 B. R. Long, J. R. Croy, F. Dogan, M. R. Suchomel, B. Key, J. Wen, D. J. Miller, M. M. Thackeray and M. Balasubramanian, *Chem. Mater.*, 2014, 26, 3565–3572.

109 A. K. Shukla, Q. M. Ramasse, C. Ophus, H. Duncan, F. Hage and G. Chen, *Nat. Commun.*, 2015, 6, 8711.

110 M. D. Radin, J. Vinckeviciute, R. Seshadri and A. Van der Ven, *Nat. Energy*, 2019, 4, 639–646.

111 M. Jiang, B. Key, Y. S. Meng and C. P. Grey, *Chem. Mater.*, 2009, 21, 2733–2745.

112 A. D. Robertson and P. G. Bruce, *Electrochem. Solid-State Lett.*, 2004, 7, A294.

113 A. D. Robertson and P. G. Bruce, *Chem. Mater.*, 2003, 15, 1984–1992.

114 N. Tran, L. Croguennec, M. Ménétrier, F. Weill, P. Biensan, C. Jordy and C. Delmas, *Chem. Mater.*, 2008, 20, 4815–4825.

115 S. Sallis, N. Pereira, P. Mukherjee, N. F. Quackenbush, N. Faenza, C. Schlueter, T. L. Lee, W. L. Yang, F. Cosandey, G. G. Amatucci and L. F. J. Piper, *Appl. Phys. Lett.*, 2016, 108, 263902.

116 L. Wu, K.-W. Nam, X. Wang, Y. Zhou, J.-C. Zheng, X.-Q. Yang and Y. Zhu, *Chem. Mater.*, 2011, 23, 3953–3960.

117 D. Aurbach, M. . Levi, K. Gamulski, B. Markovsky, G. Salitra, E. Levi, U. Heider, L. Heider and R. Oesten, *J. Power Sources*, 1999, 81–82, 472–479.

118 H. Zheng, Q. Sun, G. Liu, X. Song and V. S. Battaglia, *J. Power Sources*, 2012, 207, 134–140.

119 A. Boulineau, L. Simonin, J.-F. Colin, C. Bourbon and S. Patoux, *Nano Lett.*,

2013, 13, 3857–3863.

120 K. G. Gallagher, J. R. Croy, M. Balasubramanian, M. Bettge, D. P. Abraham, A. K. Burrell and M. M. Thackeray, *Electrochem. commun.*, 2013, 33, 96–98.

121 H. Koga, L. Croguennec, M. Ménétrier, P. Mannessiez, F. Weill and C. Delmas, *J. Power Sources*, 2013, 236, 250–258.

122 H. Koga, L. Croguennec, M. Ménétrier, K. Douhil, S. Belin, L. Bourgeois, E. Suard, F. Weill and C. Delmas, *J. Electrochem. Soc.*, 2013, 160, A786–A792.

123 K. Luo, M. R. Roberts, R. Hao, N. Guerrini, D. M. Pickup, Y.-S. Liu, K. Edström, J. Guo, A. V. Chadwick, L. C. Duda and P. G. Bruce, *Nat. Chem.*, 2016, 8, 684–691.

124 H. Kobayashi, R. Kanno, Y. Kawamoto, M. Tabuchi, O. Nakamura and M. Takano, *Solid State Ionics*, 1995, 82, 25–31.

125 J.-F. Dulac, *C. R. Acad. Sc. Paris.*, 1970, 270, 223.

126 Y. Miura, M. Sato, Y. Yamakawa, T. Habaguchi and Y. Ōno, *J. Phys. Soc. Japan*, 2009, 78, 094706.

127 B. Li, R. Shao, H. Yan, L. An, B. Zhang, H. Wei, J. Ma, D. Xia and X. Han, *Adv. Funct. Mater.*, 2016, 26, 1330–1337.

128 M. P. Jimenez-Segura, A. Ikeda, S. A. J. Kimber, C. Giacobbe, S. Yonezawa and Y. Maeno, *Phys. Rev. B*, 2016, 94, 1–8.

129 H. Kobayashi, R. Kanno, Y. Kawamoto, M. Tabuchi, O. Nakamura and M. Takano, *Solid State Ionics*, 1995, 82, 25–31.

130 M. Sathiya, K. Ramesha, G. Rousse, D. Foix, D. Gonbeau, a S. Prakash, M. L. Doublet, K. Hemalatha and J.-M. M. Tarascon, *Chem. Mater.*, 2013, 25, 1121–1131.

131 M. Sathiya, A. M. Abakumov, D. Foix, G. Rousse, K. Ramesha, M. Saubanère, M. L. Doublet, H. Vezin, C. P. Laisa, a S. Prakash, D. Gonbeau, G. VanTendeloo and J.-M. Tarascon, *Nat. Mater.*, 2015, 14, 230–8.

132 M. Sathiya, G. Rousse, K. Ramesha, C. P. Laisa, H. Vezin, M. T. Sougrati, M.-L. Doublet, D. Foix, D. Gonbeau, W. Walker, a S. Prakash, M. Ben Hassine, L. Dupont and J.-M. Tarascon, *Si Nat. Mater.*, 2013, 12, 827–35.

133 G. Assat and J. Tarascon, *Nat. Energy*, 2018, 3, 373–386.

134 L. Dahéron, R. Dedryvère, H. Martinez, M. Ménétrier, C. Denage, C. Delmas and D. Gonbeau, *Chem. Mater.*, 2007, 20, 583–590.

135 D. Seo, J. Lee, A. Urban, R. Malik, S. Kang and G. Ceder, *Nat. Chem.*, 2016, 8, 692–697.

136 W. E. Gent, K. Lim, Y. Liang, Q. Li, T. Barnes, S.-J. Ahn, K. H. Stone, M. McIntire, J. Hong, J. H. Song, Y. Li, A. Mehta, S. Ermon, T. Tyliszczak, D. Kilcoyne, D. Vine, J.-H. Park, S.-K. Doo, M. F. Toney, W. Yang, D. Prendergast and W. C. Chueh, *Nat. Commun.*, 2017, 8, 2091.

137 M. Sathiya, J.-B. Leriche, E. Salager, D. Gourier, J.-M. Tarascon and H. Vezin, *Nat. Commun.*, 2015, 6, 6276.

138 E. McCalla, A. M. Abakumov, M. Saubanère, D. Foix, E. J. Berg, G. Rousse, M.-L. Doublet, D. Gonbeau, P. Novák, G. Van Tendeloo, R. Dominko and J.-M. Tarascon, *Science*, 2015, 350, 1516–21.

139 A. R. Armstrong, M. Holzapfel, S. H. S. Kang, P. Nova, S. H. S. Kang, M. M. Thackeray, P. G. Bruce, L. Ni, L. Mn, A. R. Armstrong, M. Holzapfel, P. Nova and C. S. Johnson, *J. Am. Chem. Soc.*, 2006, 128, 8694–8698.

140 J. Hong, W. E. Gent, P. Xiao, K. Lim, D. Seo, J. Wu, P. M. Csernica, C. J. Takacs, D. Nordlund, C. Sun, K. H. Stone, D. Passarello, W. Yang, D.

Prendergast, G. Ceder, M. F. Toney and W. C. Chueh, *Nat. Mater.*, 2019, 18, 256–265.

141 W. Yang and T. P. Devereaux, *J. Power Sources*, 2018, 389, 188–197.

142 D. Foix, M. Sathiya, E. McCalla, J. M. Tarascon and D. Gonbeau, *J. Phys. Chem. C*, 2016, 120, 862–874.

143 W. S. Yoon, K. Y. Chung, J. McBreen, D. A. Fischer and X. Q. Yang, *J. Power Sources*, 2007, 174, 1015–1020.

144 F. Hennies, A. Pietzsch, M. Berglund, A. Föhlisch, T. Schmitt, V. Strocov, H. O. Karlsson, J. Andersson and J. E. Rubensson, *Phys. Rev. Lett.*, 2010, 104, 1–4.

145 Z. Zhuo, C. Das Pemmaraju, J. Vinson, C. Jia, B. Moritz, I. Lee, S. Sallies, Q. Li, J. Wu, K. Dai, Y. De Chuang, Z. Hussain, F. Pan, T. P. Devereaux and W. Yang, *J. Phys. Chem. Lett.*, 2018, 9, 6378–6384.

146 U. Maitra, R. A. House, J. W. Somerville, N. Tapia-Ruiz, J. G. Lozano, N. Guerrini, R. Hao, K. Luo, L. Jin, M. A. Pérez-Osorio, F. Massel, D. M. Pickup, S. Ramos, X. Lu, D. E. McNally, A. V. Chadwick, F. Giustino, T. Schmitt, L. C. Duda, M. R. Roberts and P. G. Bruce, *Nat. Chem.*, 2018, 10, 288–295.

147 K. Luo, M. R. Roberts, N. Guerrini, N. Tapia-ruiz, R. Hao, F. Massel, D. M. Pickup, S. Ramos, Y. Liu, J. Guo, A. V Chadwick, L. C. Duda and P. G. Bruce, 2016, 0–7.

148 J. Xu, M. Sun, R. Qiao, S. E. Renfrew, L. Ma, T. Wu, S. Hwang, D. Nordlund, D. Su, K. Amine, J. Lu, B. D. McCloskey, W. Yang and W. Tong, *Nat. Commun.*, 2018, 9, 1–10.

149 J. Keeler, *Understanding NMR spectroscopy*, John Wiley and Sons, Chichester, 1st edn., 2005.

150 M. J. Duer, *Introduction to Solid-State NMR Spectroscopy*, Blackwell Science, Oxford, 1st edn., 2004.

151 D. D. Laws, H.-M. L. Bitter and A. Jerschow, *Angew. Chemie Int. Ed.*, 2002, 41, 3096–3129.

152 C. P. Grey and N. Dupré, *Chem. Rev.*, 2004, 104, 4493–4512.

153 R. J. Kurland and B. R. McGarvey, *J. Magn. Reson.*, 1970, 2, 286–301.

154 I. Bertini, C. Luchinat and G. Parigi, *Prog. Nucl. Magn. Reson. Spectrosc.*, 2002, 40, 249–273.

155 D. Carlier, M. Ménétrier, C. Grey, C. Delmas and G. Ceder, *Phys. Rev. B*, 2003, 67, 1–14.

156 S. E. Ashbrook and S. Wimperis, in *Encyclopedia of Magnetic Resonance*, John Wiley & Sons, Ltd, Chichester, UK, 2009.

157 A. J. Vega, in *eMagRes*, American Cancer Society, 2010.

158 C. P. Grey and Y. J. Lee, *Solid State Sci.*, 2003, 5, 883–894.

159 O. Pecher, J. Carretero-Gonzalez, K. J. Griffith and C. P. Grey, *Chem. Mater.*, 2017, 29, 213–242.

160 Y. J. Lee, F. Wang and C. P. Grey, *J. Am. Chem. Soc.*, 1998, 120, 12601–12613.

161 D. Zeng, J. Cabana, W. S. Yoon and C. P. Grey, *Chem. Mater.*, 2010, 22, 1209–1219.

162 D. Zeng, J. Cabana, J. Bréger, W.-S. Yoon and C. P. Grey, *Chem. Mater.*, 2007, 19, 6277–6289.

163 D. S. Middlemiss, A. J. Ilott, R. J. Clément, F. C. Strobridge, C. P. Grey, D. S. Middlemiss, A. J. Ilott, R. J. Clément, F. C. Strobridge, C. P. Grey, D. S. Middlemiss, A. J. Ilott, R. J. Clément, F. C. Strobridge and C. P. Grey, *Chem.*

Mater., 2013, 25, 1723–1734.

164 W. D. Knight, *Philos. Mag. B Phys. Condens. Matter; Stat. Mech. Electron. Opt. Magn. Prop.*, 1999, 79, 1231–1237.

165 M. H. Levitt, *Spin Dynamics : Basics of Nuclear Magnetic Resonance*, 2000.

166 J. R. Norris, *Chem. Phys. Lett.*, 1967, 1, 333–334.

167 R. W. Schurko, *Acc. Chem. Res.*, 2013, 46, 1985–1995.

168 H. E. Rhodes, P. K. Wang, H. T. Stokes, C. P. Slichter and J. H. Sinfelt, *Phys. Rev. B*, 1982, 26, 3559–3568.

169 H. E. Rhodes, P. K. Wang, C. D. Makowka, S. L. Rudaz, H. T. Stokes, C. P. Slichter and J. H. Sinfelt, *Phys. Rev. B*, 1982, 26, 3569–3574.

170 H. T. Stokes, H. E. Rhodes, P. K. Wang, C. P. Slichter and J. H. Sinfelt, *Phys. Rev. B*, 1982, 26, 3575–3581.

171 Y. Y. Tong, *J. Magn. Reson. - Ser. A*, 1996, 119, 22–28.

172 A. J. Pell, R. J. Clément, C. P. Grey, L. Emsley and G. Pintacuda, *J. Chem. Phys.*, 2013, 138, 114201.

173 O. Pecher, D. M. Halat, J. Lee, Z. Liu, K. J. Griffith, M. Braun and C. P. Grey, *J. Magn. Reson.*, 2017, 275, 127–136.

174 M. Guilmard, L. Croguennec and C. Delmas, *Chem. Mater.*, 2003, 15, 4484–4493.

175 M. Guilmard, L. Croguennec, D. Denux and C. Delmas, *Chem. Mater.*, 2003, 15, 4476–4483.

176 N. M. Trease, I. D. Seymour, M. Radin, H. Liu, H. Liu, S. Hy, N. Chernova, P. Parikh, A. Devaraj, K. M. Wiaderek, P. J. Chupas, K. W. Chapman, M. S. Whittingham, Y. S. Meng, A. Van der Ven and C. P. Grey, *Chem. Mater.*, 2016, acs.chemmater.6b02797.

177 B. M. May, J. Serrano-Sevillano, A. L. Dauphin, A. Nazib, N. Lima, M. Casas-Cabanas and J. Cabana, *J. Electrochem. Soc.*, 2018, 165, A3537–A3543.

178 N. V. Faenza, L. Bruce, Z. W. Lebens-Higgins, I. Plitz, N. Pereira, L. F. J. Piper and G. G. Amatucci, *J. Electrochem. Soc.*, 2017, 164, A3727–A3741.

179 P. J. Reeves, I. D. Seymour, K. J. Griffith and C. P. Grey, *Chem. Mater.*, 2019, 31, 2814–2821.

180 H. Liu, H. Liu, I. D. Seymour, N. Chernova, K. M. Wiaderek, N. M. Trease, S. Hy, Y. Chen, K. An, M. Zhang, O. J. Borkiewicz, S. H. Lapidus, B. Qiu, Y. Xia, Z. Liu, P. J. Chupas, K. W. Chapman, M. S. Whittingham, C. P. Grey and Y. S. Meng, *J. Mater. Chem. A*, 2018, 6, 4189–4198.

181 A. A. Coelho, *J. Appl. Crystallogr.*, 2018, 51, 210–218.

182 A. Bielecki and D. P. Burum, *J. Magn. Reson. Ser. A*, 1995, 116, 215–220.

183 F. Dogan, J. T. Vaughey, H. Iddir and B. Key, *ACS Appl. Mater. Interfaces*, 2016, 8, 16708–16717.

184 M. Ménétrier, C. Vaysse, L. Croguennec, C. Delmas, C. Jordy, F. Bonhomme and P. Biensan, *Electrochem. Solid-State Lett.*, 2004, 7, 140–143.

185 C. Chazel, M. Ménétrier, L. Croguennec and C. Delmas, *Magn. Reson. Chem.*, 2005, 43, 849–857.

186 M. E. MacKenzie, K. J. D.; Smith, *Multinuclear Solid-State Nuclear Magnetic Resonance of Inorganic Materials*, 2002.

187 D. Massiot, F. Fayon, M. Capron, I. King, S. Le Calvé, B. Alonso, J. O. Durand, B. Bujoli, Z. Gan and G. Hoatson, *Magn. Reson. Chem.*, 2002, 40, 70–76.

188 F. Vernay, K. Penc, P. Fazekas and F. Mila, *Phys. Rev. B - Condens. Matter Mater. Phys.*, 2004, 70, 1–17.

189 A. J. Pell, G. Pintacuda and C. P. Grey, *Prog. Nucl. Magn. Reson. Spectrosc.*, 2019.

190 C. P. Grey, C. M. Dobson and A. K. Cheetham, *J. Magn. Reson.*, 1992, 98, 414–420.

191 P. C. Tsai, B. Wen, M. Wolfman, M. J. Choe, M. S. Pan, L. Su, K. Thornton, J. Cabana and Y. M. Chiang, *Energy Environ. Sci.*, 2018, 11, 860–871.

192 R. Amin, D. B. Ravnsbæk and Y.-M. Chiang, *J. Electrochem. Soc.*, 2015, 162, A1163–A1169.

193 R. Amin and Y.-M. Chiang, *J. Electrochem. Soc.*, 2016, 163, X7–X7.

194 A. Grenier, H. Liu, K. M. Wiaderek, Z. W. Lebens-Higgins, O. J. Borkiewicz, L. F. J. Piper, P. J. Chupas and K. W. Chapman, *Chem. Mater.*, 2017, 29, 7345–7352.

195 Y. Makimura, T. Sasaki, T. Nonaka, Y. F. Nishimura, T. Uyama, C. Okuda, Y. Itou and Y. Takeuchi, *J. Mater. Chem. A*, 2016, 4, 8350–8358.

196 A. Grenier, P. J. Reeves, H. Liu, K. M. Wiaderek, I. D. Seymour, C. P. Grey, P. J. Chupas and K. W. Chapman, *Intrinsic Kinetic Limitations in Ni-Containing/Substituted Layered Transition-Metal Oxide Electrodes. (in preparation)*, .

197 J. P. Peres, C. Delmas, A. Rougier, M. Broussely, F. Perton, P. Biensan and P. Willmann, *J. Phys. Chem. Solids*, 1996, 57, 1057–1060.

198 K. Kang and G. Ceder, *Phys. Rev. B - Condens. Matter Mater. Phys.*, 2006, 74, 1–7.

199 I. Saadoune, M. Ménétrier and C. Delmas, *J. Mater. Chem.*, 1997, 7, 2505–2511.

200 R. Dupree, M. H. Lewis and M. E. Smith, *J. Appl. Crystallogr.*, 1988, 21, 109–

116.

201 A. Yamasaki, *J. Coord. Chem.*, 1991, 24, 211–260.

202 J. W. Emsley, J. Feeney and L. H. Sutcliffe, *High Resolution Nuclear Magnetic Resonance Spectroscopy, Volume 2*, Pergamon, Oxford, 2nd edn., 1965.

203 I. Nakai, K. Takahashi, Y. Shiraishi, T. Nakagome and F. Nishikawa, *J. Solid State Chem.*, 1998, 140, 145–148.

204 H. Liu, H. Liu, I. D. Seymour, N. Chernova, K. M. Wiaderek, N. M. Trease, S. Hy, Y. Chen, K. An, M. Zhang, O. J. Borkiewicz, S. H. Lapidus, B. Qiu, Y. Xia, Z. Liu, P. J. Chupas, K. W. Chapman, M. S. Whittingham, C. P. Grey and Y. S. Meng, *J. Mater. Chem. A*, 2018, 4189–4198.

205 A. Grenier, H. Liu, K. M. Wiaderek, Z. W. Lebens-Higgins, O. J. Borkiewicz, L. F. J. Piper, P. J. Chupas and K. W. Chapman, *Chem. Mater.*, 2017, 29, 7345–7352.

206 H. Liu, M. Wolf, K. Karki, Y. Yu, E. A. Stach, J. Cabana, K. W. Chapman and P. J. Chupas, , DOI:10.1021/acs.nanolett.7b00379.

207 T. Mizokawa, Y. Wakisaka, T. Sudayama, C. Iwai, K. Miyoshi, J. Takeuchi, H. Wadati, D. G. Hawthorn, T. Z. Regier and G. A. Sawatzky, *Phys. Rev. Lett.*, 2013, 111, 1–5.

208 M. Saubanere, E. McCalla, J.-M. Tarascon and M.-L. Doublet, *Energy Environ. Sci.*, 2016, 984–991.

209 D. H. Seo, J. Lee, A. Urban, R. Malik, S. Kang and G. Ceder, *Nat. Chem.*, 2016, 8, 692–697.

210 C. Pan, Y. J. Lee, B. Ammundsen and C. P. Grey, *Chem. Mater.*, 2002, 14, 2289–2299.

211 B. Ammundsen, J. Paulsen, I. Davidson, R.-S. Liu, C.-H. Shen, J.-M. Chen, L.-Y. Jang and J.-F. Lee, *J. Electrochem. Soc.*, 2002, 149, A431.

212 Y. Miura, Y. Yasui, M. Sato, N. Igawa and K. Kakurai, *J. Phys. Soc. Japan*, 2007, 76, 2–5.

213 J.-G. J. Park, T.-Y. Tan, D. T. Adroja, A. Daoud-Aladine, S. Choi, D.-Y. Cho, S. Lee, J. Kim, H. Sim, T. Morioka, H. Nojiri, V. V. Krishnamurthy, P. Manuel, M. R. Lees, S. V. Streltsov, D. I. Khomskii and J.-G. J. Park, *Sci. Rep.*, 2016, 6, 25238.

214 G. Jackeli and D. I. Khomskii, *Phys. Rev. Lett.*, 2008, 100, 1–4.

215 S. A. J. Kimber, I. I. Mazin, J. Shen, H. O. Jeschke, S. V. Streltsov, D. N. Argyriou, R. Valentí and D. I. Khomskii, *Phys. Rev. B - Condens. Matter Mater. Phys.*, 2014, 89, 1–5.

216 K. R. Thurber and R. Tycko, *J. Magn. Reson.*, 2009, 196, 84–87.

217 B. H. Toby and R. B. Von Dreele, *J. Appl. Crystallogr.*, 2013, 46, 544–549.

218 G. A. Bain and J. F. Berry, *J. Chem. Educ.*, 2008, 85, 532–536.

219 D. J. Singh and L. Nordström, *Planewaves, Pseudopotentials and the LAPW Method*, Springer US, New York, 2nd edn., 2006.

220 L. Nordström, G. K. H. Madsen, P. Blaha, K. Schwarz and E. Sjöstedt, *Phys. Rev. B - Condens. Matter Mater. Phys.*, 2001, 64, 1–9.

221 The Elk Code., http://elk.sourceforge.net/, (accessed 8 March 2019).

222 J. Kim, D. S. Middlemiss, N. A. Chernova, B. Y. X. Zhu, C. Masquelier and C. P. Grey, *J. Am. Chem. Soc.*, 2010, 132, 16825–16840.

223 R. J. Clément, D. S. Middlemiss, I. D. Seymour, A. J. Ilott and C. P. Grey, *Chem. Mater.*, 2016, 28, 8228–8239.

224 D. S. Middlemiss, A. J. Ilott, R. J. Clément, F. C. Strobridge and C. P. Grey, *Chem. Mater.*, 2013, 25, 1723–1734.

225 F. T. and L. D. M. P. Blaha, K. Schwarz, G. K. H. Madsen, D. Kvasnicka, J. Luitz, R. Laskowski, *WIEN2k, An Augmented Plane Wave + Local Orbitals Program for Calculating Crystal Properties*, Karlheinz Schwarz, Techn. Universität Wien, Austria2018. ISBN 3-9501031-1-2, 2018.

226 A. Castets, D. Carlier, Y. Zhang, F. Boucher, N. Marx, L. Croguennec and M. Ménétrier, *J. Phys. Chem. C*, 2011, 115, 16234–16241.

227 Y. Zhang, A. Castets, D. Carlier, M. Ménétrier and F. Boucher, *J. Phys. Chem. C*, 2012, 116, 17393–17402.

228 J. P. Perdew, K. Burke and M. Ernzerhof, *Phys. Rev. Lett.*, 1996, 77, 3865–3868.

229 B. A. Ivanov and E. V. Tartakovskaya, *Phys. Rev. Lett.*, 1996, 77, 386–389.

230 S. Blügel, H. Akai, R. Zeller and P. H. Dederichs, *Phys. Rev. B*, 1987, 35, 3271–3283.

231 K. Hoang, M. Oh and Y. Choi, *ACS Appl. Electron. Mater.*, 2018, 1, 75–81.

232 J. C. Wang, J. Terzic, T. F. Qi, F. Ye, S. J. Yuan, S. Aswartham, S. V. Streltsov, D. I. Khomskii, R. K. Kaul and G. Cao, *Phys. Rev. B - Condens. Matter Mater. Phys.*, 2014, 90, 1–6.

233 M. P. Jimenez-Segura, A. Ikeda, S. Yonezawa and Y. Maeno, *Phys. Rev. B*, 2016, 93, 1–6.

234 E. Salager, V. Sarou-Kanian, M. Sathiya, M. Tang, J.-B. Leriche, P. Melin, Z. Wang, H. Vezin, C. Bessada, M. Deschamps and J.-M. Tarascon, *Chem. Mater.*, 2014, 26, 7009–7019.

235 I. Y. Arapova, A. L. Buzlukov, A. Y. Germov, K. N. Mikhalev, T.-Y. Tan, J.-G.

Park and S. V. Streltsov, *JETP Lett.*, 2017, 105, 375.

236 S. Lee, S. Choi, J. Kim and H. Sim, *J. Phys. Condens. Matter*, 2012, 24, 456004.

237 Y. Y. Hu, Z. Liu, K. W. Nam, O. J. Borkiewicz, J. Cheng, X. Hua, M. T. Dunstan, X. Yu, K. M. Wiaderek, L. S. Du, K. W. Chapman, P. J. Chupas, X. Q. Yang and C. P. Grey, *Nat. Mater.*, 2013, 12, 1130–1136.

238 T. J. Bastow, P. J. Dirken, M. E. Smith and H. J. Whitfield, *J. Phys. Chem.*, 1996, 100, 18539–18545.

239 M. D. Johannes, A. M. Stux and K. E. Swider-Lyons, *Phys. Rev. B - Condens. Matter Mater. Phys.*, 2008, 77, 075124.

240 D. Mori, H. Kobayashi, T. Okumura, H. Nitani, M. Ogawa, Y. Inaguma, D. Mori, H. Kobayashi, H. Nitani and Y. Inaguma, *Solid State Ionics*, 2016, 285, 66–74.

241 F. Zheng, S. Zheng, P. Zhang, X. Zhang, S. Wu, Y. Yang and Z. Z. Zhu, *J. Phys. Chem. C*, 2019, 123, 13491–13499.

242 K. Mukai, Y. Kishida, H. Nozaki and K. Dohmae, *Chem. Mater.*, 2013, 25, 2828–2837.

243 G. Assat, A. Iadecola, C. Delacourt, R. Dedryvère and J.-M. Tarascon, *Chem. Mater.*, 2017, 29, 9714–9724.

244 G. G. Amatucci, *J. Electrochem. Soc.*, 1996, 143, 1114.

245 A. O. Kondrakov, H. Geßwein, K. Galdina, L. de Biasi, V. Meded, E. O. Filatova, G. Schumacher, W. Wenzel, P. Hartmann, T. Brezesinski and J. Janek, *J. Phys. Chem. C*, 2017, 121, 24381–24388.

246 A. Van Der Ven, M. K. Aydinol and G. Ceder, *J. Electrochem. Soc.*, 1998, 145, 2149–2155.

247 H. Kobayashi, R. Kanno, Y. Kawamoto, M. Tabuchi and O. Nakamura, *Solid*

State Ionics, 1996, 86–88, 859–863.

248 A. J. Browne, C. Lithgow, S. A. J. Kimber and J. P. Attfield, *Inorg. Chem.*, 2018, 57, 2815–2822.

249 Y. Horibe, M. Shingu, K. Kurushima, H. Ishibashi, N. Ikeda, K. Kato, Y. Motome, N. Furukawa, S. Mori and T. Katsufuji, *Phys. Rev. Lett.*, 2006, 96, 2–5.

250 S. V Streltsov and D. I. Khomskii, *Physics-Uspekhi*, 2017, 60, 1121–1146.

251 S. Streltsov, I. I. Mazin and K. Foyevtsova, *Phys. Rev. B - Condens. Matter Mater. Phys.*, 2015, 92, 4–8.

252 H. F. Pen, J. Van den Brink, D. I. Khomskii and G. A. Sawatzky, *Phys. Rev. Lett.*, 1997, 78, 1323–1326.

253 B. Mortemard De Boisse, G. Liu, J. Ma, S. I. Nishimura, S. C. Chung, H. Kiuchi, Y. Harada, J. Kikkawa, Y. Kobayashi, M. Okubo and A. Yamada, *Nat. Commun.*, 2016, 7, 1–9.

254 M. Leskes, N. E. Drewett, L. J. Hardwick, P. G. Bruce, G. R. Goward and C. P. Grey, *Angew. Chemie - Int. Ed.*, 2012, 51, 8560–8563.

255 M. Leskes, A. J. Moore, G. R. Goward and C. P. Grey, *J. Phys. Chem. C*, 2013, 117, 26929–26939.

256 B. Xu, C. R. Fell, M. Chi and Y. S. Meng, *Energy Environ. Sci.*, 2011, 4, 2223.

257 A. R. Armstrong, N. Dupre, A. J. Paterson, C. P. Grey and P. G. Bruce, *Chem. Mater.*, 2004, 16, 3106–3118.

258 G. Assat, D. Foix, C. Delacourt, A. Iadecola, R. Dedryvère and J. M. Tarascon, *Nat. Commun.*, , DOI:10.1038/s41467-017-02291-9.

259 D. M. Halat, R. Dervişoğlu, G. Kim, M. T. Dunstan, F. Blanc, D. S. Middlemiss

and C. P. Grey, *J. Am. Chem. Soc.*, 2016, 138, 11958–11969.

260 P. Glans, K. Gunnelin, P. Skytt, J.-H. Guo, N. Wassdahl, J. Nordgren, H. Ågren, F. K. Gel'mukhanov, T. Warwick and E. Rotenberg, *Phys. Rev. Lett.*, 1996, 76, 2448–2451.

261 R. A. House, U. Maitra, M. A. Pérez-Osorio, J. G. Lozano, L. Jin, J. W. Somerville, L. C. Duda, A. Nag, A. Walters, K. J. Zhou, M. R. Roberts and P. G. Bruce, *Nature*, 2020, 577, 502–508.

262 A. Grimaud, W. T. Hong, Y. Shao-Horn and J. M. Tarascon, *Nat. Mater.*, 2016, 15, 121–126.

263 P. A. Lee, N. Nagaosa and X.-G. Wen, *Rev. Mod. Phys.*, 2004, 78, 1–69.